# Simulations of Laser Propagation and X-Ray Radiation Generation in Laser Wakefield Accelerators

by

Paul G. Cummings

A dissertation submitted in partial fulfillment
of the requirements for the degree of
Doctor of Philosophy
(Nuclear Engineering and Radiological Sciences)
in The University of Michigan
2014

Doctoral Committee:

Assistant Professor Alexander G. R. Thomas, Chair
Professor R. Paul Drake
Professor Karl M. Krushelnick
Professor Mark Kushner
Doctor Igor V. Sokolov

"A ship in port is safe. But that's not what ships were built for."-RADM Grace M. Hopper

To my parents, who never let me settle for anything less than the best from myself.

To my brother and sister, for supporting and inspiring me.

To my grandparents, for encouraging and believing in me.

To my friends, for putting up with me and keeping me honest.

And most of all,

For Simon.

# ACKNOWLEDGEMENTS

Listing and properly thanking everyone who has helped me get to this point would require a second dissertation. First, I want to thank my current advisor, Professor Alec Thomas. Your help, guidance, and encouragement as I worked on this research went a long way towards making my time at the University of Michigan as memorable as it was. I've heard it said that a good teacher is the difference between loving and hating a subject; you certainly proved the truth of that. I would also like to thank my first advisor, Professor John Foster, without whom I almost certainly wouldn't be here.

I also owe a bottomless thanks to my friends and colleagues, both here in the NERS department and elsewhere. Ann Arbor holds, and will always hold, an irreplaceably special place in my heart, and it's entirely because the people who lived and continue to live here. Your guidance, advice, love, and commiseration are another main reason I've managed to make it as far as I have.

Finally, I'd like to thank my family, who has been incredibly supportive of me from start to finish. Whether it's advice, shelter, an encouraging pep-talk, or a sharp smack upside the head, you've never hesitated to give me what I need, and are a constant source of motivation for me as I do my work. Mom, Dad, Alex, Elizabeth, Sam, and Simon ... I love you guys. Thank you so much.

# TABLE OF CONTENTS

# LIST OF FIGURES

**Figure**

# LIST OF APPENDICES

**Appendix**

# ABSTRACT

Simulations of Laser Propagation and X-Ray Radiation Generation in Laser Wakefield Accelerators

by

Paul G. Cummings Jr.

Chair: Alec G. R. Thomas

Chief among the advantages of of the laser-wakefield accelerator scheme is the generation of short, bright x-rays via the betatron motion of electrons in the wake fields. In addition to being useful for applications in its own right, this radiation can be used as a non-invasive diagnostic for the electron beam properties. In this dissertation, we explore the generation of betatron radiation in laser-wake-field acceleration (LWFA) experiments using particle-in-cell (PIC) simulations coupled to a Monte Carlo radiation generation algorithm.

First, we discuss the theoretical background necessary for this dissertation. Models of basic plasma physics, the particular physics of LWFA, radiation generation by charged particles, betatron motion in LWFA, and plasma optics are all presented and discussed. Additionally, we discuss the computational background necessary for the work presented in this dissertation. Methods in computational electrodynamics and plamsa physics are presented, including the basic concepts of the PIC method. Finally, the particular implementation of the PIC method used in the OSIRIS 2.0 code is presented.

Second, the method used to simulate the generation of radiation is presented, along with results from verification simulations. Detailed descriptions of the theoretical, computational, and algorithmic underpinnings of the technique are given. The results from verification simulations of electrons undergoing basic cyclotron are presented, and compared to theory. These verification simulations show excellent agreement with the theory across a wide range of radii of curvature and electron energies.

Third, we present the results from three basic LWFA parameter sweeps performed using the aforementioned method. Results from a parameter sweep over the normalized laser vector potential $a_0$ are presented and discussed. Scalings from this sweep, both between $a_0$ and total the radiated energy and between $a_0$ and the effective temperature of the emitted radiation, are established and found to be in good agreement with analytic predictions. Results from a parameter sweep over the electron plasma density $n_e$ are presented. Scalings from this sweep are also presented, and found to diverge from analytic predictions, which we attribute to the electron beam re-entering the bulk plasma and undergoing a hosing instability. Results from a simulation with an unusually long propagation distance, used to affect a parameter sweep over the propagation length, are analyzed. Further evidence of the aforementioned hosing instability is evident in this simulation, and its impact on the generated radiation is established.

Finally, we present the results from two different, related parameter sweeps. The first investigated the impact of the presence of a comatic aberration on the performance of a LWFA system as an electron accelerator. Relationships between the electron beam parameters and severity of the coma are commented upon. Scalings between the coma severity parameter $\alpha$ and the electron beam energy, beam current, and beam emittance are established; the peak electron beam energy and electron energy spectral spread were found to be relatively unaffected by the presence of even a severe coma, while the beam emittance was found to increase with coma severity in

the laser polarization direction.

The second parameter sweep investigated the impact of the presence of a comatic aberration on the synchrotron-like radiation produced by the LWFA system. Results from this parameter sweep are presented and analyzed. Scalings between the coma severity parameter $\alpha$ and both the total radiated energy and emitted radiation temperature are calculated, where appropriate. The affects of varying the relative directions of laser polarization and coma asymmetry on both of these scalings are considered. A clear relationship between the coma severity and total emitted energy is found; as the coma severity is increased, the total radiated energy initially increases by $\sim 20\%$, then decreases by roughly the same amount.

The main conclusion drawn from this work is that radiation emission in LWFA can be driven by many different affects depending on the particular LWFA parameters. Contemporary analytic models of betatron radiation in LWFA are based on the dynamics of single electrons oscillating in ion channels. Simulation results presented in this dissertation indicate that interaction with the wake-field, interaction with the laser field, and/or hosing instabilities caused by the electron beam interacting with the bulk plasma may all dominate the electron beam's betatron motion, depending on the laser vector potential, plasma density, and/or laser propagation distance.

# CHAPTER I

# Introduction

## 1.1 Overview & Outline

The following is a dissertation representing the cumulation of the author's research in pursuit of a doctor of philosophy in nuclear engineering and radiological sciences at the University of Michigan. The subject of the dissertation is the generation of synchrotron-like and betatron radiation from the motion of electrons during laser wake-field acceleration. The research was pursued computationally, using a series of simulations. This dissertation is organized as follows:

1. The remainder of this initial chapter will present the background and motivation for this research, as well as a review of the current state of the literature relating to the subject.

2. Chapter 2 will present abridged derivations of the physical theories and concepts which describe the phenomena being investigated in this dissertation.

3. Chapter 3 will present summaries of the established, pre-existing computational concepts and methodologies used.

4. Chapter 4 will present detailed explanations of the theory and methodologies underlying the new algorithm for radiation generation that was used for this

dissertation, as well as results from validation simulations used to verify the accuracy of the new algorithm.

5. Chapter 5 will present the results from using the algorithm to explore the relationship between the LWFA system parameters, the electron beam properties, and the radiation parameters.

6. Chapter 6 will present the results from research investigating the relationship between the performance of a laser wake-field acceleration-based electron accelerator and the presence of a comatic aberration in the driving laser pulse, as well as the relationship between the radiation generated and the presence of a comatic aberration.

7. Chapter 7 will present a summary of the results, a conclusion, and possible avenues for future work.

8. Appendix A will present a more detailed physical derivation of the one-dimensional generation of a plasma wake in response to an ultrashort laser pulse.

9. Appendix B will present a reproduction of the electron beam results from Chapter 6, as they were published by the author in the journal Physics of Plasmas.

## 1.2 Particle Acceleration

### 1.2.1 History & Overview

For almost a century, the technology to accelerate subatomic particles to highly relativistic energies has been one of humanity's most important tools for expanding our understanding of the universe. Initially, particle acceleration technology consisted of simple direct-current (DC) voltage, electrostatic accelerators. The maximum particle energy such a device can achieve is limited by the maximum voltage it can

sustain before undergoing breakdown. Tandem devices, and later staged devices like the Cockroft-Walton, were used to increase this maximum energy.

However, a far more efficient mechanism of acceleration was soon discovered based on alternating current voltage. By using a radio-frequency (RF) voltage applied to a cavity, and with careful tuning of the frequency and beam timing, the accelerating field can be maintained in phase with the accelerated beam. This mechanism was used in linear accelerators (LINAC), but also allowed the construction of circular accelerators, such as betatrons, cyclotrons, and synchrotrons, where magnets are used to curve the trajectory of the accelerated particles in a circle, such that the same acceleration stage can be used to impart energy to the beam over and over again.

Circular accelerators were not without their drawbacks, however. A charged particle being accelerated on a curved path of radius $\rho$ emits radiation with a power $P$ that scales with the particle energy $E$ as $P \sim E^4/\rho$ [3]. Nevertheless, the synchrotron remains a successful design for ion acceleration; high-energy synchrotrons have been used to validate the Standard Model, synthesize new elements, and push the boundaries of our understanding of the universe.

### 1.2.2 Accelerator-Based Light Sources

The phenomenon of synchrotron radiation was initially considered a drawback; it was a major energy loss mechanism in circular accelerators. For electrons, this loss mechanism is severe enough that linear accelerators are considered the only option for achieving high particle energies. For example, the design for the proposed International Linear Collider [4], which would be one of the largest electron accelerators ever build, is a linear accelerator. However, many applications for this radiation have been discovered; consequently many modern devices are designed to deliberately generate this radiation via a number of mechanisms.

One technique for harnessing this radiation is to simply construct a circular electron accelerator, and allow it to operate in a regime where the energy imparted by the accelerating RF cavity is matched by the energy lost to synchrotron radiation. In such a device, whenever the electron beam passes through a bending magnet, radiation is emitted.

Another very successful technique consists of passing a linear electron beam through a series of alternating-polarity magnetic fields, causing the beam to undergo transverse oscillations as it propagates. Such devices are characterized by the wiggler parameter $K = \gamma\psi$, where $\gamma$ is the lorentz factor $\gamma$ of the electron beam and $\psi$ is the maximum angle reached by the beam's trajectory relative to the propagation direction [5]. For $K >> 1$, such a device is known as a "wiggler," and generates a broad spectrum of radiation. For $K << 1$, such a device is known as an "undulator," and generates radiation in a narrow bandwidth around a characteristic frequency. More detail about the physics of these devices is given in Chapter 2 of this dissertation.

Additionally, devices operating in the undulator regime can be constructed such that the emitted radiation is amplified due to a stimulated emission effect as it propagates along the device; such devices are known as "free electron lasers (FEL)." In an FEL, the generated radiation and electron beam co-propagate; consequently, the electron beam forms a sequence of bunches as it interacts with the light. These bunches oscillate at the dominant radiation frequency (in the electron beam's center-of-mass frame, not the laboratory frame), coherently contributing to the radiation at that frequency and creating stimulated emission.

### 1.2.3 Current Facilities

The ubiquity of accelerator-based light sources is a testament to their usefulness. For example, the French Soleil [6] facility possess a 90-period undulator which generates radiation with a photon energy range of $3 - 18keV$. The Swiss Light Source [7]

generates radiation with a photon energy range of $5 - 40keV$. These sources do not use the stimulated emission effect associated with FELs.

For decades, the highest-energy electron accelerator in the world was the Stanford Linear Accelerator (SLAC), capable of generating $50GeV$ electron beams. So useful are the aforementioned accelerator-based light sources, however, that SLAC was converted to a free-electron laser known as the Linac Coherent Light Source (LCLS) [8]. The LCLS was the first x-ray free-electron laser in the world, providing $100fs$ pulses at a repetition rate of $60Hz$, with a photon energy range of $0.48 - 10keV$ [8]. An aerial image of some of the target facilities at SLAC is shown in Figure 1.1.

Figure 1.1: An aerial image of the Stanford Linear Accelerator [1]

LCLS is by no means the only operational FEL. The Free-Electron Laser in Hamburg (FLASH) [9] has produced coherent light pulses in a photon energy range of $200 - 300eV$. Even larger FELs are currently under construction, or being considered for construction. The European X-Ray Free-Electron Laser (XFEL) [10] is currently under construction, and is designed to use a $17.5GeV$ electron beam to produce $100fs$ pulses.

### 1.2.4 Applications

Electron accelerators have a host of applications, beyond serving as the source for FELs [11]. As sources of high-energy electrons, they can be used in nanofabrication via electron beam lithography [12], or as electron sources for radiation medicine [13]. Of course, the popularity of electron-accelerator-based light sources is due to their host of applications, including:

1. Interrogating for the presence of special nuclear materials via nuclear resonance fluorescence [14]

2. Nuclear transmutation and induced fission via photonuclear reactions [15], [16], [17], [18]

3. Probing crystalline structures via nuclear resonant scattering and absorption [19], [20]

4. Analyzing intermediate states in fast chemical reactions [21]

5. High-pressure macromolecular crystallography [22]

6. Protein crystallography (specifically, determining the structure of viruses) [23], [24], [25]

## 1.3 Laser Wake-Field Acceleration

### 1.3.1 History & Overview

The RF cavities used in modern electron accelerators are still fundamentally limited by the onset of breakdown. This places an upper limit on the maximum electric field, and consequently on the maximum accelerating gradient, these devices can maintain. For example, the proposed design for the Compact Linear Collider is projected to maintain an accelerating gradient of $\sim 107 MeV/m$ [26]. This means that,

in order to achieve electron energies on the order of $\sim 100GeV$, physical device scales on the order of $1km$ are needed.

Consequently, alternative acceleration schemes that could maintain larger gradients, and subsequently reduce these large device scales, are a subject of significant interest. One potential mechanism for particle acceleration is the ponderomotive force (see Chapter 2), which acts opposite direction of the laser intensity gradient, i.e. it acts to expel charged particles from regions of higher intensity towards regions of lower intensity.. Using the laser pulse to directly accelerate electrons is known as Direct Laser Acceleration (DLA) [27].

Another laser-based particle acceleration is laser wake-field acceleration (LWFA), where a nonlinear plasma wave is driven by a high-intensity, short-pulse laser. This mechanism was originally proposed in 1979 [28]; however contemporary laser technology was not capable of achieving the necessary parameters when the LWFA scheme was proposed. Specifically, the LWFA scheme as originally proposed required a pulse length comparable to the plasma wavelength; the first lasers used in LWFA experiments had pulse durations much longer than this. These limits were circumvented by using two lasers of slightly different frequencies to form a beat pattern in the laser envelope whose spacing was comparable to the plasma wavelength; this scheme was known as plasma beat wave acceleration [29], [30]. This scheme was validated by using a carbon dioxide laser to generate the beat waves, which were used to accelerate externally injected electrons [31]. Another approach to this scheme was to use the self-modulation of the laser [32], [33], [34], [35], [36], which is a plasma optics phenomenon discussed further in Chapter 2. These schemes relied upon wave-breaking to inject electrons into the wake structure [37], [38].

Sufficiently short ($< 100fs$) laser pulses allowed LWFA to operate in the forced regime [39], [40], and eventually the bubble regime, which will be discussed in Chapter 2. Operating in this regime, which allowed for electrons to be injected via self-injection

(also discussed in Chapter 2), three groups independently observed $\sim 100MeV$ quasi-monoenergetic beams in 2004 [41], [42], [43]. In 2006, a relatively high-quality, $\sim 1GeV$, beam was generated using a $3.3cm$ capillary discharge tube [44]. Particle acceleration via LWFA is a robust and established field for electron acceleration [45], [46], [47].

### 1.3.2 LWFA as an X-Ray Source

It is abundantly clear that LWFA is a robust method for generating high-energy electron beams. It has also been made clear that a major application of high-energy electron beams is a source of synchrotron x-rays. It is no surprise, therefore, that the generation of x-rays via synchrotron-like radiation is an important application for LWFA-based systems. One obvious motivation for LWFA as an x-ray source is the previously-mentioned reduction in device scale size for a given electron energy. Another motivation is the time-scale of the emitted radiation; the duration of the electron beam generated in a LWFA experiment is comparable to that of the laser pulse; consequently, LWFA systems are capable of producing femtosecond-time-scale bursts of x-ray radiation, permitting the investigation of ultrafast phenomenon.

The feasibility of using LWFA as an x-ray source was computationally demonstrated in 2004 [48], [49]. It was shown that self-injected electrons in the bubble regime undergo betatron oscillations because of the transverse fields of the plasma wake. Additionally, it was shown that an externally injected $28.5GeV$ electron beam emitted x-rays with a spectral peak at $210MeV$, and peak photon energies of up to $10GeV$. In 2010, it was experimentally demonstrated [2] that the x-rays generated by LWFA exhibit a high degree of spatial coherence, making them ideally suited for high-resolution micro-scale imaging; the high resolution achieved in these experiments is shown in Figure 1.2. Further theoretical work has established scalings between the LWFA and plasma parameters and the effective wiggler parameters for the generated

radiation [50].

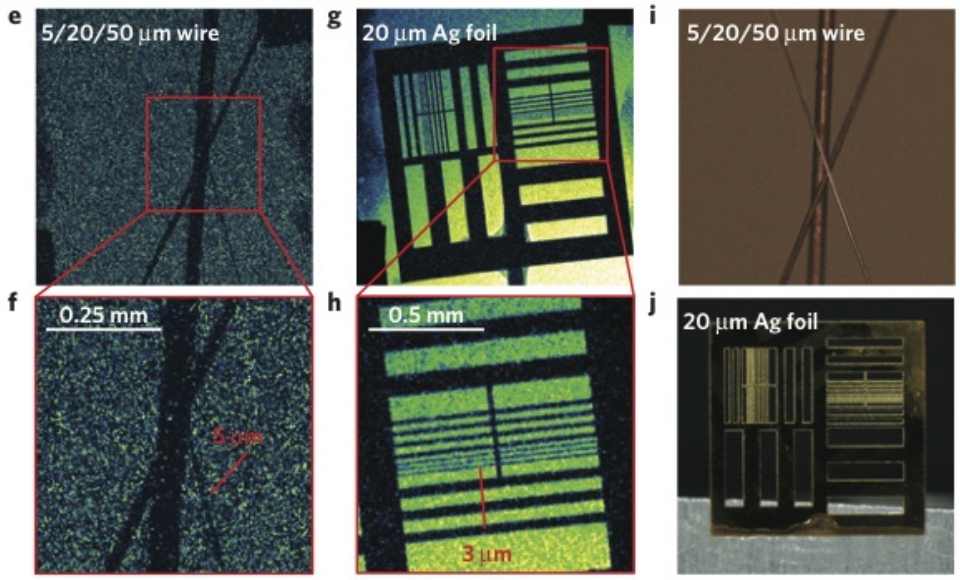


Figure 1.2: Results from using LWFA-generated synchrotron x-rays to perform phase-contrast imaging on a number test targets [2]

In the bubble regime, where the electrons are completely expelled from the region of the pulse, the electric and magnetic fields of the bubble are approximately linear, which by themselves would lead to simple harmonic motion for a monoenergetic, trapped beam [51]. Many analytic scalings for radiation generation in LWFA have been derived in this picture by considering the motion of a single electron in an ion channel [52], [53]. However, the interaction of the beam with the laser fields results in a much more complicated physical picture [51]. More advanced experiments which consider counter-propagating a laser pulse with a LWFA-accelerated electron beam [54], [55] further complicate the picture, as the radiation reaction force becomes non-negligible. More fundamentally, under certain experimental parameters, classical theory predicts that the energy of a single photon at the frequency at which the electron is radiating will exceed the electron's kinetic energy; this is obviously incorrect. Consequently, as these effects begin to dominate, a classical framework must be abandoned entirely in favor of a QED-based framework in order to accurately model

reality [55].

Simulating these effects is a non-trivial challenge, since depending on the regime in question, entirely different physical models are required. A diverse array of models exists for simulating radiation generation in particle-in-cell codes, whether that radiation is generated from shocks [56], [57], LWFA [58], or arbitrary particle motion [59]. For this dissertation, a classical treatment was used, in a regime where the radiation reaction force was negligible (although considerations were made for its inclusion).

# CHAPTER II

# Theoretical Background

## 2.1 Overview

In this chapter, we will present a general overview of the fundamental theoretical concepts which are relevant to this research. First, the relevant mathematics underlying plasma physics will be presented. The meaning of the plasma approximation in the context of computational methods is presented. Cursory summaries of plasma modeling via the Klimontovich and Vlasov-Maxwell equations are presented for completeness. A one-dimensional derivation of the nonlinear response of a plasma to a short laser pulse of arbitrary intensity is presented as a demonstration of the basic physics of laser wake field acceleration (LWFA).

## 2.2 Basic Plasma Physics

### 2.2.1 The Plasma Parameter

In brief, a plasma is an ionized gas; the resulting free charges mean that the plasma is strongly affected by electromagnetic fields. A defining characteristic of ideal, weakly-coupled plasmas is that the plasma parameter $N_D >> 1$; in other

words, that there are many particles within a Debye sphere:

$$N_D = \frac{4}{3}\pi\lambda_D^3 n = \frac{4\pi}{3q^3}\sqrt{\frac{1}{n}}\left(\epsilon_0 k T_e\right)^{3/2} >> 1 \tag{2.1}$$

where n is the plasma density, $\epsilon_0$ is the permittivity of free space, $k$ is the Boltzmann constant, $T_e$ is the electron temperature, and $N_D$ is the number of particles in a Debye sphere. A Debye sphere is a sphere whose radius is equal to the Debye length $\lambda_D = \sqrt{kT_e/4\pi ne^2}$, which represents the characteristic length scale in a plasma over which electrostatic shielding occurs. This condition means that there are enough particles within a Debye sphere for charge shielding to occur, and therefore collective effects (as opposed to particle-particle interactions) dominate the system dynamics. It can be shown that this statement is nearly equivalent to stating that the electron plasma frequency, $\omega_p$, is greater than the electron-ion collision frequency, $\nu_{e,i}$:

$$\omega_p >> \nu_{e,i} \tag{2.2}$$

Note that the electron plasma frequency, given by $\omega_p = \sqrt{4\pi ne^2/m_e}$, represents the characteristic response frequency of the electrons in a plasma. This is an important result for computational plasma physics, as it means that a model written to include one of these conditions will automatically include the other. Consequently, if a computational technique can be written that ensures the collision frequency is much less than the plasma frequency, the system will also behave as though there are a large number of particles within a Debye sphere (i.e., the system will behave like a plasma). It should be noted that, while matter which meets these conditions is plasma, not all plasmas meet these conditions.

### 2.2.2 The Klimontovich Equation

The Klimontovich equation [60] is a basic plasma physics model which, while not particularly useful for modeling real physical systems, does provide a basis for deriving other plasma physics models. A plasma species is modeled as a collection of N point-like particles in a six-dimensional spatial/velocity phase-space; the phase-space density of this collection of particles is represented by:

$$N\left(\vec{x},\vec{v},\vec{t}\right)=\sum_{i=1}^{N}\delta\left[\vec{x}-\vec{x}_i\left(t\right)\right]\delta\left[\vec{v}-\vec{v}_i\left(t\right)\right] \tag{2.3}$$

where $\vec{x}_i\left(t\right)$ and $\vec{v}_i\left(t\right)$ are, respectively, the position and velocity of the $i^{th}$ particle in the distribution. The individual particle positions and velocities are given by:

$$\frac{d}{dt}\vec{x}_i\left(t\right)=\vec{v}_i\left(t\right) \tag{2.4}$$

$$\frac{d}{dt}\vec{v}_i\left(t\right)=\frac{q_i}{m_i}\left\{\vec{E}\left[\vec{x}_i\left(t\right),t\right]+\vec{v}_i\times\vec{B}\left[\vec{x}_i\left(t\right),t\right]\right\} \tag{2.5}$$

where $q_i$ is the charge of the $i^{th}$ particle, $m_i$ is the mass of the $i^{th}$ particle, and the electric field $\vec{E}$ and magnetic field $\vec{B}$ are determined by Maxwell's equations:

$$\vec{\nabla}\cdot\vec{E}=4\pi\rho \tag{2.6}$$

$$\vec{\nabla}\times\vec{E}=-\frac{1}{c}\frac{\partial\vec{B}}{\partial t} \tag{2.7}$$

$$\vec{\nabla}\cdot\vec{B}=0 \tag{2.8}$$

$$\vec{\nabla} \times \vec{B} = 4\pi \vec{J} + \frac{1}{c} \frac{\partial \vec{E}}{\partial t} \tag{2.9}$$

where $\rho$ is the charge density, $\vec{J}$ is the current density, and $c$ is the speed of light. By differentiating the density equation, Equation 2.3, with respect to time, we can find the Klimontovich equation for the $j^{th}$ particle species:

$$\frac{\partial}{\partial t}\left[N_j\left(\vec{x},\vec{v},\vec{t}\right)\right] = \left(\vec{v}\cdot\vec{\nabla}_x\right) N_j\left(\vec{x},\vec{v},\vec{t}\right) + \left[\frac{q_j}{m_j}\left(\vec{E}+\vec{v}\times\vec{B}\right)\cdot\vec{\nabla}_v\right] N_j\left(\vec{x},\vec{v},\vec{t}\right) \tag{2.10}$$

where $\vec{\nabla}_x$ is the position-space gradient, $\vec{\nabla}_v$ is the velocity-space gradient, and we have assumed that every particle of the $j^{th}$ species has an identical charge $q_j$ and mass $m_j$. This equation, though accurate, is practically not very useful, as solving it ultimately entails solving for the individual trajectories of every particle in the plasma. Such a calculation becomes computationally infeasible well before any physically meaningful amount of plasma can be simulated.

### 2.2.3 The Vlasov Equation

These models can be streamlined be either following the BBGKY hierarchy [61], or by introducing the Vlasov equation; here we pursue the latter model. The Vlasov equation trades accuracy, by approximating the plasma as a smooth distribution in $\vec{x}+\vec{v}$ phase-space, for ease of use, by allowing the plasma density to be modeled as a 6-dimensional function in phase space rather than a set of N individual particle trajectories. By taking equation 2.10 and integrating out the small-scale effects resulting from treating the plasma as a collection of points, we can replace our discrete phase-space density, $N_j\left(\vec{x},\vec{v},t\right)$, with a smoothed phase-space distribution $f_j\left(\vec{x},\vec{v},t\right)$:

$$\frac{\partial f_j}{\partial t} + \left(\vec{v}\cdot\vec{\nabla}_x\right) f_j + \left\{\frac{q_j}{m_j}\left[\vec{E}+\left(\vec{v}\times\vec{B}\right)\right]\cdot\vec{\nabla}_v\right\} f_j = \left(\frac{\partial f_j}{\partial t}\right)_{collisions} \tag{2.11}$$

where, physically, $f_j\left(\vec{x},\vec{v},t\right)$ represents the number of particles in a phase-space volume $dx\cdot dy\cdot dz\cdot dv_x\cdot dv_y\cdot dv_z$, centered about the position $\vec{x}$ and the velocity $\vec{v}$, for the $j^{th}$ species in the plasma. Consequently, the units of f, in three dimensions, are particles per unit length cubed per unit velocity cubed. If collisional effects are ignored, this becomes:

$$\frac{\partial f_j}{\partial t}+\left(\vec{v}\cdot\vec{\nabla}_x\right)f_j+\left\{\frac{q_j}{m_j}\left[\vec{E}+\left(\vec{v}\times\vec{B}\right)\right]\cdot\vec{\nabla}_v\right\}f_j=0 \tag{2.12}$$

Furthermore, the charge and current densities can be rewritten in terms of the distribution functions $f_i$; consequently equations 2.6 and 2.9 become:

$$\vec{\nabla}\cdot\vec{E}=\sum_j^M 4\pi q_j\int_\infty^\infty f_j\left(\vec{x},\vec{v},t\right)d\vec{v} \tag{2.13}$$

$$\vec{\nabla}\times\vec{B}=\left[4\pi\sum_j^M q_j\int_\infty^\infty \vec{v}f_j\left(\vec{x},\vec{v},t\right)d\vec{v}\right]+\frac{1}{c}\frac{\partial\vec{E}}{\partial t} \tag{2.14}$$

where $M$ is the total number of species, and the differential element $d\vec{v}=dv_xdv_ydv_z$ represents the differential volume element in velocity space. These two equations, along with the other two Maxwell's equations (equations 2.7 and 2.8), combined with the Vlasov equation (equation 2.12), form a set of five integro-differential equations that govern the evolution of a plasma species' distribution in the six-dimensional phase space.

By representing the plasma as a smooth distribution, and therefore allowing the plasma to be computationally modeled on a gridded phase space, this equation proves far more useful for modeling real physical systems than the Klimontovich equation. It is the method of choice for modeling kinetic, anisotropic plasmas. However, the Vlasov equation is defined on a six-dimensional phase-space, which can make model-

ing larger systems, or systems with higher resolutions, computationally challenging. The dimensionality of the Vlasov equation means that doubling the resolution requires increasing the total number of grid points (and therefore the total amount of computational resources) by a factor of 64.

## 2.3 Laser Wake-Field Acceleration

### 2.3.1 Basic LWFA Scalings

Laser wake-field acceleration is an experimental particle acceleration technique where the strong electric fields established within the wake driven by the interaction of an ultrashort laser pulse with a plasma are used to accelerate electrons to relativistic energies [28]. When the system was initially proposed, several important scalings were derived for the linear limit where the wave does not break; the maximum electron Lorentz factor $\gamma$ attainable by an electron accelerated in this limit is [28]:

$$\gamma_{max} = 2\frac{\omega^2}{\omega_p^2} \tag{2.15}$$

where $\omega$ is the laser frequency and $\omega_p$ is the electron plasma frequency. The propagation distance of the laser pulse required to achieve this energy (called the "dephasing length," as this is the distance over which the electron beam dephases with the accelerating wake field) is given by [28]:

$$L_d \approx 2\frac{\omega^2 c}{\omega_p^3} \tag{2.16}$$

where $c$ is the speed of light. The critical longitudinal field is given by [28], [62]:

$$E_L \approx \frac{mc\omega_p}{e} \tag{2.17}$$

where $m$ and $e$ are, respectively, the mass and charge of an electron. This is the field above which wave-breaking (the point at which the electron motion in a single wave cycle exceeds the wavelength, i.e. the point at which electrons "jump" from one wave to the next) occurs. For a nonlinear wave, the maximum Lorentz factor $\gamma$ is given by [63]:

$$\gamma_{max} = \gamma_p \left(1 + \gamma_p \Delta\phi\right) + \gamma_p \beta_p \left[\left(1 + \gamma_p \Delta\phi\right)^2 - 1\right]^{1/2} \tag{2.18}$$

where $\gamma_p$ is the Lorentz factor $\gamma$ associated with the phase velocity of the wave, $\beta_p$ is the phase velocity of the wave divided by the speed of light $c$, and $\Delta\phi = \phi_{max} - \phi_{min}$ is the difference between the maximum and minimum electrostatic potentials of the nonlinear plasma wave. These maximum and minimum electrostatic potentials are given by [64]:

$$\phi_{max/min} = \gamma_\perp - 1 + \frac{1}{2}\tilde{E}_m^2 \pm \beta_p \left[\left(\gamma_\perp + \frac{1}{2}\tilde{E}_m^2\right)^2 - \gamma_\perp^2\right]^{1/2} \tag{2.19}$$

where $\gamma_\perp$ is the Lorentz factor $\gamma$ associated with the electrons' transverse motion, and $\tilde{E}_m$ is the maximum longitudinal electric field normalized to the previously-mentioned critical longitudinal field $E_L$.

### 2.3.2 Laser Wake-Field Acceleration in One Dimension

In one dimension, the nonlinear response of a plasma to a short laser pulse can be calculated. While the results of this calculation do not encapsulate all of the physics of LWFA, they nevertheless can provide valuable insight into the dynamics of the LWFA mechanism. Here we present a summary of this calculation; a more detailed overview of the results are shown in Appendix A.

We will derive a closed set of 5 differential equations that govern the response of the plasma to the laser pulse of arbitrary field strength $\vec{A}$ (i.e., the nonlinear response).

We start with the Maxwell-Lorentz system of equations for electrons[65]:

$$\frac{\partial \vec{p}}{\partial t} + \left(\vec{v} \cdot \vec{\nabla}\right) \vec{p} = -e \left[\vec{E} + \frac{1}{c}\left(\vec{v} \times \vec{B}\right)\right] \tag{2.20}$$

$$\vec{\nabla} \cdot \vec{E} = 4\pi e \left(n_0 - n_e\right) \tag{2.21}$$

$$\vec{\nabla} \times \vec{E} = -\frac{1}{c}\frac{\partial \vec{B}}{\partial t} \tag{2.22}$$

$$\vec{\nabla} \times \vec{B} = -\frac{4\pi}{c} e n_e \vec{v} + \frac{1}{c}\frac{\partial \vec{E}}{\partial t} \tag{2.23}$$

$$\vec{\nabla} \cdot \vec{B} = 0 \tag{2.24}$$

where $\vec{p}$ is the fluid momentum, $n_0$ is the background ion density (assumed to be static) and $n_e$ is the electron density. We begin by assuming a one-dimensional geometry, in the direction of laser propagation, with an arbitrary laser pulse defined by the vector potential [65]:

$$\vec{A} = A_y \left(x - v_g t\right) \hat{y} \tag{2.25}$$

Additionally, we employ a coordinate transform, boosting to a co-moving frame with an arbitrary group velocity $v_g$ [65]:

$$\tau \equiv t; \xi \equiv x - v_g t \tag{2.26}$$

along with the the quasi-static approximation (QSA). This approximation says that,

in the comoving frame, the characteristic time over which the pulse evolves is much greater than the period of the laser pulse. Mathematically, the QSA lets us say [65]:

$$\frac{\partial}{\partial \tau} << v_g \frac{\partial}{\partial \xi} \tag{2.27}$$

By applying this coordinate transformation and approximation, we can derive the following set of equations [65]:

$$\psi \equiv \sqrt{1 - \frac{\left(1 + a_y^2\right)}{\gamma_g^2 \left(\tilde{\phi} + 1\right)^2}} \tag{2.28}$$

$$\gamma = \gamma_g^2 \left(\tilde{\phi} + 1\right) \left(1 - \beta_g \psi\right) \tag{2.29}$$

$$u_x = \frac{\beta_g - \psi}{\left(1 - \beta_g \psi\right)} \tag{2.30}$$

$$n = \beta_g \gamma_g^2 \left(\frac{1}{\psi} - \beta_g\right) \tag{2.31}$$

$$\frac{\partial^2 \tilde{\phi}}{\partial \xi^2} = k_{pe}^2 \gamma_g^2 \left( \frac{\beta_g \left(1 + \tilde{\phi}\right)}{\sqrt{\left(1 + \tilde{\phi}\right)^2 - \gamma_g^{-2} \left(1 + a_y^2\right)}} - 1 \right) \tag{2.32}$$

where $\psi$ is a parameter defined for convenience, $\gamma_g$ is the relativistic Lorentz factor associated with the group velocity, $a_y$ is the laser vector potential normalized to $e/mc^2$, $\tilde{\phi}$ is the electrostatic potential normalized to $e/mc^2$, $\gamma$ is the electron relativistic Lorentz factor, $\beta_g$ is the group velocity normalized to the speed of light $c$, and $u_x$ is the electron fluid velocity normalized to the speed of light $c$ [65].

The results of these equations are plotted in Figures 2.1 and 2.2 for the following parameters:

1. Peak laser potential $a_{y0} = 5.0$
2. Bulk plasma density $n_0 = 0.01 n_{crit}$
3. Group velocity $\beta_g = 0.99$
4. Pulse spread $\sigma = 5\lambda_{laser}$

where $n_{crit}$ is the critical density of the laser, i.e. the density for which $\omega_p = \omega_{laser}$, so $n_{crit} = \omega_{laser}^2 m_e / 4\pi e^2$, and $\lambda_{laser}$ is the laser wavelength. From Figure 2.1, it is

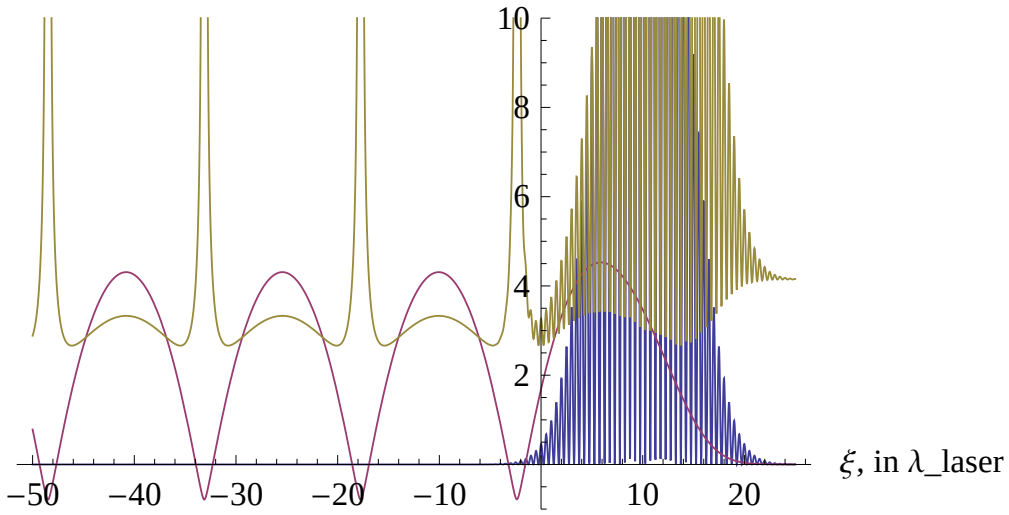


Figure 2.1: The bulk parameters of a plasma in response to the propagation of a short, nonlinear laser pulse in one dimension. The laser intensity is shown in blue. The normalized electrostatic potential $\tilde{\phi}$, is shown in maroon. The electron relativistic Lorentz factor $\gamma$ is shown in gold. The units of the horizontal axis are laser wavelengths (i.e. $\lambda_{laser}$)

apparent that there are sharp gradients in the wake electrostatic potential, resulting in strong accelerating fields. These fields result in relativistic electrons within the wake structure. Figure 2.2 confirms this, showing a trapped bunch of electrons propagating at $u_x \sim 1$ (i.e., $v_x \sim c$). While this one-dimensional calculation is only a rough

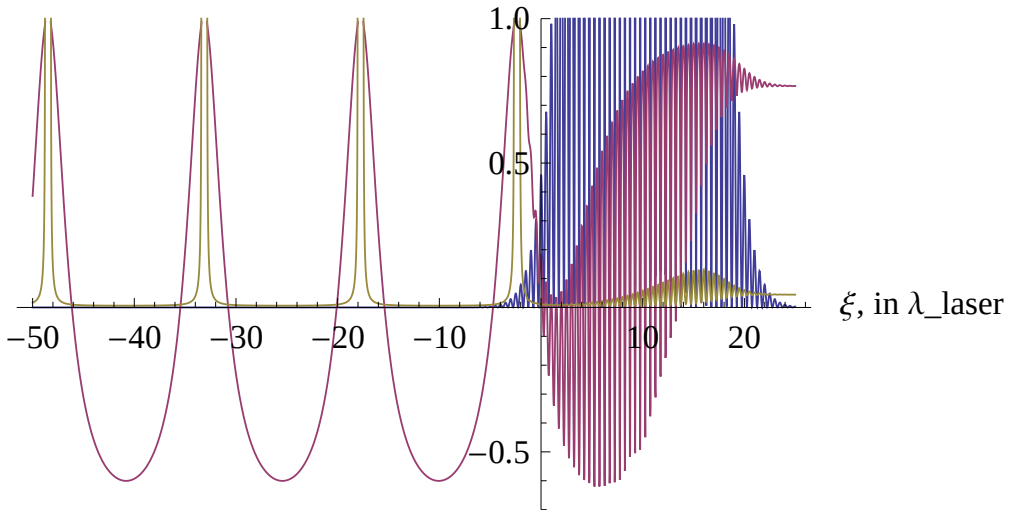


Figure 2.2: The bulk parameters of a plasma in response to the propagation of a short, nonlinear laser pulse in one dimension. The laser intensity is shown in blue. The electron velocity $u_x$, normalized to the speed of light c, is shown in maroon. The electron density $n_e$, shown as a fraction of the critical density $n_{crit}$, is shown in gold.

approximation to the true three-dimensional case, it nevertheless demonstrates the key physical characteristics of LWFA systems: the generation of a plasma wake, by a short pulse laser, which traps and accelerates electrons to relativistic velocities [65].

### 2.3.3 Electron Trapping

The injection and trapping of electrons into the plasma wake is the last essential step necessary for the laser wake-field acceleration scheme to function. We will consider electron trapping in the one-dimensional formulation discussed in the previous section.

Electron trapping is best understood by considering the dynamics of a single test electron interacting with the plasma wake [63], [64]. The Hamiltonian of such an electron is given by [64]:

$$H\left(u,\xi\right)=\left(\gamma_{\perp}^{2}+u^{2}\right)^{1/2}-\beta_{p}u-\phi\left(\xi\right) \tag{2.33}$$

where $u$ is the electron momentum normalized to $m_e c$, $\xi = z - v_p t$ is the comoving longitudinal coordinate as before, and $\phi$ is the plasma wave's electrostatic potential. Note that here the Hamiltonian is normalized to $m_e c^2$. The Hamiltonian is a constant of the particle's motion and, therefore, is constant in time; the above equation therefore describes to a set of trajectories in the $(u, \xi)$ phase-space. Each trajectory corresponds to a single, constant value of $H$.

It is important to note that, in this phase-space, an electron is trapped when the $(u, \xi)$-trajectory corresponding to its Hamiltonian $H$ asymptotically approaches some minimum, finite value for $\xi$. Remembering that $\xi$ corresponds to the electron's longitudinal position in the comoving frame, if the particle's trajectory in $(u, \xi)$-space does not drop below some finite value of $\xi$, then that electron will remain co-propagating with the laser pulse. The trajectory which separates trapped electrons from untrapped electrons (the "separatrix") is given by [64]:

$$H = H_s = \frac{\gamma_\perp (\xi_m)}{\gamma_p} - \phi (\xi_m) \tag{2.34}$$

where $\xi_m$ is the position that maximizes the Hamiltonian $H [\gamma_\perp (\xi) \gamma_p \beta_p, \xi]$.

First, however, we consider the consequences of this Hamiltonian formulation. Noting that [64]:

$$\gamma_\perp^2 = 1 + \frac{a^2}{2} + u_{\perp,0}^2 \tag{2.35}$$

where $a$ is the normalized laser vector potential and $u_{\perp,0}$ is the initial transverse momentum of the electron normalized to $m_e c$, and making the assumption that $u_{\perp,0}$ is negligible when compared to the magnitude of the laser field $a$ in this nonlinear limit, we may say:

$$H (u, \xi) = \left(1 + \frac{a^2}{2} + u^2\right)^{1/2} - \beta_p u - \phi (\xi) \tag{2.36}$$

Plots of the resulting electron trajectories for various values of H are shown in Figure 2.3. Note that trapped electrons are accelerated to arbitrarily high momenta in this one-dimensional, quasi-static picture. Figure 2.3 shows that electrons can be trapped and accelerated in the wake structure as long as their initial momenta are high enough.

It is worth noting that Figure 2.3 also captures the physics of another popular injection scheme, that of ionization injection [66], [67]. In this scheme, the high-intensity fields near the center of the pulse are used to ionize the inner-shell electrons of a dopant in the background gas; this results in the introduction of low-momentum electrons in regions of sufficiently high laser intensity.

As seen in Figure 2.3, low-energy electrons (i.e., $u \approx 0$) from the bulk plasma (i.e., those which are introduced from the right hand-side) are introduced in the untrapped region, and therefore do not see significant acceleration. However, in the region of high-intensity on the back end of the pulse, we see that that minimum momentum necessary for trapping is much lower; an electron with $u \approx 0$ in this region resides comfortably within the trapping region and will be accelerated.

### 2.3.4 The Ponderomotive Force & the Bubble Regime

An important effect in LWFA systems is the ponderomotive force, which is a nonlinear effect that arises in the presence of oscillating, high-intensity electric fields. Here, we present a brief summary of the derivation of this effect, and a derivation of its impact on LWFA systems.

We begin with the expression for the Lorentz force on an electron [68]:

$$\frac{d\vec{p}}{dt} = -e\left\{ \vec{E}\left(\vec{r},t\right) + \frac{1}{c}\left[\vec{v} \times \vec{B}\left(\vec{r},t\right)\right] \right\} \tag{2.37}$$

and consider an oscillating electric field of the form [68]:

$$\vec{E} = \vec{E}_s\left(\vec{r}\right) cos\left(\omega t\right) \tag{2.38}$$

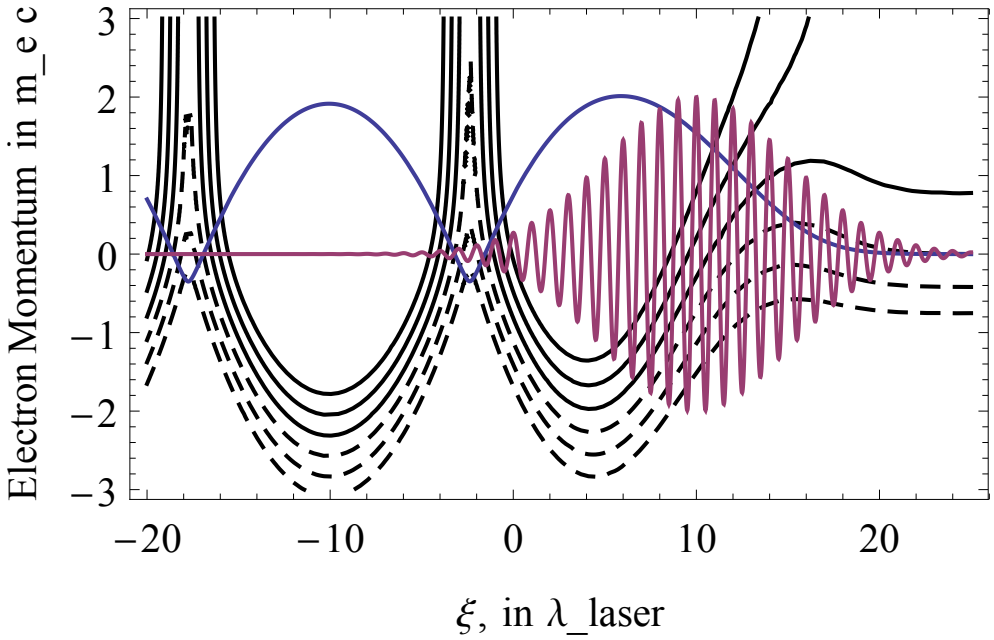


Figure 2.3: The electron trajectories in $(u, \xi)$-space for various values of the Hamiltonian. Dashed black lines show untrapped electrons, while solid black lines show trapped electrons. For clarity, the normalized laser vector potential and electrostatic wake potential (in red and blue respectively) are shown in arbitrary units as functions of position.

where $\vec{E}_s(\vec{r})$ is the spatial envelope of the wave. We consider both the first- and second- order consequences of this equation by considering linearized parameters of the form $a = a_0 + a_1$. For a single, initially stationary electron interacting with the wave, we have [68]:

$$m\frac{d(\vec{v}_0+\vec{v}_1)}{dt} = -e\left\{\vec{E}(\vec{r}_0+\vec{r}_1,t) + \frac{1}{c}\left[(\vec{v}_0+\vec{v}_1)\times\vec{B}_1(\vec{r}_0+\vec{r}_1,t)\right]\right\}; \quad v_0 = 0 \quad (2.39)$$

$$m\frac{d\vec{v}_1}{dt} = -e\left\{\vec{E}(\vec{r}_0+\vec{r}_1,t) + \frac{1}{c}\left[\vec{v}_1\times\vec{B}_1(\vec{r}_0+\vec{r}_1,t)\right]\right\} \quad (2.40)$$

We expand the electric field about $\vec{r}_0$ [68]:

$$\vec{E}(\vec{r}_0+\vec{r}_1) = \vec{E}(\vec{r}_0) + \left[\left(\vec{r}_1\cdot\vec{\nabla}\right)\vec{E}\right]\Big|_{r=r_0} + [h.o.t.] \quad (2.41)$$

Using this expression, in first order, Equation 2.40 becomes [68]:

$$m\frac{d\vec{v}_1}{dt} = -e\vec{E}(\vec{r}_0,t) = -e\vec{E}_s(\vec{r}_0)\,cos(\omega t) \quad (2.42)$$

(note that, to first order, we can ignore the magnetic field). We may solve for the first order velocity and position perturbations, $\vec{v}_1$ and $\vec{r}_1$ [68]:

$$\vec{v}_1 = \frac{-e}{m}\vec{E}_s(\vec{r}_0)\int cos(\omega t)\,dt = \frac{-e}{m\omega}\vec{E}_s(\vec{r}_0)\,sin(\omega t) = \frac{d\vec{r}_1}{dt} \quad (2.43)$$

$$\vec{r}_1 = \frac{-e}{m\omega}\vec{E}_s(\vec{r}_0)\int sin(\omega t)\,dt = \frac{e}{m\omega^2}\vec{E}_s(\vec{r}_0)\,cos(\omega t) \quad (2.44)$$

In second order (with terms of the form $a = a_0 + a_1 + a_2$), we may no longer ignore

the magnetic field; we calculate the magnetic field from the electric field [68]:

$$\vec{\nabla} \times \vec{E} = -\frac{1}{c}\frac{\partial \vec{B}}{\partial t} \tag{2.45}$$

$$\vec{B}_1 = -c \int \left[\vec{\nabla} \times \vec{E}\right] \Big|_{r=r_0} dt = -c \left[\vec{\nabla} \times \vec{E}_s\left(\vec{r}\right)\right] \Big|_{r=r_0} \int cos\left(\omega t\right) dt \tag{2.46}$$

$$\vec{B}_1 = \frac{-c}{\omega} sin\left(\omega t\right) \left[\vec{\nabla} \times \vec{E}_s\left(\vec{r}\right)\right] \Big|_{r=r_0} \tag{2.47}$$

We consider the second-order terms in Equation 2.40 (noting that we may cancel out the first order terms) [68]:

$$m\frac{d\vec{v}_2}{dt} = -e\Big\{ \left[\left(\vec{r}_1 \cdot \vec{\nabla}\right)\vec{E}\right] \Big|_{r=r_0} \frac{1}{c}\left(\vec{v}_1 \times \vec{B}_1\right) \Big\} \tag{2.48}$$

and insert the results from Equations 2.43, 2.44, and 2.47 (we evaluate at $\vec{r} = \vec{r}_0$; we omit explicit statements to this effect for brevity) [68]:

$$m\frac{d\vec{v}_2}{dt} = \frac{-e^2}{m\omega^2}\Big\{ cos^2\left(\omega t\right)\left(\vec{E}_s \cdot \vec{\nabla}\right)\vec{E}_s + sin^2\left(\omega t\right)\left[\vec{E}_s \times \left(\vec{\nabla} \times \vec{E}_s\right)\right] \Big\} \tag{2.49}$$

We take the time average of this equation [68]:

$$m\langle\frac{d\vec{v}_2}{dt}\rangle = \frac{-e^2}{2m\omega^2}\Big\{ \left(\vec{E}_s \cdot \vec{\nabla}\right)\vec{E}_s + \left[\vec{E}_s \times \left(\vec{\nabla} \times \vec{E}_s\right)\right] \Big\} \tag{2.50}$$

Noting via the vector identity that [68]:

$$\vec{E}_s \times \left(\vec{\nabla} \times \vec{E}_s\right) = \frac{1}{2}\vec{\nabla}\left(\vec{E}_s \cdot \vec{E}_s\right) - \left(\vec{E}_s \cdot \vec{\nabla}\right)\vec{E}_s \tag{2.51}$$

we have an expression for the time-averaged, second-order, nonlinear force acting on

a single particle [68]:

$$m\langle\frac{d\vec{v}_2}{dt}\rangle = \vec{F}_{pon} = \frac{-e^2}{4m\omega^2}\vec{\nabla}\left(\vec{E}_s \cdot \vec{E}_s\right) \tag{2.52}$$

which we identify as the ponderomotive force. We may rewrite this expression slightly [68]:

$$\vec{F}_{pon} = -\vec{\nabla}\left(\frac{e^2}{4m\omega^2}\vec{E}_s \cdot \vec{E}_s\right) \tag{2.53}$$

to identify the ponderomotive potential [68]:

$$\phi_{pon} = \frac{e}{4m\omega^2}\left(\vec{E}_s \cdot \vec{E}_s\right) \tag{2.54}$$

such that $\vec{F}_{pon} = -e\vec{\nabla}\phi_{pon}$. Note that this result is non-relativistic; the relativistic result was derived by Quesnel and Mora [69]:

$$\frac{d\vec{p}}{dt} = \vec{F}_{pon,rel} = \frac{-1}{2m\bar{\gamma}}\vec{\nabla}|q\tilde{\vec{A}}|^2 \tag{2.55}$$

where bars represent averaging over fast time-scales (i.e. the laser frequency) and tildes represent quantities which vary over these same fast time scales (i.e. $\tilde{\vec{A}}$ is the laser field).

The ponderomotive force is an important effect in laser wake-field acceleration. For sufficiently high-intensity pulses, it expels electrons from the region of the laser, forming a "bubble" of positive charge co-propagating with the laser. To demonstrate the significance of this effect, we will assume that the ponderomotive force is exclusively balanced by the electrostatic force established in the positive charge "bubble:"

$$\vec{F}_{pon} = \vec{F}_e s = -e\vec{E} \tag{2.56}$$

Note that this is a crude assumption, which neglects entirely the effect of the background ion current, electric current, magnetic fields, and direct interaction between the laser and the plasma. We seek only to demonstrate the significance of the ponderomotive force as a contributor to the electron dynamics. We assume a laser pulse propagating through a plasma with the following parameters:

1. Plasma Density $n_0 = 0.01 n_{crit} = 1.75 \times 10^{19} cm^{-3}$
2. Laser Wavelength $\lambda = 0.8 \mu m$
3. Gaussian Transverse Laser Profile, FWHM spot size $= 5 \mu m$
4. Gaussian Temporal Laser Profile, FWHD pulse length $= 25 fs$
5. Normalized Peak Laser Vector Potential $a_0 = 4.0$
6. Peak Laser Intensity $= 3.5 \times 10^{19} W/cm^2$

where the acronym "FWHM" refers to the "Full-Width at Half-Maximum", i.e. the distance between the locations where the intensity is half of the maximum, and similarly the acronym "FWHD" refers to the "Full-Width at Half-Duration," and refers to the length of time between the points in the pulse where the intensity is half of its maximum. The electric field and intensity of this laser pulse are shown in Figures 2.4 and 2.5, respectively. The ponderomotive potential produced by this laser pulse is shown in Figure 2.6, which results in the density perturbation shown in Figure 2.7. The electric fields established by this density perturbation are shown in Figure 2.8. It is apparent that the ponderomotive force is a dominant effect in LWFA experiments where $a_0 > 1$.

To make more accurate, quantitative statements about the evolution of the plasma in this regime, a far more rigorous theoretical treatment is necessary. Unfortunately, the details of this, more precise analytic treatment are beyond the scope of this dissertation; consequently only their results will be summarized here. These results are

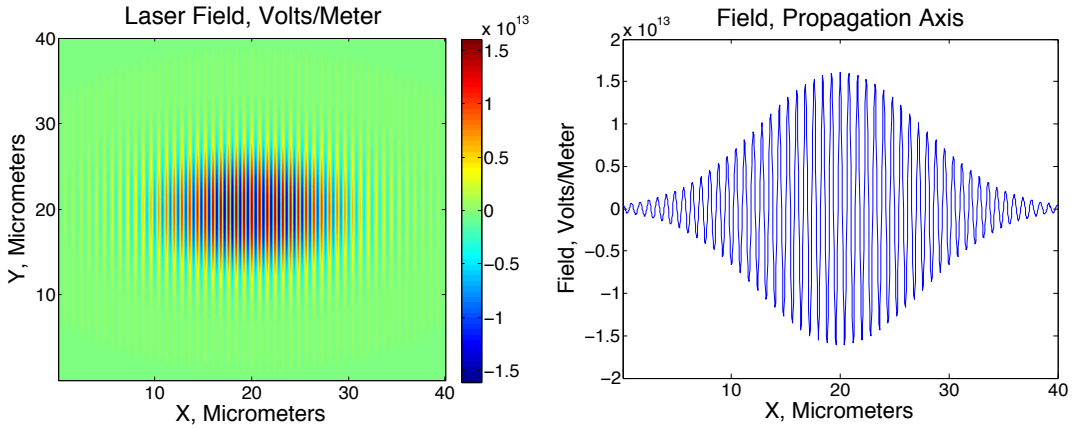


Figure 2.4: The electric field of an example laser pulse in (left) two dimensions and (right) one dimension, respectively.

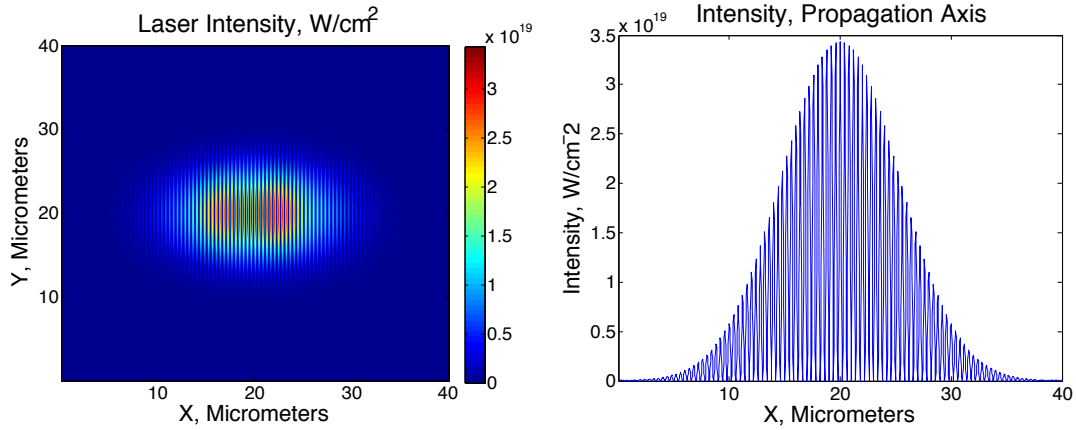


Figure 2.5: The intensity of an example laser pulse in (left) two dimensions and (right) one dimension, respectively.

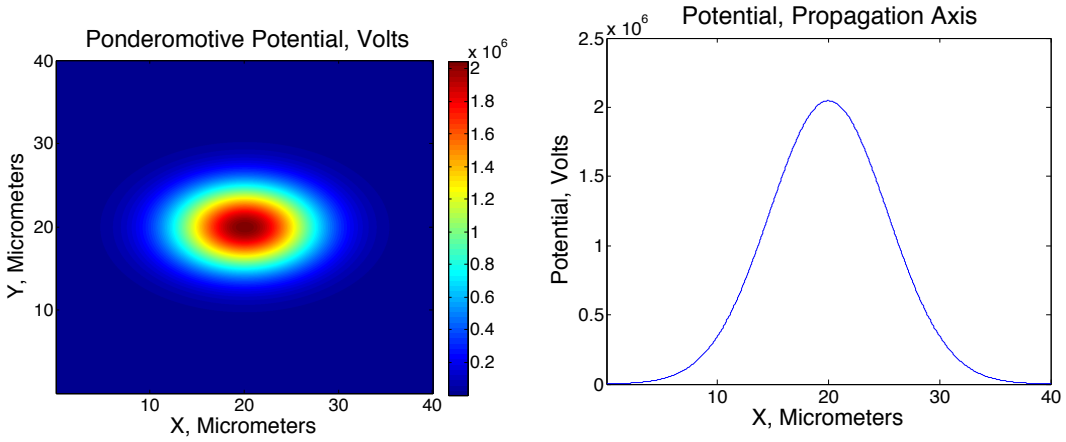


Figure 2.6: The ponderomotive potential generated by a laser pulse in (left) two dimensions and (right) one dimension, respectively.

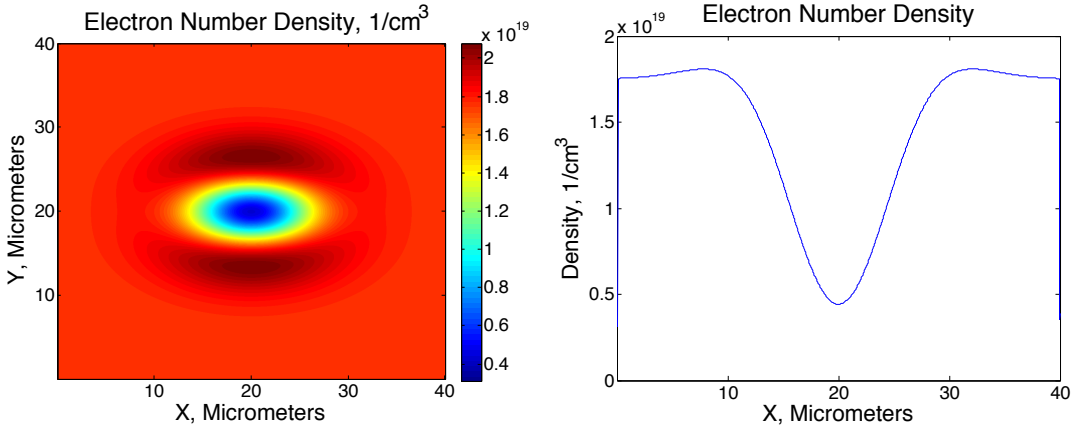


Figure 2.7: The electron density profile resulting from the interaction of a laser pulse with the plasma via the ponderomotive force in (left) two dimensions and (right) one dimension, respectively.

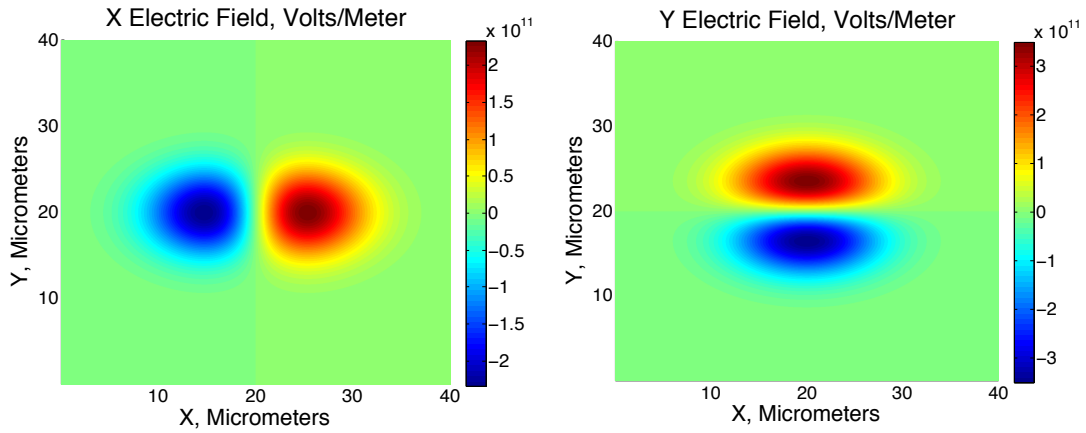


Figure 2.8: The electrostatic fields in the propagation direction (left) and transverse direction (right) generated in the unrealistic approximation that the ponderomotive force is balanced purely by the electrostatic fields of the density perturbation shown in the previous figure.

drawn from the article "A nonlinear theory for multidimensional relativistic plasma wave wakefields," published in Physics of Plasmas in 2006 by W. Lu et al [70].

The first analytical result is the simplified ring model, which is used to look for trajectory crossing. Basically, this model treats the electrons in the plasma as a series of nested, cylindrically symmetric rings which respond to the driving laser pulse. Trajectory crossing is an important concept used to consider the formation of the propagating "bubble" region of positive charge discussed previously [70].

Consider the cylindrically symmetric electron rings of the ring model. The motion of these electrons will be confined to the radial and propagation directions by definition; the trajectories formed by electrons which start at various initial radii can either cross or not cross. If the electron trajectories do not cross, then any given electron trajectory which confines electrons at smaller radii will continue to confine the same number of electrons at smaller radii for all time. Therefore, if the electron trajectories do not cross, and the electron density is initially non-zero and uniform, electrons will always be present in the region of space occupied by the laser pulse [70].

Conversely, if the electron trajectories do cross, then it is no longer true that elec-

trons confined by a given trajectory will remain confined by that trajectory. Under these conditions it is possible for the electrons to be excluded entirely from the region of the pulse, leaving only ions (this is known as the "blowout" regime). Thus, trajectory crossing provides a necessary (but not sufficient) condition for the formation of a propagating ion "bubble." [70]

The trajectory of an electron ring in the simplified ring model, in the non-relativistic limit where $v_z << v_\perp << 1$ and $v_\perp \approx dr/d\xi$ (remember that these limits are defined in terms of the electron velocity within the copropagating frame, not the laboratory frame) is given by [70]:

$$\frac{d^2r}{d\xi^2} = -\frac{1}{2}r + \frac{c\left(r_0, r, \xi\right)}{r} \tag{2.57}$$

where r is the electron beam radius, $\xi = c_0 t - z$ is the position of the electron in the propagation direction, boosted to the frame co-propagating with the laser (which is assumed to be propagating at the speed of light $c_0$), and $c\left(r_0, r, \xi\right)$ is the total electron charge per unit length within a sheet, which starts at $r_0$, and has a radius $r$ at a longitudinal position $\xi$ [70].

Although laser-driven wake-fields are the focus of this dissertation, the dynamics of bubble formation are similar regardless of whether or not the wake-field is driven by a laser pulse or an electron beam. Since the case of a beam-driven wakefield is somewhat easier to consider analytically, we will numerically solve equation 2.57 for the electron-beam-driven wake-field case. If a bi-flat-top model is assumed for the driving beam, so that the driving beam's charge density profile is given by[70]:

$$n_b\left(r, \xi\right) = n_{b0}, \quad r < a, \quad 0 < \xi < L$$

$$n_b\left(r, \xi\right) = 0.0, \quad elsewhere \tag{2.58}$$

where $n_{b0}$ is the peak beam charge density normalized to the background plasma density, $a$ is the beam spot size, and $L$ is the beam length, the function $c\,(r_0, r, \xi)$ in Equation 2.57 becomes[70]:

$$c\,(r_0, r, \xi) = \frac{1}{2}\left(r_0^2 + n_{b0} r^2\right) \tag{2.59}$$

for $r < a$, and:

$$c\,(r_0, r, \xi) = \frac{1}{2}\left(r_0^2 + n_{b0} a^2\right) \tag{2.60}$$

for $r > a$. Therefore, equation 2.57 becomes[70]:

$$\frac{d^2 r}{d\xi^2} = -\frac{1}{2} r + \frac{r_0^2 + n_{b0} r^2}{2r} \tag{2.61}$$

for $r < a$ and:

$$\frac{d^2 r}{d\xi^2} = -\frac{1}{2} r + \frac{r_0^2 + n_{b0} a^2}{2r} \tag{2.62}$$

for $r > a$. We solve these equations for $a = 0.5$, $L = 4.0$, and $n_{b0} = 0.2, 2.0$ for a range of initial radii $r_0$; these plots are shown in Figure 2.9.

Figure 2.9 shows that trajectory crossing can occur for sufficiently intense (i.e., non-linear) driving pulses. Further calculation reveals that the initial condition $r_0$ which corresponds to the onset of trajectory crossing is given by[70]:

$$ln\left(\frac{\bar{r}_m^2}{\bar{r}_0^2}\right) = \frac{n_b}{\bar{r}_0^2} \tag{2.63}$$

where the bar indicates that the radii have been normalized to $a$, and $r_m$ is the maximum radii reached by a trajectory starting at $r_0$. The value of $r_0$ at which this

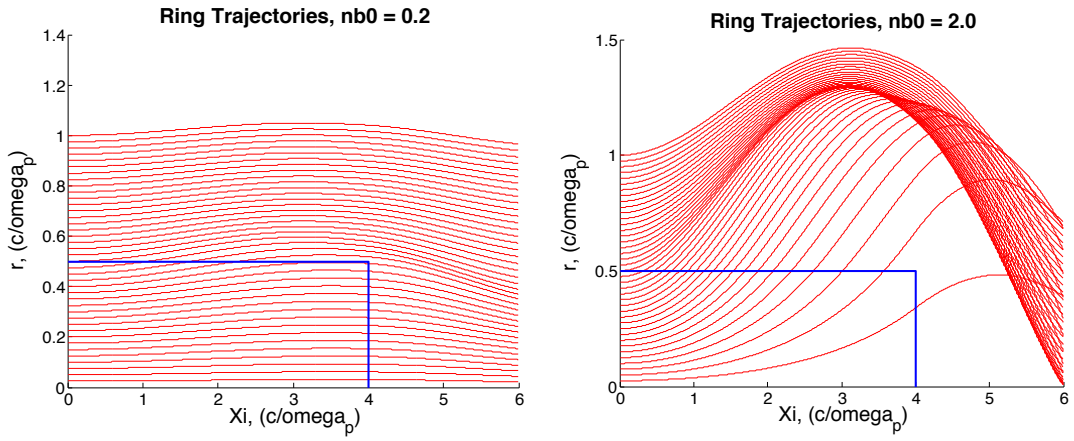


Figure 2.9: The trajectories of electron rings (shown in red) in the simplified ring model for $n_{b0} = 0.2$ (on the left) and $n_{b0} = 2.0$ (on the right). Both plots have $a = 0.5$ and $L = 4.0$. The blue line shows the radius and length of the driving beam.

equation is true is noted as $r_{0m}$. Solving this equation yields[70]:

$$\frac{n_b}{\bar{r}_{0m}^2} = 1.7933 \tag{2.64}$$

If we assume that $r_{0m} > a$ (as this is the blowout regime), then $\bar{r}_{0m} > 1.0$ and $n_b > 1.7933$ is the condition for trajectory crossing. In addition, the blowout radius, the maximum radius $r_m$ for the electron trajectory which starts at $r_{0m}$, is given by[70]:

$$r_{max} = r_m\left(r_{0m}\right) = 1.831\sqrt{n_b a^2} \tag{2.65}$$

From these analyses, it is clear that for a sufficiently nonlinear driver, the system will enter a bubble regime, where electrons are excluded from the region surrounding the driver pulse, leaving a propagating ion column behind[70].

### 2.3.5 Wave Breaking

The phenomenon of trajectory crossing discussed in the previous section is closely related to the phenomenon of nonlinear wave breaking, an important nonlinear effect in laser wake-field acceleration. The wave-breaking limit represents the maximum field a plasma can sustain according to the fluid model. In general (and unsurprisingly), the wave-breaking limit requires that the maximum longitudinal electric field not exceed the critical electric field given in Equation 2.17 [63], [71]:

$$\tilde{E}_m \equiv \frac{E_{max}}{E_L} = \frac{eE_{max}}{mc\omega_p} > 1$$

Beyond this limit, trajectory crossing and wave-breaking occur, the fluid equations break down, and the field will not increase. However, this is a non-relativistic limit; the relativistic wave-breaking limit is given by [71]:

$$\tilde{E}_{m,r} \equiv \frac{E_{max,r}}{E_{WB}} = \frac{E_{max,r}}{\sqrt{2\left(\gamma_p - 1\right)}E_L} > 1$$

where $\gamma_p$ is the Lorentz factor gamma associated with the phase velocity of the laser. Effectively the relativistic critical electric field is given by $\sqrt{2\left(\gamma_p - 1\right)}E_L$.

### 2.3.6 Betatron Motion in LWFA Systems

Based on the density profile shown in figure 2.7, we can make some qualitative statements about the behavior of particles that become trapped within this bubble. Unlike the bulk electrons of the plasma, trapped electrons are not affected by the ponderomotive force; this can be seen immediately from equation 2.55, where the relativistic ponderomotive force scales as $1/\gamma$. Ergo, electrons which are trapped and accelerated to relativistic energies (i.e., with $\gamma >> 1$) are only weakly affected by the ponderomotive force; the motion of these electrons will instead be dominated by the

laser field and the electrostatic response to the ponderomotive force.

Now consider the approximated electrostatic fields in Figure 2.8. Even in this crude model, the accelerating fields in the propagation direction (shown on the left in Figure 2.8) are accompanied by transverse restoring fields (shown on the right in Figure 2.8). It is apparent that, according to this crude model, trapped electrons with $\gamma >> 1$ which are injected off-axis will undergo oscillations about the axis of propagation.

The more detailed analysis based on the work of Lu et al., and illustrated by Figure 2.9, reinforces this picture with a far more robust calculation of the formation of the blowout regime. The radial particle and charge densities assumed by this work (which show excellent agreement with simulation) are shown in Figure 2.10. The transverse electric field resulting from these density distributions is shown in Figure 2.11. The

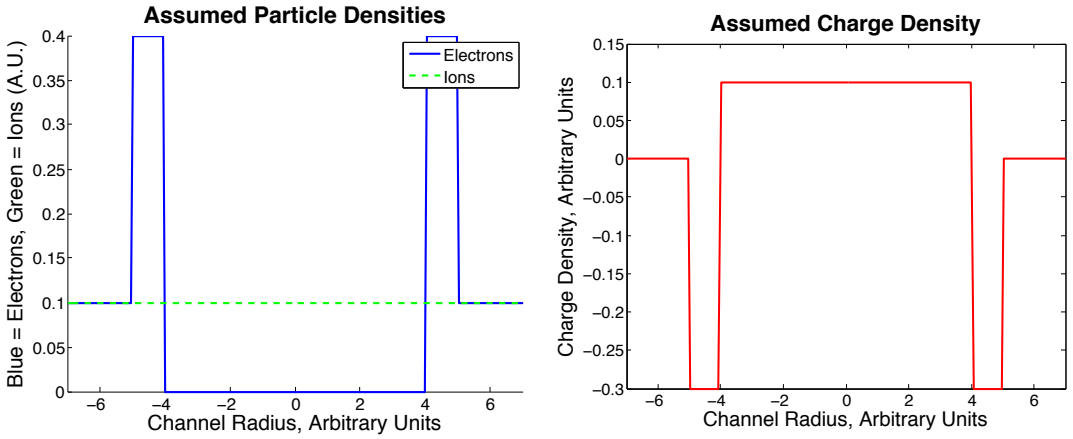


Figure 2.10: (Left) The electron density (in blue) and ion density (in green) assumed by the theoretical models of Lu et al. (Right) The resulting charge density from these particle density distributions.

area highlighted by the dashed black box in Figure 2.11 shows that there exists a roughly linear restoring force along the central axis of the channel; this field drives trapped electrons to undergo simple harmonic motion in the transverse direction, which, when coupled with their acceleration along the propagation direction, results in betatron motion. For a sufficiently non-linear driver, this phenomenon occurs

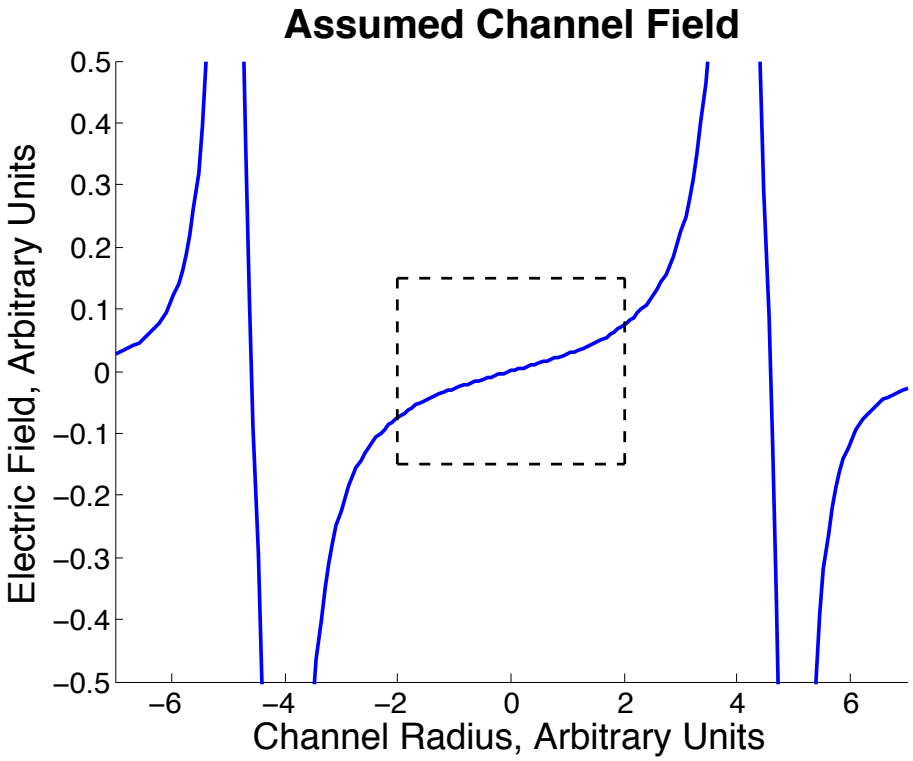


Figure 2.11: The electric field resulting from the particle densities shown in Figure 2.10. Note the boxed area highlighting the approximately linear restoring force along the central axis of the channel.

automatically for electrons injected off-center from the propagation axis.

## 2.4 Plasma Optics

### 2.4.1 Overview

Obviously, the propagation of light waves through plasmas is a critical subject for this dissertation. A full treatment of this subject is beyond the scope of this work; however we would be remiss if we did not include a discussion of some of the phenomena most relevant to laser wake-field acceleration. Therefore, we will discuss three particularly relevant processes in plasma optics: Raman forward scattering (RFS), relativistic self-focusing (RSF), and relativistic self-phase modulation (RSPM).

The interaction of a propagating laser with a plasma can be understood in terms of the index of refraction of the plasma. In a plasma with electron plasma frequency $\omega_p$, the index of refraction for an electromagnetic wave of frequency $\omega_0$ is given by [72]:

$$\eta = \sqrt{1 - \frac{\omega_p^2}{\gamma_\perp \omega_0^2}}$$

where $\gamma_\perp$ is the Lorentz factor $\gamma$ of the transverse momentum of the electrons as they oscillate in the laser field, and is given by [72]:

$$\gamma_\perp = \sqrt{1 + \frac{a_0^2}{2}}$$

These two equations can be combined, and $\eta$ can be expanded for small values of the perturbation $\omega_p^2/\gamma_\perp\omega_0^2$ [72]:

$$\eta = \left[1 - \frac{1}{2}\frac{\omega_p^2}{\omega_0^2}\left(1 + \frac{\delta n}{n} - \frac{\langle a^2\rangle}{2} - 2\frac{\delta\omega_0}{\omega_0}\right)\right] \tag{2.66}$$

where $\delta n$ and $\delta\omega_0$ are the density and laser frequency perturbations, respectively. Note that both the light's frequency and intensity affect the index of refraction, which in turn affects the propagation of the light, creating a complicated interaction between the light and the plasma. Recalling that the phase velocity $v_p$ is given by $v_p = c\eta^{-1}$, we have [72]:

$$v_p = c\left[1 + \frac{1}{2}\frac{\omega_p^2}{\omega_0^2}\left(1 + \frac{\delta n}{n} - \frac{\langle a^2\rangle}{2} - 2\frac{\delta\omega_0}{\omega_0}\right)\right] \tag{2.67}$$

Finally, the group velocity can be written as [72]:

$$v_g = c\left[1 - \frac{1}{2}\frac{\omega_p^2}{\omega_0^2}\left(1 + \frac{\delta n}{n} - \frac{\langle a^2\rangle}{2} - 2\frac{\delta\omega_0}{\omega_0}\right)\right] \tag{2.68}$$

To consider plasma optical phenomena, we will analyze how the laser envelope $\langle a^2\rangle$ is effected by interaction with the plasma in the speed-of-light frame (with the variables $\tau = t$ and $\psi = t - x/c$). If we assume that the total number of photons within some length $L$ is constant, we can say [72]:

$$\langle a^2\rangle\omega_0\sigma^2 L = constant$$

where $\sigma$ is the laser spot size; this means the change in the the time-average of the laser intensity $\Delta\langle a^2\rangle$ is given by [72]:

$$\Delta\langle a^2\rangle = -\frac{\Delta L}{L}\langle a^2\rangle - 2\frac{\Delta\sigma}{\sigma}\langle a^2\rangle - \frac{\Delta\omega_0}{\omega_0}\langle a^2\rangle \tag{2.69}$$

We can see that the laser intensity can be altered via three parameters: longitudinal extent $L$, spot size $\sigma$, and laser frequency $\omega_0$. These three quantities evolve according

to the following differential equations [72]:

$$\frac{1}{L}\frac{\partial L}{\partial \tau} = -\frac{1}{c}\frac{\partial v_g}{\partial \psi} \tag{2.70}$$

$$\frac{1}{L}\frac{\partial^2 \sigma}{\partial \tau^2} = -\left(\frac{v_{p1} - v_{p2}}{\sigma}\right) c \tag{2.71}$$

$$\frac{1}{\omega}\frac{\partial \omega}{\partial \tau} = -\frac{1}{c}\eta^{-2}\frac{\partial \eta}{\partial \psi} \tag{2.72}$$

where, in Equation 2.71, $v_{p1}$ and $v_{p2}$ are the phase velocities at the edge of the beam a distance $\sigma$ from the axis and on the axis of laser propagation, respectively [72].

### 2.4.2 Raman Forward Scattering

RFS is an instability by which the $a^2/2$ term in Equation 2.66 drives a modulation in the plasma density, $\delta n$, which in turn drives a modulation in the laser intensity, $\langle a^2 \rangle_1$ [72]. Effectively, there exist two decay modes ($k_+$ and $k_-$) which interact with the light wave $k_0$ and the plasma wave $k_p$ such that $k_0 + k_p = k_+$ and $k_- + k_p = k_0$; these two decay modes grow exponentially as they interact with the laser and plasma waves simultaneously [65]. A diagram of the relationship between these waves in k-space is shown in Figure 2.12. Note that because there are two decay waves interacting with two driving waves, FRS is a "four-wave" process.

If we consider RFS as a one-dimensional process (i.e., the growth rate of the laser field perturbation, $\Delta\langle a^2 \rangle_1$, is unaffected by perturbations to the spot size) where the modulations in the index of refraction $\eta$ are driven only by modulations in the plasma density, then by considering Equations 2.69, 2.70, and 2.72, it can be shown that the

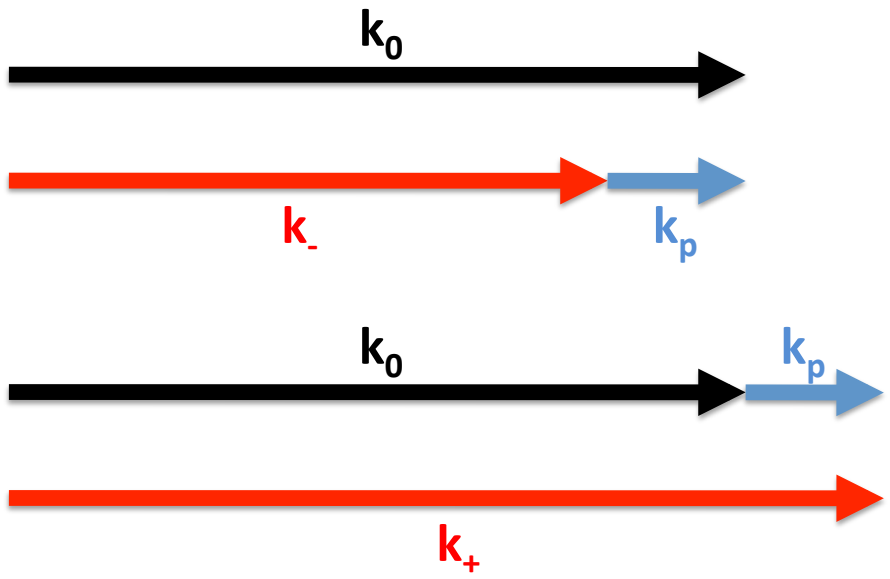


Figure 2.12: The k-space relationship between the plasma wave, laser wave, and scattered waves in Raman Forward Scattering.

density perturbations cause modulations to the laser intensity according to [72]:

$$\frac{\partial \Delta \langle a^2 \rangle_1}{\partial \tau} = ic \frac{\omega_p^2}{\omega_0^2} k_p \frac{a_0^2}{2} \frac{\delta n}{n} \tag{2.73}$$

Note that the factor of $i$ on the right-hand side of this equation means that the density modulations are out of phase with the intensity modulations by a factor of $\pi/2$. Simultaneously, modulations to the laser intensity also drive density perturbations according to [72]:

$$\left[ \frac{\partial^2}{\partial \psi^2} + \omega_p^2 \right] \frac{\delta n}{n} = \frac{\partial^2}{\partial \psi^2} \frac{\langle a^2 \rangle}{2} \tag{2.74}$$

Equations 2.73 and 2.74 can be combined to yield [72]:

$$\frac{\partial^2}{\partial \psi} \partial \tau \langle a^2 \rangle_1 = \gamma_0^2 \langle a^2 \rangle_1$$

$$\gamma_0 = \frac{a_0 \omega_p^2}{\sqrt{8}\omega_0} \tag{2.75}$$

For the limit where $a_0 << 1$, $\gamma_0$ is the growth rate $\Gamma$ of the RFS instability [65]. In general, the growth rate for the RFS instability is given by [65]:

$$\Gamma = \frac{\omega_p^2 a_0}{\sqrt{8}\omega_0 \left(1 + \frac{a_0^2}{2}\right)} \tag{2.76}$$

### 2.4.3 Relativistic Self-Phase Modulation

Similar to RFS, RSPM is a process by which the $a^2/2$ term in Equation 2.66 drives a modulation in the laser frequency perturbation $\Delta\omega$, which in turn drives a modulation in the laser intensity $\langle a^2 \rangle$. However, unlike RFS, in RSPM, the secondary modulations in $\langle a^2 \rangle$ are out of phase with the original modulations driving the process. The net result is a modulation of the group velocity $v_g$, which leads to longitudinal energy bunching [72].

If we begin with Equation 2.69, assuming that the perturbations to $\Delta\langle a^2 \rangle$ are caused only by the $\Delta L/L$ term; and combine it with Equation 2.68, assuming that the perturbations to $v_g$ are caused only by the $\partial\omega_0/\omega_0$ term, we may say that perturbations in the laser intensity are driven by perturbations in the the laser frequency according to [72]:

$$\frac{\partial^2 \Delta\langle a^2 \rangle}{\partial \tau^2} = \frac{\omega_p^2}{\omega_0^2} \frac{\partial}{\partial \psi} \left( \frac{1}{\omega_0} \frac{\partial \Delta\omega_0}{\partial \tau} \frac{a_0^2}{2} \right) \tag{2.77}$$

Meanwhile, perturbations to the laser frequency $\omega_0$ are driven by perturbations in the laser intensity $a_0^2$ are driven by [72]:

$$\frac{1}{\omega_0} \frac{\partial \Delta\omega_0}{\partial \tau} = -\frac{1}{4} \frac{\omega_p^2}{\omega_0^2} \frac{\partial}{\partial \psi} \langle a^2 \rangle \tag{2.78}$$

Equations 2.77 and 2.78 can be combined to find the equation for relativistic self-phase modulation [72]:

$$\frac{\partial^2 \langle a^2 \rangle_1}{\partial \tau^2} = \frac{c^2 k^2}{8} \frac{\omega_p^4}{\omega_0^4} a_0^2 \left( 1 - \frac{2k^2}{\omega_0^2} \frac{c^2}{a_0^2} \right) \langle a^2 \rangle_1 \tag{2.79}$$

where $\langle a^2 \rangle_1$ is the laser vector potential perturbation. The threshold for the RSPM instability is therefore [72]:

$$c^2 k^2 < \frac{\omega^2}{2} a_0^2 \tag{2.80}$$

and the maximum growth rate of the instability is [72]:

$$\Gamma_m = \frac{1}{8} \frac{a_0^2 \omega_p^2}{\omega_0} \tag{2.81}$$

### 2.4.4 Relativistic Self-Focusing

RSF is a process by which the intensity-dependent index of refraction interacts with the variable intensity of the laser spot to produce a self-focusing effect [72]. If we start with Equation 2.71, and insert Equation 2.67 while assuming that the phase velocity is driven only by the $\langle a^2 \rangle / 2$ term in Equation 2.67, we can say that the spot size $\sigma$ evolves according to [72]:

$$\frac{\partial^2 \sigma}{\partial \tau^2} = -\frac{1}{8} \frac{\omega_p^2}{\omega_0^2} \frac{c^2}{\sigma} a_0^2 \tag{2.82}$$

However, this equation fails to take into account variations in the spot size due to vacuum diffraction, which is given by [72]:

$$\sigma = \sigma_0 \sqrt{1 + \frac{\tau^2}{t_R^2}} \tag{2.83}$$

where $\sigma_0$ is the spot size at the focus and $t_R \equiv 1/2k_0/2\sigma_0^2$ is the diffraction time. We can differentiate this equation near the focus [72]:

$$\frac{\partial^2 \sigma}{\partial \tau^2} \approx \frac{4}{k_0^2 \sigma_0^3} \tag{2.84}$$

We can combine Equations 2.82 and 2.84 [72]:

$$\frac{\partial^2 \sigma}{\partial \tau^2} \approx \frac{4}{k_0^2 \sigma_0^3} \left[ 1 - \frac{a_0^2 \sigma_0^2 \omega_p^2}{32c^2} \right] \tag{2.85}$$

Self-focusing occurs when $\frac{\partial^2 \sigma}{\partial \tau^2} < 0$, i.e. when [72]:

$$\frac{a_0^2 \sigma_0^2 \omega_p^2}{32c^2} > 1 \tag{2.86}$$

Since this product is proportional to $a_0^2 \sigma_0^2$, it is proportional to the power [72], and we can rewrite the condition of Equation 2.86 as:

$$\frac{P}{P_{crit}} > 1$$

where the critical power is given by [72]:

$$P_{crit} = 17 \frac{\omega_0^2}{\omega_p^2} \, [GW] \tag{2.87}$$

## 2.5 Radiation Emission by Charged Particles

### 2.5.1 Instantaneous Radiation Spectrum

The four-potentials produced by a charged particle moving with a four-velocity $V^{\alpha}(\tau)$ are known as the Liénard-Wiechert potentials:

$$A^{\alpha}(x) = \left.\frac{eV^{\alpha}(\tau)}{\vec{V}\cdot[\vec{x}-\vec{r}(\tau)]}\right|_{\tau=\tau_0} \tag{2.88}$$

where $\tau_0$ is the retarded proper time. These potentials can be evaluated to yield the field strength tensor:

$$F^{\alpha\beta} = \frac{e}{V\cdot(x-r)}\frac{d}{d\tau}\left[\frac{(x-r)^{\alpha}V^{\beta}-(x-r)^{\beta}V^{\alpha}}{\vec{V}\cdot(\vec{x}-\vec{r})}\right] \tag{2.89}$$

which can itself be rewritten as explicit statements of the electric and magnetic fields:

$$\vec{E}(\vec{x},t) = e\left[\frac{\vec{n}-\vec{\beta}}{\gamma^2\left(1-\vec{\beta}\cdot\vec{n}\right)^3R^2}\right]_{ret} + \frac{e}{c}\left\{\frac{\vec{n}\times\left[\left(\vec{n}-\vec{\beta}\right)\times\dot{\beta}\right]}{\left(1-\vec{\beta}\cdot\vec{n}\right)^3R}\right\}_{ret} \tag{2.90}$$

$$\vec{B} = \left(\vec{n}\times\vec{E}\right)_{ret} \tag{2.91}$$

If we consider that the power radiated per unit solid angle is given by:

$$\frac{dP(t)}{d\Omega} = \frac{c}{4\pi}\left|\left[R\vec{E}\right]_{ret}\right|^2 \tag{2.92}$$

we can can calculate energy radiated per unit frequency, per unit solid angle by a particle traveling instantaneous circular motion with a radius of curvature $\rho$:

$$\frac{d^2I}{d\omega d\Omega} = \frac{3\gamma^2e^2}{\pi^2c}\tilde{\omega}^2\left(1+\tilde{\theta}^2\right)^2\left[K^2_{\frac{2}{3}}(\xi)+\frac{\tilde{\theta}^2}{1+\tilde{\theta}^2}K^2_{\frac{1}{3}}(\xi)\right]$$

$$\xi \equiv \frac{\tilde{\omega}}{2}\left(1+\tilde{\theta}^2\right)^{3/2} \tag{2.93}$$

where $\gamma$ is the radiating particle's relativistic Lorentz factor, $e$ is the charge of an electron, $c$ is the speed of light in a vacuum, $\tilde{\theta}$ is the angle-of-emission normalized to $\theta_{crit} \equiv 1/\gamma$, and $\tilde{\omega}$ is the frequency normalized to $\omega_{crit} \equiv (3/2)\,\gamma^3\,(c/\rho)$, where $\rho$ is the radius of curvature of the particle's instantaneous circular motion. This spectrum is shown both linearly and logarithmically in Figure 2.13. The angular dependence of this spectrum can be integrated out to yield the one-dimensional synchrotron spectrum:

$$\frac{dI}{d\omega} = \frac{2\sqrt{3}e^2\gamma}{c}\tilde{\omega}\int_{2\tilde{\omega}}^{\infty} K_{\frac{5}{3}}(x)\,dx \tag{2.94}$$

This spectrum is shown in Figure 2.14. Note that Equation 2.93 is in units of energy per unit frequency, per unit angle (i.e., ergs-second per radian), while Equation 2.94 is in units of energy per unit frequency (i.e., ergs-seconds). Both represent the total energy emitted (either per unit angle per unit frequency as in Equation 2.93, or per unit frequency as in Equation 2.94) by a particle that travels in one complete orbit of its circular motion.

### 2.5.2 Radiation Regimes

When being emitted by electrons traveling along a sinusoidal trajectory, radiation can be broadly classified into two separate regimes: "undulator" radiation and "wiggler" radiation. These two regimes are defined by the wiggler parameter, K [5]:

$$K = \gamma\psi$$

where $\gamma$ is the relativistic Lorentz factor of the radiating electron and $\psi$ is the maximum angle reached by the electron's trajectory relative to its averaged, forward

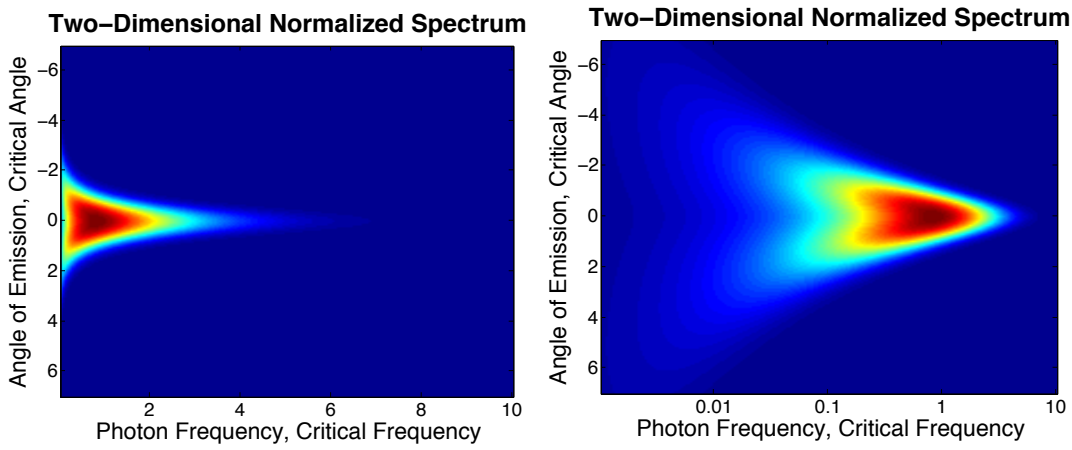


Figure 2.13: The two-dimensional, angular and frequency spectrum produced by a charged particle moving in instantaneous circular motion with a linear frequency scale (left) and a logarithmic frequency scale (right), in terms of the critical frequency and angle

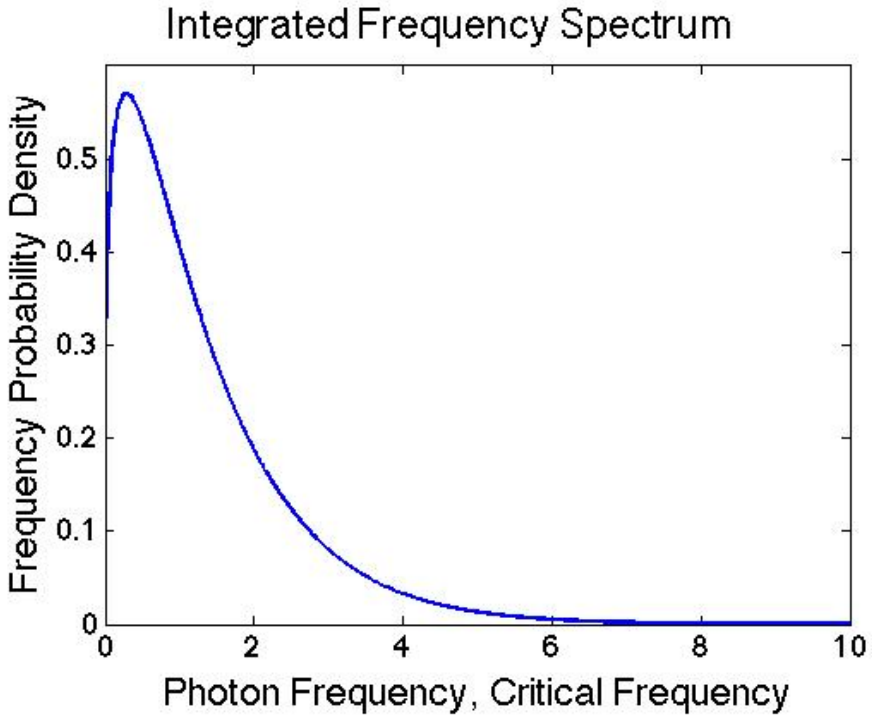


Figure 2.14: The distribution of radiation frequencies (presented as a probability density function), in terms of the critical frequency.

propagation direction. For the undulator regime, $K << 1$, while for the wiggler regime, $K >> 1$ [5]. The difference between these two regimes is shown in Figure 2.15, along with a graphical representation of the angle $\psi$.

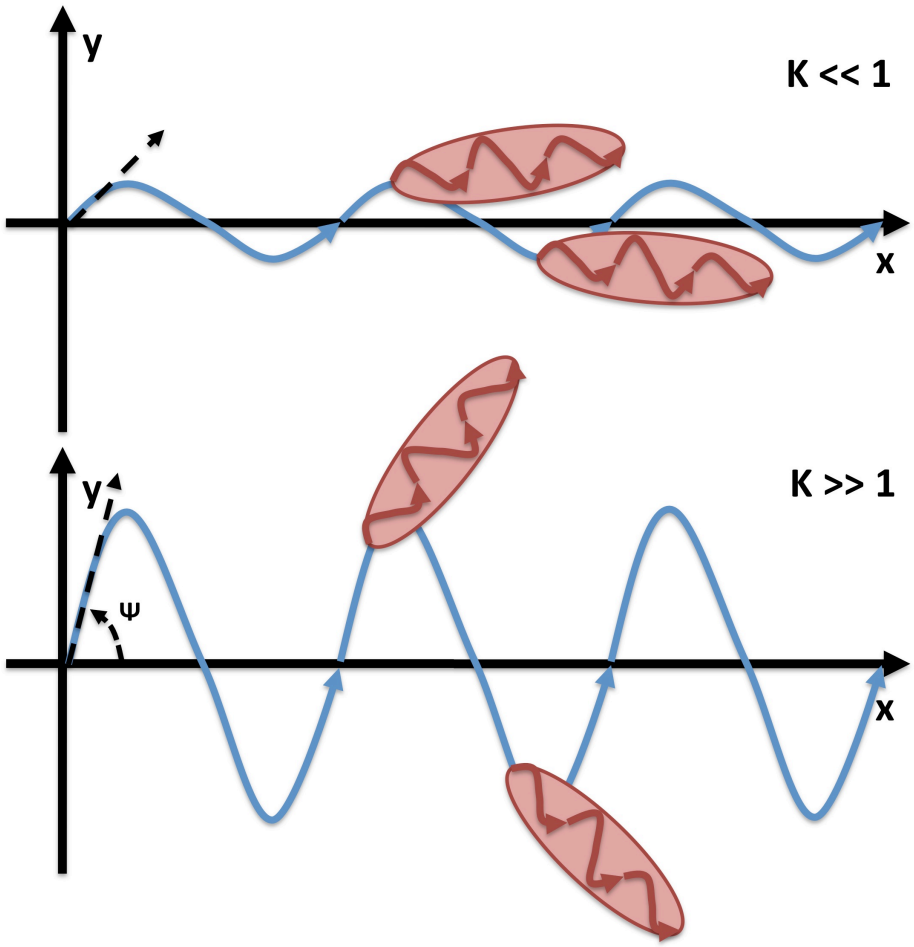


Figure 2.15: A cartoon of the electron trajectories for the undulator case (top) and wiggler case (bottom). The electron trajectories are shown in blue, and the emitted radiation is shown in red. Note that the wiggler parameter K is the ratio between the maximum angle between the electron trajectory and the propagation direction (shown in the figure) and the critical angle of the emitted radiation spectrum, $\theta_{crit} = 1/\gamma$, which depends on the emitting particle's Lorentz factor $\gamma$ and is not shown in the figure.

Recalling from the previous section that the characteristic angle-of-emission is given by $\theta_{crit} = 1/\gamma$, we can write $K = \psi/\theta_{crit}$. This reformulation clarifies the physical difference between the undulator and wiggler regimes. For the undulator

regime, $K << 1$ means that $\psi << \theta_{crit}$. The angular divergence of the emitted radiation is primarily due to the angular dependence of the synchrotron spectrum as defined by Equation 2.93 in this case. Conversely, for the wiggler regime, $K >> 1$ means that $\psi >> \theta_{crit}$. The angular divergence of the emitted radiation is primarily due to the radiating electron's trajectory in this case [5].

More significant than the differences in the angular distributions, however, are the differences in the spectrum of radiation emitted in each of these two regimes. For the undulator regime (where $K << 1$), the radiation is continuously emitted in the same direction, resulting in a coherent superposition of the radiation [3]. Consequently, the spectrum takes the form of a single, sharp peak at a frequency $\omega_u$ given by [3]:

$$\omega_u \approx \frac{2\gamma^2}{1+\gamma^2\theta^2}\left(\frac{2\pi}{\lambda_0}\right) \tag{2.95}$$

where $\lambda_0$ is the wavelength of the electron's periodic motion. While an ideal infinite-length undulator would emit light at a single frequency, a real undulator of N periods emits light with a frequency bandwidth of $\Delta\omega/\omega \sim 1/N$ [3].

Conversely, for the wiggler regime (where $K >> 1$), the radiation is emitted in a broad spectrum resembling that described by Equations 2.93 and 2.94 [3]. In this case, the effective critical frequency of the radiation, $\omega_{c,wig}$ is given by [3]:

$$\omega_{c,wig} = 2\pi c\gamma^3\frac{\psi}{\lambda_0} \tag{2.96}$$

For the transitional regime where $K \sim 1$, a full treatment is beyond the scope of this dissertation. Qualitatively, the spectrum for this regime shows a number of sharp peaks located at harmonics of the fundamental frequency given by Equation 2.95. As the wiggler parameter $K$ increases, the heights of these peaks increase and broaden, asymptotically approaching a synchrotron-like spectrum with a critical frequency given by Equation 2.96 [5].

By analyzing the trajectory of a single electron undergoing betatron motion in an ion channel, scalings can be found that relate the wiggler parameter $K$ and the betatron frequency $\omega_\beta$ to the plasma parameters [50], [2]:

$$\omega_\beta = \frac{\omega_p}{\sqrt{2\gamma}}; \quad K = \gamma r_\beta \frac{\omega_\beta}{c} \tag{2.97}$$

where $\omega_p$ is the electron plasma frequency, $\gamma$ is the Lorentz factor of the radiating electron, and $r_\beta$ is the maximum distance the radiating particle travels away from the centerline as it undergoes betatron oscillation.

# CHAPTER III

# Computational Background & Methodology

## 3.1 Introduction

In this section we will present a general overview of the fundamental computational concepts which are relevant to this research. First, the relevant mathematics of computational electrodynamics will be presented, specifically the forward-differencing time domain used in this research's simulations. The important concept of the Courant-Friedrichs-Lewy (CFL) condition will also be presented, and how it relates to numerical diffusion and dispersion will be discussed.

Second, the mathematics and techniques of the particle-in-cell (PIC) model are presented. An explanation of the computational cycle of PIC codes is presented. Also, a review of the instabilities and nonphysical phenomena which occur when using PIC codes is presented.

Finally, the implementation specific to the PIC code OSIRIS 2.0 (used for the majority of this research) is presented. An explanation of how OSIRIS 2.0 specifically implements each step in the PIC computational cycle is given.

## 3.2 Computational Electrodynamics

We first present the relevant methods for numerically solving Maxwell's equations [3]:

$$\vec{\nabla} \cdot \vec{E} = 4\pi\rho \tag{3.1}$$

$$\vec{\nabla} \times \vec{E} = -\frac{1}{c}\frac{\partial \vec{B}}{\partial t} \tag{3.2}$$

$$\vec{\nabla} \cdot \vec{B} = 0 \tag{3.3}$$

$$\vec{\nabla} \times \vec{B} = 4\pi\vec{J} + \frac{1}{c}\frac{\partial \vec{E}}{\partial t} \tag{3.4}$$

for the time evolution of the electric and magnetic fields $\vec{E}$ and $\vec{B}$ in the presence of charge and current densities $\rho$ and $\vec{J}$.

### 3.2.1 Forward-Differencing Time Domain (FDTD)

The FDTD algorithm begins with equations 3.2 and 3.4 rearranged:

$$\frac{\partial \vec{B}}{\partial t} = -c\vec{\nabla} \times \vec{E} \tag{3.5}$$

$$\frac{\partial \vec{E}}{\partial t} = c\left(\vec{\nabla} \times \vec{B} - 4\pi\vec{J}\right) \tag{3.6}$$

The time derivatives in equations 3.5 and 3.6 are replaced with approximate numerical forms:

$$\frac{\partial \vec{B}}{\partial t} \approx \frac{\vec{B}_{t+1} - \vec{B}_t}{\Delta t} \tag{3.7}$$

$$\frac{\partial \vec{E}}{\partial t} \approx \frac{\vec{E}_{t+1} - \vec{E}_t}{\Delta t} \tag{3.8}$$

where $t$ is the time-index of the numeric calculation. The revised Maxwell's equations become [73]:

$$\frac{\vec{B}_{t+1} - \vec{B}_t}{\Delta t} \approx -c \left(\vec{\nabla} \times \vec{E}\right)_{t+1/2} \tag{3.9}$$

$$\frac{\vec{E}_{t+1/2} - \vec{E}_{t-1/2}}{\Delta t} \approx c \left[\left(\vec{\nabla} \times \vec{B}\right)_t - 4\pi \vec{J}_i\right] \tag{3.10}$$

(An explanation of how the spatial derivatives of $\vec{E}$ and $\vec{B}$ are calculated numerically is provided in the section 3.2.2). We rewrite these equations in a form that permits iteration:

$$\vec{B}_{t+1} = \vec{B}_t - c\Delta t \left(\vec{\nabla} \times \vec{E}\right)_{t+1/2} \tag{3.11}$$

$$\vec{E}_{t+1/2} \approx \vec{E}_{t-1/2} + c\Delta t \left[\left(\vec{\nabla} \times \vec{B}\right)_t - 4\pi \vec{J}_t\right] \tag{3.12}$$

These two numerical equations have two features of note. First, the electric and magnetic fields iterate one half-step out of sync with one another; consequently the FDTD method first iterates one field, than uses that new value to iterate the other field, and so on, effectively leap-frogging back and forth between the electric and

magnetic field [73].

Second, the charge density $\rho$ does not appear at all in these equations. While this seems counterintuitive at first, the presence of the current density $\vec{J}$ in these equations encapsulates all of the information necessary about the evolution of the charge density $\rho$. The only information missing is the initial charge distribution $\rho_0$, which is accounted for if the initial electric field is defined according to equation 3.1.

### 3.2.2 Yee Cell

The next step when numerically calculating the electric and magnetic fields is to numerically calculate the spatial derivatives in equations 3.11 and 3.12. For simplicity, we initially consider only the x-component of equation 3.11 [73]:

$$B_{x,i+1} = B_{x,i} - c\Delta t \left(\vec{\nabla} \times \vec{E}\right)_{x,i+1/2} \tag{3.13}$$

$$B_{x,i+1} = B_{x,i} - c\Delta t \left(\frac{\partial E_{z,i+1/2}}{\partial y} - \frac{\partial E_{y,i+1/2}}{\partial z}\right)$$

We introduce the indices $a$, $b$, and $c$ to represent the discretization of quantities in, respectively, the x, y, and z directions, and discretize these derivatives [73]:

$$B_{x,a,b+\frac{1}{2},c+\frac{1}{2},t+1} = B_{x,a,b+\frac{1}{2},c+\frac{1}{2},t} - c\Delta t \left(\frac{E_{z,a,b+1,c+\frac{1}{2},t+1/2} - E_{z,a,b,c+\frac{1}{2},t+1/2}}{\Delta y}\right)$$

$$+c\Delta t \left(\frac{E_{y,a,b+\frac{1}{2},c+1,t+1/2} - E_{y,a,b+\frac{1}{2},c,t+1/2}}{\Delta z}\right) \tag{3.14}$$

Similarly, we find for the remaining two components of equation 3.11 [73]:

$$B_{y,a+\frac{1}{2},b,c+\frac{1}{2},t+1} = B_{y,a+\frac{1}{2},b,c+\frac{1}{2},t} - c\Delta t \left( \frac{E_{x,a+\frac{1}{2},b,c+1,t+1/2} - E_{x,a+\frac{1}{2},b,c,t+1/2}}{\Delta z} \right)$$

$$+c\Delta t \left( \frac{E_{z,a+1,b,c+\frac{1}{2},t+1/2} - E_{z,a,b,c+\frac{1}{2},t+1/2}}{\Delta x} \right) \tag{3.15}$$

$$B_{z,a+\frac{1}{2},b+\frac{1}{2},c,t+1} = B_{z,a+\frac{1}{2},b+\frac{1}{2},c,t} - c\Delta t \left( \frac{E_{y,a+1,b+\frac{1}{2},c,t+1/2} - E_{y,a,b+\frac{1}{2},c,t+1/2}}{\Delta x} \right)$$

$$+c\Delta t \left( \frac{E_{x,a+\frac{1}{2},b+1,c,t+1/2} - E_{x,a+\frac{1}{2},b,c,t+1/2}}{\Delta y} \right) \tag{3.16}$$

and for the three components of the electric field (from equation 3.12) [73]:

$$E_{x,a+\frac{1}{2},b,c,t+\frac{1}{2}} = E_{x,a+\frac{1}{2},b,c,t-\frac{1}{2}} + c\Delta t \left( \frac{B_{z,a+\frac{1}{2},b+\frac{1}{2},c,t} - B_{z,a+\frac{1}{2},b-\frac{1}{2},c,t}}{\Delta y} \right)$$

$$-c\Delta t \left( \frac{B_{y,a+\frac{1}{2},b,c+\frac{1}{2},t} - B_{y,a+\frac{1}{2},b,c-\frac{1}{2},t}}{\Delta z} \right) - c\Delta t 4\pi J_{x,a+\frac{1}{2},b,c,t+\frac{1}{2}} \tag{3.17}$$

$$E_{y,a,b+\frac{1}{2},c,t+\frac{1}{2}} = E_{y,a,b+\frac{1}{2},c,t-\frac{1}{2}} + \Delta t \left( \frac{B_{x,a,b+\frac{1}{2},c+\frac{1}{2},t} - B_{x,a,b+\frac{1}{2},c-\frac{1}{2},t}}{\Delta z} \right)$$

$$-\Delta t \left( \frac{B_{z,a+\frac{1}{2},b+\frac{1}{2},c,t} - B_{z,a-\frac{1}{2},b+\frac{1}{2},c,t}}{\Delta x} \right) - \Delta t 4\pi J_{y,a,b+\frac{1}{2},c,t+\frac{1}{2}} \tag{3.18}$$

$$E_{z,a,b,c+\frac{1}{2},i+\frac{1}{2}} = E_{z,a,b,c+\frac{1}{2},t-\frac{1}{2}} + \Delta t \left( \frac{B_{y,a+\frac{1}{2},b,c+\frac{1}{2},t} - B_{y,a-\frac{1}{2},b,c+\frac{1}{2},t}}{\Delta x} \right)$$

$$-\Delta t \left( \frac{B_{x,a,b+\frac{1}{2},c+\frac{1}{2},t} - B_{x,a,b-\frac{1}{2},c+\frac{1}{2},t}}{\Delta y} \right) - \Delta t 4\pi J_{z,a,b,c+\frac{1}{2},t+\frac{1}{2}} \tag{3.19}$$

Note again that, as with the time derivatives, the spatial indices of the electric and magnetic fields are 1/2 step out of sync with one another in the dimensions in which the derivatives are taken. Functionally, this means that the electric and magnetic fields are defined at different points on the grid. For a given (cubic) grid cell, the electric field lines are defined at the centers of each cell edge, and are defined parallel to the edge. By contrast, the magnetic fields are defined at the centers of each cell face, and are defined normal to the face [73].

The use of indices obfuscates the layout of this complicated arrangement, which is much easier to understand graphically. The definitions of the magnetic field vector components shown with respect to a grid cell are shown in Figure 3.1. The same definitions for the electric field are shown in Figure 3.2.

This seemingly complex arrangement greatly simplifies calculating the curls in equations 3.11 and 3.12. Each vector component requires that one component of a curl be numerically calculated for iteration. The Yee lattice ensures that each vector component lies exactly halfway between both pairs needed for its iteration [73].

### 3.2.3 CFL Condition

The Courant-Friedrichs-Lewy condition, or CFL condition, is an important concept when numerically solving differential equations of hyperbolic form [74]. Consequently, it is an important factor to consider in computational plasma physics. The CFL condition is a stability relating the spatial resolution, time-step, and characteristic velocity of a gridded differential equation being solved with explicit, numerical

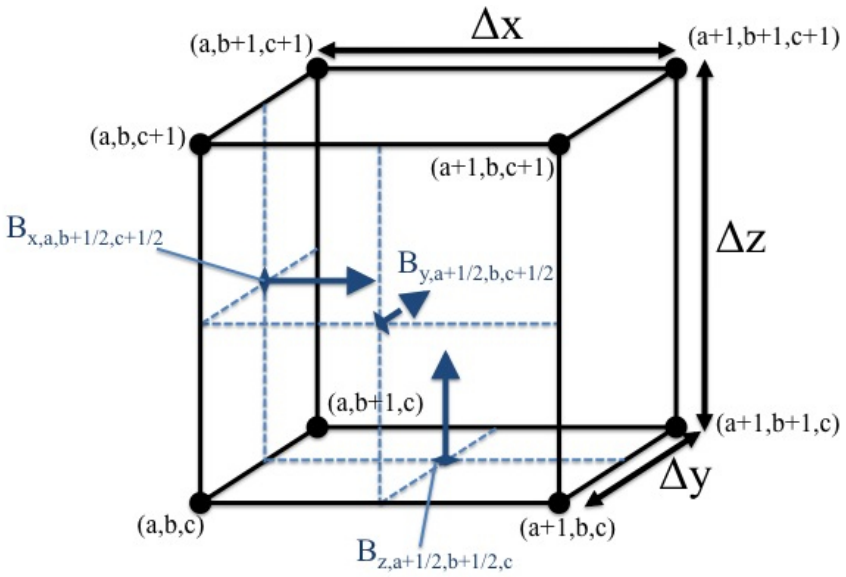


Figure 3.1: The definitions of the magnetic field (shown in blue) with respect to the numeric grid (shown in black). Also shown for clarity are the grid cell spacings (also in black). Note that the magnetic field vector components are defined normal to, and originating at the center of, the cell surfaces.

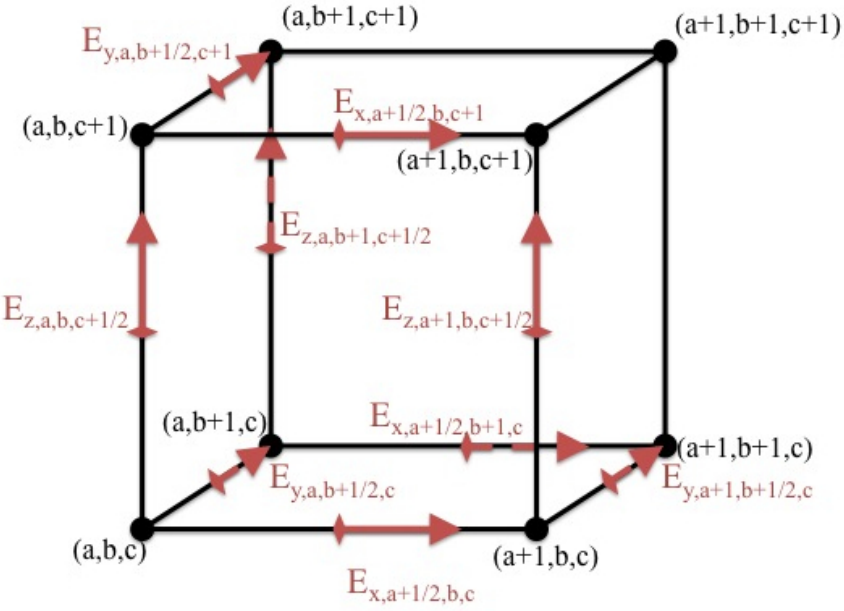


Figure 3.2: The definitions of the electric field (shown in red) with respect to the numeric grid (shown in black). Note that the electric field vector components are defined parallel to, and originating ath the center of, the cell edges.

methods [75],[76], and is defined in terms of the Courant number $S$; in one dimension this parameter and the stability condition related to it are given by [73]:

$$S \equiv \frac{c\Delta t}{\Delta x} \leq 1 \tag{3.20}$$

where $c$ is the velocity, $\Delta t$ is the time step, and $\Delta x$ is the grid spacing. In three dimensions, this becomes [73]:

$$S \equiv c\Delta t \sqrt{\frac{1}{\Delta x^2} + \frac{1}{\Delta y^2} + \frac{1}{\Delta z^2}} \leq 1 \tag{3.21}$$

It is important note that applying this condition too severely, i.e.:

$$S \equiv c\Delta t \sqrt{\frac{1}{\Delta x^2} + \frac{1}{\Delta y^2} + \frac{1}{\Delta z^2}} << 1 \tag{3.22}$$

can introduce a non-physical (though stable) numerical diffusion [76]. This diffusion is minimized when $S \sim 1$ [76].

### 3.2.4 Numerical Dispersion

Non-physical dispersion (i.e., when the phase velocity of a wave can differ from $c$ by an amount varying with the wavelength) is introduced by the FDTD method [73]; this dispersion is dependent on the grid discretization. Moreover, the numerical dispersion varies with propagation direction if the grid discretization is different in different dimensions. Consider that, in real-space, the dispersion of a wave with wave-number $\vec{k} \equiv k_x\hat{x} + k_y\hat{y} + k_z\hat{z}$ is given by [73]:

$$\left(\frac{\omega}{c}\right)^2 = k_x^2 + k_y^2 + k_z^2 \tag{3.23}$$

For a similar wave propagating via the FDTD method, the dispersion relationship is given by [73]:

$$\left[\frac{1}{c\Delta t}\sin\left(\frac{\omega\Delta t}{2}\right)\right]^2 = \left[\frac{1}{\Delta x}\sin\left(\frac{k_x\Delta x}{2}\right)\right]^2 + \left[\frac{1}{\Delta y}\sin\left(\frac{k_y\Delta y}{2}\right)\right]^2 +$$

$$\left[\frac{1}{\Delta z}\sin\left(\frac{k_z\Delta z}{2}\right)\right]^2 \tag{3.24}$$

It is immediately apparent from Equation 3.24 that, if the quantities $\Delta x$, $\Delta y$, and $\Delta z$ are not equal (i.e., if the grid is discretized differently in different directions), then the numerical dispersion of a wave will depend upon its direction of propagation (i.e., the relative values of $k_x$, $k_y$, and $k_z$), unless $k_a\Delta a << 1$ (where $a = (x, y, \&z)$).

It is of course desirable to reduce the effects of this dispersion in order to accurately capture the propagation of electromagnetic waves. For a simple electromagnetic wave, recall that the dispersion relationship for a non-magnetized electromagnetic plasma wave propagating entirely in the z-direction is given by [77]:

$$\omega^2 = \omega_p^2 + c^2k_z^2 = \omega_p^2 + k_z^2 \tag{3.25}$$

when $c$ is normalized to one (a common normalization scheme chosen for laser plasma simulation to avoid excessively large/small floating point numbers). It can be shown [78]that Equation 3.25 is a solution to Equation 3.24 if the time-step is given by:

$$\Delta t = \Delta z\frac{k_z}{\omega} \tag{3.26}$$

which becomes $\Delta t = \Delta zc$ for a sufficiently under-dense plasma ($\Delta t = \Delta z$ for $c$ normalized to 1). Recall that, for a three-dimensional simulation with $c$ normalized

to 1, the CFL condition is:

$$\Delta t \sqrt{\frac{1}{\Delta x^2} + \frac{1}{\Delta y^2} + \frac{1}{\Delta z^2}} < 1 \tag{3.27}$$

However, recall that to minimize numerical diffusion, we want:

$$\Delta t \sqrt{\frac{1}{\Delta x^2} + \frac{1}{\Delta y^2} + \frac{1}{\Delta z^2}} \sim 1 \tag{3.28}$$

Introducing the $\Delta t = \Delta z c$ constraint (with $c$ normalized to 1) necessary to accurately model our desired electromagnetic wave, we have:

$$\left( \frac{\Delta z^2}{\Delta x^2} + \frac{\Delta z^2}{\Delta y^2} + \frac{\Delta z^2}{\Delta z^2} \right) \sim 1 \tag{3.29}$$

$$\left( \frac{\Delta z^2}{\Delta x^2} + \frac{\Delta z^2}{\Delta y^2} \right) \sim 0 \tag{3.30}$$

It is clear that both of these constraints cannot be realized with finite grid sizes. Nevertheless, we can come close by having $\Delta x > \Delta z$ and $\Delta y > \Delta z$.

In conclusion, the two non-physical effects of simulating electromagnetic waves via the FDTD method, namely numerical dispersion and numerical diffusion, can be minimized for waves traveling in one direction by making the grid discretization in the transverse dimensions larger than the grid discretization in the propagation direction, while still satisfying the CFL condition. Obviously, the more severely this constraint is applied, the more poorly the simulation will model waves traveling in directions other than the chosen propagation direction.

### 3.2.5 Field Boundary Conditions

Since it is impossible to simulate an infinite domain, it is necessary to specify how the electromagnetic field solver interacts with the boundaries of the simulation domain. This is done by determining the boundary conditions used by the code; the choice of boundary condition is an important design decision, and many codes permit a choice of boundary conditions [73].

Mathematically, recall that the updating the value of some field $\vec{A}_a$ at the $a^{th}$ grid cell requires defined values for the field at $\vec{A}_{a-1}$ and $\vec{A}_{a+1}$. For the majority of cells in the grid, there is no problem with this requirement; however, for a grid with $A$ cells defined from $a = 1$ to $a = A$, updating the values of the fields at $\vec{A}_1$ and $\vec{A}_A$ require defined values of the fields at cells $a = 0$ and $a = A + 1$, which do not (by definition) exist. The algorithm by which values for cells outside of the grid are determined, so that values at the boundaries of the grid may be updated, is known as the boundary condition of the model [73].

One of the most common and basic set of boundary conditions for electromagnetic field solvers are periodic boundaries. Mathematically, periodic boundary conditions are calculated by [73]:

$$\vec{A}_{1-a} = \vec{A}_{A+1-a}; \quad \vec{A}_{A+a} = \vec{A}_a \tag{3.31}$$

Effectively, the system is assumed to be simulating one of an infinite series of adjacent cells which repeat in the direction in which periodic boundaries have been chosen.

Another common, basic set of boundary conditions which are closely related to periodic boundaries are reflecting boundaries.. Mathematically, reflecting boundary conditions are calculated by [73]:

$$\vec{A}_{1-a} = -\vec{A}_{1+a}; \quad \vec{A}_{A+a} = -\vec{A}_{A-a} \tag{3.32}$$

Effectively, the system is assumed to be simulating one of an infinite series of adjacent cells, similar to that of periodic boundary conditions, but which mirror one another at the boundaries. Since this behavior is identical to that of a perfect conductor being placed on the boundaries, this boundary condition is sometimes also called a conducting boundary.

Lindmann open-space boundary conditions are somewhat more complex boundary conditions which absorb, rather than reflect, incident waves, acting (in effect) as though the simulation domain resides within an infinite region of free space [79]. A rigorous mathematical development of this boundary condition is beyond the scope of this dissertation; instead we will only say that it consists of applying corrections to the electromagnetic wave's source term at the boundaries, so that the reflection coefficient at the boundaries is reduced to zero. These corrections must be updated as the simulation proceeds[79].

## 3.3 Particle-in-Cell (PIC) Codes

### 3.3.1 Overview

The Particle-in-Cell method, or PIC method, is a kinetic plasma modeling technique which is ideally suited for simulating anisotropic, collisionless plasmas. The PIC method consists of two components: the electromagnetic field, defined on a Yee grid and iterated via the FDTD method as previously described in section 3.2.1, and the plasma, which is defined as a collection of kinetic macroparticles which move in response to the electromagnetic fields. The charge and current densities of the plasma are calculated from this collection of macroparticles, and these quantities are then fed back into the FDTD iteration of the electromagnetic field [80].

At first glance, the PIC method sounds very similar to the Klimontovich equation discussed in section 2.2.2, which was stated to be computationally infeasible for physi-

cally interesting plasmas. One might be inclined to suspect the same thing of the PIC method, except for one important distinction: the PIC method does not track every particle in the plasma, but rather a much smaller number of macroparticle "clouds" that each represent many individual particles. Additionally, these macroparticles are not point-like, but rather given finite a finite physical size; this effectively treats the particles as diffuse [80].

The diffuse nature of the PIC particles circumvents a major disadvantage of the Klimontovich equation, in that the small-scale, microscopic elements of the electromagnetic field are averaged out, leaving smoother macroscopic fields. However, another possible concern about the PIC model is that, by reducing the number of particles to a computationally feasible level, we risk violating the plasma condition (as discussed in section 2.2.1), thereby preventing collective effects from dominating the system dynamics. We are saved from this pitfall, however, by the near-equivalence of the conditions that $N_D >> 1$ and $\omega_{p,e} >> \nu_{e,i}$, The diffuse nature of the PIC macroparticles means that the impact of inter-particle collisions (which derive from the point-like nature of the interacting particles) is greatly reduced, which in turn reduces the effective collision frequency to a point where $\omega_{p,e} >> \nu_{e,i}$. Therefore, the system will behave as though $N_D >> 1$; i.e., it will behave like a plasma [80]. It should be noted that, even though the effect of inter-particle collisions in PIC codes is greatly reduced, it is possible to include collisions in these models. However, collisions were not considered for the work presented in this dissertation.

From an algorithmic point of view, the PIC method has four steps; these steps repeat cyclically until the conclusion of the simulation [80]:

1. Iterating the Macroparticle Momenta and Positions from the Fields

2. Weighting the Particle Momenta to the Grid to Calculate the Current Density

3. Iterating the Electromagnetic Fields Using the Particle Current and FDTD

Method

4. Weighting the Electromagnetic Fields Back to the Particles

Note that particle collisions are not modeled by the method as presented; for this dissertation particle collisions were not considered.

### 3.3.2 Computational Cycle: Macroparticle Pushing

Advancing the particle positions and momenta requires numerical approximations to the equations of motion [3]:

$$\frac{\partial \vec{x}}{\partial t} = \frac{\vec{p}c}{\sqrt{m^2c^2 + p^2}} \tag{3.33}$$

$$\frac{\partial \vec{p}}{\partial t} = q\left\{\vec{E} + \left[\left(\frac{\vec{p}}{\sqrt{m^2c^2 + p^2}}\right) \times \vec{B}\right]\right\} \tag{3.34}$$

where $p \equiv |\vec{p}|$ is the magnitude of the momentum. Discretizing the first equation is fairly straightforward [80]:

$$\frac{\vec{x}_{t+\frac{1}{2}} - \vec{x}_{t-\frac{1}{2}}}{\Delta t} = \frac{c}{\sqrt{m^2c^2 + p_t^2}}\vec{p}_t \tag{3.35}$$

$$\vec{x}_{t+\frac{1}{2}} = \vec{x}_{t-\frac{1}{2}} + \left(\frac{c\Delta t}{\sqrt{m^2c^2 + p_t^2}}\vec{p}_t\right) \tag{3.36}$$

Note that, much as with the electric and magnetic fields in the FDTD method, we solve for the positions and momenta of the particles one half-time-step out of sync with one another. Unfortunately, such a neat discretization does not exist for the

momentum equation:

$$\frac{\vec{p}_{t+1} - \vec{p}_t}{\Delta t} = q\left\{ \vec{E}\left(\vec{x}_{t+\frac{1}{2}}\right) + \left[ \left( \frac{\vec{p}_{t+\frac{1}{2}}}{\sqrt{m^2c^2 + p^2_{t+\frac{1}{2}}}} \right) \times \vec{B}\left(\vec{x}_{t+\frac{1}{2}}\right) \right] \right\}$$

as observant readers will no doubt note that the momentum $\vec{p}$ is not defined at the timestep $t + \frac{1}{2}$. The most common solution to this problem is known as the "Boris pusher;" wherein the particle undergoes half of the acceleration due to the electric field [81]:

$$\vec{p}_- = \vec{p}_t + \frac{q\vec{E}\left(\vec{x}_{t+\frac{1}{2}}\right)}{2}\Delta t \tag{3.37}$$

then is rotated according to the magnetic field [81], [80]:

$$\frac{\vec{p}_+ - \vec{p}_-}{\Delta t} = q\left[ \left( \frac{\vec{p}_+ + \vec{p}_-}{2} \right) \times \vec{B} \right] \tag{3.38}$$

which can be solved via the following sequence[81], [80]:

$$\vec{p}_{prime} = \vec{p}_- + \left[ \vec{p}_- \times \left( \frac{q\vec{B}\Delta t}{2\gamma mc} \right) \right] \tag{3.39}$$

$$\vec{p}_+ = \vec{p}_- + \left\{ \vec{p}_{prime} \times \left[ \frac{q\vec{B}\Delta t}{\gamma mc} \left( \frac{1}{1 + \frac{q^2|\vec{B}|^2\Delta t^2}{4\gamma^2 m^2 c^2}} \right) \right] \right\} \tag{3.40}$$

and finally the particle undergoes the remaining half of its acceleration due to the electric field [81], [80]:

$$\vec{p}_{t+1} = \vec{p}_+ + \frac{q\vec{E}\left(\vec{x}_{t+\frac{1}{2}}\right)}{2}\Delta t \tag{3.41}$$

The Boris scheme allows the momentum to be effectively center-differenced explicitly [81], and is a standard method for PIC particle pushers.

### 3.3.3 Computational Cycle: Macroparticle Weighting

Determining the charge and current densities of the particles requires mapping the particles' finite shapes and locations (which are defined continuously) onto the discrete grid upon which the fields are defined. Effectively, each particle's "mass" needs to be weighted to one or more of the grids' cells; the precise nature of the algorithm which performs this operation effectively determines the "shape" of the particle in physical space [80].

Macroparticle weighting schemes are defined by their order; higher-order weighting schemes are more computationally intensive, and distribute a macroparticle's mass over more cells. However, they also result in much smoother charge and current densities, and therefore produce less noisy results. Figures 3.3 and 3.4 present graphical representations of, respectively, first- and second-order one-dimensional weighting schemes. In each of these figures, the macroparticle's "mass" is shown by its height above the axis; the "area" of the figure contained within the boundaries of a given cell therefore represents the proportional "weight" that macroparticle contributes to that cell's charge and current density. Consequently, the weight a macroparticle contributes to a given cell can be thought of as the ratio of the "area" contained within that cell to the macroparticle's total "area." [80]

Assume we have a macroparticle at position $x_{mp}$, on a one-dimensional grid with a grid spacing of $\Delta x$. Assuming the particle lies within $\Delta x/2$ of the location of the $a^{th}$ grid cell (i.e., within the range $x_a - \Delta x/2 < x_{mp} < x_a + \Delta x/2$), then for a first-order weighting scheme, the proportional contribution of the particle to cells $a$ and $a-1$ is

[80]:

$$w_a = \frac{\left[\left(x_{mp} + \frac{\Delta x}{2}\right) - x_a\right]}{\Delta x} \tag{3.42}$$

$$w_{a-1} = \frac{\left[x_a - \left(x_{mp} - \frac{\Delta x}{2}\right)\right]}{\Delta x} \tag{3.43}$$

Graphically, this scheme is shown in Figure 3.3. Graphically, the weight of a particle's contribution to a given cell is equal to the "area" of the particle that lies within that cell's borders. The scheme is slightly different in second order. Here, we assume the

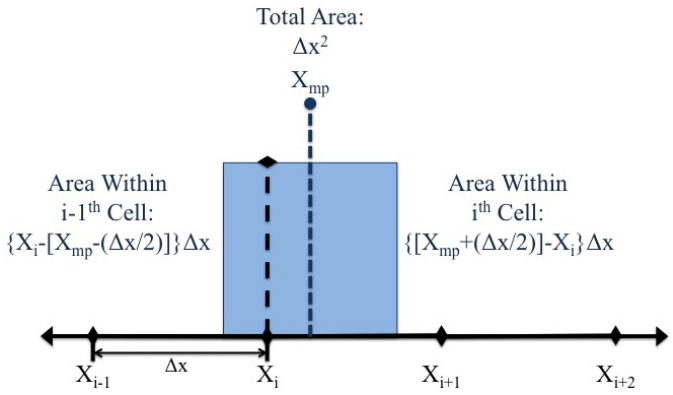


Figure 3.3: A graphical representation of a one-dimensional, first-order weighting scheme for a PIC code; the proportional weight of a particle assigned to a given cell is represented by the proportional area of the shape contained within that cell's boundaries.

particle lies within the $a^{th}$ cell (i.e., such that $x_a < x_{mp} < x_{a+1}$). For this weighting scheme, the proportional contribution of the particle to cells $a-1$, $a$, and $a+1$ is [80]:

$$w_{a-1} = \frac{\left(x_{a+1} - x_{mp}\right)^2}{2\Delta x^2} \tag{3.44}$$

$$w_a = 1 - \frac{\left(x_{a+1} - x_{mp}\right)^2}{2\Delta x^2} - \frac{\left(x_{mp} - x_a\right)^2}{2\Delta x^2} \tag{3.45}$$

$$w_{a+1} = \frac{(x_{mp} - x_a)^2}{2\Delta x^2} \tag{3.46}$$

Graphically, this scheme is shown in Figure 3.4. Ultimately, determining which

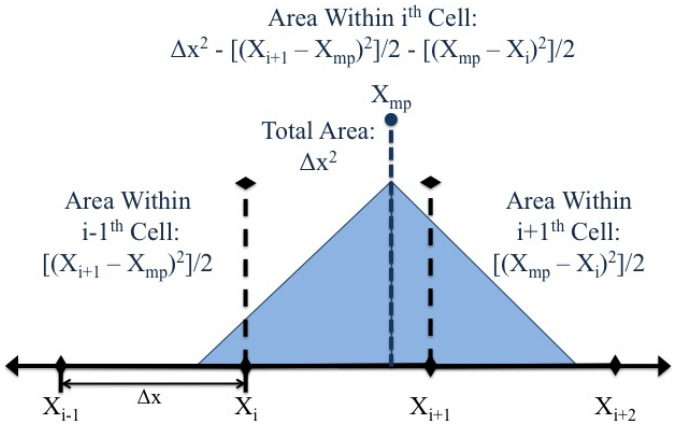


Figure 3.4: A graphical representation of a one-dimensional, second-order weighting scheme for a PIC code; the proportional weight of a particle assigned to a given cell is represented by the proportional area of the shape contained within that cell's boundaries.

weighting scheme to use in a PIC code is a design decision made between the increased smoothing of a higher-order weighting scheme and the reduced computational complexity of a lower-order weighting scheme.

Semantically, it should be noted that we have presented the particle densities and currents as being weighted to "cells" on the discrete grid. Astute readers will note, however, that the electric and magnetic fields, as modeled using the Yee cell, are not defined on individual cells, but rather on cell faces (in the case of the magnetic field) or cell edges (in the case of the electric field). This distinction does not fundamentally alter the nature of weighting particle currents to the discrete grid, but it does mean that weighting needs to be implemented with care to ensure that the points at which the discrete current is defined correctly correspond to the fields as defined by the Yee cell.

### 3.3.4 Computational Cycle: Electromagnetic Field Iteration

Once the current density has been mapped to the spatial grid, the electric and magnetic fields can be iterated using the FDTD method (i.e., equations 3.14 through 3.19). Note that the positions and individual components of the momenta of the macroparticles have to be carefully mapped to the correct index points and half-index points to properly integrate the fields using the FDTD method [80].

### 3.3.5 Computational Cycle: Electromagnetic Field Weighting

The final step in the PIC computational cycle involves calculating the electromagnetic fields at the positions of the particles; effectively this involves weighting the gridded fields back to the continuous positions of the particles, and is therefore the reverse of the macroparticle weighting scheme described in section 3.3.3 [80].

Once again, assume we have a macroparticle at position $x_{mp}$, on a one-dimensional grid with a grid spacing of $\Delta x$. Assuming the particle lies within $\Delta x/2$ of the location of the $a^{th}$ grid cell (i.e., within the range $x_a - \Delta x/2 < x_{mp} < x_a + \Delta x/2$), then for a first-order weighting scheme, the value of a given field $\vec{A}$ at the particle's position is given by a weighted average of the fields defined grid points $a$ and $a-1$ [80]:

$$\vec{A}_{mp} = w_{a-1}\vec{A}_{a-1} + w_i\vec{A}_a \tag{3.47}$$

$$\vec{A}_{mp} = \frac{\left[x_a - \left(x_{mp} - \frac{\Delta x}{2}\right)\right]}{\Delta x}\vec{A}_{a-1} + \frac{\left[\left(x_{mp} + \frac{\Delta x}{2}\right) - x_a\right]}{\Delta x}\vec{A}_a \tag{3.48}$$

Once again, note that these weights can be thought of as the ratios of the "area" of the particle within the cells to the total "area" of the particle, as depicted in Figures 3.3 and 3.4. For a second-order weighting scheme, where $\vec{x}_{mp}$ lies between $\vec{x}_a$ and

$\vec{x}_{a+1}$, we have [80]:

$$\vec{A}_{mp} = w_{a-1}\vec{A}_{a-1} + w_a\vec{A}_a + w_{a+1}\vec{A}_{a+1} \tag{3.49}$$

$$\vec{A}_{mp} = \frac{(x_{a+1} - x_{mp})^2}{2\Delta x^2}\vec{A}_{a-1} + \left[1 - \frac{(x_{a+1} - x_{mp})^2}{2\Delta x^2} - \frac{(x_{mp} - x_a)^2}{2\Delta x^2}\right]\vec{A}_a +$$

$$\frac{(x_{mp} - x_a)^2}{2\Delta x^2}\vec{A}_{a+1} \tag{3.50}$$

Additionally, recall once more that the electric and magnetic fields are defined on the edges and faces of the discrete grid cells, rather than the center of the cells. This does not fundamentally alter the nature of the process by which the electric and magnetic fields are weighted to the macroparticle positions. However, it does mean that, for example, the weighting factors $w_x$ for the electric and magnetic fields may differ.

Finally, it is important to note that it is not entirely necessary to use the same order scheme to both weight the particles to the grid, and to weight the electromagnetic fields to the particles. Using the same scheme for both weighting processes generally ensures a conservation of momentum; however by varying the two schemes, other quantities (such as energy) can instead be conserved [80].

### 3.3.6 Particle Boundary Conditions

As with the field solver, it is impossible to simulate an infinite number of particles. Consequently, the behavior of the particles when they exit the simulation domain needs to be determined. Again, as with the field solver, choosing which boundary conditions to use for the particle solver is an important design decision, and many codes permit a choice of boundary conditions.

For particle solvers, periodic and reflecting boundary conditions are conceptually very similar to their field-solver counterparts. For periodic boundary conditions, any particles which exit the domain re-enter the domain through the opposite boundary. For reflecting boundary conditions, particles which exit the domain are redirected back into the domain with the component of their momentum in the exiting direction reversed. In both cases, the boundary conditions effective simulate an infinite series of repeating domains, exactly as with their field-solver counterparts.

For absorbing boundary conditions, particles which exit the simulation are assumed to be lost, and are removed from the simulation. Effectively, the simulation domain is assumed to be suspended in an infinitely-absorbing medium.

## 3.4 OSIRIS 2.0 Features & Implementations

The previous section presented the basic concepts and methods underlying all PIC codes. For this section, we present the specific implementation of these concepts in OSIRIS 2.0, the PIC code used for the entirety of this dissertation; it was developed by the Osiris Consortium at IST Portugal and UCLA.

### 3.4.1 PIC Cycle

The computational cycle used by OSIRIS is as follows [82]:

1. The selected diagnostics are executed
2. The particle positions and momenta are pushed using the current field values
3. The particle and current boundaries are updated, and the nodes communicate if necessary
4. The current grid is calculated from the weighted particle momenta.
5. The deposited currents are smoothed, if smoothing has been specified

6. The electric and magnetic fields are updated, and their boundaries are updated

7. If it has been requested, the code's last step is to write restart information

### 3.4.2 Boundary Conditions & Moving Box

A major advantage of OSIRIS 2.0 is its moving window feature [82]. For LWFA simulations, the interaction length is substantially longer than the pulse length; consequently, a simultaneous simulation of the entire plasma would inefficiently devote a majority of the system's computational resources to simulating non-interacting bulk plasma [82]. OSIRIS 2.0 circumvents this difficulty by only simulating the plasma locally around the pulse in the laboratory frame. As the pulse advances through the plasma, the simulation window (and the simulation grid) moves with the pulse; cells exiting the back of the window are removed from the simulation, while new, un-interacted cells are introduced at the leading edge of the box [82]. The initial validation simulations considering simple cyclotron motion used a stationary box; however, all other simulations used in this dissertation featured a moving window.

OSIRIS allows the user to chose from the following boundary conditions for the fields [82]:

1. Periodic

2. Reflecting/Conducting

3. Lindmann Open-Space

and from the following boundary conditions for the particles [82]:

1. Periodic

2. Absorbing

3. Reflecting

4. Thermal Bath

Note that "thermal bath" boundary conditions consist of re-injecting exiting particles with new velocities taken from a specified thermal distribution [82]. Additionally, the boundary conditions for the particles at the leading and trailing edge of the moving simulation window are determined by the moving box dynamics as previously discussed. For this dissertation, periodic boundary conditions were used for both the particles and fields out of simplicity, and the domain was made large enough to minimize edge effects.

### 3.4.3 Pulse Definition, Field Calculation, & Pulse Propagation

OSIRIS supports a number of mechanisms for defining and generating laser pulses on its grid. The method used for this dissertation was the "zpulse" routine, wherein the electromagnetic fields in the simulation window are initialized as a laser pulse of the specified characteristics; the electromagnetic field solver then propagates the pulse as normal. This routine is supported for both moving and stationary simulation windows [82]. The transverse pulse envelope (i.e. the laser spot) can be specified to have one of the following shapes [82]:

1. Planar: A simple plane wave
2. Hermite/Gaussian: A pulse shape of the form $\sim e^{-r^2/\sigma^2}$
3. Bessel: The bessel function of the first kind $\sim J_1(r)$
4. Asymmetric Gaussian: An off-axis Gaussian profile

For the aberrant pulse simulations in the next chapter, "aberrant hermite" and "aberrant Gaussian" profiles (profiles consisting of hermite/Gaussian profiles modified by the presence of an optical aberration) were also added. The longitudinal pulse envelope can be specified to have one of the following shapes:

1. Hermite/Gaussian: A longitudinal profile of the form $\sim e^{-z^2/L_z^2}$

2. Polynomial: A fifth-order polynomial approximation to the Gaussian envelope

3. Sine-squared: A longitudinal profile of the form $\sim \sin^2(z)$, over a single half-period of the sine function.

4. Math: A user-specified mathematical function

For this dissertation, a (fifth-order) polynomial longitudinal profile was used.

Additionally, OSIRIS allows fields to be launched from the simulation boundaries via an antenna routine [82]. This routine allows pulses to be generated which propagate in non-orthogonal directions, or which start at some time after the start of the simulation.

The propagation of the pulse is determined by the field solver used; OSIRIS uses a finite difference solver like that previously discussed. Consequently, waves propagating in OSIRIS are subject to a directionally-dependent numerical dispersion if the grid discretization varies with dimension, as shown in equation 3.24. This was the case for the simulations featured in this dissertation; the grid spacing in the pulse propagation direction was four times smaller than the grid spacing in the transverse directions. This decision was made because the dominant electromagnetic waves in the simulation were traveling in the propagation direction; consequently the differential grid spacing was chosen to minimize the effects of both numerical diffusion and numerical dispersion. This allowed us to model the laser pulse propagation in the forward direction as accurately as possible, as previously discussed in the sections regarding numerical dispersion and the CFL condition.

### 3.4.4 Weighting, Deposition, & Conservation Properties

OSIRIS permits the user to select a weighting scheme from between $1^{st}$ and $4^{th}$ order. The current deposition scheme used in OSIRIS is covered in detail in Appendix

B of [83]. This scheme was chosen because it is charge-conserving, and allows the local field solver to be used [82]. It works as follows:

1. The particle's position is advanced as normal.
2. The total change in the particle's position in one time-step, $\Delta\vec{r}$, is calculated.
3. The half-way point of the particle's displacement, $\Delta\vec{r}/2$, is calculated.
4. The distances between this half-way point and the centers of the nearby local cells are calculated according to the chosen weighting scheme.

### 3.4.5 Other Features

OSIRIS supports a number of other features which were not directly relevant this dissertation but are included here for completeness [82].

1. The code outputs data as HDF5 files, which is platform-independent.
2. Current versions of the code also simulate the effects of ionization using several different models. This feature was not used for this dissertation.
3. OSIRIS is massively parallel; its parallelization scheme is based on the MPI library.
4. OSIRIS also features dynamic load balancing, where the domain mapping to the available nodes is dynamically altered to maximize efficiency.

# CHAPTER IV

# Simulation of Synchrotron-Like Radiation: Algorithm Methodology

## 4.1 Algorithm Motivation

The simulation of radiation generated by LWFA-accelerated electrons is a non-trivial problem. An exact analytical solution requires that the retarded field equations be integrated over the entire trajectory of each radiating particle:

$$\vec{E}\left(\vec{x},t\right)=e\left[\frac{\vec{n}-\vec{\beta}}{\gamma^{2}\left(1-\vec{\beta}\cdot\vec{n}\right)^{3}R^{2}}\right]_{ret}+\frac{e}{c}\left\{\frac{\vec{n}\times\left[\left(\vec{n}\times\vec{B}\right)\times\dot{\vec{\beta}}\right]}{\left(1-\vec{\beta}\cdot\vec{n}\right)^{3}R}\right\}_{ret} \tag{4.1}$$

$$\vec{B}\left(\vec{x},t\right)=\left(\vec{n}\times\vec{E}\right)_{ret} \tag{4.2}$$

where $\vec{\beta}$ is the particle's velocity normalized to the speed-of-light $c$, $\vec{n}$ is the direction of observation, $\gamma$ is the particle's relativistic Lorentz factor, and $R$ is the distance from the particle to the observer. When this radiation is of sufficiently high intensity, the situation is made more difficult still by the nontrivial radiation reaction force experienced by the emitting particle.

One approach to this problem used by the makers of OSIRIS 2.0, the Osiris

Consortium, is as follows [84]:

1. Run the simulation normally
2. Determine which particles' spectra are relevant
3. Flag the particles-of-interest and rerun the simulation
4. Extract the trajectories of the particles-of-interest
5. Integrate equations 4.2 over the particle trajectories to calculate the radiation spectra and intensities

If the radiation reaction force is expected to be significant, the particle equations-of-motion:

$$m_e c \frac{du^\mu}{ds} = \frac{e}{c} F^{\mu\nu} u_\nu; \quad \frac{dx^\mu}{ds} = u^\mu \tag{4.3}$$

(shown here in four-vector notation) are modified to include this effect by including a radiation friction term $g^\mu$:

$$m_e c \frac{du^\mu}{ds} = \frac{e}{c} F^{\mu\nu} u_\nu + g^\mu \tag{4.4}$$

This term represents the recoil force acting on the radiating particles by the emitted radiation. There are several forms for the radiation friction term; one such term is the Landau-Lifshitz equation:

$$g^\mu = \frac{2e^3}{3m_e c^3} \left\{ \frac{\partial F^{\mu\nu}}{\partial x^\lambda} u_\nu u_\lambda - \frac{e}{m_e c^2} \left[ F^{\mu\lambda} F_{\nu\lambda} u^\nu - \left( F_{\nu\lambda} u^\lambda \right) \left( F^{\nu\kappa} u_\kappa \right) u^\mu \right] \right\} \tag{4.5}$$

A reduced version of this equation is featured in the previously-described method used by the Osiris consortium.

A more in-depth summary of methods for the simulation radiation emission in PIC codes is given by Sokolov et al [85]. Different methods of radiation simulation are presented depending on the strength of the electric field $E$, characterized by the parameter $\chi$:

$$\chi = \frac{2}{3}\frac{E}{E_s} \tag{4.6}$$

where $E_s = 1.3 \times 10^18 V/m$ is the Schwinger limit [86], a threshold electric field above which QED effects become significant. For $\chi << 1$ (QED-weak fields), QED effects are negligible. For $\chi \sim 1$ (QED-moderate fields), QED corrections need to be incorporated to accurately model the physics, and when $\chi >> 1$ (QED-strong fields), QED effects like electron-positron pair production are dominant [85].

### 4.1.1 QED-Weak Fields

For $\chi << 1$, the spectral distribution can be calculated first from the following integral [85]:

$$\frac{dE^m_{rad}}{d\vec{n}d\bar{\omega}} = \int_0^t \left[ \sum_i^N \frac{I_{cl}}{\omega_c} \delta^2 \left( \vec{n} - \frac{\vec{p}}{p} \right) \delta \left( log\left(\bar{\omega}\right) - log\left(\omega_c\right) \right) \right] dt \tag{4.7}$$

and convoluting it [85]:

$$\frac{dE_{rad}}{d\vec{n}d\omega'} = \int Q_{cl} \left( \frac{\omega'}{\bar{\omega}} \right) \frac{dE^m_r ad}{d\vec{n}d\bar{\omega}} dlog\left(\bar{\omega}\right) \tag{4.8}$$

where $\vec{n}$ is the direction of observation of the emitted radiation, $\bar{\omega}$ is the radiation frequency, $I_{cl}$ is the radiation energy loss rate, $Q_{cl}$ is the unity-normalized spectrum of the synchrotron emission, $\omega_c$ is the critical frequency, and $\vec{p}$ is the individual particle momentum. Note that the first integral includes a summation over all particles $i$, and is integrated over time $t$. Radiation reaction force can be handled by altering the

equations of motion for the individual particles [85]:

$$\frac{d\vec{p}}{dt} = \frac{\vec{F}_L}{m_e c} + \frac{e\left(\vec{\vec{u}} \times \vec{B}\right)}{m_e c^2} - \frac{\vec{u} E^2 \left(\vec{\vec{u}} \cdot \vec{F}_L\right)}{m_e c^3} \tag{4.9}$$

$$\frac{d\vec{x}}{dt} = \vec{u} + \vec{\vec{u}} \tag{4.10}$$

$$\vec{\vec{u}} = \frac{\tau_0}{m_e} \frac{\vec{F}_L - \vec{u}\frac{\vec{u}\cdot\vec{F}_L}{c^2}}{1 + \tau_0 \frac{\vec{u}\cdot\vec{F}_L}{mc^2}} \tag{4.11}$$

where $\vec{F}_L$ is the Lorentz force, $\vec{\vec{u}}$ is the back-reaction effect on the electron velocity, $\vec{u}$ is the electron velocity normalized to the speed of light, and $\tau_0$ is the initial proper time.

### 4.1.2 QED-Moderate & QED-Strong Fields

For this dissertation, QED effects were not considered; consequently we only briefly summarize the methods for simulating radiation in QED-moderate and QED-strong fields. For $\chi \sim 1$, i.e. QED-moderate fields, the methods presented in the previous section can be modified so that the radiation spectrum (and resulting effects like radiation back-reaction) are consistent with QED effects. For $\chi >> 1$, i.e. QED-strong fields, however, photons must be treated as kinetic macroparticles which can interact with the plasma. Effects like electron-positron pair production are important in this regime.

### 4.1.3 Comparisons with Chosen Algorithm

The results presented in this dissertation are from simulations in an entirely classical regime. For simplicity of implementation, a monte carlo algorithm approximating

the classical spectrum was implemented. This algorithm was initially also chosen to allow in-situ radiation simulation, as opposed to the methods described in the previous which require integration over the entire simulation time; however this utility was ultimately not taken advantage of in the results.

## 4.2 Mathematical Basis

We begin by reiterating the expression for the energy radiated per unit frequency, per unit solid angle, by a charged particle traveling in instantaneous circular motion, as previously stated in chapter 2:

$$\frac{d^2I}{d\omega d\Omega} = \frac{3\gamma^2 e^2}{\pi^2 c}\tilde{\omega}^2 \left(1+\tilde{\theta}^2\right)^2 \left[K^2_{\frac{2}{3}}(\xi) + \frac{\tilde{\theta}^2}{1+\tilde{\theta}^2}K^2_{\frac{1}{3}}(\xi)\right] \tag{4.12}$$

$$\xi \equiv \frac{\tilde{\omega}}{2}\left(1+\tilde{\theta}^2\right)^{3/2} \tag{4.13}$$

as well as the one-dimensional, angularly-integrated spectrum:

$$\frac{dI}{d\omega} = \frac{2\sqrt{3}e^2\gamma}{c}\tilde{\omega}\int_{2\tilde{\omega}}^{\infty} K_{\frac{5}{3}}(x)\,dx \tag{4.14}$$

where $\tilde{\omega}$ is the normalized frequency of the emitted radiation, $\tilde{\theta}$ is the out-of-plane angle at which the radiation is emitted, $\gamma$ is the particle's relativistic Lorentz factor, and the frequency and angle are normalized to the critical values:

$$\tilde{\omega} \equiv \frac{\omega}{\omega_c}; \quad \tilde{\theta} \equiv \frac{\theta}{\theta_c}; \quad \omega_{crit} \equiv 3\gamma^3\left(\frac{c}{\rho}\right); \quad \theta_{crit} \equiv \frac{1}{\gamma} \tag{4.15}$$

This normalization scheme allows the frequency and angle-of-emission of a particle's instantaneous radiation to be characterized independently of its motion.

The algorithm used for this dissertation uses equations 4.13 as a two-dimensional probability distribution to randomly determine a normalized frequency/normalized angle pair ($\tilde{\omega},\ \tilde{\theta}$) for each radiating particle at a particular time step (i.e., a Monte Carlo method is used). The real frequency and angle are then calculated by multiplying $\tilde{\omega}$ and $\tilde{\theta}$ by $\omega_{crit}$ and $\theta_{crit}$, respectively. Finally, a "macrophoton" is emitted with this frequency and at this angle; rather than representing a single photon, this macrophoton represents all of the energy the particle would have radiated over the timestep. While the utility to model the interaction of the macrophoton with the plasma was considered, it was ultimately not included in this research, and the macrophotons' properties were immediately printed after generation.

To determine the total amount of energy radiated by a charged particle in motion in a given time step, we begin with Liénard's result for the power radiated by a moving charge [[3]]:

$$P = \frac{2}{3}\frac{e^2}{c}\gamma^6\left\{ \left(\dot{\vec{\beta}}\cdot\dot{\vec{\beta}}\right) - \left[\left(\vec{\beta}\times\dot{\vec{\beta}}\right)\cdot\left(\vec{\beta}\times\dot{\vec{\beta}}\right)\right] \right\} \tag{4.16}$$

and simply multiply by the simulation timestep:

$$E = \Delta t\frac{2}{3}\frac{e^2}{c}\gamma^6\left\{ \left(\dot{\vec{\beta}}\cdot\dot{\vec{\beta}}\right) - \left[\left(\vec{\beta}\times\dot{\vec{\beta}}\right)\cdot\left(\vec{\beta}\times\dot{\vec{\beta}}\right)\right] \right\} \tag{4.17}$$

## 4.3 Implementation & Normalization in OSIRIS 2.0

### 4.3.1 Normalization Scheme

The normalization scheme for the algorithm is, ultimately, the normalization scheme used by the code in which the algorithm is implemented: OSIRIS 2.0. In OSIRIS 2.0, spatial and temporal quantities are normalized to the laser parameters

as follows:

$$\lambda_{norm} = \frac{\lambda_l}{2\pi}; \quad \tau_{norm} = \frac{\lambda_{norm}}{c} \tag{4.18}$$

where $\lambda_l$ is the laser wavelength, c is the speed of light, and $\lambda_{norm}$ and $\tau_{norm}$ are the normalizing length and time, respectively. In other words, to convert from normalized spatial and temporal units ($x_{norm}$ and $t_{norm}$, respectively) to real spatial and temporal units ($x_{real}$ and $t_{real}$, respectively), we multiply:

$$x_{real} = \lambda_{norm} x_{norm}; \quad t_{real} = \tau_{norm} t_{norm} \tag{4.19}$$

For the primary laser simulated by the code, HERCULES, $\lambda_l = 800$ nm; therefore we assume unless explicitly stated otherwise:

$$\lambda_{norm} = \frac{800nm}{2\pi} = 127nm; \quad \tau_{norm} = \frac{1.27 \times 10^{-7} m}{3.0 \times 10^{8} m/s} = 0.423fs \tag{4.20}$$

### 4.3.2 Implementation Overview

The algorithm is implemented in the following sequence:

1. The particle's initial and final positions and momenta are used to calculate the radius-of-curvature of its instantaneous circular motion.

2. The particle's critical frequency and critical angle are determined according to equation 4.15.

3. A normalized frequency $\tilde{\omega}$ is generated according to the distribution given by equation 4.14.

4. The normalized frequency is compared to the two-dimensional distribution for $\tilde{\omega}$ and $\tilde{\theta}$ given by equation 4.13 to determine the probability density function for the normalized angle-of-emission $\tilde{\theta}$.

5. The normalized angle-of-emission is randomly generated from this probability density function.

6. The normalized frequency and angle-of-emission are then multiplied by the critical frequency and angle, respectively, to determine the frequency and angle-of-emission in normalized units.

7. The energy of the macrophoton is calculated according to equation 4.16.

8. To capture the effects of radiation friction (i.e., the loss of particle energy to the emitted radiation), the momentum of the photon is taken to be $E/c$, and the emitting particle is recoiled from the photon, if the user has chosen to consider photon recoil. For the work presented in this dissertation, regimes were chosen where radiation friction was not a significant effect, so this step was not used.

9. Finally, the macrophoton's direction-of-emission, frequency, and total energy are all outputted.

10. To improve statistics, the macrophoton generation is repeated $N$ times, where $N$ is a user-specified integer.

A semantic note: we are using the term "macrophoton" to refer to the kinetic particles generated at each time-step. However, since we are diving the total radiated energy into $N$ particles, it is possible that the total energy of a given generated macrophoton of frequency $\omega$ may be less than the energy of a photon of that frequency $E_{h\nu} = h\omega/2\pi$. If we wish to consider the system in a regime where QED effects are important, then this eventuality needs to be considered. However, for the result

### 4.3.3 Radius of Curvature Calculation

The radius of curvature at the $t^{th}$ time step, $\rho_t$, is calculated from the particle position and momenta at time steps $t$ and $t-1$, $\vec{r}_t$, $\vec{p}_{t+1/2}$, $\vec{r}_{t-1}$, and $\vec{p}_{t-1/2}$, as shown

in Figure 4.1.

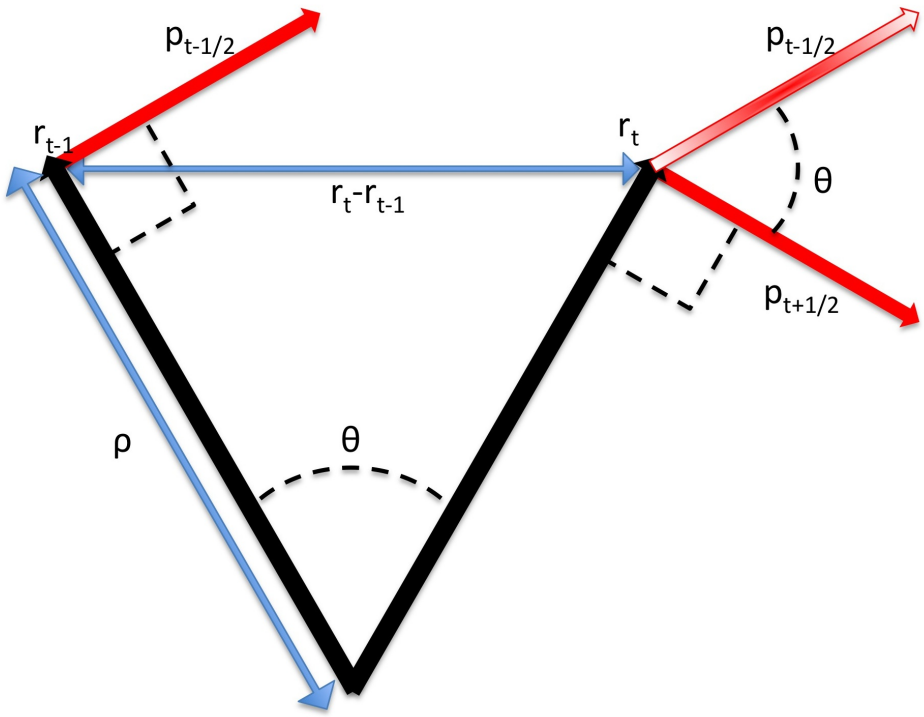


Figure 4.1: The calculation of the radius of curvature from the particle positions and momenta before and after a single time step. It is apparent from basic trigonometry that the angle between the two vectors $\vec{r}_t$ and $\vec{r}_{t-1}$ is the same as the angle between the two vectors $\vec{p}_{t-1/2}$ and $\vec{p}_{t+1/2}$, when the vectors $\vec{r}_t$ and $\vec{r}_{t-1}$ both originate at the center of the circle to which both $\vec{p}_{t-1/2}$ and $\vec{p}_{t+1/2}$ are tangent. This is the circle along which the particle is assumed to be traveling instantaneously for this time step.

To calculate the radius of curvature $\rho$, we assume that the particle momenta before and after the time-step are both tangential to a circle of radius $\rho$. Figure 4.1 shows that the angle $\theta$ of the arc along this circle through which the particle moves is equal to the angle between the particle momenta, which can be calculated from the dot product of these two vectors:

$$\vec{p}_{t+1/2} \cdot \vec{p}_{t-1/2} = |\vec{p}_{t+1/2}||\vec{p}_{t-1/2}| \cos(\theta) \tag{4.21}$$

$$\theta = arccos\left(\frac{\vec{p}_{t+1/2}\cdot\vec{p}_{t-1/2}}{|\vec{p}_{t+1/2}||\vec{p}_{t-1/2}|}\right) \tag{4.22}$$

Once this angle has been calculated, the radius of curvature $\rho$ can be calculated. We may construct a right triangle whose hypotenuse is $\rho$, whose height is the half the distance separating the two points $\vec{r}_t$ and $\vec{r}_{t-1}$, and whose angle opposite that height is $\theta/2$:

$$\sin\left(\frac{\theta}{2}\right) = \frac{|\vec{r}_t - \vec{r}_{t-1}|}{\rho} \tag{4.23}$$

$$\rho_i = \frac{|\vec{r}_t - \vec{r}_{t-1}|}{2\sin\left(\frac{\theta}{2}\right)} \tag{4.24}$$

Therefore, the radius of curvature is given by:

$$\rho_i = \frac{|\vec{r}_t - \vec{r}_{t-1}|}{2\sin\left[\frac{1}{2}arccos\left(\frac{\vec{p}_{t+1/2}\cdot\vec{p}_{t-1/2}}{|\vec{p}_{t+1/2}||\vec{p}_{t-1/2}|}\right)\right]} \tag{4.25}$$

Note that it is possible to make this calculation more efficient by considering the relativistic centripetal force equation [87]:

$$F_\perp = \frac{p^2}{\gamma m \rho} \tag{4.26}$$

$$\rho = \frac{p^2}{\gamma F_\perp m} \tag{4.27}$$

where $F_\perp$ is the component of the force acting on the particle perpendicular to the particle's motion. For the work presented in this dissertation, however, Equation 4.25 was used.

### 4.3.4 Random Number Generation

Random numbers were generated using Fortran 90's "RANDOM_NUMBER" function. To ensure variability, the index of the radiating particle was combined with the date and time to generate new seeds for each radiating particle and simulation run.

### 4.3.5 Normalized Frequency Generation

To generate the normalized frequency $\tilde{\omega}$, the one-dimensional distribution, given by equation 4.14 and shown in Figure 4.2, is used as an arbitrary probability density function (a PDF).

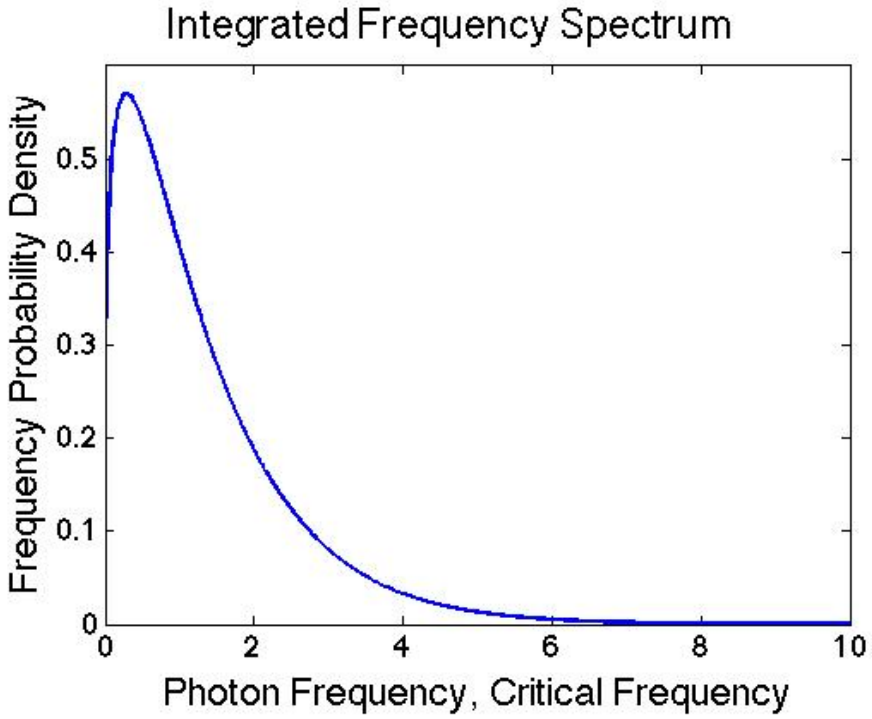


Figure 4.2: The one-dimensional frequency spectrum as a probability density function.

The first step to implementing an arbitrary function as a PDF is to divide the function's domain into equally-spaced bins, and calculate the height of those bins. This is shown graphically in Figure 4.3, along with the normalized frequencies $\tilde{\omega}$ corresponding to each bin.

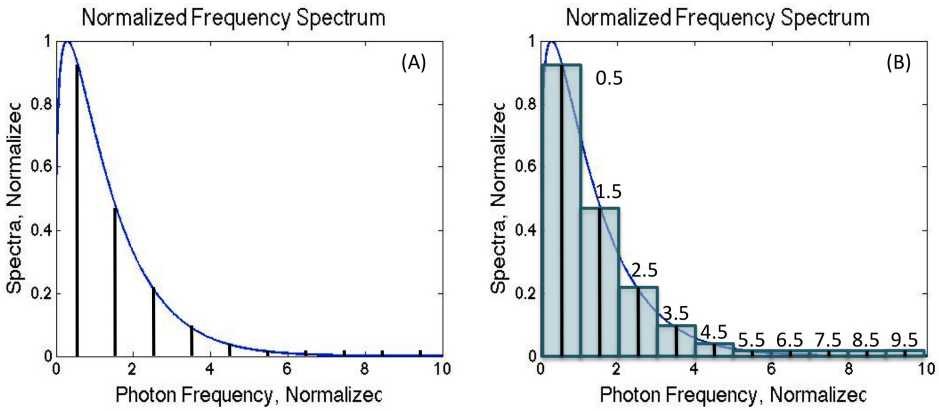


Figure 4.3: A: The normalized frequency spectrum divided into bins. B: The heights of those bins, and the normalized frequency associated with each bin.

Once the heights of the individual bins have been calculated, they are combined into a single, monotonically-increasing array of values that can be compared to a randomly-generated number $R$ that is linearly distributed between 0.0 and 1.0 (producing such a number can be done easily with commonly available functions and/or subroutines available in most standard programming languages). This process is best thought of graphically, as shown in Figure 4.4.

The array of values is constructed from the individual bin heights as follows: the first value of the array is equal to the height of the first bin. The second value of the array is equal to the first value plus the height of the second bin, the third value is equal to the second plus the height of the third bin, and so forth. The relationship between the bin heights and the length of this array is shown graphically on the bottom of Figure 4.4.

Once this array is constructed, its values are normalized to the maximum (i.e. final) value of the array so that it increases monotonically from 0.0 to 1.0. There is now a direct correlation between the spectrum of numbers $R$ randomly generated from a uniform distribution between 0.0 and 1.0, and the spectrum of normalized frequencies that we started with. The correlation works as follows: if a random

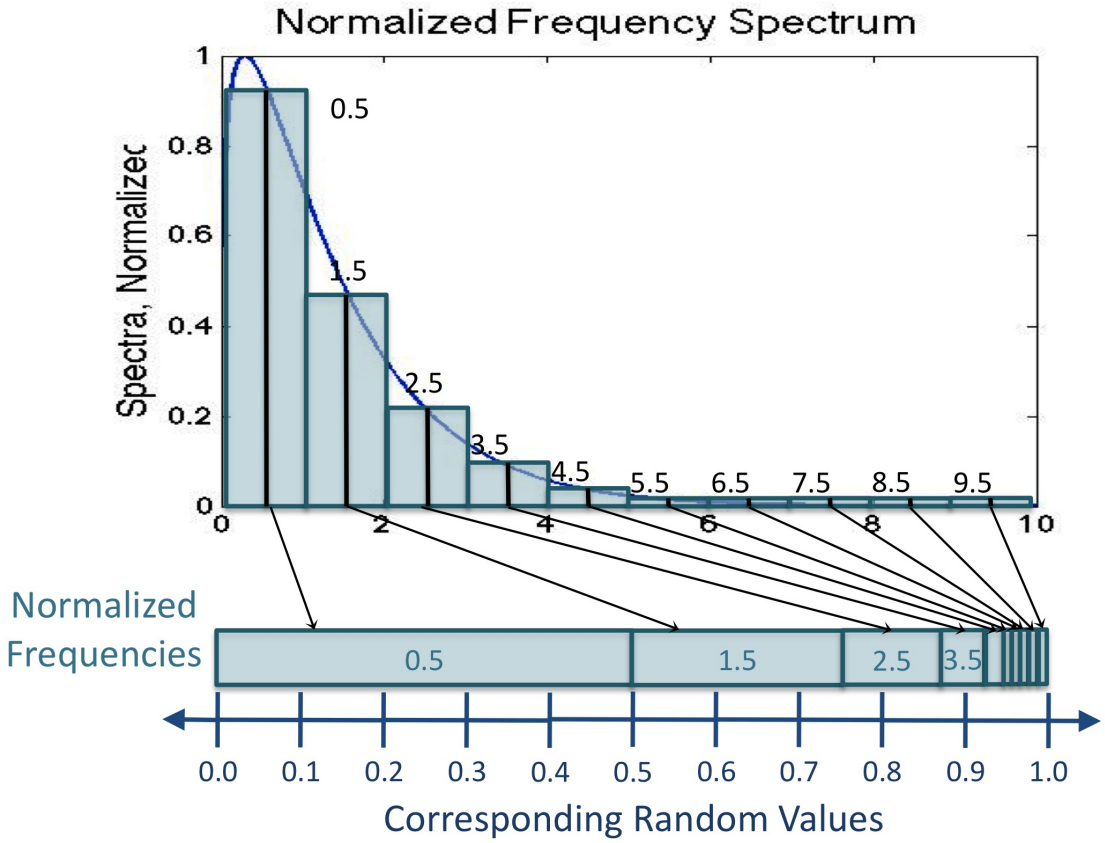


Figure 4.4: A graphical representation of the process by which the bins of the normalized frequency distribution are compared to a randomly generated number between 0.0 and 1.0, to calculate a normalized frequency between 0 and 10 according to a PDF given by equation 4.14.

Observe that each bin is effectively "stacked" on top of the previous bin, creating an array of "widths" wherein the normalized frequency corresponding to each bin is assigned a weight equivalent to the height of that bin.

The distribution of randomly generated values on the bottom of the figure is compared to the weighted array above it, which is in turn based on the bin heights as previously discussed. So, in this example, a randomly generated number between 0.0 and 0.5 would correspond to a normalized frequency of 0.5 A randomly generated number between 0.5 and 0.75 would correspond to a normalized frequency of 1.5. A randomly generated number between 0.75 and 0.86 would correspond to a normalized frequency of 2.5, and so forth.

number $R$ is generated, and is greater than 0.0, but less than the first value of the array, then $R$ corresponds to the normalized frequency of the first bin. If $R$ is greater than the first value of the array, but less than the second, $R$ corresponds to the normalized frequency of the second bin. If $R$ is greater than the the second, but less than the third, $R$ corresponds to the $\tilde{\omega}$ of the third bin, and so on.

This correlation is shown graphically along the bottom of Figure 4.4. We see the spectrum of randomly generated numbers $R$ underneath the array constructed from the bin heights of the normalized frequency spectrum. In this example, the method results in a 50% (i.e., $0.0 < R < 0.5$) chance that the first value (0.5) will be generated, a 25% ($0.5 < R < 0.75$) chance that the second value will be generated, a 10% ($0.75 < R < 0.85$) chance that the third value will be generated, and so on.

Since the normalized frequency spectrum is continuous, rather than discrete, it is necessary to interpolate between the values of the aforementioned array to produce a continuous spectrum of randomly-generated normalized frequencies. The algorithm uses linear interpolation for this process. So, if the randomly generated number $R$ is half-way between 0.0 and the first value of the array, the corresponding normalized frequency $\tilde{\omega}$ that is generated is equal to half the value of the normalized frequency that corresponds to the first value of the array (one-half of 0.5, or 0.25, in the example shown in Figure 4.4). If $R$ is halfway between the first and second values of the array, then $\tilde{\omega}$ is halfway between the normalized frequencies corresponding to those array values (halfway between 0.5 and 1.5, or 1.0, in Figure 4.4), and so forth.

The example shown in Figures 4.3 and 4.4 split the distribution into 10 bins, covering a range from $\tilde{\omega} = 0.0$ to $\tilde{\omega} = 10.0$. The actual implementation of the algorithm used 1000 bins, covering a range from $\tilde{\omega} = 0.001$ to $\tilde{\omega} = 10.0$.

### 4.3.6 Normalized Angle Generation

The normalized angle-of-emission $\tilde{\theta}$ is generated in a similar fashion to the normalized frequency, however the process is somewhat more complicated, as the probability distribution function for the angle-of-emission is the two-dimensional equation 4.13. This equation is shown in Figure 4.5 (note that the frequency scale in this image is logarithmic).

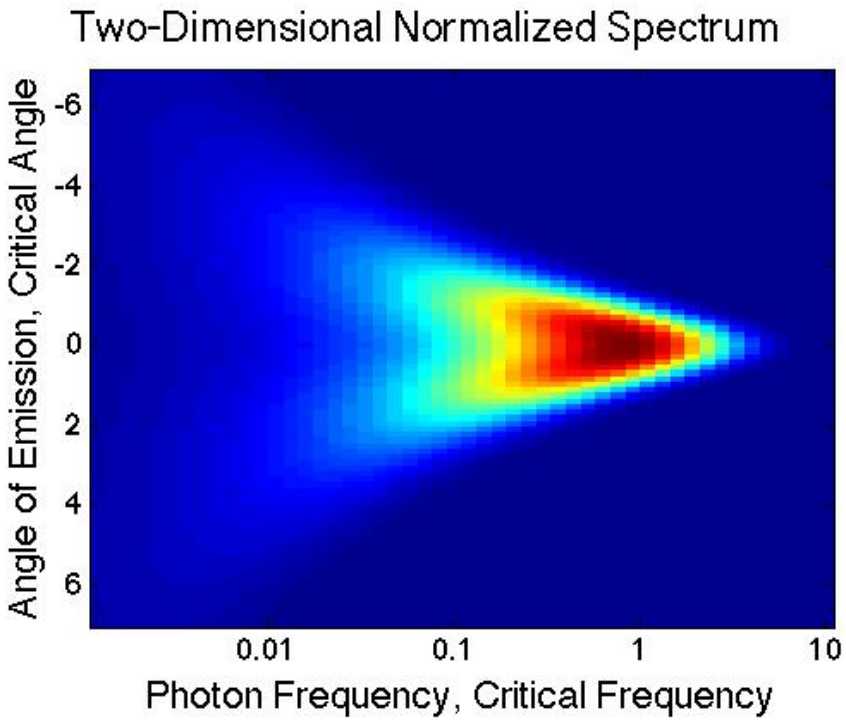


Figure 4.5: The normalized two-dimensional frequency spectrum. Note that this image shows the resolution used in the code.

Once the normalized frequency $\tilde{\omega}_{h\nu}$ has been calculated (as shown in the previous section), the (one-dimensional) angular distribution of the radiation can be determined. From this distribution, a normalized angle $\tilde{\theta}$ can be generated alongside the normalized frequency.

The first step in this process is to determine the one-dimensional angular distribution of the radiation from the two-dimensional distribution shown in Figure 4.5.

To do this, it is helpful to think of the two-dimensional distribution of Figure 4.5 as a sequence of one-dimensional angular distributions, each corresponding to a different normalized frequency $\tilde{\omega}_n$. Since we have the macrophoton's normalized frequency $\tilde{\omega}_{h\nu}$, determining the angular distribution is as simple as comparing the value of $\tilde{\omega}_{h\nu}$ to the values $\tilde{\omega}_n$. This comparison is shown in Figure 4.6. Note that the frequency distribution in this Figure is not linear, but logarithmic; this scaling was chosen because the structure of the angular distribution varies more significantly for small values of $\tilde{\omega}$ than for large values.

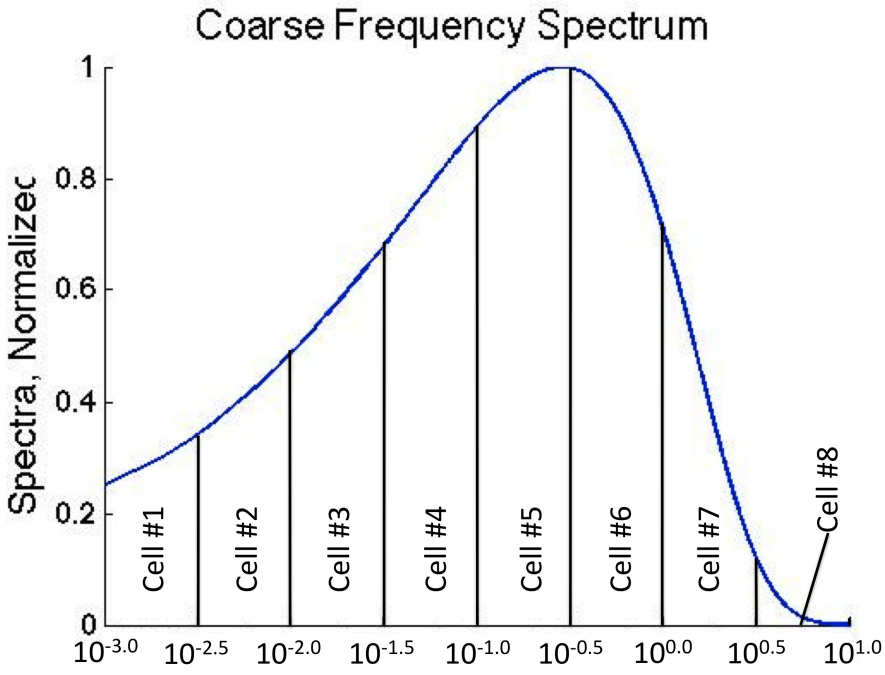


Figure 4.6: The logarithmic coarse 1D grid. The relationship between the values of the normalized frequency $\tilde{\omega}$ and the distribution grid cell numbers is shown. This example shows the distribution split into 8 cells; in other words, for this example, the two-dimensional distribution shown in Figure 4.5 would consist of 8 separate, sequential angular distributions. Note that the frequency scale is logarithmic.

In Figure 4.6, the logarithmic frequency spectrum is divided up into cells. Each cell corresponds to a different angular distribution (i.e., each cell corresponds to a

different vertical column in the two-dimensional distribution shown Figure 4.5). So, in the example shown in Figure 4.6, if $10^{-2.0} < \tilde{\omega}_{h\nu} < 10^{-1.5}$, the angular distribution for the macrophoton would correspond to the $3^{rd}$ distribution out of 8.

For greater accuracy, this method was expanded to include linear interpolation. Instead of a single distribution (column) from Figure 4.5 being used to generate the macrophoton's angle-of-emission, the two distributions at $\tilde{\omega}_n$ and $\tilde{\omega}_{n+1}$ which bound the macrophoton's normalized frequency $\tilde{\omega}_{h\nu}$ such that $\tilde{\omega}_n < \tilde{\omega}_{h\nu} < \tilde{\omega}_{n+1}$ are both used to generate normalized angles $\tilde{\theta}_{h\nu}$, and a weighted average of the two is taken. This process is demonstrated graphically in Figures 4.7 and 4.8 .

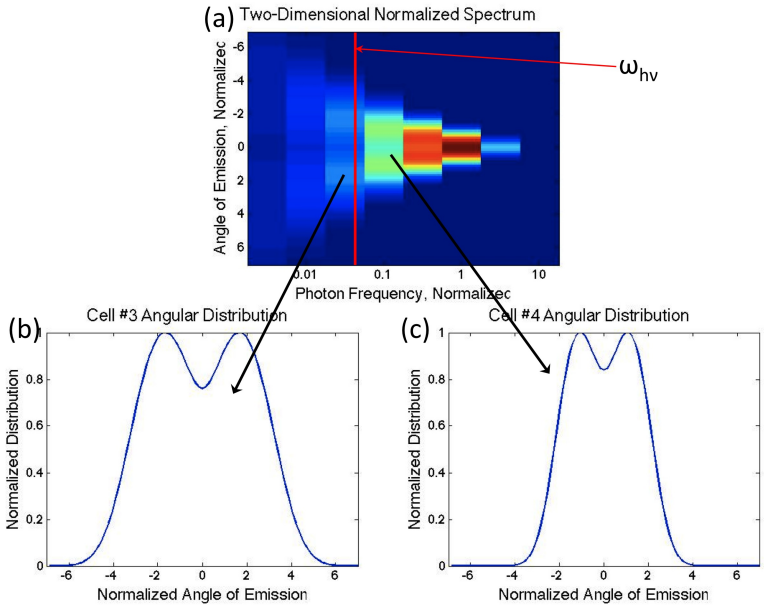


Figure 4.7: (a) The two-dimensional angular resolution with 8 bins in the frequency dimension to match Figure 4.6. The location of sample random normalized frequency $\tilde{\omega}_{h\nu}$ is shown. (b) The angular distribution corresponding to cell 3, which is the lower bound for $\tilde{\omega}_{h\nu}$. (c) The angular distribution corresponding to cell 4, which is the upper bound for $\tilde{\omega}_{h\nu}$.

Figure 4.7 shows the first step in calculating the normalized angle of emission $\tilde{\theta}$. A randomly generated normalized frequency $\tilde{\omega}_{h\nu}$ is shown on Figure 4.7-a, which shows

Equation 4.13 with the same frequency resolution as shown in Figure 4.6. Figures 4.7-b and 4.7-c are, respectively, the angular distributions corresponding to the lower and upper boundary frequencies, $\tilde{\omega}_n$ and $\tilde{\omega}_{n+1}$, such that $\tilde{\omega}_n < \tilde{\omega}_{h\nu} < \tilde{\omega}_{n+1}$. The normalized angle-of-emission is calculated from these distributions via the process shown in Figure 4.8.

Figure 4.8 shows the final step in calculating the normalized angle-of-emission $\tilde{\theta}$. The two angular distributions (from the previous step) are each mapped to a uniform distribution of random numbers between 0.0 and 1.0 in exactly the same manner as the randomly-generated normalized frequency $\tilde{\omega}_{h\nu}$. Only one random number is generated from this distribution.

Once this single number has been generated, it is mapped to both angular distributions (again, via exactly the same process as that used to calculate the normalized frequency $\tilde{\omega}$). The same random number is used with both the upper-bounding and lower-bounding distribution; this results in two normalized-angles-of-emission that are only slightly divergent. The final normalized angle-of-emission is a weighted average of these two values, where the weights are based on the mapping of the normalized frequency $\tilde{\omega}_{h\nu}$ to the coarse frequency grid, as shown in Figure 4.6.

Note that, in the above example, the coarse frequency grid contained 8 elements, and the angular distributions contained 10 elements. In the code implementation, the coarse frequency grid contained 50 elements, and the angular distributions contained 100 elements, for a total grid size of 5000.

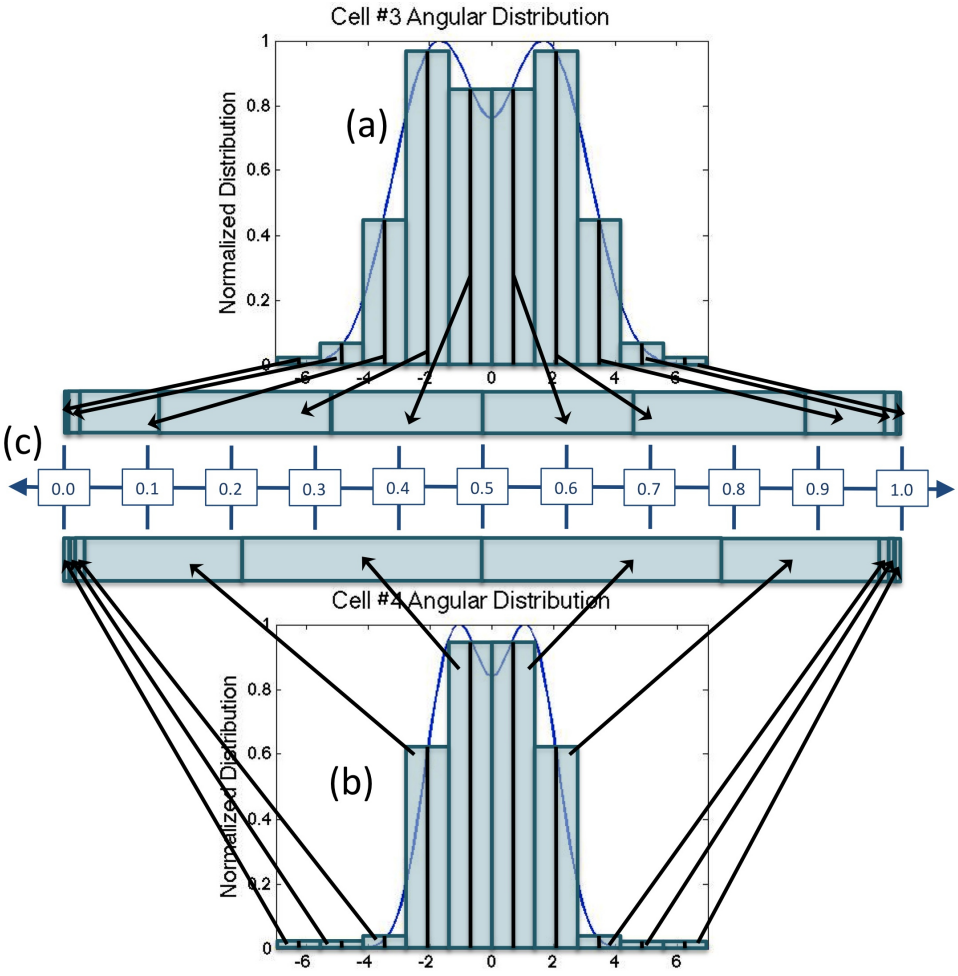


Figure 4.8: (a) The angular distribution corresponding to the lower-boundary normalized frequency $\tilde{\omega}_n$ and (b)the angular distribution corresponding to the upper-boundary normalized frequency $\tilde{\omega}_{n+1}$ mapped to (c) a uniform distribution of random numbers between 0.0 and 1.0. Note that this mapping process is identical to that shown in Figure 4.4, except that the two adjacent angular distributions are simultaneously mapped to the same random number distribution.

When a single random number, between 0.0 and 1.0, is generated, it is mapped to both distributions, producing a slightly different normalized angle-of-emission $\tilde{\theta}$. These two divergent normalized angles-of-emission are then averaged together to calculate the macrophoton's final angle-of-emission. By this process, we can effectively linearly interpolate between the two distributions.

### 4.3.7 Photon Direction-of-Emission

The direction-of-emission of the photon is calculated from the angle-of-emission (the generation of which is described in the previous section) and the initial momentum vector of the radiating particle. The angle-of-emission $\theta$ describes the angle out of the plane of particle rotation at which the radiation is generated; this is illustrated graphically in Figure 4.9.

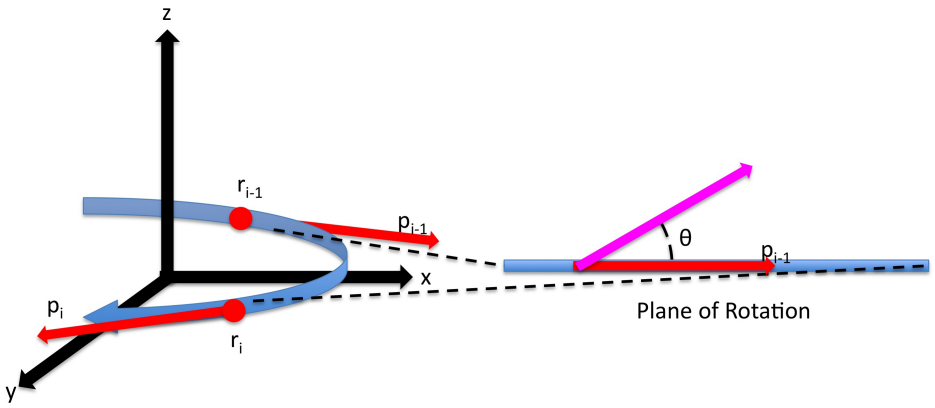


Figure 4.9: The relationship between the particle's initial and final positions and momenta, the particle's plane of rotation, and the direction-of-emission of the particle's radiation.

The vector describing the radiation's direction-of-emission is constructed as follows: first, a unit vector is constructed parallel to the particle's initial momentum. This unit vector is then raised orthogonally out of the particle's plane-of-rotation until the angle between the particle's plane of rotation and the radiation's direction-of-emission is equal to $\theta$.

As-written, there is an inaccuracy in this method: the radiation angle-of-emission does not take into account angular deviations that occur in the plane of rotation, only angular deviations that occur out of the plane of rotation. The accuracy of this method for taking into account angular deviations in the emitted radiation is therefore predicated on the approximation that plane-of-rotation angular deviations

in the spectrum are dominated by the electron motion, rather than the synchrotron spectrum. Additionally, for the results presented in this dissertation, the angular properties of the emitted radiation are not considered (all spectra presented are angularly integrated); consequently we are confident that this approximation does not diminish the accuracy of the presented results.

### 4.3.8 Radiative Cooling

The method of radiation generation described in the previous section provides an ancillary benefit: including the radiation reaction force is straightforward. The magnitude of the momentum, $|\vec{p}|$, of a photon of energy $E$ is given by:

$$|\vec{p}| = \frac{E}{c} \tag{4.28}$$

Therefore, the radiation reaction force can be included by multiplying this value (previously calculated according to Equation 4.17) by the unit vector $\vec{u}$ which describes the radiation's direction-of-emission, and subtracting this quantity from the particle's final momentum:

$$\vec{p}_f = \vec{p}_{i+1} - \frac{E}{c}\vec{u} \tag{4.29}$$

Again, the simulations shown in this dissertation were run in a regime where radiation reaction could be ignored.

## 4.4 Verification Simulations

Verification tests were performed on the algorithm by running simulations of a single particle undergoing simple gyrotron motion, affected using a static magnetic field and with photon recoil deactivated. The parameters for these simulations were

as follows:

1. 27 particles: OSIRIS 2.0 requires a minimum grid size of 3 x 3 x 3 cells, with a minimum of 1 particle per cell. Consequently, these "single-particle" verification simulations contained 27 particles simultaneously undergoing gyrotron motion, all of which generated radiation which was averaged together.

2. Electron Lorentz factor $\gamma = 500, 1000, \& \ 2000$.

3. Magnetic field strength: 10, 50, & 250 normalized units, or 0.0844, 0.422, & 2.11 MT. Note that these field strengths were not chosen to be realistic, only to produce high energy x-ray radiation.

The results from these simulations are shown in Figures 4.10 through 4.12. The simulated results are plotted alongside the theoretical spectrum as given by equation 4.14; these results show excellent agreement between the numerical and analytic spectra over a wide range of critical frequencies. Additionally, note that, for electrons undergoing cyclotron motion with a radius $\rho$ [[3]]:

$$P = \frac{2}{3}\frac{e^2 c}{\rho^2}\beta^4\gamma^4 \tag{4.30}$$

Figure 4.13 shows the total radiated energy for these simulations (in normalized units) as a function of the cyclotron radius $\rho$, alongside the relationship given by this equation. Again, the simulation results show excellent agreement with theoretical values. There is one final salient fact regarding these verification simulations; the energy of the radiated photons greatly exceeds the kinetic energy of the radiated electrons; to actually capture the physics of the systems being simulated would require a QED-complete model. However, these simulations are not intended to represent a physically accurate picture of the system, rather they are simply intended to verify that the classical radiation spectrum is being correctly generated.

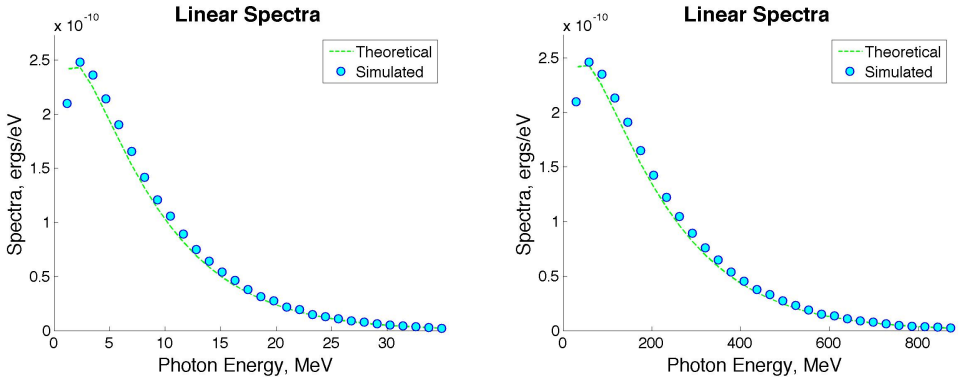


Figure 4.10: The spectra produced when simulating the radiation emitted by 27 electrons with $\gamma = 500$, undergoing gyrotron motion with radii of, from left to right, 50, 10, and 2 normalized units, or 6.365, 1.273 and 0.2546 $\mu m$. Simulated data is shown in blue; theoretical spectra are shown in green.

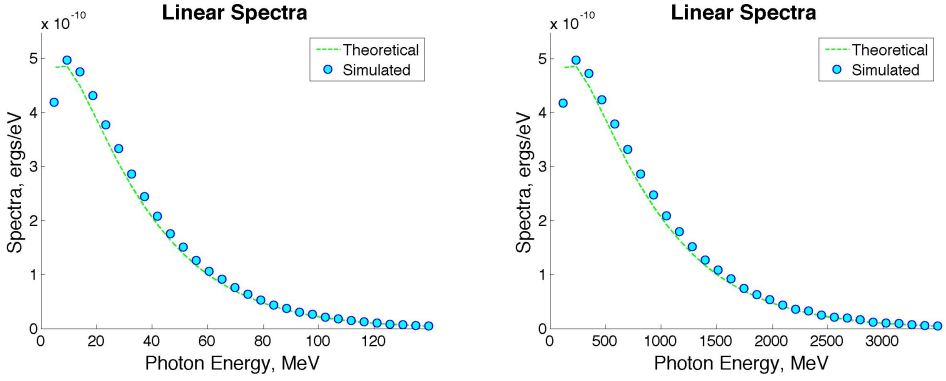


Figure 4.11: The spectra produced when simulating the radiation emitted by 27 electrons with $\gamma = 1000$, undergoing gyrotron motion with radii of, from left to right, 100, 20, and 4 normalized units, or 12.73, 2.546 and 0.5092 $\mu m$. Simulated data is shown in blue; theoretical spectra are shown in green.

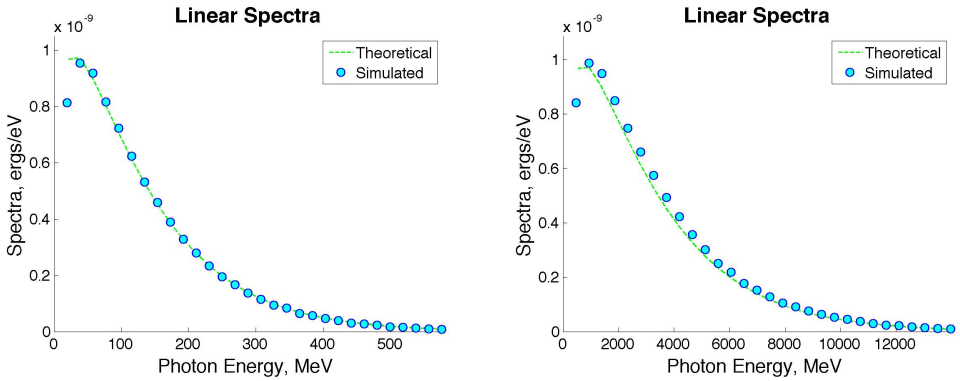


Figure 4.12: The spectra produced when simulating the radiation emitted by 27 electrons with $\gamma = 2000$, undergoing gyrotron motion with radii of, from left to right, 194, 40, and 8 normalized units, or 24.70, 5.092 and 1.018 $\mu m$. Simulated data is shown in blue; theoretical spectra are shown in green.

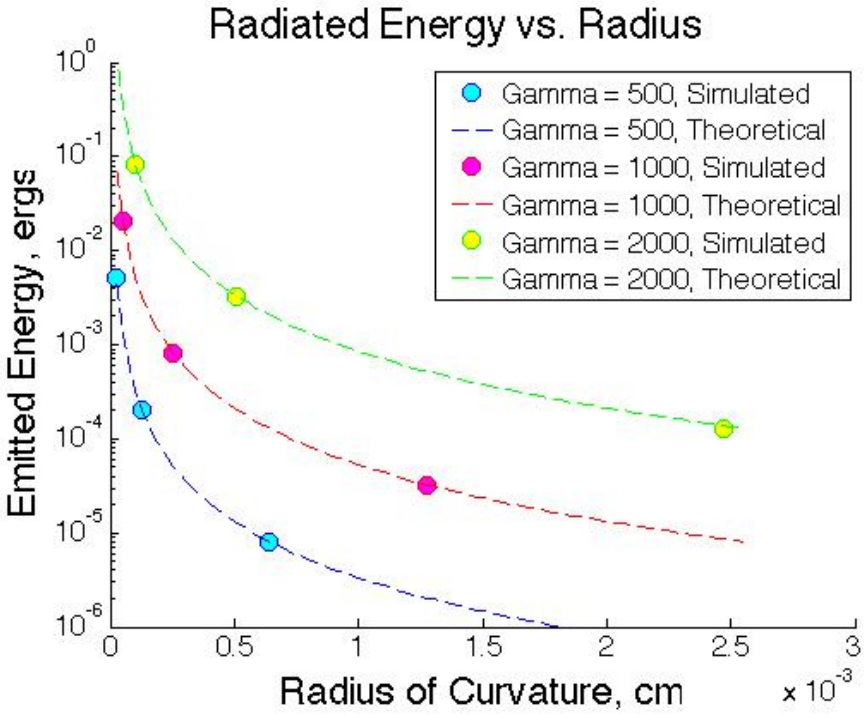


Figure 4.13: The total radiated energy as a function of radius of curvature for $\gamma = 500, 1000, \& 2000$. The circles represent the simulated results, while the dashed lines represent the theoretical values for the radiated energy as a function of radius of curvature.

# CHAPTER V

# Simulation of Synchrotron-Like Radiation: Betatron Radiation Scalings

## 5.1 Introduction

In this chapter, we present results from simulating several fundamental LWFA parameter sweeps, using the algorithm discussed in the previous section. Data are presented describing the phase-space behavior of the electrons, the radiation generated during the simulation, and the correlations between the electron trajectories and radiation properties.

The first three sections of this chapter contain descriptions of the visualization methods used in this and the next chapter. Visualization methods for the electron phase-space data, betatron radiation, and radiation/trajectory correlation data are presented and explained.

The next three sections contain the simulation results. Each section first presents the simulation parameters used for the parameter sweep, the results of the parameter sweep, and commentaries on observed trends and behaviors. Where appropriate, comparisons between the computational results and theoretical models are presented. First, results are presented from a sweep over the laser vector potential $a_0$. Then, results are presented from a sweep over the electron plasma density $n_e$. Finally, a

single simulation with a very long propagation time was used to affect a sweep over the propagation distance $L$.

## 5.2 Phase Space Data Visualization

There are two different types of phase-space data presented in this chapter: the time-evolution of the electron energy distribution function (EEDF), and the time-evolution of the electron beam's momentum phase-space profile. An example of the EEDF time-evolution plot is shown on the left of Figure 5.1; an example of the momentum profile evolution plot is shown on the right of this figure..

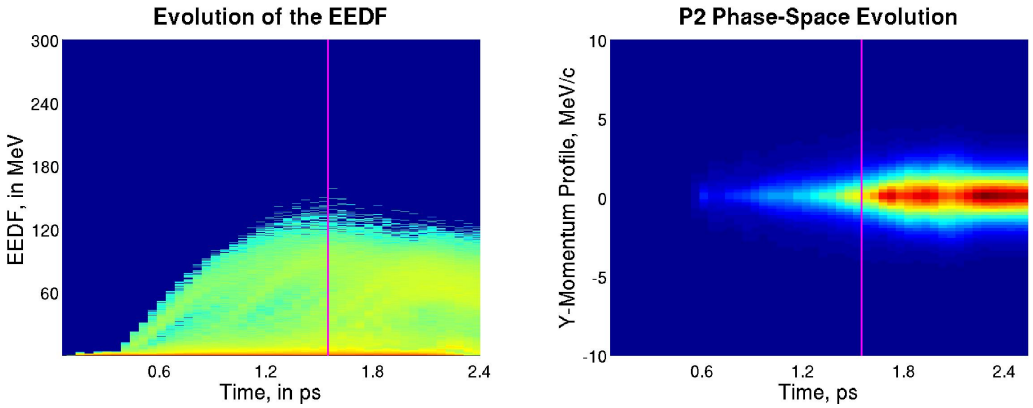


Figure 5.1: (Left) An example plot of the time-evolution of the electron energy distribution function; (right) an example plot of the time-evolution of the electron beam momentum profile

For the EEDF plots, the electron energy spectrum is shown on the vertical axis, and is calculated for the entire plasma. The EEDF is calculated at each time step, and its height at a given energy is translated to a logarithmic color scale. The EEDF at each time step forms a single column of the image; in this way, the horizontal axis of the image corresponds to time. A vertical magneta line is used to indicate the point where the system passes the dephasing length (as given by Tajima and Dawson in [28]); for systems with very long propagation times, a second magenta line indicates the point where the system passes twice the dephasing length.

For the momentum phase-space evolution, the system pXp1 momentum phase-space files were used, where X corresponds to either transverse direction and p1 corresponds to the electron momentum in the propagation direction. These data files were integrated in p1 for all electrons whose forward momentum exceeded $25MeV/c$; this cutoff was used to isolate the electron beam from the bulk plasma. This integration was done at each time step to produce the total beam profile in the corresponding momentum's phase space. The profile at each time step was then mapped to a linear color scale, and used to form a single column of the image; as with the EEDF, the horizontal axis corresponds to time. Similarly, the magenta line(s) represent the point(s) where the system passes the dephasing length (and twice the dephasing length, where appropriate).

## 5.3 Radiation Data Visualization

There are three plots of radiation data presented in this chapter: the time-evolution of the radiation spectra, the total time-integrated radiation spectra, and the total radiated power and energy with respect to time. Examples of the first two kinds of plots are shown in Figure 5.2. The spectral evolution plot (shown on the left of Figure 5.2 is constructed in a fashion similar to that of the EEDF evolution plot; the total spectrum of radiation emitted at each time-step is calculated, and mapped to a logarithmic color scale. The spectrum at each time-step is used to make that time-step's corresponding column in the image; consequently the vertical axis corresponds to photon frequency, while the horizontal axis corresponds to simulation time.

The radiated power plot (shown on the right of Figure 5.2) is calculated from the total amount of radiated energy in a given time-step divided by the length of the time-step; the radiated energy plot is simple the radiated energy plot integrated from the start time to that time. The total time-integrated spectra (not shown) is

calculated by simply integrating the time-evolution of the spectra.

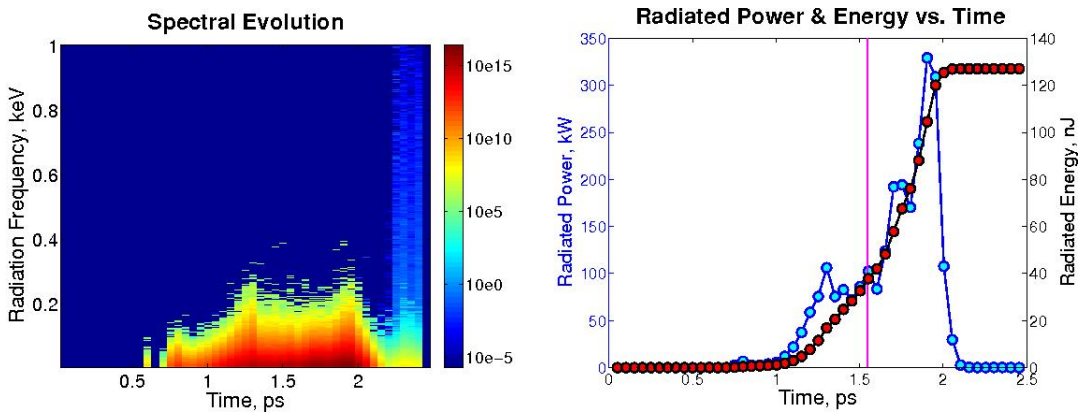


Figure 5.2: (Left) An example plot of the time-evolution of the radiation spectrum; (right) an example plot of the radiated power and total radiated energy vs. time

## 5.4 Radiation and Phase-Space Correlation Visualization

There are two different plots used to represent the correlation between the radiation and phase-space data: density plots of the emitted frequency of radiation and the kinetic energy of the emitting electron, and density plots of the emitted frequency of radiation and the instantaneous radius-of-curvature of the emitting electron's trajectory. Examples of these plots are shown in Figure 5.3.

For both plots, the total number of emitted macrophotons, frequency of the emitted radiation macrophotons, Lorentz factor gamma of the emitting electrons, and radius-of-curvature of the emitting electron trajectories were printed. These data were then used to generate the density plots (representing the total number of macrophotons with the given frequency, emitted by electrons with the given energy or radius of curvature), which were then mapped to a logarithmic color scale. These plots were used to correlate the electron motion with the radiation properties.

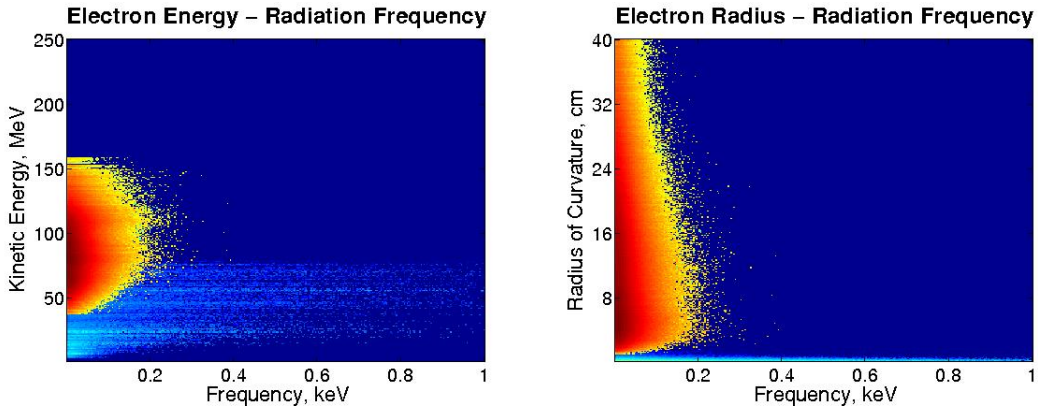


Figure 5.3: (Left) An example plot of the correlation between the emitting electron energy and emitted radiation frequency; (right) an example plot of the correlation between the emitting electron trajectory radius-of-curvature and emitted radiation frequency

| Parameter | Normalized Value | Real Value |
|---|---|---|
| Peak Plasma Density: | $0.01 n_{crit}$ | $1.75 \times 10^{19} cm^{-3}$ |
| Simulation Box Size: | $300 \times 200 \times 200$ | $39 \times 26 \times 26 \mu m$ |
| Box Propagation Speed: | c | $3.0 \times 10^{10} cm/s$ |
| Total Propagation Time: | 5900 | $2.5 ps$ |

Table 5.1: The plasma parameters for the normalized vector potential sweep

## 5.5 Normalized Vector Potential Sweep

### 5.5.1 Simulation Parameters

The plasma parameters, plasma density profile, laser parameters, and computational parameters used for the normalized vector potential sweep are listed in tables 5.1, 5.2, 5.3, and 5.4, respectively. These were serial (i.e. single-processor) runs that took $\sim 16 - 17$ hours to finish. For each value of the parameter sweep, a single simulation was performed.

### 5.5.2 Electron Phase-Space Results

A number of clear trends arise when analyzing the phase-space behavior of the electron population in response to the sweep over $a_0$. From the time-evolution plots

| Density | Initial Position | Final Position |
|---|---|---|
| 0.0 (Vacuum) | $0.0\mu m$ | $65\mu m$ |
| Linear Ramp from 0.0 to $0.01n_{crit}$ | $65\mu m$ | $130\mu m$ |
| $0.01n_{crit}$ (Bulk Plasma) | $130\mu m$ | $637\mu m$ |
| Linear Ramp from $0.01n_{crit}$ to 0.0 | $637\mu m$ | $702\mu m$ |
| 0.0 (Vacuum) | $702\mu m$ | $767\mu m$ |

Table 5.2: The density profile for the normalized vector potential sweep

| Parameter | Normalized Value | Real Value |
|---|---|---|
| FWHM Spot Size: | 40 | 5.2 $\mu m$ |
| FWHD Pulse Length: | 64 | 28 $fs$ |
| Peak Normalized Vector Potential: | Swept from 3.0 to 8.0 in 1.0 increments | |
| Peak Laser Intensity: | $1.9 - 14.0 \times 10^{19} W/cm^2$ | |

Table 5.3: The laser parameters for the normalized vector potential sweep

| Parameter | Value |
|---|---|
| Simulation Grid Size: | $600 \times 100 \times 100$ cells |
| Particles Per Cell: | 2 |
| System Grid Spacing: | $0.066 \times 0.26 \times 0.26\mu m$ |
| System Time-Step: | $0.172fs$ |
| Printing Time-Step: | $50.1fs$ |

Table 5.4: The computational parameters for the normalized vector potential sweep. Note that the highest resolution was in the propagation direction.

of the EEDF, we can see that the peak electron energy increases as the laser intensity is increased. This is consistent with the basic physics of LWFA, as higher-intensity laser pulses drive stronger, more non-linear wakes. Additionally, we see that the electron beam structure tends to become less well-defined relative to the background plasma(i.e., the density of the beam is smaller relative to the density at the minima that lies between the beam and the bulk plasma) for higher-intensity drive pulses.

The time-evolution plots of the electron momentum profiles show a very interesting trend. The lower-intensity simulations ($a_0 = 3.0$ and $a_0 = 4.0$) show relatively long-wavelength betatron oscillations, indicating that the dominant effect driving betatron motion at these intensities is the field structure of the plasma wake. Conversely, the higher-intensity simulations ($a_0 = 7.0$ and $a_0 = 8.0$) show much shorter-wavelength betatron oscillations, indicating that the dominant effect driving betatron motion at these intensities could be direct interaction between the electron beam and the laser field. At intermediate intensities ($a_0 = 5.0$ and $a_0 = 6.0$), we see that the betatron motion is initially driven by the plasma wake fields, but transitions to this higher-frequency regime as the system passes the dephasing length.

Unfortunately, two salient facts complicate the conclusion that this higher-frequency betatron motion is due to direction interaction with the laser. First, the frequency of these oscillations approaches the sampling frequency of the simulation (recall from Table 5.4 that the printing time step significantly exceeded the system time-step). Second, the effective frequency of the laser in the center-of-mass frame of the electrons in the beam will vary depending on the individual electrons' kinetic energies. These issues must first be resolved before the higher-frequency motion can be definitively attributed to interaction with the laser field; this is left to future work (see Chapter 7).

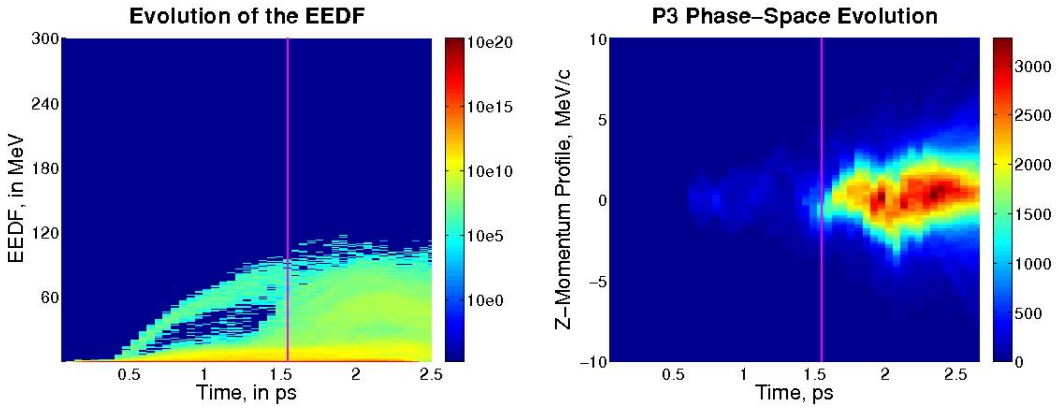


Figure 5.4: (Left) The time-evolution of the EEDF and (right) the time-evolution of the electron beam p3 momentum phase-space profile for the $a_0 = 3.0$ simulation. The magenta line indicates the location of the dephasing length. The color scales on the left are logarithmic, and in units of normalized charge per MeV per ps. The color scales on the right are linear, and are in units of normalized charge per $m_e c$ per ps.

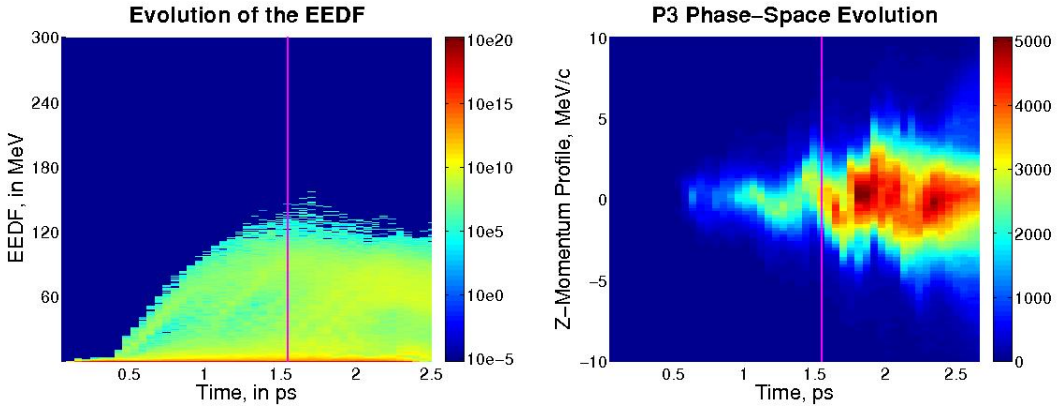


Figure 5.5: (Left) The time-evolution of the EEDF and (right) the time-evolution of the electron beam p3 momentum phase-space profile for the $a_0 = 4.0$ simulation. The magenta line indicates the location of the dephasing length. The color scales on the left are logarithmic, and in units of normalized charge per MeV per ps. The color scales on the right are linear, and are in units of normalized charge per $m_e c$ per ps.

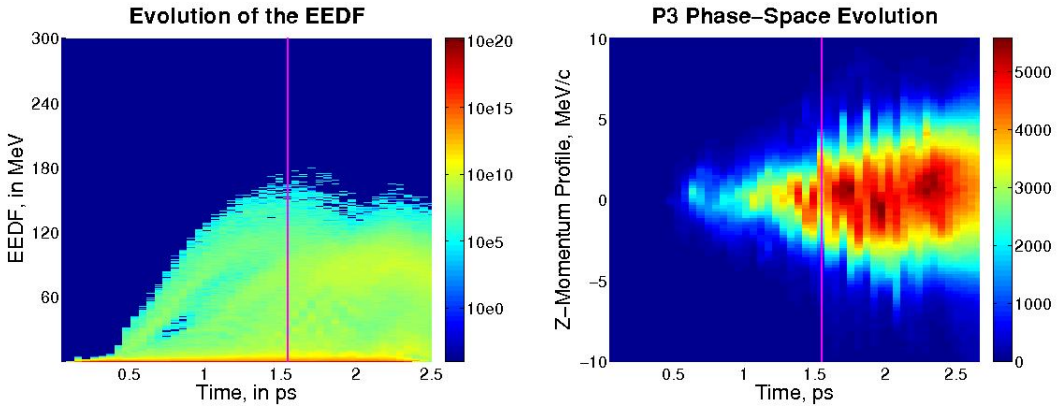


Figure 5.6: (Left) The time-evolution of the EEDF and (right) the time-evolution of the electron beam p3 momentum phase-space profile for the $a_0 = 5.0$ simulation. The magenta line indicates the location of the dephasing length. The color scales on the left are logarithmic, and in units of normalized charge per MeV per ps. The color scales on the right are linear, and are in units of normalized charge per $m_e c$ per ps.

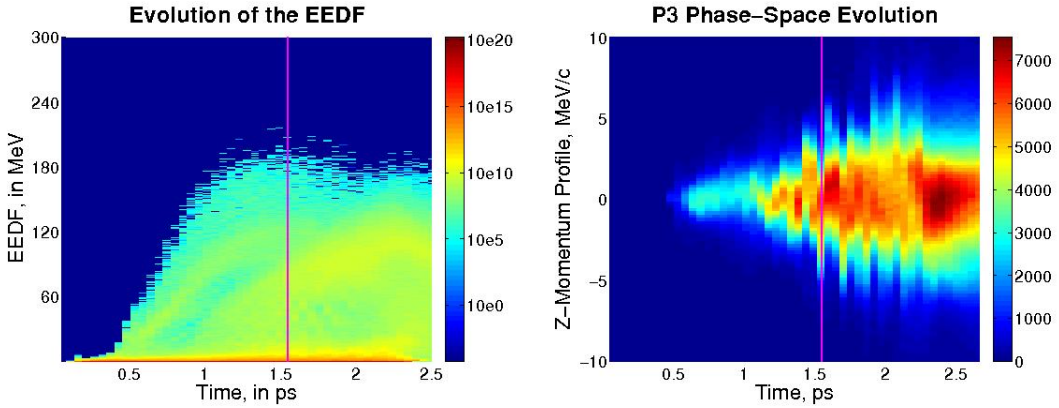


Figure 5.7: (Left) The time-evolution of the EEDF and (right) the time-evolution of the electron beam p3 momentum phase-space profile for the $a_0 = 6.0$ simulation. The magenta line indicates the location of the dephasing length. The color scales on the left are logarithmic, and in units of normalized charge per MeV per ps. The color scales on the right are linear, and are in units of normalized charge per $m_e c$ per ps.

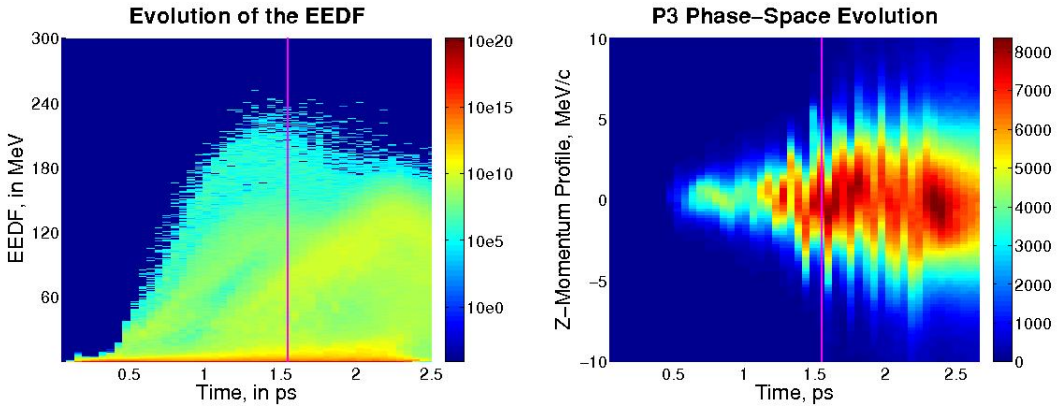


Figure 5.8: (Left) The time-evolution of the EEDF and (right) the time-evolution of the electron beam p3 momentum phase-space profile for the $a_0 = 7.0$ simulation. The magenta line indicates the location of the dephasing length. The color scales on the left are logarithmic, and in units of normalized charge per MeV per ps. The color scales on the right are linear, and are in units of normalized charge per $m_e c$ per ps.

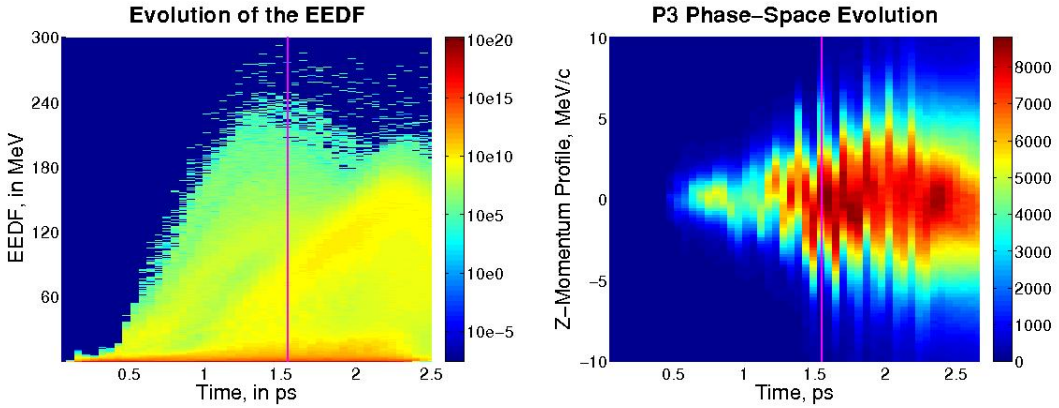


Figure 5.9: (Left) The time-evolution of the EEDF and (right) the time-evolution of the electron beam p3 momentum phase-space profile for the $a_0 = 8.0$ simulation. The magenta line indicates the location of the dephasing length. The color scales on the left are logarithmic, and in units of normalized charge per MeV per ps. The color scales on the right are linear, and are in units of normalized charge per $m_e c$ per ps.

### 5.5.3 Radiation Emission Results

The first and most obvious trend in the radiation emission results from the $a_0$ parameter sweep is the power-law increase in total emitted energy as $a_0$ is increased. This trend is summarized in Figure 5.16. It has been analytically demonstrated, for an idealized bubble structure, that the total radiated energy in a LWFA system is given by [[88]]:

$$E_{rad} = \frac{L_{int}\omega_p}{c}\frac{\pi^{3/2}\gamma_p^{3/2}}{8}a_0^{9/2}m_e c^2 \tag{5.1}$$

where $E_{rad}$ is the total radiated energy, $L_{int}$ is the interaction length, $c$ is the speed of light, $\gamma_p$ is the Lorentz factor corresponding to the bubble's phase velocity, $m_e$ is the electron mass, and $a_0$ is the normalized laser vector potential. The important conclusion to draw from this equation is that the total emitted energy scales with the normalized vector potential as $E_{rad} \sim a_0^{9/2}$; a 9/2 scaling has been fitted to the data in Figure 5.16, showing excellent agreement.

The time-evolutions of the radiated power, shown on the right-hand sides of Figures 5.10 through 5.15, also show some interesting consistencies; noticeably that the radiated power tends to increase over time as the simulation continues to propagate. This slope seems to increase somewhat for higher-intensity simulations, but does not appear to fundamentally change. Furthermore, these consistently show significant fluctuations in power as the power increases. It is unclear whether these fluctuations are due to noise, or some underlying secondary effect that results in periodic increases in radiated power.

The time-evolution of the radiated spectra (shown on the left in Figures 5.10 through 5.15) show an interesting, if somewhat qualitative, trend in addition to the simple scaling previously observed. All of the simulations show that the maximum frequency of the emitted radiation (the tail of the spectrum) initially increases in

time up to a certain point. However, for lower-intensity simulations, the tail energy then either drops off or plateaus, while for higher-intensity simulations, two separate peaks in the maximum tail energy are observable, at two different times.

More quantitative trends can be seen by observing the time-integrated spectra, shown logarithmically in Figure 5.17. Upon first observation, it appears that there are two distinct "regions" in these spectra, with the energy of the higher-frequency region several orders of magnitude smaller than the energy of the lower-frequency region. These two regions are separated by an intermediate region of statistical noise; however the time evolutions of the radiated spectra (Figures 5.10 through 5.15) shows that the high-energy regions of these spectra are consistently emitted at the end of the simulation after the laser-plasma interaction has concluded; this radiation is presumed to be a numerical artifact.

It is not entirely accurate to describe these spectra with a single critical frequency, since each spectrum represents the outputs of many electrons with a spread of energies and many different trajectories. Consequently, we will characterize these spectra by the effective temperatures of the high frequency tails of their distributions (the regions for which $\omega > 3\omega_c$) , which were found by fitting exponential curves to these regions of the spectra. Plots of both of these quantities scaling with $a_0$ are shown in Figure 5.18. It has been analytically demonstrated that the effective critical frequency of the radiation emitted by a LWFA system is given by [[88]]:

$$\omega_c = \omega_p 6 a_0^{5/2} \left( \frac{n_c}{3 n_e} \right)^{13/8} \tag{5.2}$$

where $\omega_c$ is the critical frequency of the emitted radiation spectrum, $\omega_p$ is the plasma frequency, $a_0$ is the normalized laser vector potential, $n_c$ is the critical density calculated from the laser frequency, and $n_e$ is the electron plasma density. The important conclusion to draw from this equation is that the critical frequency of the emitted

radiation spectrum scales with the normalized vector potential as $\omega_c \sim a^{5/2}$; consequently, a 5/2 scaling has been fitted to the data in Figure 5.18. The plot of the high-energy tail temperature shows a slight power scaling, which does not contradict these analytic predictions. However it is clear that there is a significant amount of noise (at least 10%) in the calculation of the high-energy tail temperature, so we should be conservative in drawing conclusions from this plot.

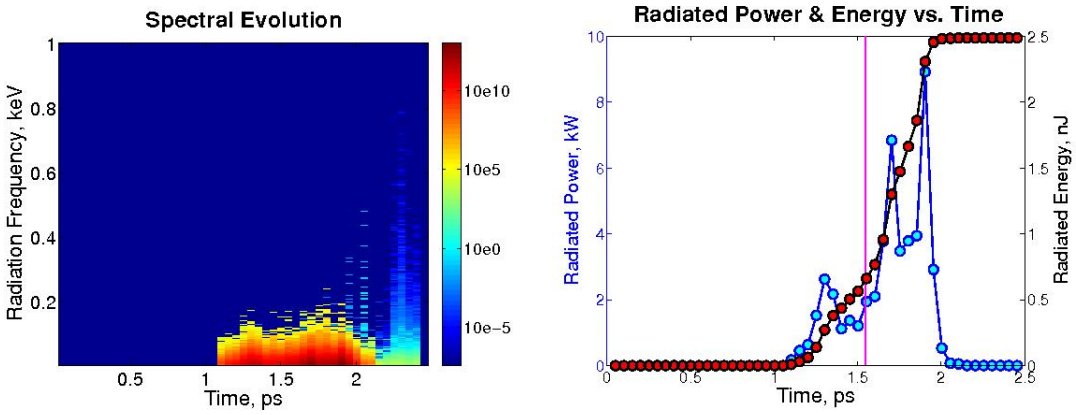


Figure 5.10: (Left) The time-evolution of the radiated spectrum and (right) the emitted power (blue) and total emitted radiation (red) vs. time for the $a_0 = 3.0$ simulation. The magenta line indicates the location of the dephasing length. Note that the color scale for the left-hand plot is logarithmic, and the units are Joules/(keV*second)

### 5.5.4 Radiation and Phase-Space Correlations

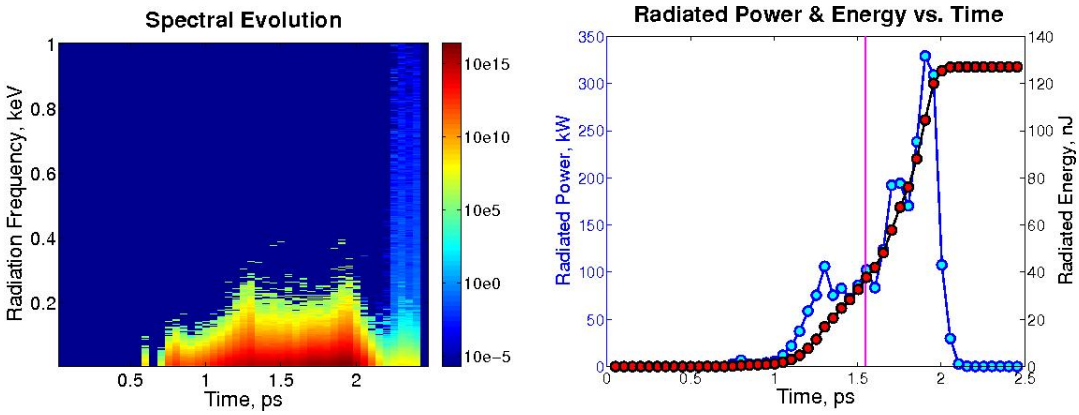


Figure 5.11: (Left) The time-evolution of the radiated spectrum and (right) the emitted power (blue) and total emitted radiation (red) vs. time for the $a_0 = 4.0$ simulation. The magenta line indicates the location of the dephasing length. Note that the color scale for the left-hand plot is logarithmic, and the units are Joules/(keV*second)

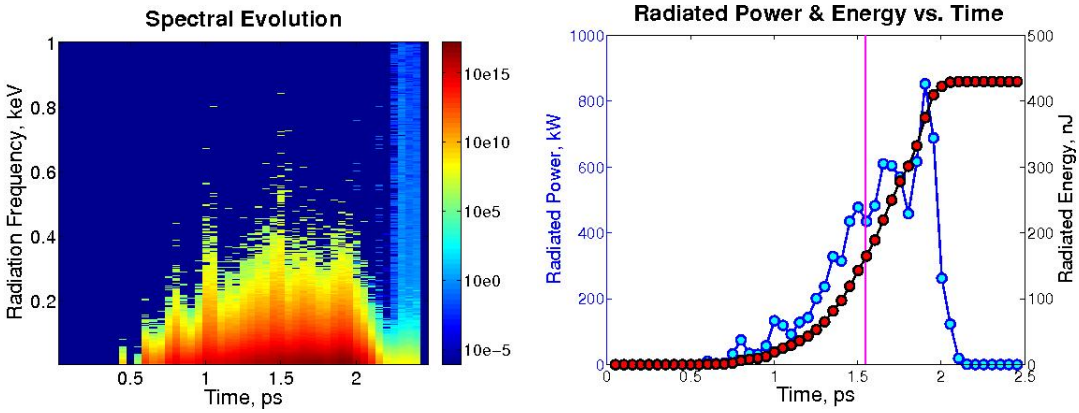


Figure 5.12: (Left) The time-evolution of the radiated spectrum and (right) the emitted power (blue) and total emitted radiation (red) vs. time for the $a_0 = 5.0$ simulation. The magenta line indicates the location of the dephasing length. Note that the color scale for the left-hand plot is logarithmic, and the units are Joules/(keV*second)

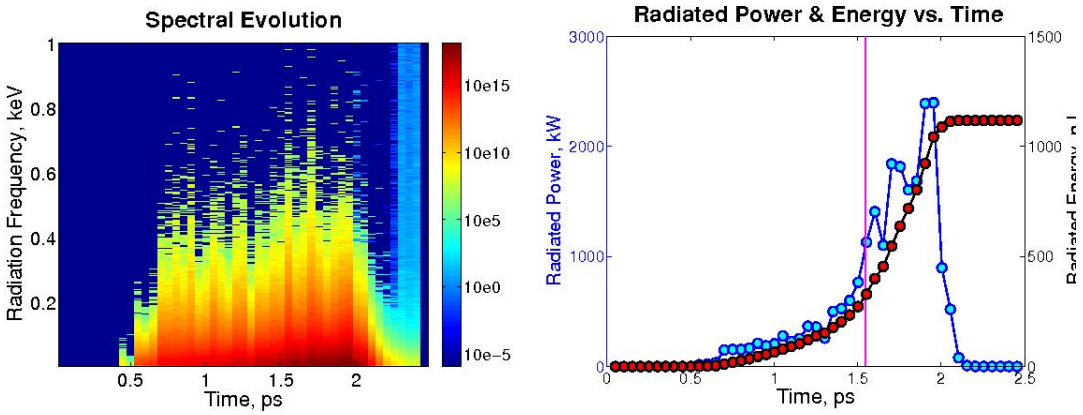


Figure 5.13: (Left) The time-evolution of the radiated spectrum and (right) the emitted power (blue) and total emitted radiation (red) vs. time for the $a_0 = 6.0$ simulation. The magenta line indicates the location of the dephasing length. Note that the color scale for the left-hand plot is logarithmic, and the units are Joules/(keV*second)

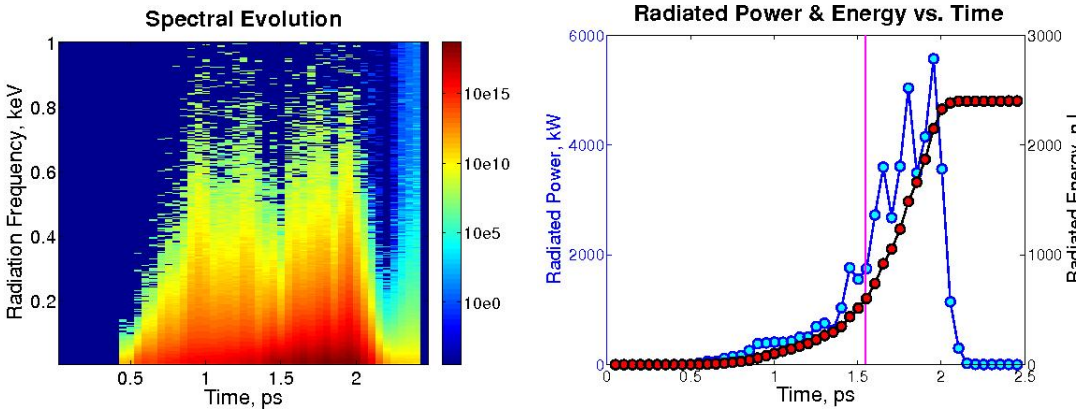


Figure 5.14: (Left) The time-evolution of the radiated spectrum and (right) the emitted power (blue) and total emitted radiation (red) vs. time for the $a_0 = 7.0$ simulation. The magenta line indicates the location of the dephasing length. Note that the color scale for the left-hand plot is logarithmic, and the units are Joules/(keV*second)

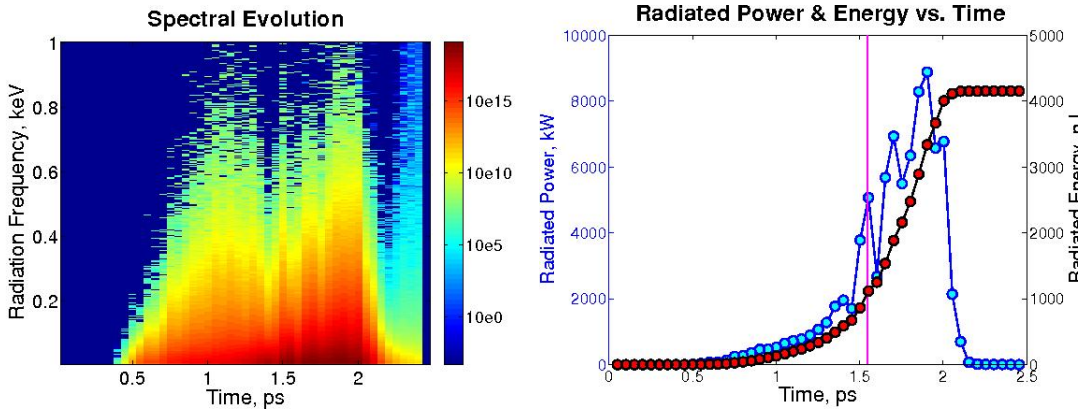


Figure 5.15: (Left) The time-evolution of the radiated spectrum and (right) the emitted power (blue) and total emitted radiation (red) vs. time for the $a_0 = 8.0$ simulation. The magenta line indicates the location of the dephasing length. Note that the color scale for the left-hand plot is logarithmic, and the units are Joules/(keV*second)

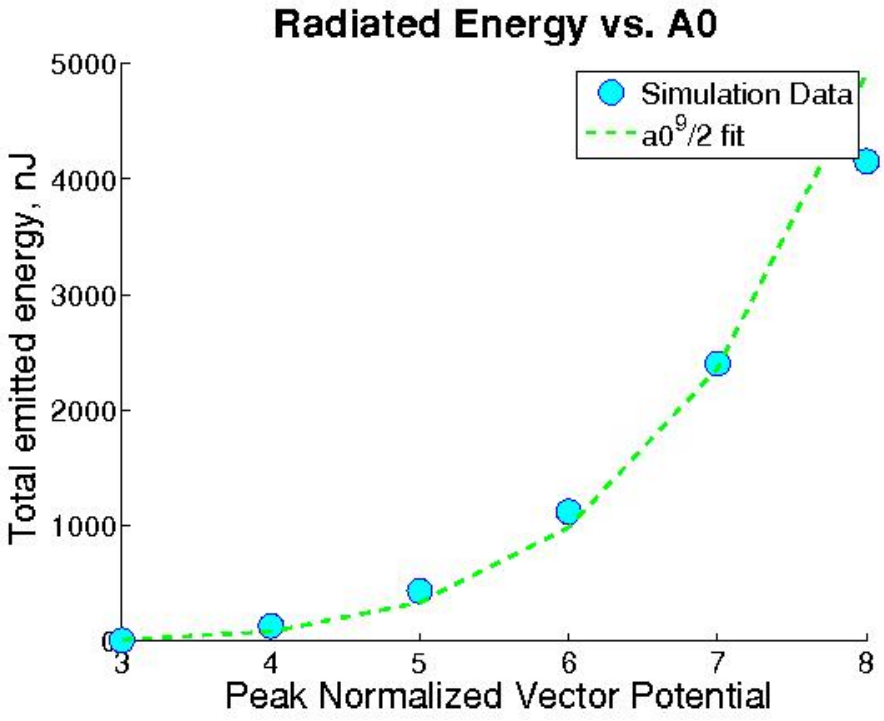


Figure 5.16: The total energy emitted produced by the simulation (shown in blue). A fit to $a_0^{9/2}$ is shown in green.

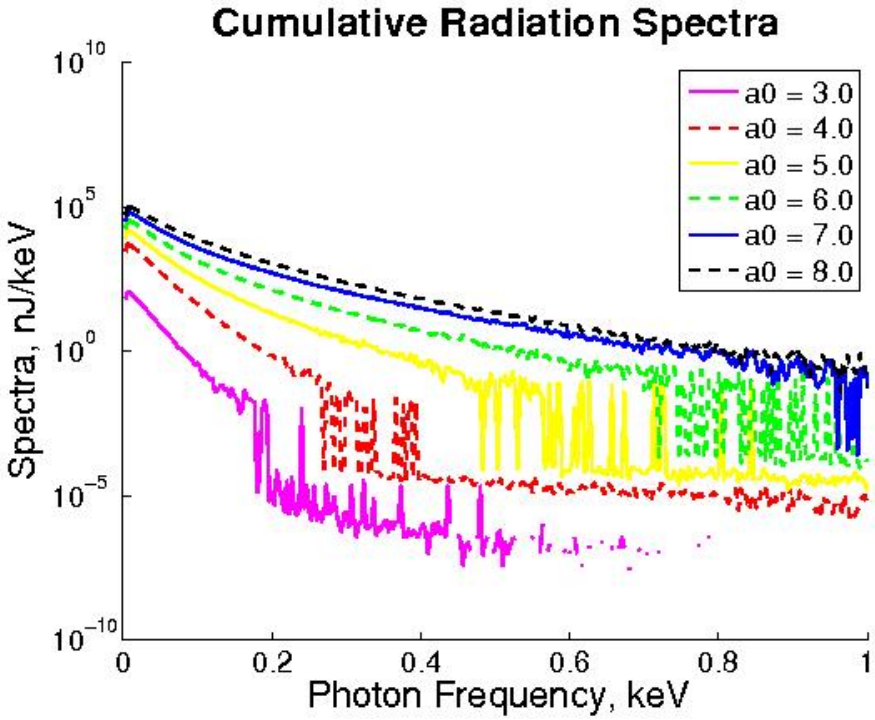


Figure 5.17: The logarithmic, cumulative spectra as a function of the normalized vector potential $a_0$.

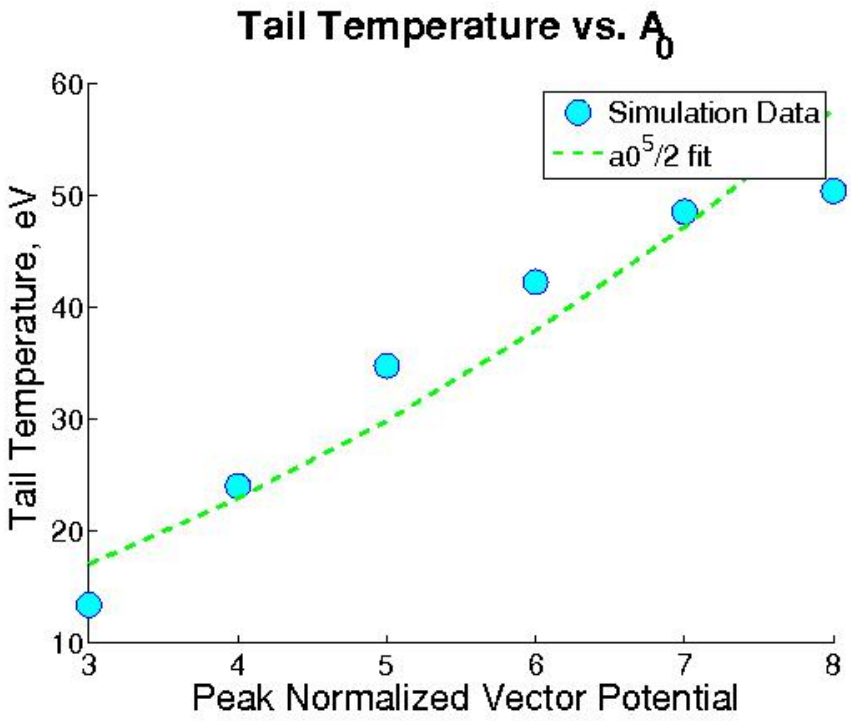


Figure 5.18: The temperature of the high-frequency tail of the spectrum. Data are shown in blue. A fit to $a_0^{5/2}$ is shown in green.

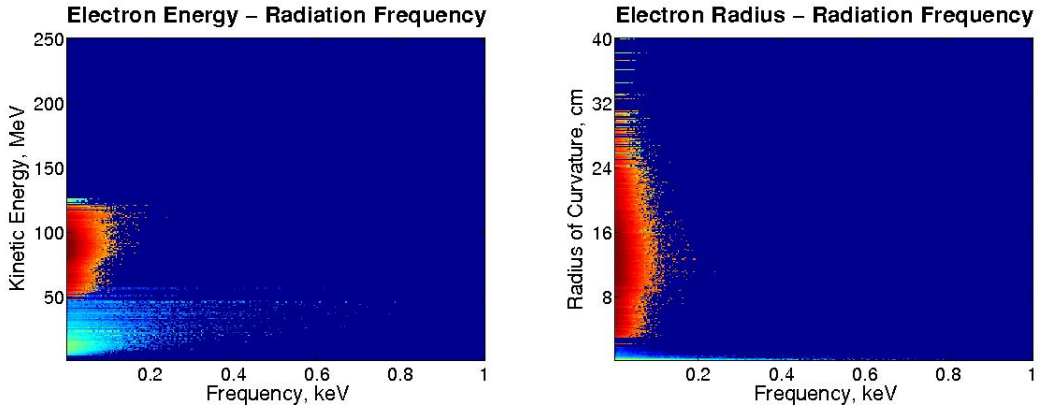


Figure 5.19: (Left) The correlation between the kinetic energy of the emitting electrons and the frequency of the emitted radiation and (Right)the correlation between the radius of curvature of the emitting electrons' trajectories and the frequency of the emitted radiation for the $a_0 = 3.0$ simulation. Note that the color scale for these plots is logarithmic.

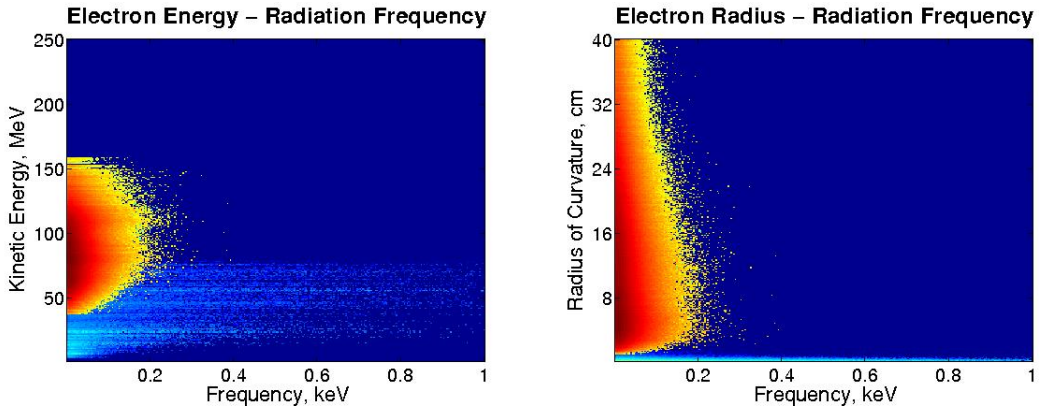


Figure 5.20: (Left) The correlation between the kinetic energy of the emitting electrons and the frequency of the emitted radiation and (Right)the correlation between the radius of curvature of the emitting electrons' trajectories and the frequency of the emitted radiation for the $a_0 = 4.0$ simulation. Note that the color scale for these plots is logarithmic.

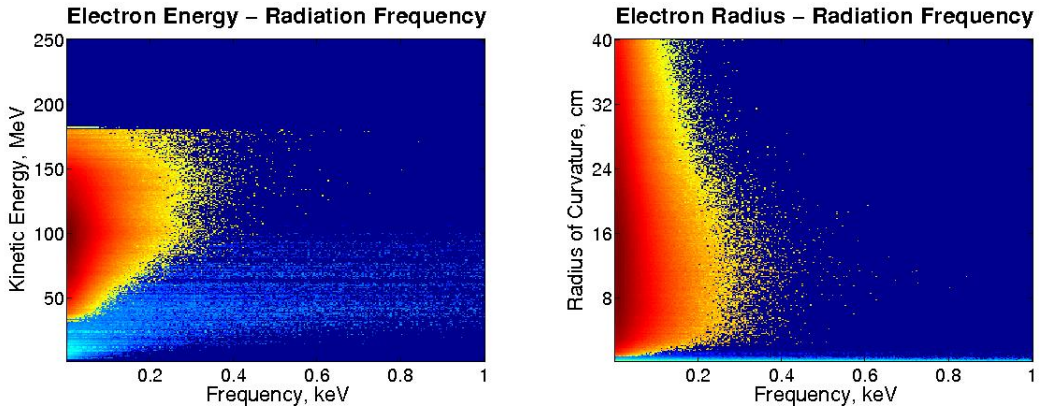


Figure 5.21: (Left) The correlation between the kinetic energy of the emitting electrons and the frequency of the emitted radiation and (Right)the correlation between the radius of curvature of the emitting electrons' trajectories and the frequency of the emitted radiation for the $a_0 = 5.0$ simulation. Note that the color scale for these plots is logarithmic.

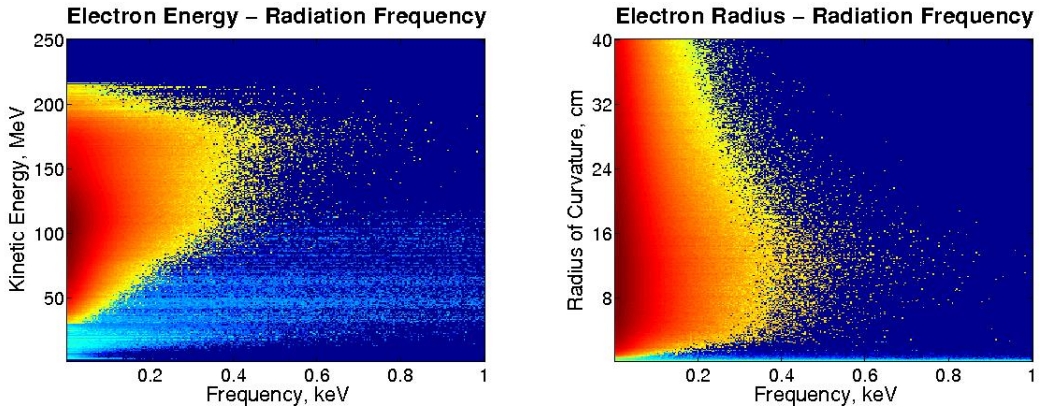


Figure 5.22: (Left) The correlation between the kinetic energy of the emitting electrons and the frequency of the emitted radiation and (Right)the correlation between the radius of curvature of the emitting electrons' trajectories and the frequency of the emitted radiation for the $a_0 = 6.0$ simulation. Note that the color scale for these plots is logarithmic.

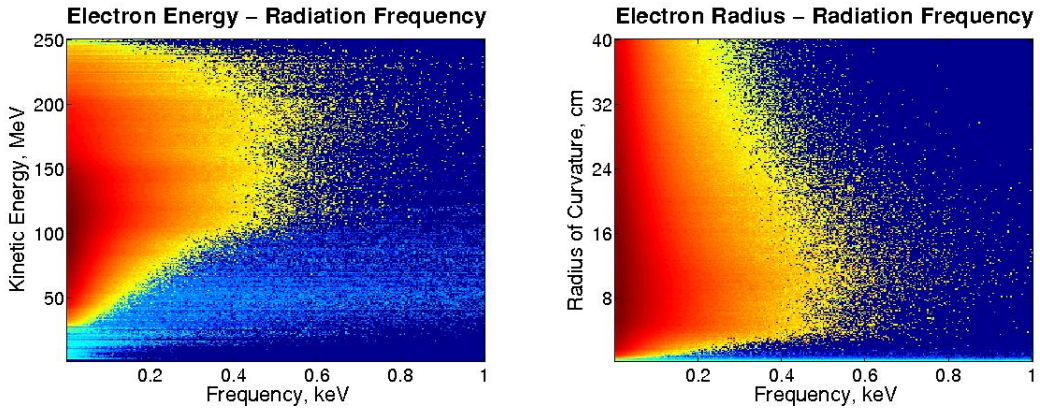


Figure 5.23: (Left) The correlation between the kinetic energy of the emitting electrons and the frequency of the emitted radiation and (Right)the correlation between the radius of curvature of the emitting electrons' trajectories and the frequency of the emitted radiation for the $a_0 = 7.0$ simulation. Note that the color scale for these plots is logarithmic.

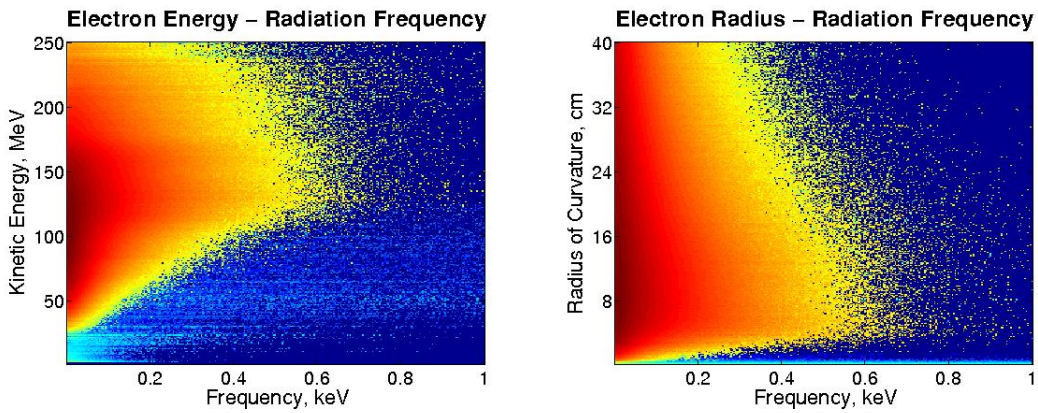


Figure 5.24: (Left) The correlation between the kinetic energy of the emitting electrons and the frequency of the emitted radiation and (Right)the correlation between the radius of curvature of the emitting electrons' trajectories and the frequency of the emitted radiation for the $a_0 = 8.0$ simulation. Note that the color scale for these plots is logarithmic.

| Parameter | Normalized Value | Real Value |
|---|---|---|
| Peak Plasma Density: | $0.01 - 0.06 n_{crit}$ | $1.75 - 10.5 \times 10^{19} cm^{-3}$ |
| Simulation Box Size: | $300 \times 200 \times 200$ | $39 \times 26 \times 26 \mu m$ |
| Box Propagation Speed: | c | $3.0 \times 10^{10} cm/s$ |
| Total Propagation Time: | 5900 | $2.5 ps$ |

Table 5.5: The plasma parameters for the electron density sweep

## 5.6 Electron Density Sweep

### 5.6.1 Simulation Parameters

The plasma parameters, plasma density profile, laser parameters, and computational parameters used for the electron density sweep are listed in tables 5.5, 5.6, 5.7, and 5.8, respectively. These were serial (i.e. single-processor) runs that took $\sim 16 - 17$ hours to finish. For each value of the parameter sweep, a single simulation was performed.

| Density | Initial Position | Final Position |
|---|---|---|
| 0.0 (Vacuum) | $0.0\mu m$ | $65\mu m$ |
| Linear Ramp from 0.0 to Peak Density | $65\mu m$ | $130\mu m$ |
| Peak Density (Bulk Plasma) | $130\mu m$ | $637\mu m$ |
| Linear Ramp from Peak Density to 0.0 | $637\mu m$ | $702\mu m$ |
| 0.0 (Vacuum) | $702\mu m$ | $767\mu m$ |

Table 5.6: The density profile for the electron density sweep

| Parameter | Normalized Value | Real Value |
|---|---|---|
| FWHM Spot Size: | 40 | 5.2 $\mu m$ |
| FWHD Pulse Length: | 64 | 28 $fs$ |
| Peak Normalized Vector Potential: | 4.0 | |
| Peak Laser Intensity: | $3.4 \times 10^{19} W/cm^2$ | |

Table 5.7: The laser parameters for the electron density sweep

| Parameter | Value |
|---|---|
| Simulation Grid Size: | $600 \times 100 \times 100$ cells |
| Particles Per Cell: | 2 |
| System Grid Spacing: | $0.066 \times 0.26 \times 0.26\mu m$ |
| System Time-Step: | $0.172fs$ |
| Printing Time-Step: | $50.1fs$ |

Table 5.8: The computational parameters for the electron density sweep. Note that the highest resolution was in the propagation direction.

### 5.6.2 Electron Phase-Space Results

The first and most obvious trend in the electron phase-space results is the reduction in the dephasing length and total interaction length; this is to be expected, as the dephasing length as calculated by Tajima and Dawson is given by:

$$L_d = \frac{2\omega^2 c}{\omega_p^3}$$

and since the plasma frequency $\omega_p$ scales with the square root of the plasma density $n_e$, the dephasing length scales with the density as $L_d \sim n_e^{-3/2}$. The time-evolution of the EEDF shows an initial increase in the peak electron energy (as the density moves to $n_e = 0.02 n_{crit}$, however the peak electron energy quickly falls off as the density increases.

The transverse momentum profiles of the electron beams show an interesting trend: for most of these simulations, the dephasing length is reached relatively early, and the largest-amplitude betatron motion occurs after the system passes twice the dephasing length. This indicates that the strongest drive of betatron motion for many of these simulations is not the interaction of the electron beam with the wake structure, but rather is the hosing instability caused by the electron beam re-entering the bulk plasma [89]. The hosing instability is a transverse instability in current filaments, where the magnetic field generated by the current causes transverse oscillations in the filament structure to be amplified in time. This hypothesis is further supported by the fact that the radiated power is transient in nature; if the betatron motion is driven by this affect, the motion will vanish as the beam ultimately breaks apart during the final stages of the hosing instability.

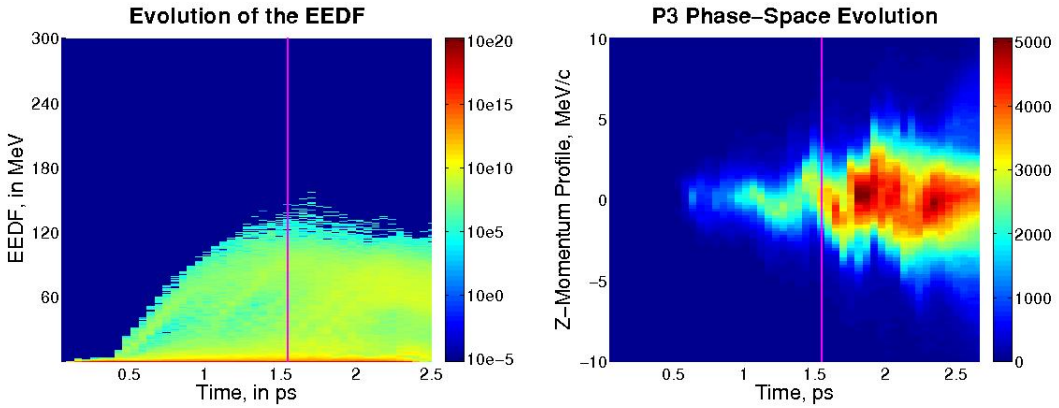


Figure 5.25: (Left) The time-evolution of the EEDF and (right) the time-evolution of the electron beam p3 momentum phase-space profile for the $n_0 = 0.01 n_{crit}$ simulation. The magenta line indicates the location of the dephasing length. The color scales on the left are logarithmic, and in units of normalized charge per MeV per ps. The color scales on the right are linear, and are in units of normalized charge per $m_e c$ per ps.

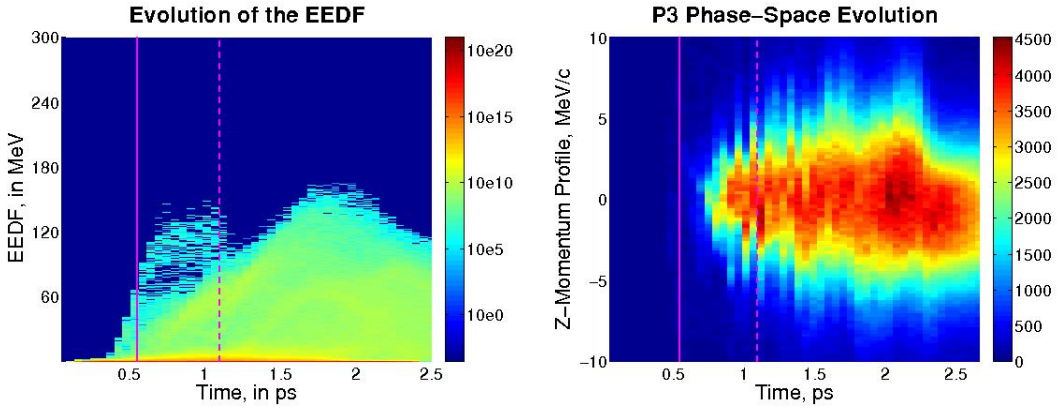


Figure 5.26: (Left) The time-evolution of the EEDF and (right) the time-evolution of the electron beam p3 momentum phase-space profile for the $n_0 = 0.02 n_{crit}$ simulation. The magenta line indicates the location of the dephasing length. The color scales on the left are logarithmic, and in units of normalized charge per MeV per ps. The color scales on the right are linear, and are in units of normalized charge per $m_e c$ per ps.

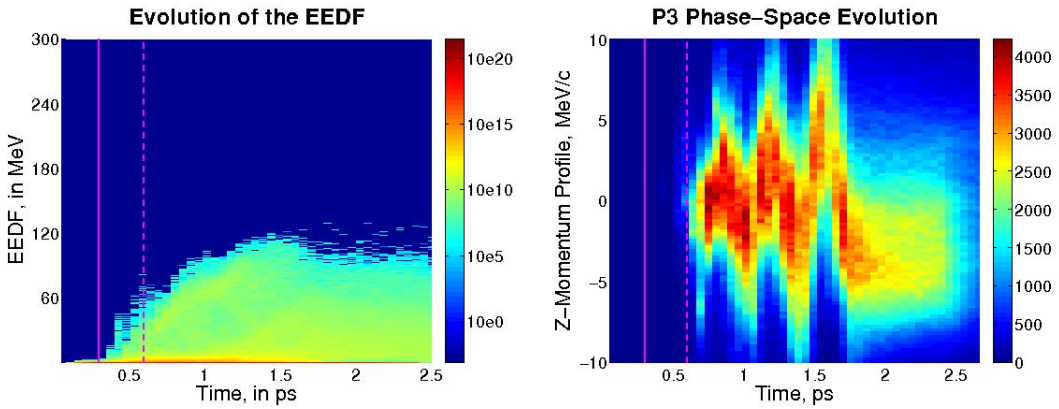


Figure 5.27: (Left) The time-evolution of the EEDF and (right) the time-evolution of the electron beam p3 momentum phase-space profile for the $n_0 = 0.03 n_{crit}$ simulation. The magenta line indicates the location of the dephasing length, and the dashed magenta line indicates the location of twice the dephasing length. The color scales on the left are logarithmic, and in units of normalized charge per MeV per ps. The color scales on the right are linear, and are in units of normalized charge per $m_e c$ per ps.

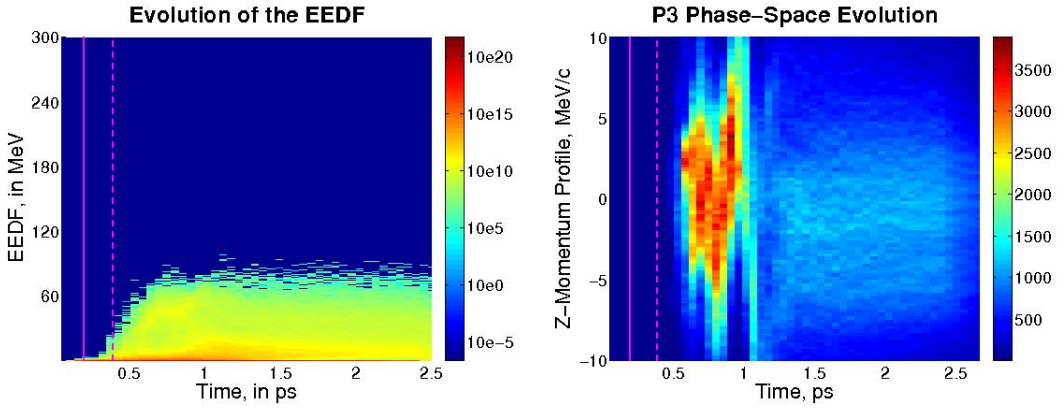


Figure 5.28: (Left) The time-evolution of the EEDF and (right) the time-evolution of the electron beam p3 momentum phase-space profile for the $n_0 = 0.04 n_{crit}$ simulation. The magenta line indicates the location of the dephasing length, and the dashed magenta line indicates the location of twice the dephasing length. The color scales on the left are logarithmic, and in units of normalized charge per MeV per ps. The color scales on the right are linear, and are in units of normalized charge per $m_e c$ per ps.

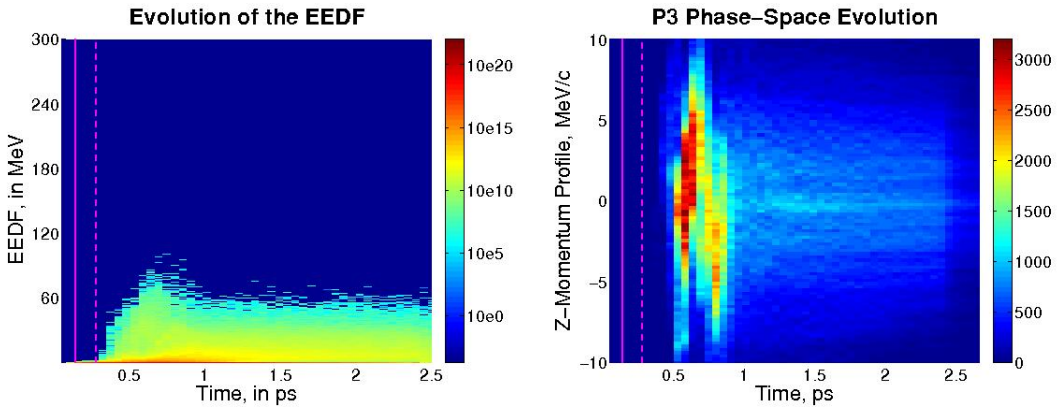


Figure 5.29: (Left) The time-evolution of the EEDF and (right) the time-evolution of the electron beam p3 momentum phase-space profile for the $n_0 = 0.05 n_{crit}$ simulation. The magenta line indicates the location of the dephasing length, and the dashed magenta line indicates the location of twice the dephasing length. The color scales on the left are logarithmic, and in units of normalized charge per MeV per ps. The color scales on the right are linear, and are in units of normalized charge per $m_e c$ per ps.

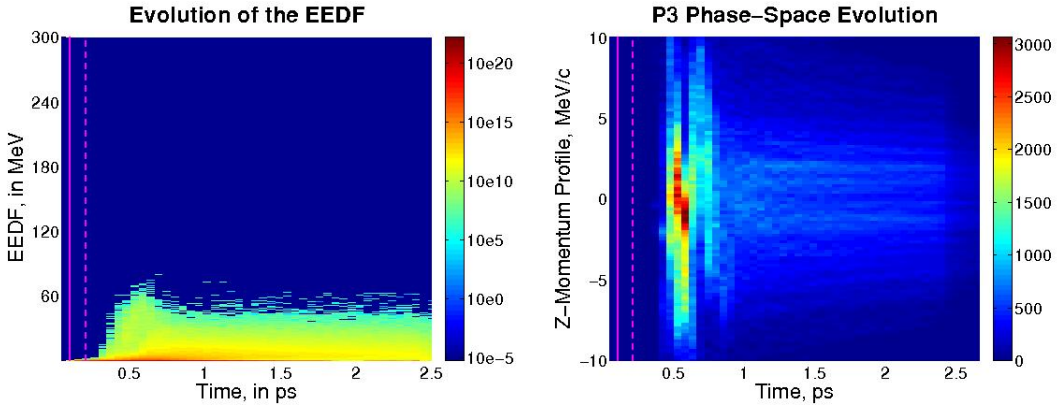


Figure 5.30: (Left) The time-evolution of the EEDF and (right) the time-evolution of the electron beam p3 momentum phase-space profile for the $n_0 = 0.06 n_{crit}$ simulation. The magenta line indicates the location of the dephasing length, and the dashed magenta line indicates the location of twice the dephasing length. The color scales on the left are logarithmic, and in units of normalized charge per MeV per ps. The color scales on the right are linear, and are in units of normalized charge per $m_e c$ per ps.

### 5.6.3 Radiation Emission Results

The radiation emission trends track very closely with the electron phase-space trends. The time-evolution plots of the radiation spectra show that the peak radiation frequencies are emitted while the electron beam is undergoing betatron radiation; the plots of the radiated power and energy show that the peak radiated power also occurs at this time. Furthermore, results from the higher-density simulations show that both the peak radiated power and peak radiated frequency occur after the system has passed twice the dephasing length, providing further indication that the primary driving effect for these simulations is the hosing instability of the electron beam as it re-enters the bulk plasma. Additionally, the plots of the radiated power as a function of time consistently show significant fluctuations in power as the power increases, just as with the normalized vector potential sweep. It is again unclear whether these fluctuations are due to noise, or some underlying secondary effect.

The scaling of the total radiated energy as a function of density, shown in Figure 5.37 further elucidates these data. Recall from Equation 5.1 that the total emitted energy is expected to scale as $E_{rad} \sim n_e^{-1/4}$; it is clear from Figure 5.37 that these simulations do not follow this trend. This is to be expected, however, as the derivation of Equation 5.1 did not consider the large instability-driven betatron motion that can be observed in Figures 5.27 through 5.30, which occurs as the electron beam re-enters the bulk plasma after propagating past a distance equal to twice the dephasing length and undergoes a hosing instability.

The spectra for these simulations are shown in Figure 5.38, and the trend for the high-energy tail temperature with plasma density is shown in Figure 5.39. As with the normalized vector potential sweep, two distinct regions are observed in the integrated spectra; again, the higher-energy region is presumed to be a numerical artifact.

Recall from Equation 5.2 that the critical frequency is expected to scale as $\omega_c \sim$

$n_e^{9/8}$; as with the total emitted energy is clear that these simulations do not follow this trend. This is also to be expected, and for the same reason; the dominant driving mechanism for the betatron motion in these simulations appears to be the hosing instability caused by the electron beam propagating past twice the dephasing length, which is an effect that was not taken into account in the derivation of Equation 5.2.

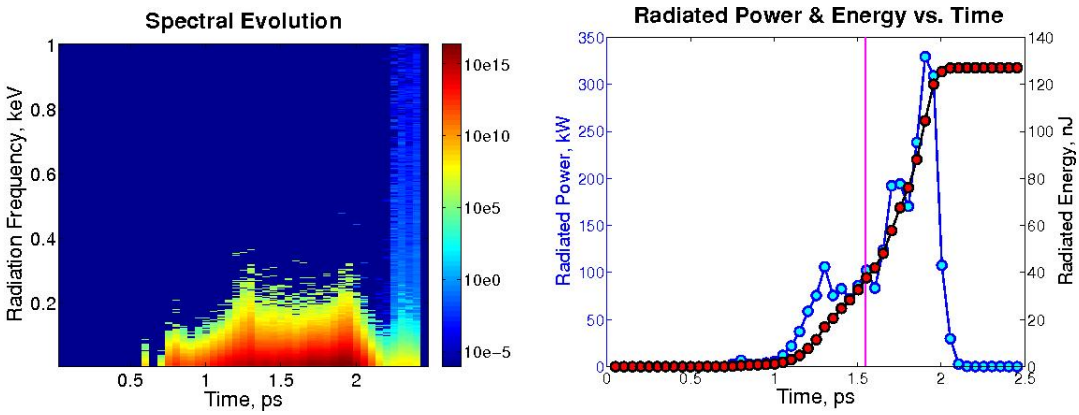


Figure 5.31: (Left) The time-evolution of the radiated spectrum and (right) the emitted power (blue) and total emitted radiation (red) vs. time for the $n_e = 0.01 n_{crit}$. simulation. The magenta line indicates the location of the dephasing length. Note that the color scale for the left-hand plot is logarithmic, and the units are Joules/(keV*second)

### 5.6.4 Radiation and Phase-Space Correlations

The electron energy/radiation frequency plots (shown on the left-hand-side of Figures 5.40 through 5.45) consistently show that the overwhelming majority of radiated energy is emitted by the high-energy electron beam. A small amount of energy is emitted by lower-energy electrons; this amount proportionally increases as the density increases and the total radiated energy decreases.

The radius-of-curvature/radiation frequency plots (shown on the right-hand-side of Figures 5.40 through 5.45) show that the highest-frequency energy is emitted by electrons with very low radii-of-curvature; this trend becomes stronger as the density

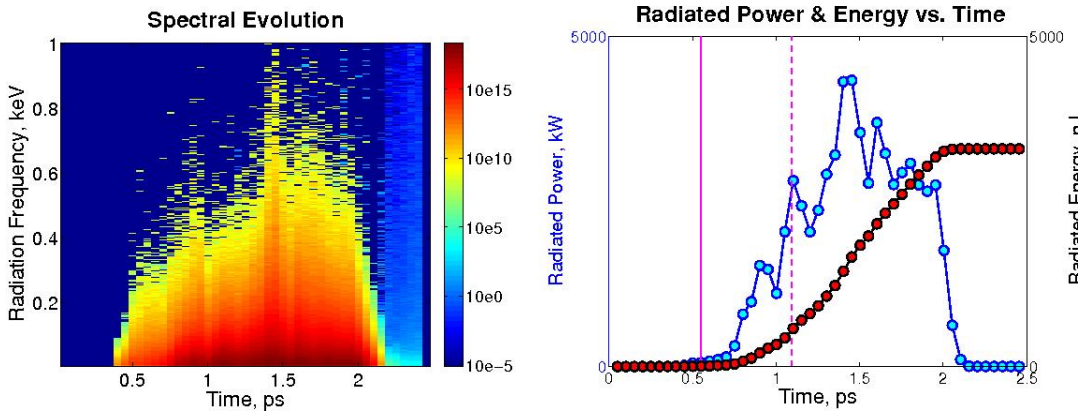


Figure 5.32: (Left) The time-evolution of the radiated spectrum and (right) the emitted power (blue) and total emitted radiation (red) vs. time for the $n_e = 0.02 n_{crit}$. simulation. The magenta line indicates the location of the dephasing length. Note that the color scale for the left-hand plot is logarithmic, and the units are Joules/(keV*second)

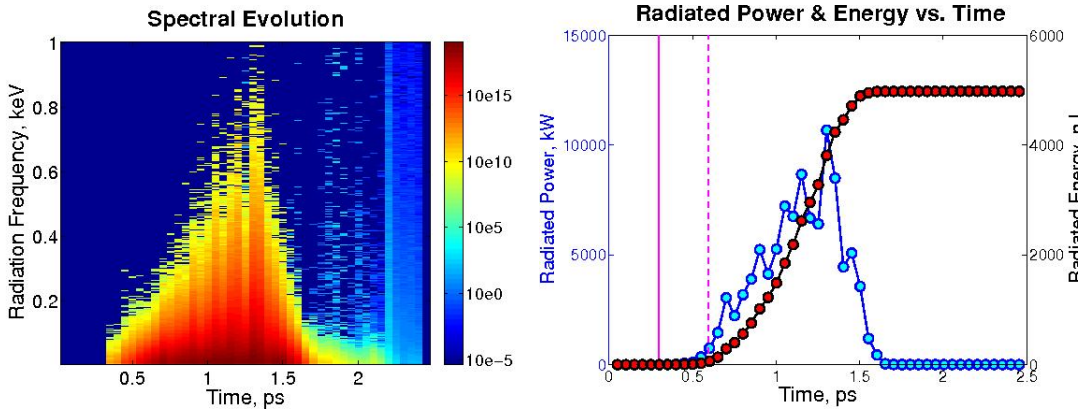


Figure 5.33: (Left) The time-evolution of the radiated spectrum and (right) the emitted power (blue) and total emitted radiation (red) vs. time for the $n_e = 0.03 n_{crit}$. simulation. The magenta line indicates the location of the dephasing length. Note that the color scale for the left-hand plot is logarithmic, and the units are Joules/(keV*second)

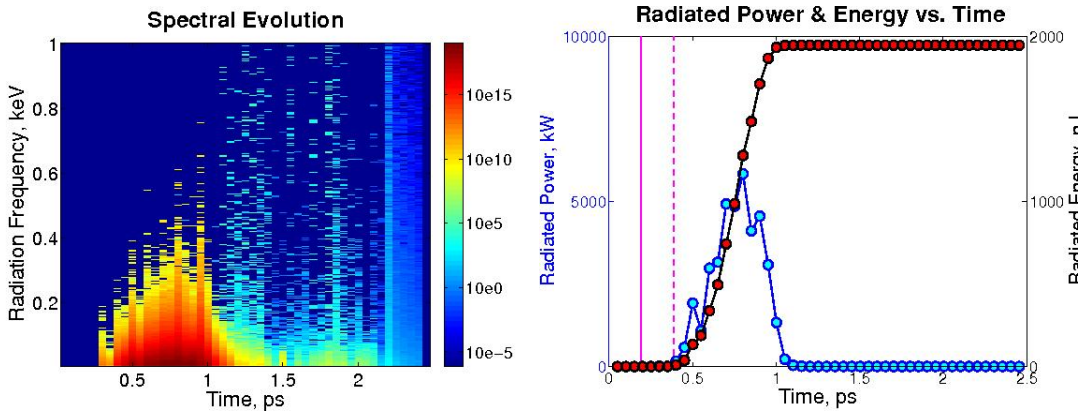


Figure 5.34: (Left) The time-evolution of the radiated spectrum and (right) the emitted power (blue) and total emitted radiation (red) vs. time for the $n_e = 0.04 n_{crit}$. simulation. The magenta line indicates the location of the dephasing length. Note that the color scale for the left-hand plot is logarithmic, and the units are Joules/(keV*second)

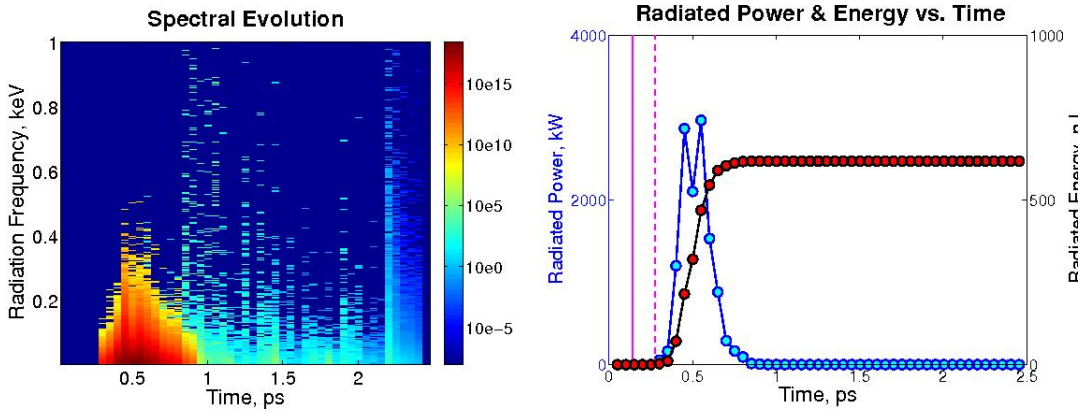


Figure 5.35: (Left) The time-evolution of the radiated spectrum and (right) the emitted power (blue) and total emitted radiation (red) vs. time for the $n_e = 0.05 n_{crit}$. simulation. The magenta line indicates the location of the dephasing length. Note that the color scale for the left-hand plot is logarithmic, and the units are Joules/(keV*second)

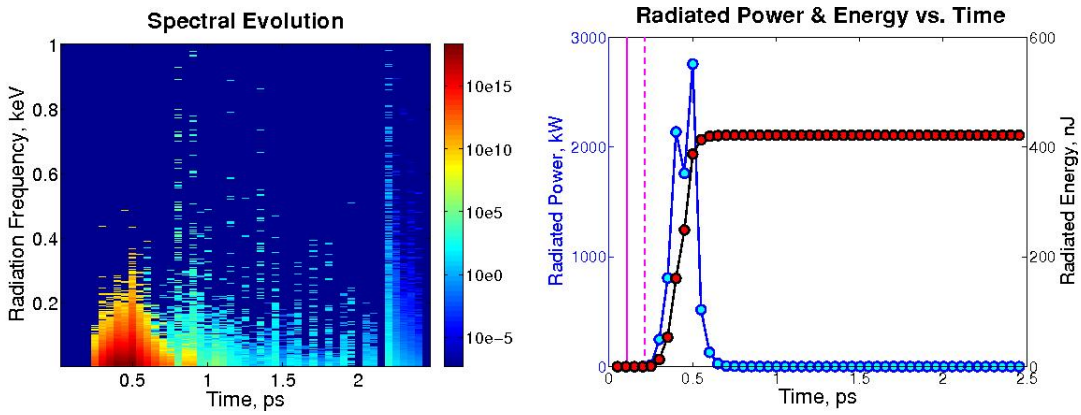


Figure 5.36: (Left) The time-evolution of the radiated spectrum and (right) the emitted power (blue) and total emitted radiation (red) vs. time for the $n_e = 0.06 n_{crit}$. simulation. The magenta line indicates the location of the dephasing length. Note that the color scale for the left-hand plot is logarithmic, and the units are Joules/(keV*second)

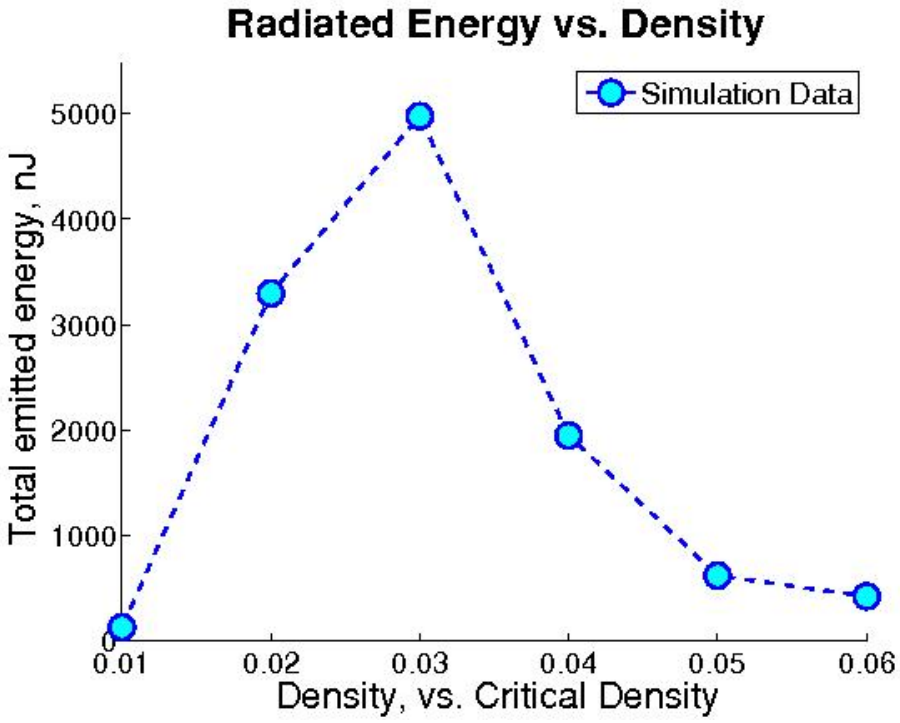


Figure 5.37: The total energy emitted produced by the simulations, as a function of density.

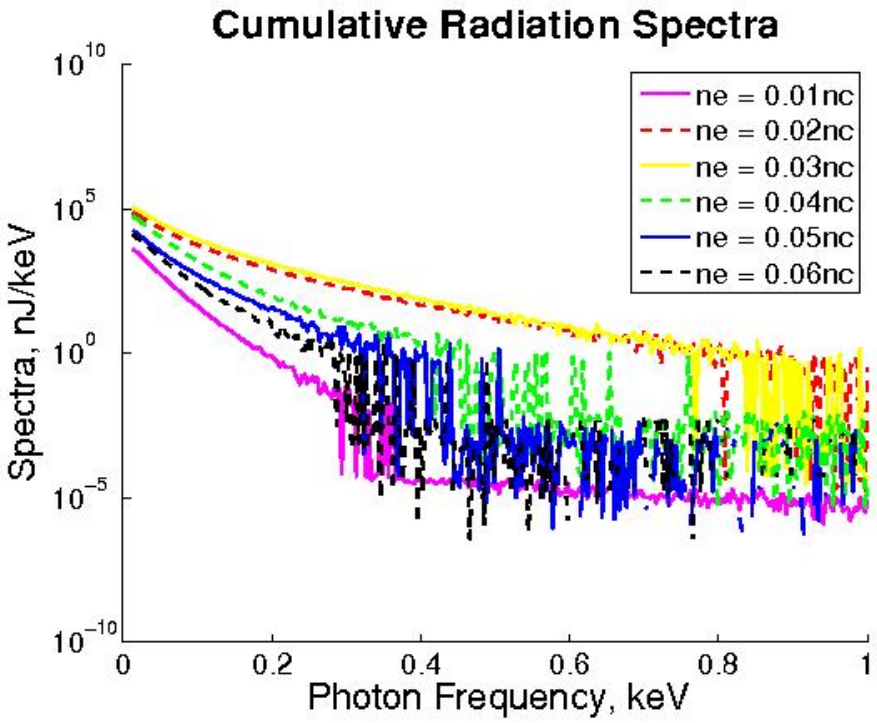


Figure 5.38: The logarithmic spectra for the density sweep

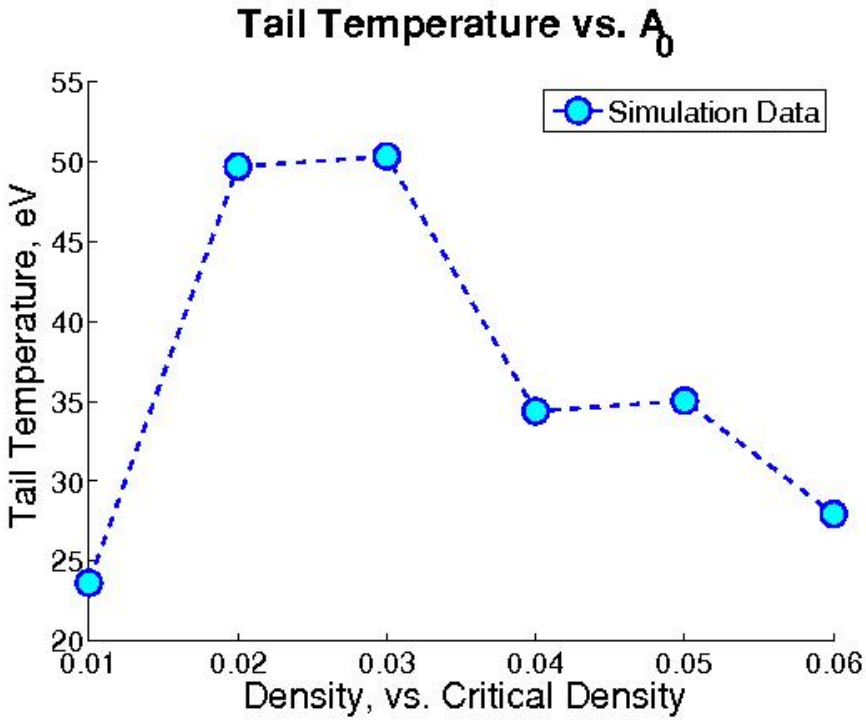


Figure 5.39: The temperature of the high-frequency tail of the spectrum, as a function of density

increases. Recall that the transverse momentum profile evolutions of the electron beams showed that the betatron wavelength decreases as the density increases; this is consistent with a decrease in the radius of curvature of the electron beam as it emits radiation.

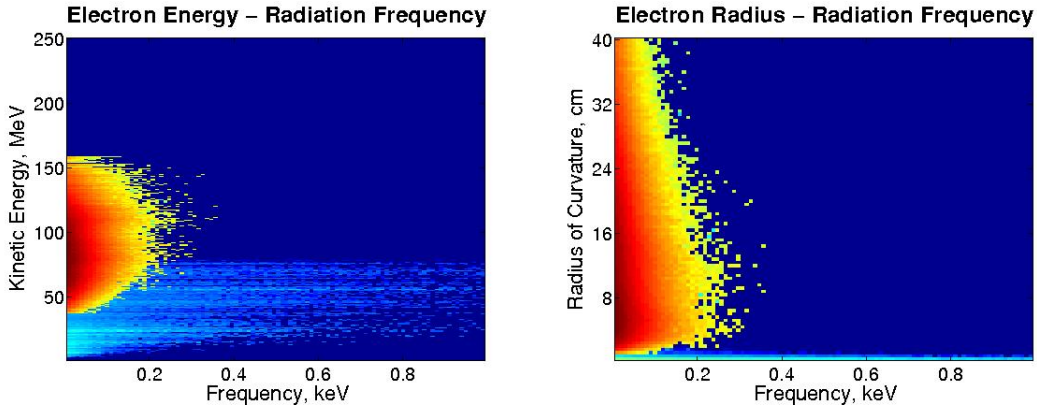


Figure 5.40: (Left) The correlation between the kinetic energy of the emitting electrons and the frequency of the emitted radiation and (Right)the correlation between the radius of curvature of the emitting electrons' trajectories and the frequency of the emitted radiation for the $n_e = 0.01 n_{crit}$ simulation. Note that the color scale for these plots is logarithmic.

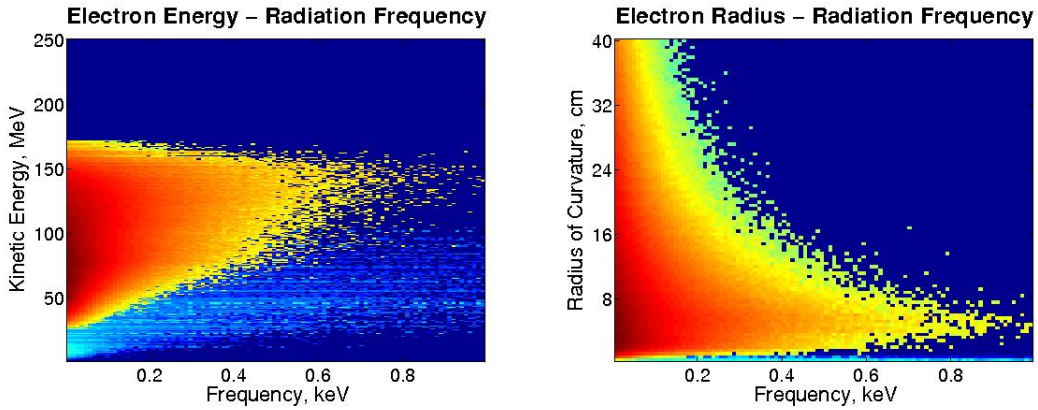


Figure 5.41: (Left) The correlation between the kinetic energy of the emitting electrons and the frequency of the emitted radiation and (Right)the correlation between the radius of curvature of the emitting electrons' trajectories and the frequency of the emitted radiation for the $n_e = 0.02 n_{crit}$ simulation. Note that the color scale for these plots is logarithmic.

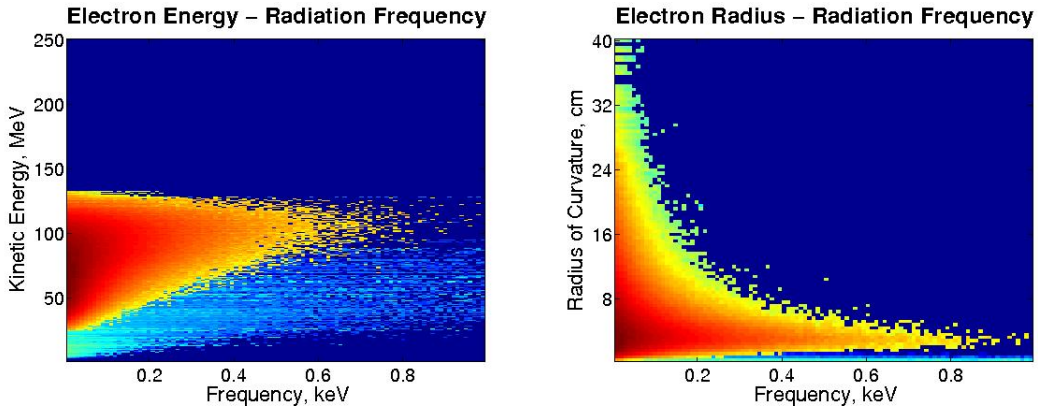


Figure 5.42: (Left) The correlation between the kinetic energy of the emitting electrons and the frequency of the emitted radiation and (Right)the correlation between the radius of curvature of the emitting electrons' trajectories and the frequency of the emitted radiation for the $n_e = 0.03 n_{crit}$ simulation. Note that the color scale for these plots is logarithmic.

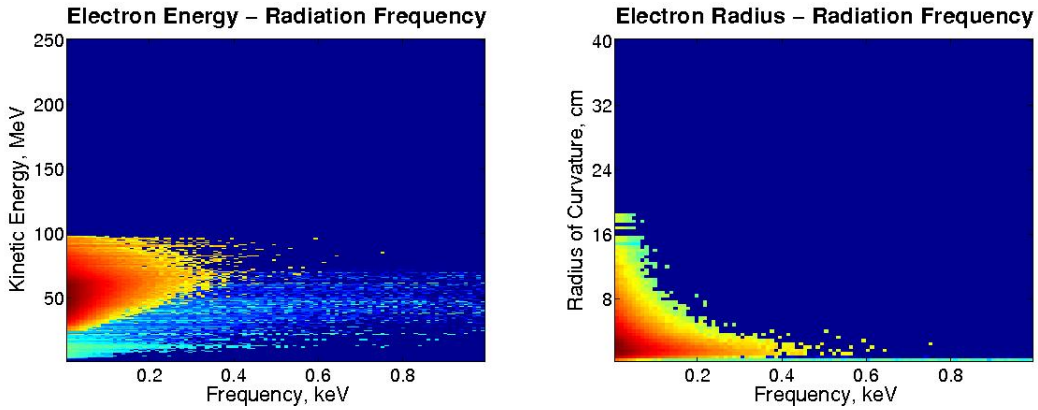


Figure 5.43: (Left) The correlation between the kinetic energy of the emitting electrons and the frequency of the emitted radiation and (Right)the correlation between the radius of curvature of the emitting electrons' trajectories and the frequency of the emitted radiation for the $n_e = 0.04 n_{crit}$ simulation. Note that the color scale for these plots is logarithmic.

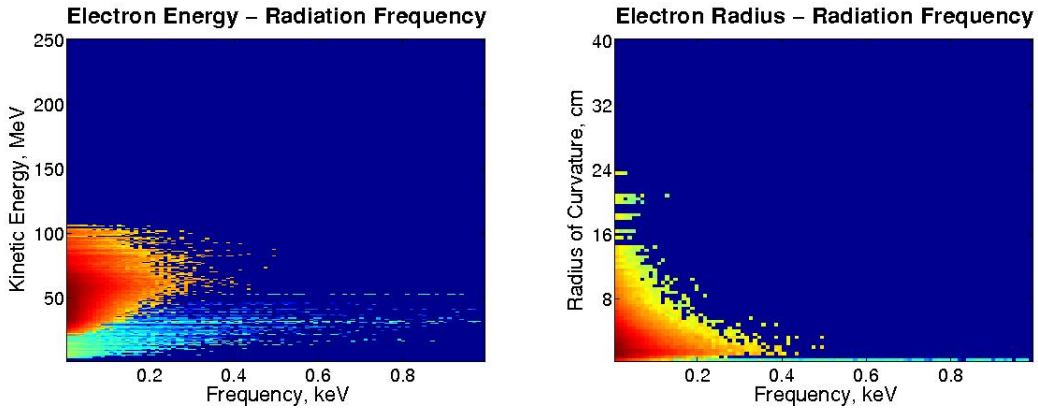


Figure 5.44: (Left) The correlation between the kinetic energy of the emitting electrons and the frequency of the emitted radiation and (Right)the correlation between the radius of curvature of the emitting electrons' trajectories and the frequency of the emitted radiation for the $n_e = 0.05 n_{crit}$ simulation. Note that the color scale for these plots is logarithmic.

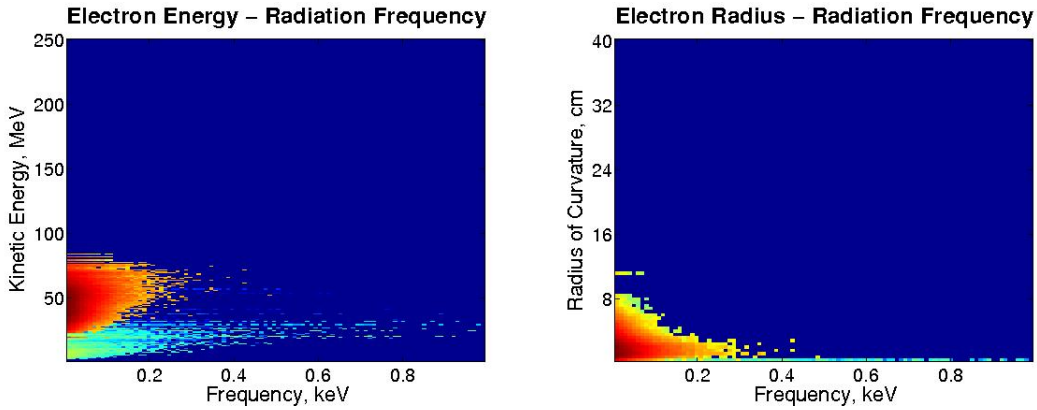


Figure 5.45: (Left) The correlation between the kinetic energy of the emitting electrons and the frequency of the emitted radiation and (Right)the correlation between the radius of curvature of the emitting electrons' trajectories and the frequency of the emitted radiation for the $n_e = 0.06 n_{crit}$ simulation. Note that the color scale for these plots is logarithmic.

| Parameter | Normalized Value | Real Value |
|---|---|---|
| Peak Plasma Density: | $0.01 n_{crit}$ | $1.75 \times 10^{19} cm^{-3}$ |
| Simulation Box Size: | $300 \times 200 \times 200$ | $39 \times 26 \times 26 \mu m$ |
| Box Propagation Speed: | c | $3.0 \times 10^{10} cm/s$ |
| Total Propagation Time: | 5900 | $2.5 ps$ |

Table 5.9: The plasma parameters for the electron density sweep

## 5.7 Propagation Length Sweep

### 5.7.1 Simulation Parameters

The plasma parameters, plasma density profile, laser parameters, and computational parameters used for the propagation length sweep are listed in tables 5.9, 5.10, 5.11, and 5.12, respectively. Note that, for this parameter sweep, a single simulation was simply allowed to propagate until it passed twice the dephasing length. This was a serial (i.e. single-processor) run which ran for 34 hours and 38 minutes.

| Density | Initial Position | Final Position |
|---|---|---|
| 0.0 (Vacuum) | $0.0\mu m$ | $65\mu m$ |
| Linear Ramp from 0.0 to $0.01n_{crit}$ | $65\mu m$ | $130\mu m$ |
| $0.01n_{crit}$ (Bulk Plasma) | $130\mu m$ | $1742\mu m$ |
| Linear Ramp from $0.01n_{crit}$ to 0.0 | $1742\mu m$ | $1807\mu m$ |
| 0.0 (Vacuum) | $1807\mu m$ | $1872\mu m$ |

Table 5.10: The density profile for the propagation length sweep

| Parameter | Normalized Value | Real Value |
|---|---|---|
| FWHM Spot Size: | 40 | 5.2 $\mu m$ |
| FWHD Pulse Length: | 64 | 28 $fs$ |
| Peak Normalized Vector Potential: | 4.0 | |
| Peak Laser Intensity: | $3.4 \times 10^{19} W/cm^2$ | |

Table 5.11: The laser parameters for the propagation length sweep

| Parameter | Value |
|---|---|
| Simulation Grid Size: | $600 \times 100 \times 100$ cells |
| Particles Per Cell: | 2 |
| System Grid Spacing: | $0.066 \times 0.26 \times 0.26\mu m$ |
| System Time-Step: | $0.172fs$ |
| Printing Time-Step: | $52.7fs$ |

Table 5.12: The computational parameters for the propagation length sweep. Note that the highest resolution was in the propagation direction.

### 5.7.2 Electron Phase-Space Results

The first and most obvious trend in the electron phase-space results can be observed in the plot of the time-evolution of the EEDF, shown in Figure 5.46. As the system approaches and passes the dephasing length, the maximum electron energy increases, peaks, and decreases. Then, the as the system approaches twice the dephasing length, the electron beam re-enters the bulk plasma and a second period of acceleration is observed as the system enters a beam-driven wake-field regime.

The evolution of the transverse momentum profile, shown in Figure 5.47, supports the picture suggested by the time-evolution of the EEDF. The amplitude of the betatron oscillation increases dramatically at the same time as the second period of acceleration observed in the EEDF evolution plot; this suggests that the electron beam is undergoing a hosing instability as it re-enters the bulk plasma. Furthermore, the beam begins to vanish as soon as this increased amplitude is observed, suggesting that the beam is breaking up due to the instability.

### 5.7.3 Radiation Emission Results

The time-evolution of the radiation spectra, shown in Figure 5.48, shows that the maximum frequency of emitted radiation increases along with the betatron amplitude, as is expected. Additionally, the maximum frequency decays along with the magnitude of the beam as shown in Figure 5.47, further suggesting that the beam is breaking up due to a hosing instability.

The plot of the radiated power and energy as functions of time, Figure 5.49, clearly show that the vast majority of the energy radiated by the system is radiated after it passes the dephasing length and enters the unstable, beam-driven wake-field regime. Combined with the density sweep of the previous section, these results provide a strong indication that allowing the simulation to propagate well past the dephasing length is the most effective way to increase the total amount of emitted radiation in

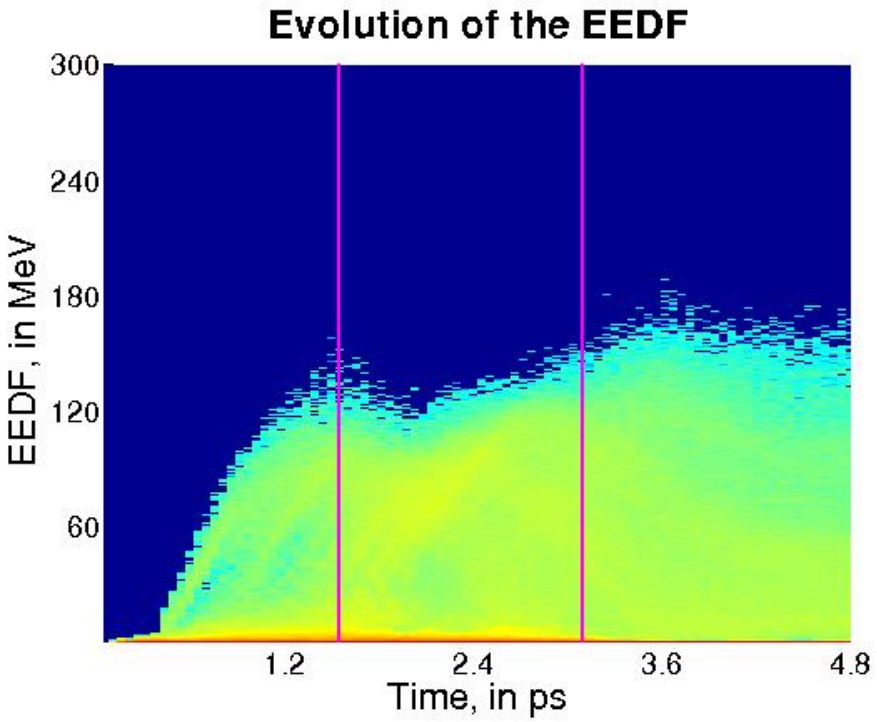


Figure 5.46: The time-evolution of the EEDF; the points where the system passes the dephasing length and twice the dephase length are marked in magenta. Note that the color scale for this plots is logarithmic.

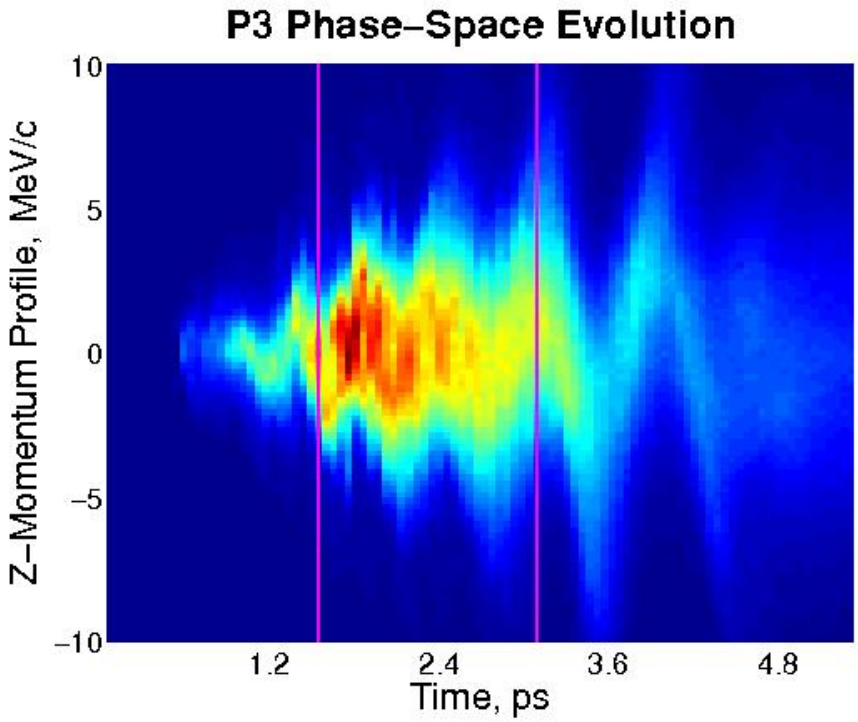


Figure 5.47: The time-evolution of the electron beam p3 momentum phase-space profile; the points where the system passes the dephasing length and twice the dephase length are marked in magenta.

a LWFA system. As before, there appears to be significant jumps in the radiated power that may either be due to noise or some underlying periodic phenomenon.

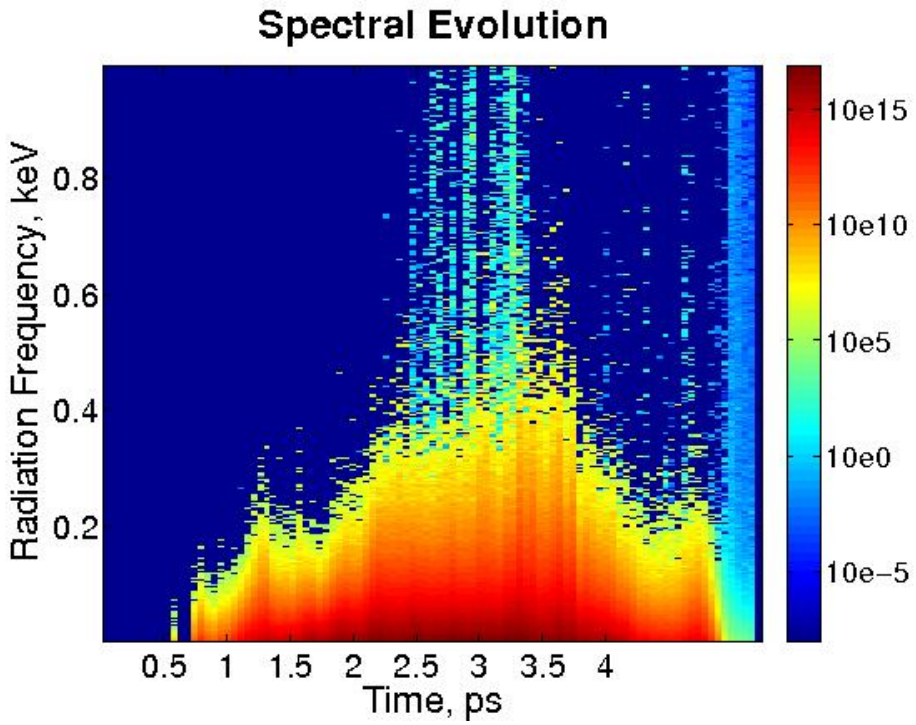


Figure 5.48: The time-evolution of the radiated spectrum; note that the color scale for this plot is logarithmic, and the units are Joules/(keV*second)

### 5.7.4 Radiation and Phase-Space Correlations

As with the previous simulations, the correlations between the radiation frequency and electron trajectory characteristics indicate that the vast majority of the electron energy is radiated by the high-energy electron beam; and that while radiation is emitted by electrons with a wide range of radii of curvatures, the highest-frequency radiation is emitted by electrons with the lowest radii of curvature.

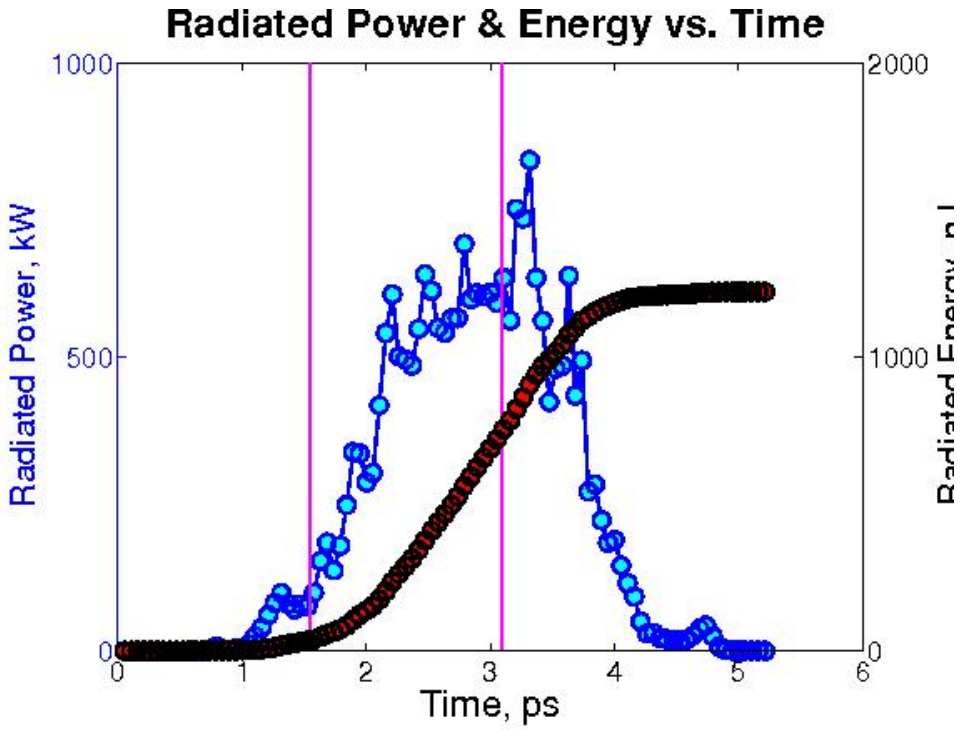


Figure 5.49: The emitted power (blue) and total emitted radiation (red) vs. time; the points where the system passes the dephasing length and twice the dephase length are marked in magenta.

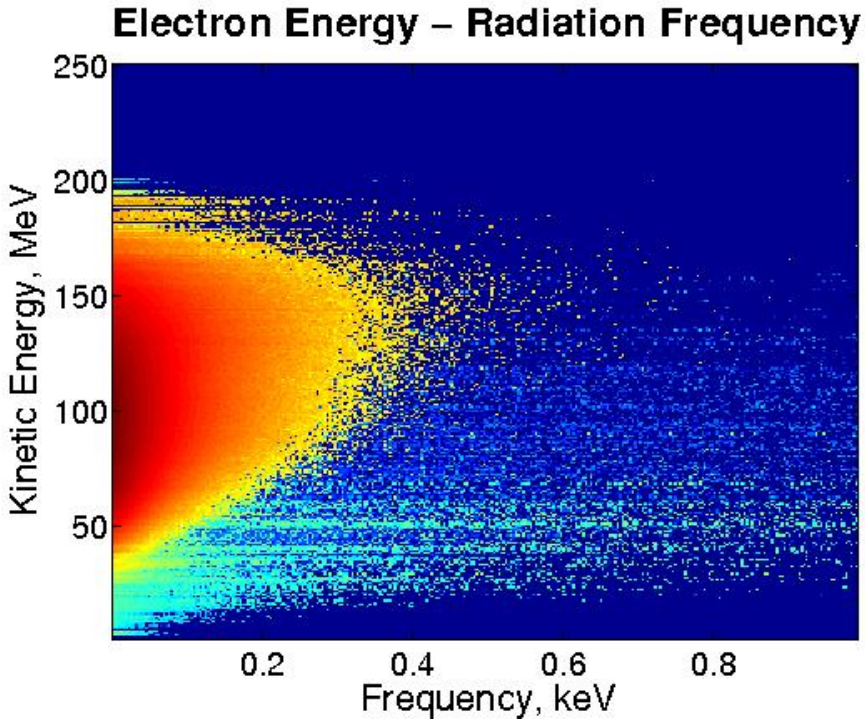


Figure 5.50: The correlation between the kinetic energy of the emitting electrons and the frequency of the emitted radiation. Note that the color scale for this plots is logarithmic.

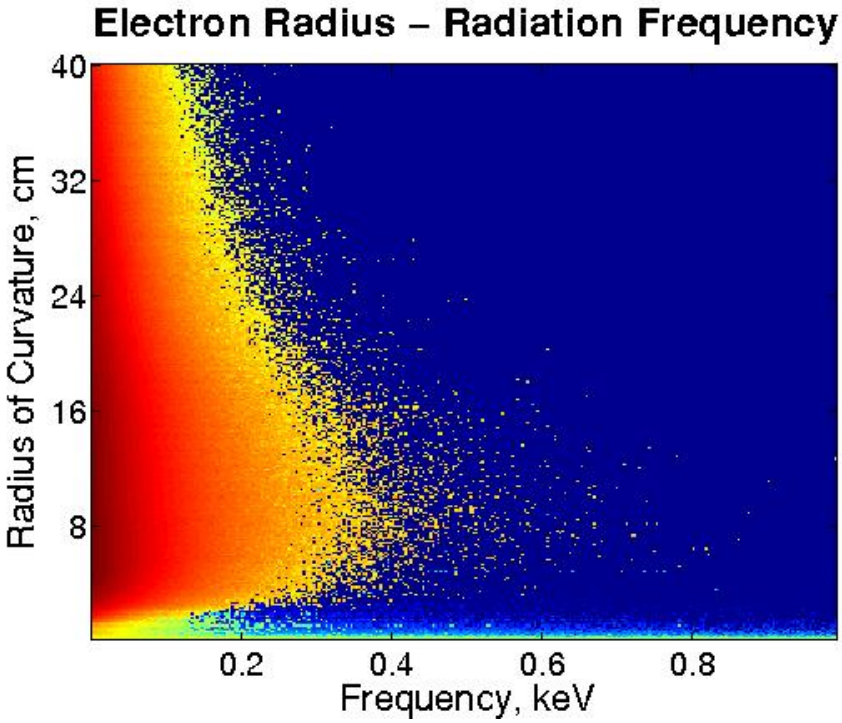


Figure 5.51: The correlation between the radius of curvature of the emitting electrons' trajectories and the frequency of the emitted radiation. Note that the color scale for this plots is logarithmic.

# CHAPTER VI

# The Impact of the Coma on the Electron Beam and Betatron Radiation Properties in LWFA Experiments

## 6.1 Overview

This chapter presents both results which provided the impetus for this entire dissertation, as well as results representing its culmination. First, results are presented from a computational investigation of the impact of the presence of a comatic aberration in the driving laser pulse on the electron beam properties produced by a laser wake-field accelerator. These results are taken from a published work that is reproduced as-published in Appendix B, which was, chronologically, the first piece of research done for this dissertation. Second, results are presented from a computational investigation using the radiation simulation algorithm presented in Chapter 4 to simulate the impact of the presence of a coma on the betatron radiation generated by a LWFA system.

## 6.2 Introduction: The Impact of the Coma on the Electron Beam Properties in a LWFA

The impetus for this entire dissertation was, initially, a study of the impact of aberrant (i.e. non-Gaussian) laser pulses on the performance of LWFA devices. Figure 6.1-A shows an idealized Gaussian laser pulse; this is the transverse pulse profile typically used for simulations and analytic calculations of LWFA physics [[78]]. However, the transverse pulse profile typically produced by a real laser more closely resembles Figure 6.1-B; a decidedly non-ideal, non-Gaussian, "aberrant" pulse profile; these deviations can modify the laser pulse propagation [[90], [91], [92]].

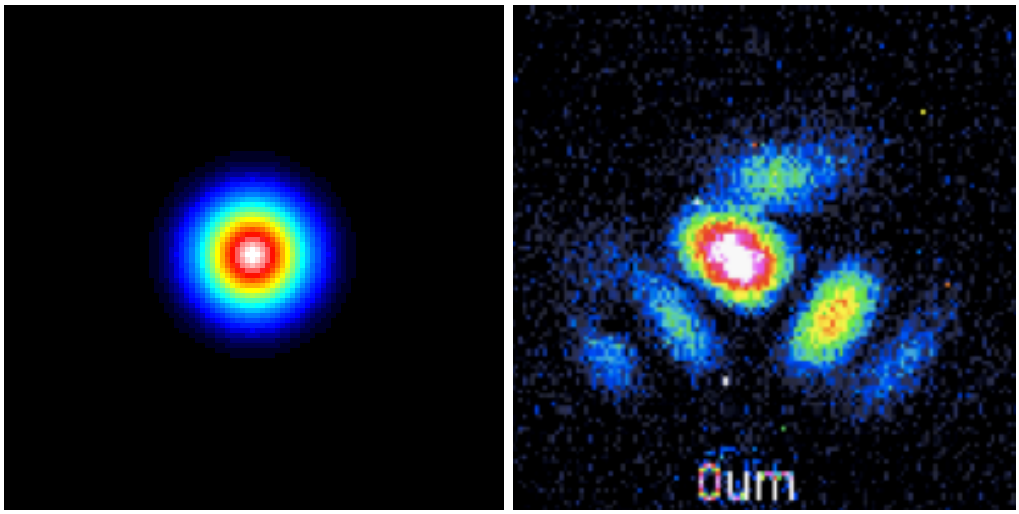


Figure 6.1: A (Left): An idealized Gaussian pulse (calculated analytically). B (Right): An example of a typical pulse produced by a real laser (measured at the focal point of the HERCULES laser, using an $f/10$ focusing optic.

The cost of LWFA as a particle acceleration technology will be dependent on the required precision of the laser system. Since the required precision of the laser system will ultimately depend on how the system's performance as an accelerator is affected by errors in the pulse profile, an understanding of this dependance is an important step towards developing cost-effective LWFA technology. Consequently,

the initial study used the PIC code OSIRIS 2.0 to perform a computational study of the relationships between the presence of optical aberrations in the laser pulse, and the parameters of the electron beam produced by the system.

The study considered the comatic aberration, one of the primary aberrations that can occur in an optical system. This aberration (shown in Figures 6.2 and 6.3), one of the five primary "Seidel aberrations" which occurs in geometric optics [[93]], was chosen for investigation due to experimental evidence linking the presence and strength of the coma to the spectra of synchrotron-like radiation generated by the electron beam in LWFA experiments[[94]].

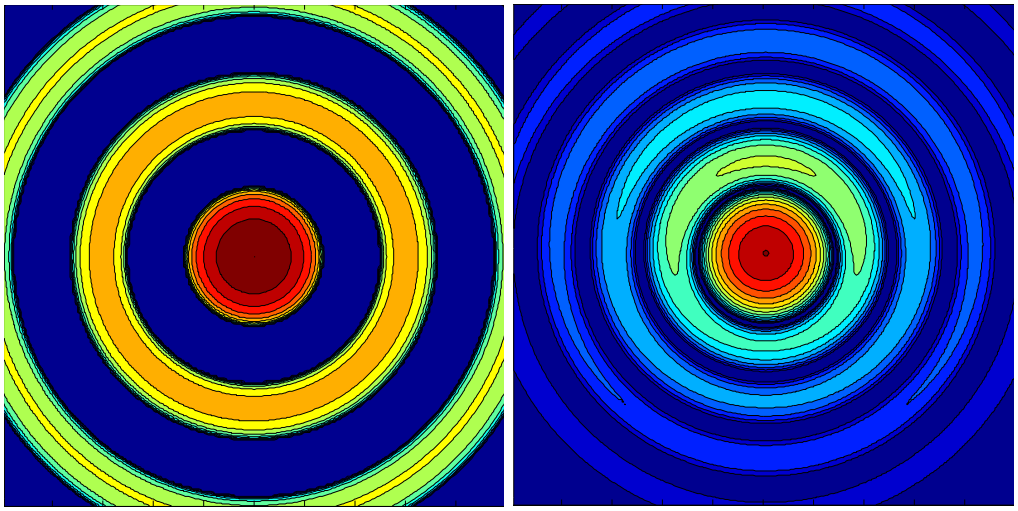

Figure 6.2: Logarithmic intensity profiles of an Airy laser spot without an aberration (left), and aberrated with a coma of severity $\alpha = 0.25$.

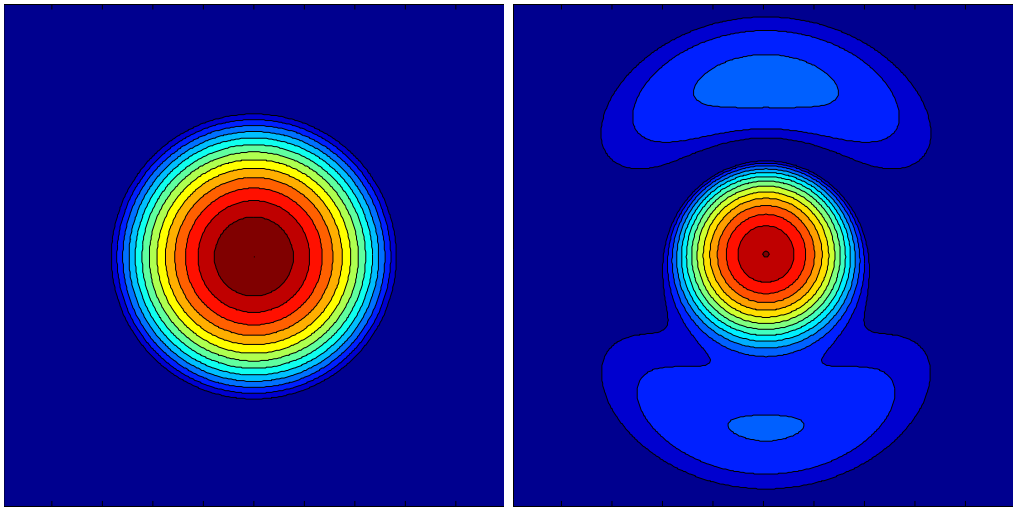

Figure 6.3: Logarithmic intensity profiles of a gaussian laser spot without an aberration (left), and aberrated with a coma of severity $\alpha = 0.25$.

## 6.3 Background & Theory: The Impact of the Coma on the Electron Beam Properties in a LWFA

In the diffraction theory of optics, the electric and magnetic fields at a given frequency $\omega$, $\vec{E}_\omega$ and $\vec{H}_\omega$, are both related to the scalar diffraction integral $U_\omega$ by[[93]]:

$$\vec{E}_\omega(x,y,z,t) = Re\left\{\frac{\omega^2}{c^2}U_\omega(x,y,z)\,a(\omega)\,\vec{\alpha}(\omega)\,e^{i[\delta(\omega)-\omega t]}\right\} \tag{6.1}$$

$$\vec{B}_\omega(x,y,z,t) = Re\left\{\frac{\omega^2}{c^2}U_\omega(x,y,z)\,a(\omega)\,\vec{\beta}(\omega)\,e^{i[\delta(\omega)-\omega t]}\right\} \tag{6.2}$$

Since the intensity is proportional to the Poynting vector (in cgs units)[[93]]:

$$\vec{S} = \frac{c}{4\pi}\vec{E}\times\vec{B} \tag{6.3}$$

we may say that the laser intensity is proportional to the square of the scalar diffraction integral, $I \sim U_\omega^2$.

The primary, or Seidel, aberrations, are characterized by expansions to this diffraction integral [[93]]:

$$U(u,v,\psi) = -\frac{i}{\lambda}\frac{Aa^2}{R^2}e^{i\left(\frac{R}{a}\right)^2 u} \times \int_0^1 \int_0^{2\pi} e^{i\left[k\phi\left(Y_1^*,\rho,\theta\right) - v\rho cos(\theta-\psi) - \frac{1}{2}u\rho^2\right]}\rho d\rho d\theta \tag{6.4}$$

where $u, v, \& \psi$ are the optical coordinates, $\lambda$ is the wavelength, $A$ is the amplitude, $a$ is the radius of the exit pupil, $R$ is the radius of the Gaussian reference sphere, $k$ is the wave number, $\theta \& \rho$ are coordinates on the Gaussian reference sphere, and$\phi\left(Y_1^*, \rho, \theta\right)$ is the aberration function. We expand $\phi$ in terms of Zernike polynomials $R_n^m$:

$$\phi\left(Y_1^*, \rho, \theta\right) = \sum_l \sum_n \sum_m a_{lnm} Y_1^{*2l+m} R_n^m(\rho)\, cos(m\theta) \tag{6.5}$$

Inserting this expansion into the expression for the diffraction integral (and removing the explicit dependence on $Y_1^*$ by assuming a fixed image size) yields the following expression for the diffraction pattern associated with a single aberration [[93]]:

$$U(u,v,\psi) = 4C{\sum_{s=0}^{\infty}}' (-i)^{(m-1)s} \cos(ms\psi) \int_0^1 e^{-\frac{1}{2}iu\rho^2} J_s\left[\alpha_{lnm} R_n^m(\rho)\right] J_{ms}(v\rho)\, \rho d\rho \tag{6.6}$$

The integers l, n, and m in this expression specify the type of of aberration, according to Table 6.1 [[93]]: This expression can be expanded for small $\alpha$:

Table 6.1: Aberration Types and Integers[12]

| *Aberration Type* | *l* | *n* | *m* |
|---|---|---|---|
| Spherical | 0 | 4 | 0 |
| Comatic | 0 | 3 | 1 |
| Astigmatic | 0 | 2 | 2 |
| Curvature | 1 | 2 | 0 |
| Distortion | 1 | 1 | 1 |

$$U\left(u,v,\psi\right)=C\sum_{i=0}^{\infty}\left(i\alpha_{lnm}\right)^{i}U_{i} \tag{6.7}$$

The first four terms of this expansion are given by [93]:

$$U_0=2\int_0^1 e^{-\frac{1}{2}iu\rho^2}J_0\left(v\rho\right)\rho d\rho \tag{6.8}$$

$$U_1=2(-i)^m cos\left(m\psi\right)\int_0^1 e^{-\frac{1}{2}iu\rho^2}R_n^m\left(\rho\right)J_m\left(v\rho\right)\rho d\rho \tag{6.9}$$

$$U_2=\frac{1}{2!}\Big\{\int_0^1 e^{-\frac{1}{2}iu\rho^2}\{R_n^m\left(\rho\right)\}^2J_0\left(v\rho\right)\rho d\rho+$$

$$i^{2m}\cos\left(2m\psi\right)\int_0^1 e^{-\frac{1}{2}iu\rho^2}\{R_n^m\left(\rho\right)\}^2J_2m\left(v\rho\right)\rho d\rho\Big\} \tag{6.10}$$

$$U_3=\frac{1}{2\times 3!}\Big\{3\left(-i\right)^m\cos\left(m\psi\right)\int_0^1 e^{-\frac{1}{2}iu\rho^2}\{R_n^m\left(\rho\right)\}^3J_m\left(v\rho\right)\rho d\rho$$

$$i^{2m}\cos\left(2m\psi\right)\int_0^1 e^{-\frac{1}{2}iu\rho^2}\{R_n^m\left(\rho\right)\}^2J_2m\left(v\rho\right)\rho d\rho\Big\} \tag{6.11}$$

Note that in this expansion, the unaberrated pulse profile (given by $U_0$) is an Airy

function. For a Gaussian pulse, equation 6.8 instead becomes [[93]]:

$$U_0 = \frac{1}{\sqrt{2\pi}} e^{-\frac{v^2}{2}}$$

As previously discussed, the aberration considered in this research was the coma. Using the integers contained in table 6.1, Equations 6.8 through 6.11 become [[93]]:

$$U_1 = i\cos(\psi)\frac{2J_4(v)}{v} \tag{6.12}$$

$$U_2 = \frac{1}{2v}\left\{\frac{1}{4}J_1(v) - \frac{1}{20}J_3(v) + \frac{1}{4}J_5(v)\right.$$

$$\left. -\frac{9}{20}J_7(v) - \cos(2\psi)\left[\frac{2}{5}J_3(v) + \frac{3}{5}J_7(v)\right]\right\} \tag{6.13}$$

$$U_3 = \frac{-i}{12v}\left\{3\cos(m\psi)\left\{\frac{3}{14}J_{10}(v) - \frac{6}{35}J_8(v) + \frac{9}{70}J_6(v) - \frac{44}{105}J_4(v) + \frac{1}{15}J_2(v)\right\} +\right.$$

$$\left.\cos(3m\psi)\left\{\frac{9}{28}J_{10}(v) + \frac{9}{20}J_6(v) - \frac{8}{35}J_4(v)\right\}\right\} \tag{6.14}$$

It should be noted that, for this research, the expansion was carried out to $U_4$; however this term is omitted from the above equations for brevity.

## 6.4 Two-Dimensional Simulations: The Impact of the Coma on the Electron Beam Properties in a LWFA

### 6.4.1 Overview & Motivation

The utility to directly simulate the coma is not included in the standard version of OSIRIS 2.0; however, in two dimensions, and for small values of $\alpha$, we will represent the coma as an superposition of a $TEM00$ and a $TEM10$ pulse, which will represent an asymmetric pulse profile not entirely unlike that of the coma. Since OSIRIS 2.0 can simulate this pulse configuration, and since two-dimensional simulations are much less resource-intensive than three-dimensional simulations, a computational parameter sweep was performed in two-dimensions, studying how the performance of the system as an accelerator was affected by the deviation of the pulse from the "ideal" $TEM00$ mode. Examples of these initial pulse structures are shown in Figure 6.4, while examples of the LWFA "bubble" structure formed in the plasma are shown in Figure 6.5, and examples of the electron beams produced at the end of these simulations are shown in Figure 6.5

### 6.4.2 Methodology

For the two-dimensional simulations, a $TEM00$-mode pulse and a $TEM10$-mode pulse were superimposed upon one another such that the total pulse energy remained constant. The relative energy deposited in each pulse was varied to represent different aberration strengths. The relative energy was quantified via the mixing fraction, which is defined as follows:

$$f_{00} \equiv \frac{a_{0,00}}{a_0} \quad f_{10} \equiv \frac{a_{0,10}}{a_0} \tag{6.15}$$

$$a_0^2 = a_{00}^2 + a_{10}^2 = (f_{00}a_0)^2 + (f_{10}a_0)^2 = \left(f_{00}^2 + f_{10}^2\right) a_0^2 \tag{6.16}$$

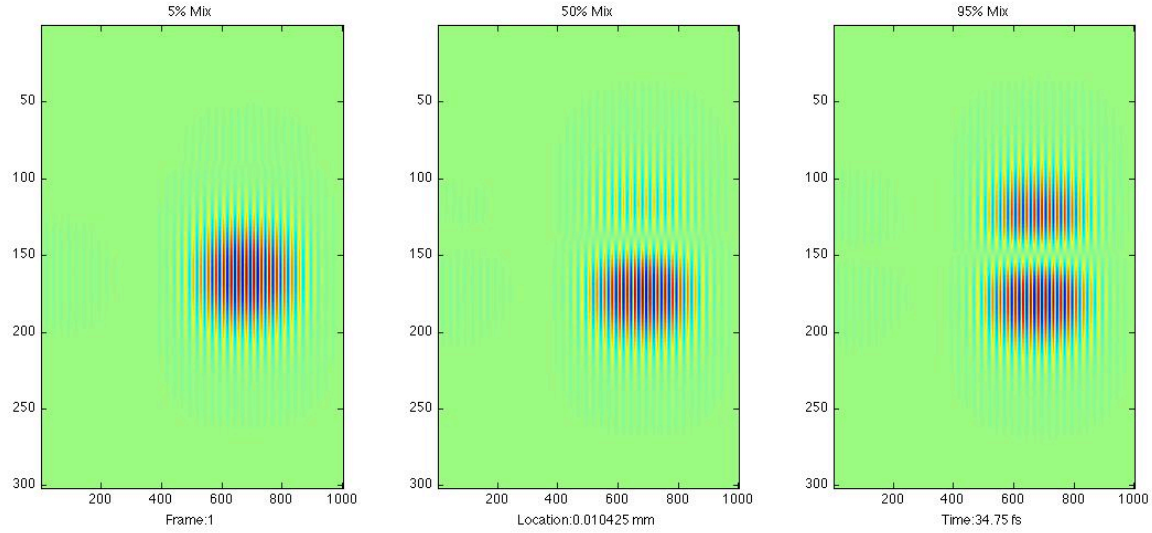


Figure 6.4: The initial laser pulses used in the two-dimensional simulations, for mixing percentages of (from left to right): 5%, 50%, and 95%

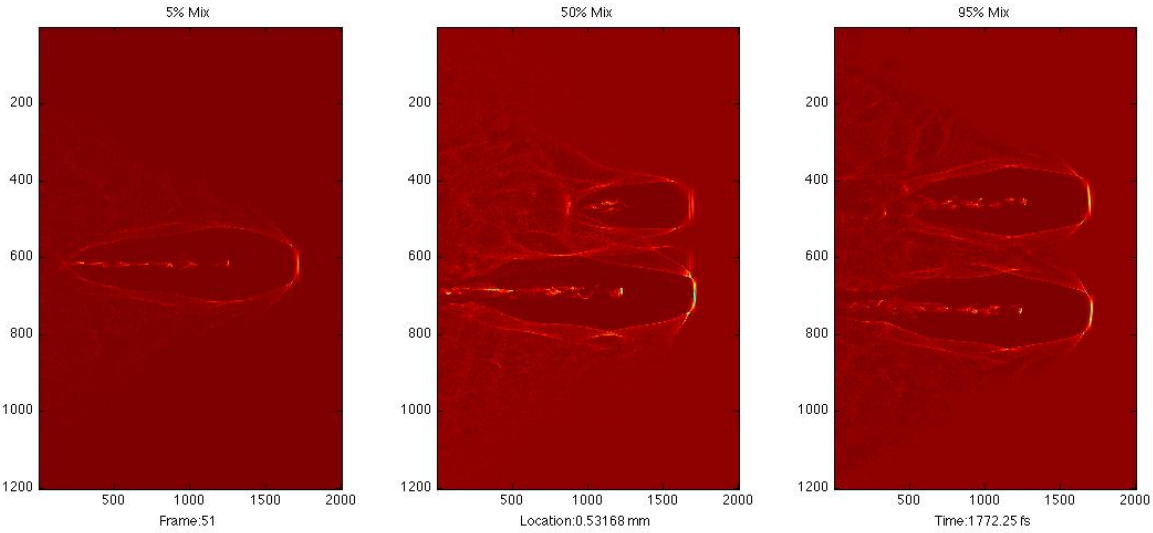


Figure 6.5: The two-dimensional plasma bubble structures half-way through the simulation, for mixing percentages of (from left to right): 5%, 50%, and 95%

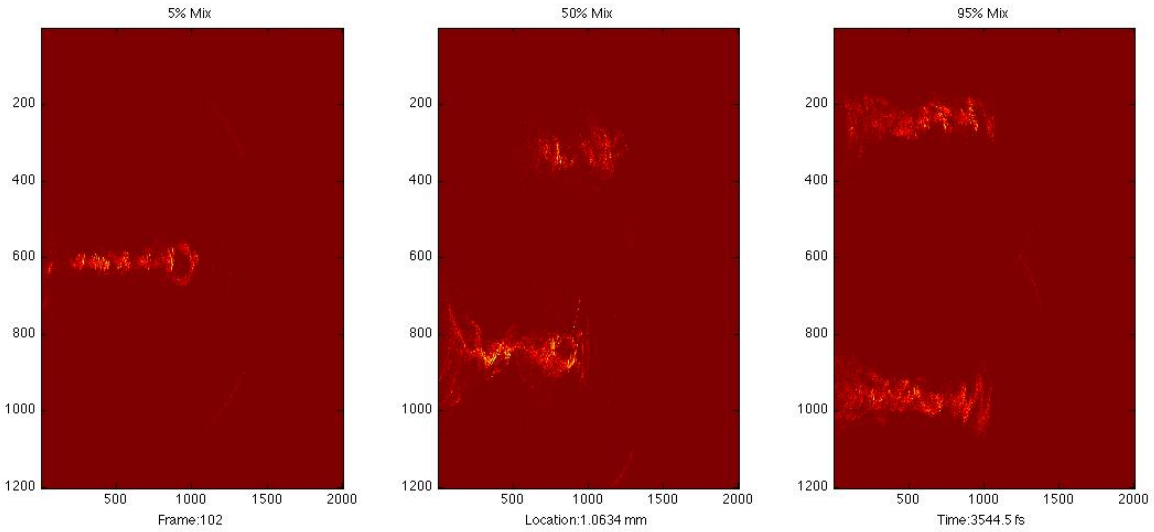


Figure 6.6: The final two-dimensional electron beams, for mixing percentages of (from left to right): 5%, 50%, and 95%

$$\left(f_{00}^2 + f_{10}^2\right) = 1 \tag{6.17}$$

The mixing fraction was therefore taken to be the quantity $f_{10}^2$; a parameter sweep in this variable was the basis of the two-dimensional simulations.

For each simulation, the pulse was allowed to propagate into vacuum. At this point the only remaining electrons were assumed to be the electron beam (for an example, see Figure 6.6), and the beam properties were measured. This density profile is shown in Figure 6.7 The properties were plotted against the mode-mixing percentage to assess the system's response to deviations from the Gaussian pulse.

The parameters for the two-dimensional simulations are listed in Figures 6.2, 6.3, and 6.4.

### 6.4.3 Results

For the 2D simulations, the peak of the electron energy spectrum and transverse beam emittance were measured as functions of the mixing fraction. The peak electron

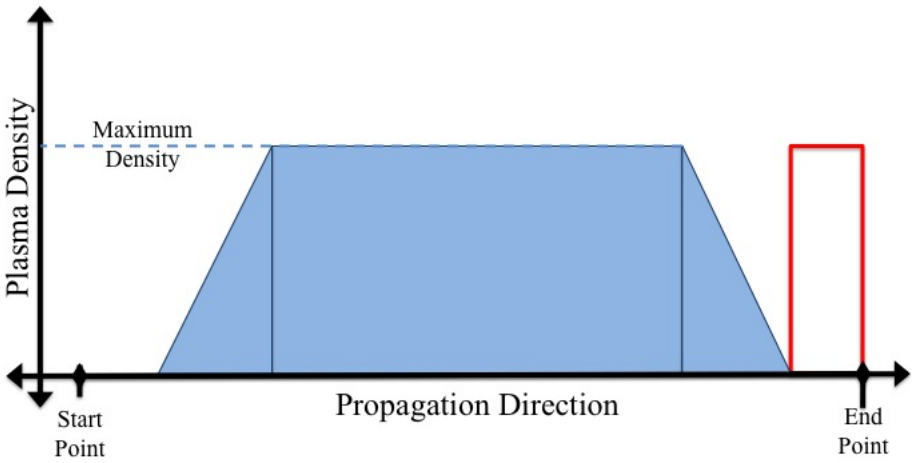


Figure 6.7: The density profile in the propagation direction for the simulations. The region indicated by the red box is where the beam properties were measured. The transverse density profile was uniform.

| Parameter | Value |
|---|---|
| Peak Plasma Density: | $0.01 n_{crit} = 1.75 \times 10^{19} cm^{-3}$ |
| Simulation Box Size: | $38.2 \times 63.7 \mu m$ |
| Box Propagation Speed: | c |
| Total Propagation Time: | $3.5 ps$ |

Table 6.2: The plasma parameters for the two-dimensional beam properties sweep

| Parameter | Value |
|---|---|
| FWHM Spot Size: | $5.1 \mu m$ |
| FWHD Pulse Length: | $35\ fs$ |
| Peak Normalized Vector Potential: | 4.0 |
| Peak Laser Intensity: | $3.5 \times 10^{19} W/cm^2$ |

Table 6.3: The laser parameters for the two-dimensional beam properties sweep; note that the laser vector potentials of the two constituent pulses were chosen such that the total pulse energy remained constant

| Parameter | Value |
|---|---|
| Simulation Grid Size: | $1200 \times 500$ cells |
| Particles Per Cell: | 2 |
| System Grid Spacing: | $0.03185 \times 0.1274 \mu m$ |

Table 6.4: The computational parameters for the two-dimensional beam properties sweep. Note that the highest resolution was in the propagation direction.

energy is plotted against the mixing fraction in Figure 6.8. The transverse beam emittance is plotted against the mixing fraction in Figure 6.9

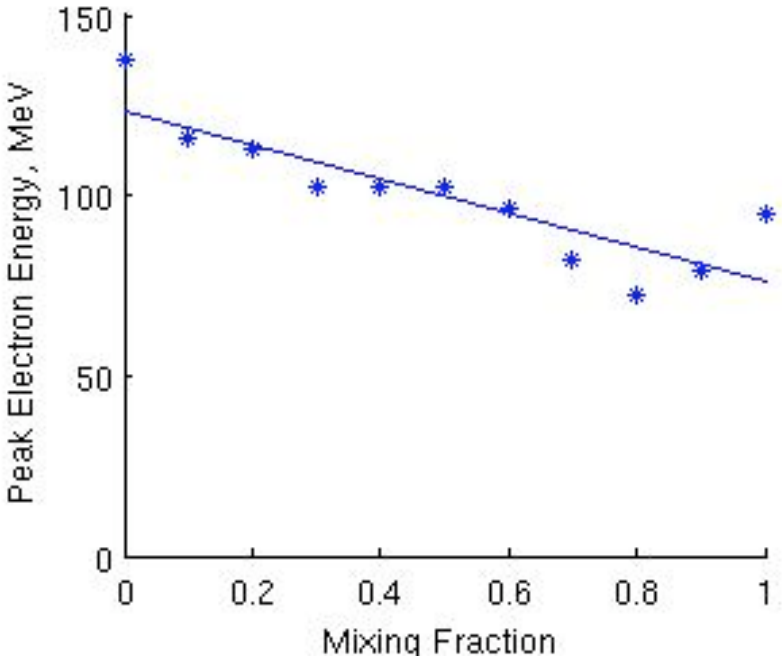


Figure 6.8: The peaks of the electron energy spectra as the mixing fraction is varied in the two-dimensional simulations.

Figure 6.8 shows that the beak beam energy decreases by $\sim 30\% - 40\%$ as the pulse transitions from 100% $TEM00$ to 100% $TEM10$. Figure 6.9 shows that the beam emittance increases by a factor of $\sim 5$ over the course of this transition. This is most likely due to the nature of the $TEM10$ pulse, which behaves like two pulses propagating side-by-side. It has been showed [[95]] that nonlinear interactions between co-propagating, side-by-side pulses can cause the pulses to either attract or repel, based on the relative phases of the two pulses. Both figures show that the performance of a LWFA experiment as a particle accelerator is significantly affected by deviations from the Gaussian in the pulse intensity profile, demonstrating the need for more precise three-dimensional simulations.

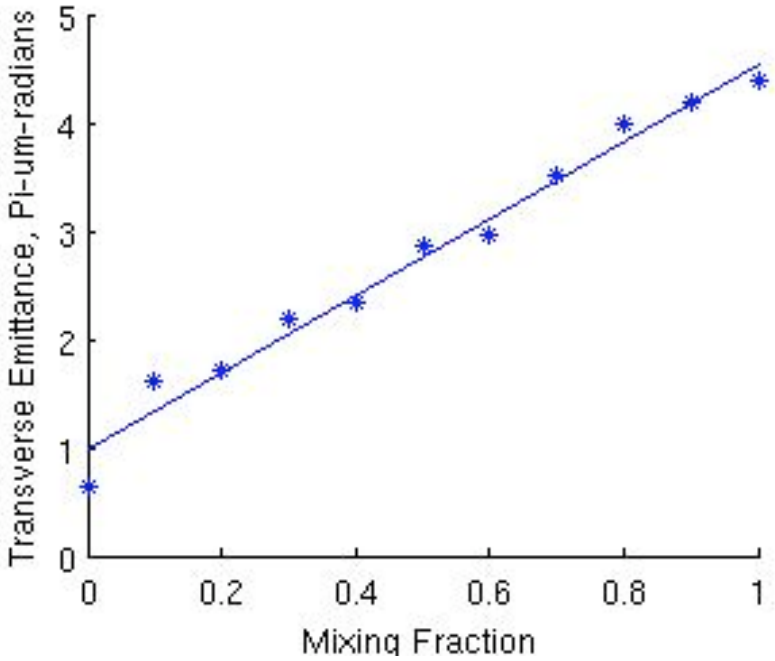


Figure 6.9: The transverse emittances of the final electron beams as the mixing fraction is varied in the two-dimensional simulations.

## 6.5 Three-Dimensional Simulations: The Impact of the Coma on the Electron Beam Properties in a LWFA

### 6.5.1 Overview & Motivation

After the two-dimensional simulations demonstrated that deviations from the Gaussian can significantly affect the performance of the LWFA system as an accelerator, three dimensional simulations that explicitly included the coma were run and analyzed. Equations 6.12 through 6.14 (as well as $U_4$ term in the expansion which is omitted for brevity) were integrated into the OSIRIS 2.0 pulse envelope initialization routine so that the coma could be directly simulated. A simulated pulse featuring these modifications is shown in Figure 6.10.

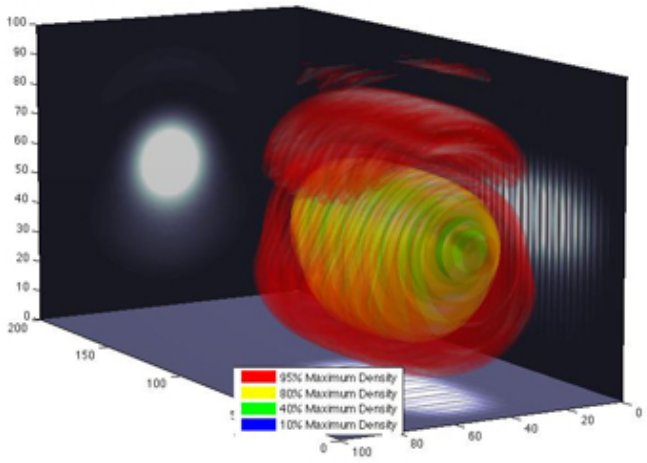


Figure 6.10: The intensity of a laser pulse as simulated by OSIRIS 2.0, modified to feature a coma.

| Parameter | Value |
|---|---|
| Peak Plasma Density: | $0.01 n_{crit} = 1.75 \times 10^{19} cm^{-3}$ |
| Simulation Box Size: | $38.2 \times 31.8 \times 31.8 \mu m$ |
| Box Propagation Speed: | c |
| Total Propagation Time: | $3.4 ps$ |

Table 6.5: The plasma parameters for the three-dimensional beam properties sweep

### 6.5.2 Methodology

The expansion parameter $\alpha$ appearing in Equations 6.12 through 6.14 was used to quantify the severity of the aberration (for reference, the aberration shown in Figure 6.10 has $\alpha = 1.005$). The parameter $\alpha$ was varied from 0.0 to 1.0. As with the two-dimensional simulations, the pulse was allowed to propagate into vacuum, at which point the electron beam properties were measured (the density profile in the propagation direction was again that shown in Figure 6.7).

The parameters for the three-dimensional simulations are listed in Figures 6.5, 6.6, and 6.7.

| Parameter | Value |
|---|---|
| FWHM Spot Size: | $5.1\mu m$ |
| FWHD Pulse Length: | $35\ fs$ |
| Peak Normalized Vector Potential: | 4.0 |
| Peak Laser Intensity: | $3.5 \times 10^{19} W/cm^2$ |

Table 6.6: The laser parameters for the three-dimensional beam properties sweep

| Parameter | Value |
|---|---|
| Simulation Grid Size: | $1200 \times 250 \times 250$ cells |
| Particles Per Cell: | 2 |
| System Grid Spacing: | $0.03175 \times 0.1272 \times 0.1272\mu m$ |

Table 6.7: The computational parameters for the three-dimensional beam properties sweep. Note that the highest resolution was in the propagation direction.

### 6.5.3 Results

For the 3D simulations, the electron energy spectra, peak electron beam energy, peak electron beam current, as well as the beam emittances in both the polarization and transverse directions were all measured as functions of the parameter $\alpha$. The electron energy spectra for five values of $\alpha$ are shown in Figure 6.11. The energies at which the maxima of these spectra lie, plotted vs. $\alpha$, are shown in Figure 6.12. The peak electron beam current as a function of $\alpha$ is shown in Figure 6.13. Finally, the electron beam emittances as functions of $\alpha$ are shown in Figure 6.14.

Figures 6.11 and 6.12 show how varying the parameter $\alpha$ affects the energetic properties of the electron beam produced by the LWFA system. These results are very promising, as they show that the spectral shape is not dramatically affected, even by the presence of a significant aberration. Similarly, the peak electron beam energy remains relatively unaffected by the presence of a coma, varying by less than $\sim 10\%$ as $\alpha$ varies from 0.0 to 1.0. Figure 6.13 shows that the peak forward current is similarly robust against the presence of an aberration, varying by only $\sim 20\%$ as $\alpha$ varies from 0.0 to 1.0.

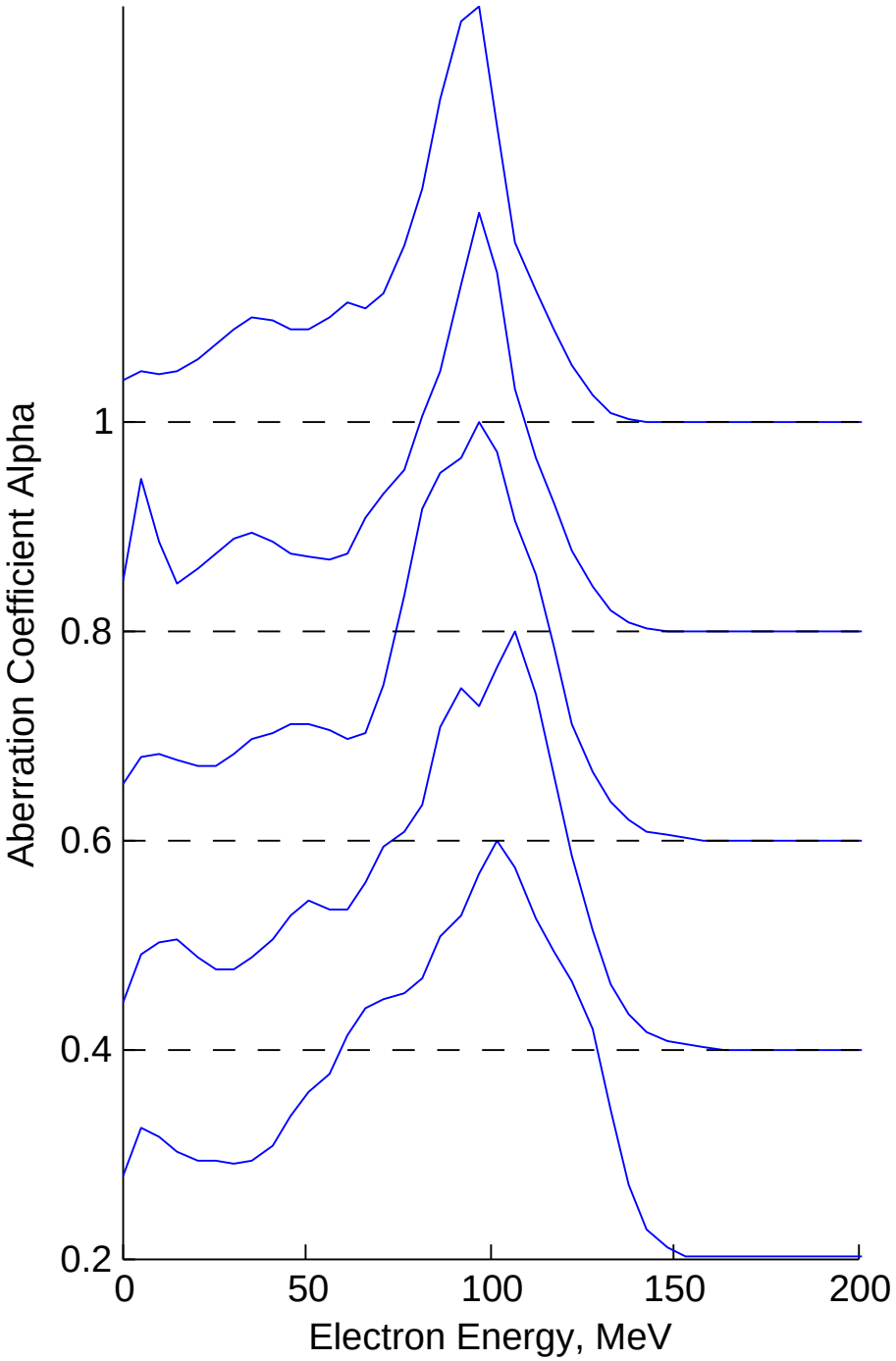


Figure 6.11: The electron energy spectra for increasing values of $\alpha$. The the spectra have been offset for clarity.

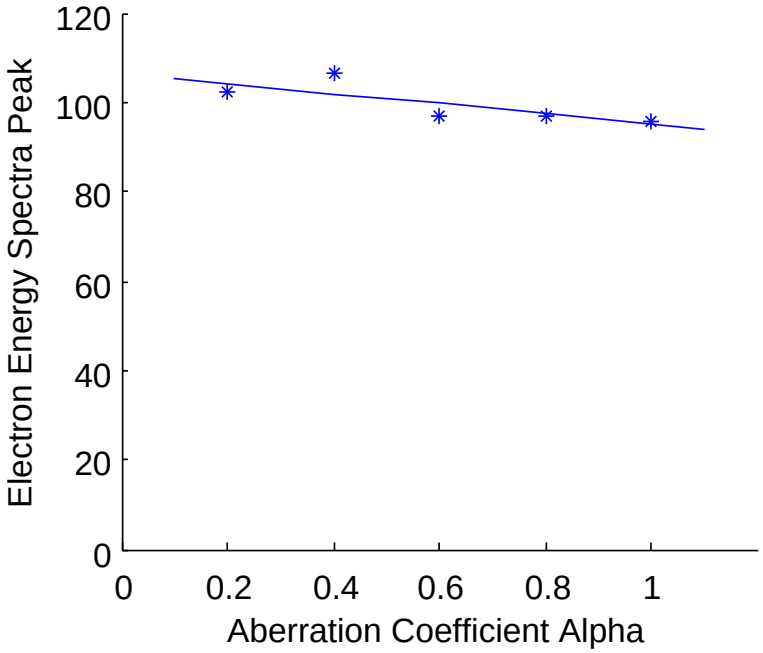


Figure 6.12: The peaks of the electron energy spectra for increasing values of $\alpha$. These are the energies at which the maximum values of the spectra lie.

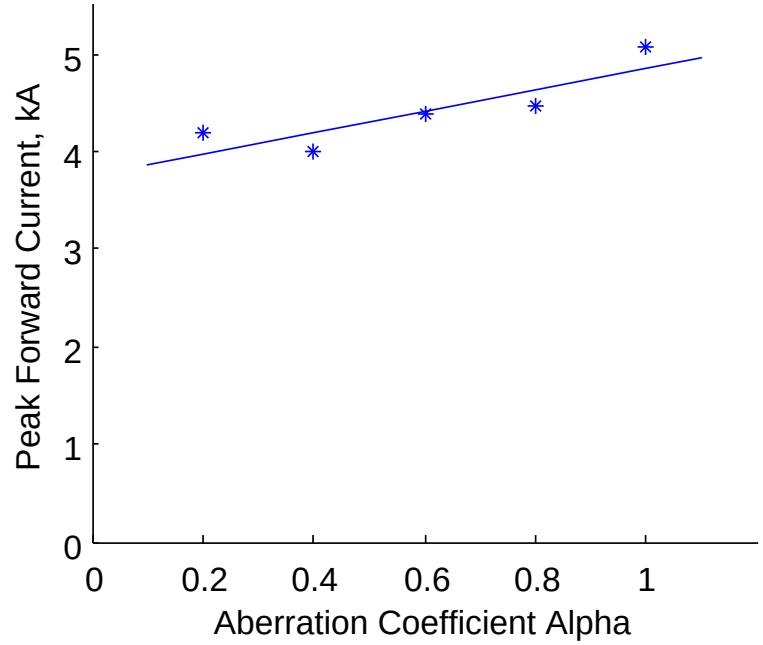


Figure 6.13: The peaks of the electron beam current for increasing values of $\alpha$.

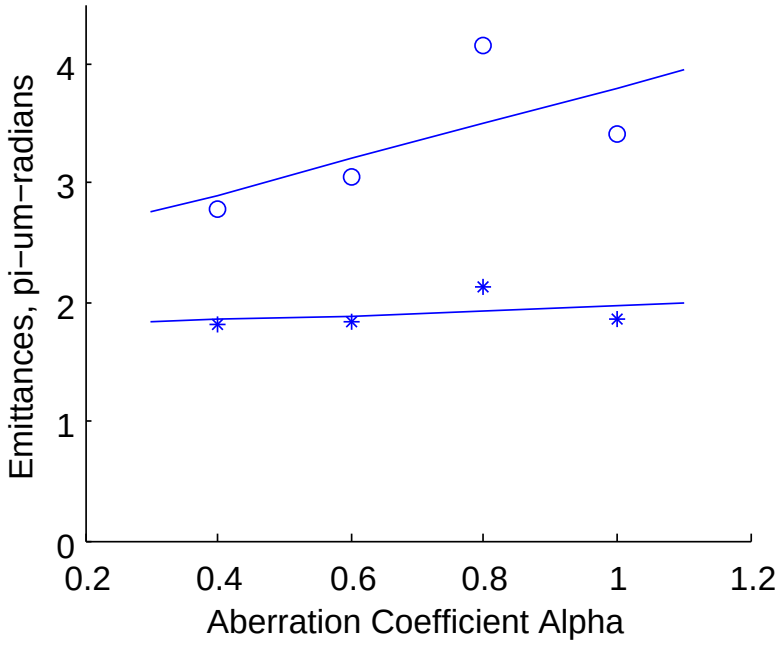


Figure 6.14: The electron beam emittances in the polarization (top) and transverse (bottom) directions, for increasing values of $\alpha$.

By contrast, Figure 6.14 shows that the beam emittance in the polarization direction is affected by the presence of a coma, while the emittance in the transverse direction (i.e., orthogonal to both the direction of laser polarization and the direction of laser propagation) remains unaffected. The increase in the difference between the two emittances as $\alpha$ increases indicates that the beam ellipticity is also increasing; this could, in turn, indicate the presence of increased betatron motion, which would enhance the generation of synchrotron-like radiation.

## 6.6 Conclusion: The Impact of the Coma on the Electron Beam Properties in a LWFA

The results of this computational parameter sweep were promising for two reasons. First, while preliminary two-dimensional simulations indicated that deviations from the ideal Gaussian pulse can significantly affect the performance of a laser wake field accelerator, more precise three-dimensional simulations indicated that many key performance parameters of the system are robust against the presence of even a strong coma. The peak beam energy was relatively unaffected, decreasing by no more than $\sim 10\%$ for the strongest aberration considered. The electron energy spectrum was also relatively unaffected by the presence of the aberration; if anything the spectral peak narrowed as the aberration severity increased.

Second, the emittance of the beam in the polarization direction was significantly affected by the presence of an aberration, while the emittance of the beam in the transverse direction was relatively unaffected. This could indicate that the increasing aberration strength corresponds to an increase in the beam ellipticity. This could, in turn, indicate an increase in the magnitude of the beam's betatron oscillations, which would lead to an increase in the strength and critical frequency of the emitted betatron radiation.

| Parameter | Normalized Value | Real Value |
|---|---|---|
| Peak Plasma Density: | 0.01 | $1.75 \times 10^{19} cm^{-3}$ |
| Simulation Box Size: | $300 \times 200 \times 200$ | $39 \times 26 \times 26 \mu m$ |
| Box Propagation Speed: | c | $3.0 \times 10^{10} cm/s$ |
| Total Propagation Time: | 5900 | $2.5 ps$ |

Table 6.8: The plasma parameters for the coma radiation sweep

## 6.7 The Impact of the Coma on Betatron Radiation Properties in LWFA

### 6.7.1 Overview

This section combines the radiation-generation algorithm from Chapter 4 with the coma simulations of the previous section to investigate the impact of the presence of a coma on the generation of betatron radiation in LWFA experiments. First, we present an overview of the simulation parameters used for this investigation. Then, we present the electron phase-space results from these simulations, using the same visualizations as in Chapter 5. Subsequently, the radiation results are presented, followed by correlations between the electron trajectories and radiation properties. Again, the same visualizations as those in Chapter 5 are used. Trends are commented upon and analyzed.

### 6.7.2 Simulation Parameters

The parameters used for the coma radiation simulations are listed in Tables 6.8, 6.9, 6.10, and 6.11.

### 6.7.3 Electron Phase-Space Results

For the electron phase-space results from the coma sweep simulations, we present the results from the non-aberrated pulse simulation with the same visualization as in Chapter 5. However, for the time-evolution of the EEDF, we instead compare the

| Density | Initial Position | Final Position |
|---|---|---|
| 0.0 (Vacuum) | $0.0\mu m$ | $65\mu m$ |
| Linear Ramp from 0.0 to Peak Density | $65\mu m$ | $130\mu m$ |
| Peak Density (Bulk Plasma) | $130\mu m$ | $637\mu m$ |
| Linear Ramp from Peak Density to 0.0 | $637\mu m$ | $702\mu m$ |
| 0.0 (Vacuum) | $702\mu m$ | $767\mu m$ |

Table 6.9: The density profile for the coma radiation sweep

| Parameter | Normalized Value | Real Value |
|---|---|---|
| FWHM Spot Size: | 40 | 5.2 $\mu m$ |
| FWHD Pulse Length: | 64 | 28 $fs$ |
| Peak Normalized Vector Potential: | 4.0 | |
| Peak Laser Intensity: | $3.4 \times 10^{19} W/cm^2$ | |

Table 6.10: The laser parameters for the coma radiation sweep

| Parameter | Value |
|---|---|
| Simulation Grid Size: | $600 \times 100 \times 100$ cells |
| Particles Per Cell: | 2 |
| System Grid Spacing: | $0.066 \times 0.26 \times 0.26\mu m$ |
| System Time-Step: | $0.172fs$ |

Table 6.11: The computational parameters for the coma radiation sweep. Note that the highest resolution was in the propagation direction.

results from the two different polarizations side-by-side. These data are shown in Figures 6.15 through 6.25. Some slight trends are observable. First, we notice that the initial electron beam tends to become more well defined relative to the background plasma for more severe comae. This is true regardless of the polarization. However, we also notice that for a polarization angle of 90 degrees (i.e., when the angle of laser polarization and angle of coma asymmetry align), we tend to see even more definition of the electron beam compared to the background plasma.

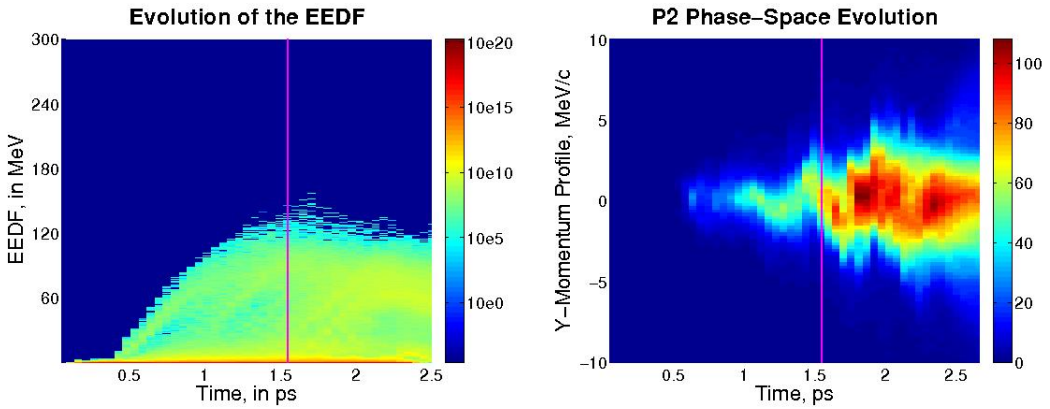


Figure 6.15: The time-evolution of (left) the EEDF and (right) the momentum profile in the laser polarization direction for the $\alpha = 0.0$ (i.e, non-aberrated) simulations. The color scales on the left are logarithmic, and in units of normalized charge per MeV per ps. The color scales on the right are linear, and are in units of normalized charge per $m_e c$ per ps.

The most compelling data of this parameter sweep, however, comes from an analysis of the momentum phase-space profiles of the electron beams. Note that for these data, the laser propagation direction was the x-direction, the direction of coma asymmetry was the z-direction, and the direction of laser polarization was either in the y-direction (for the 0-degree polarization case) or the z-direction (for the 90-degree polarization case). In these data, we see a clear, consistent, and compelling trend. For the simulations where the direction of laser polarization and the direction of coma asymmetry are perpendicular (i.e., the 0-degree polarization cases), we see very low-amplitude, high-frequency betatron motion in the direction of laser polarization,

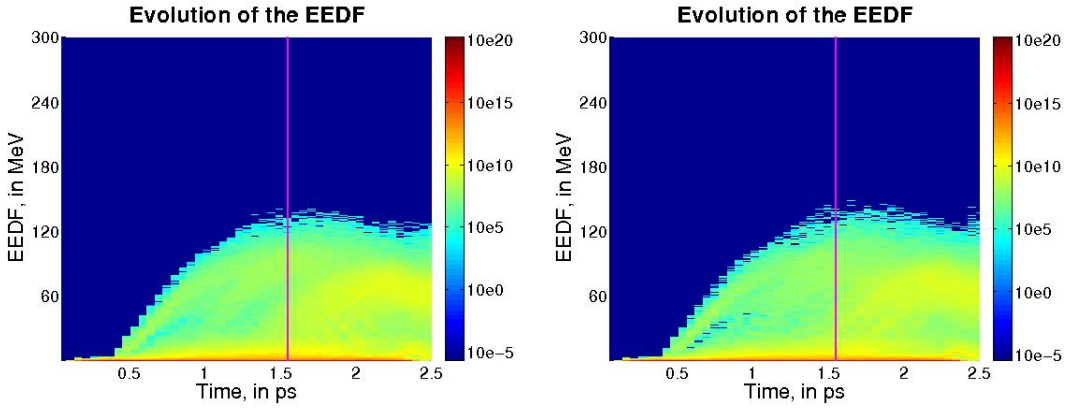


Figure 6.16: The time-evolution of the EEDF for the $\alpha = 0.1$ simulations for (left) 0-degree and (right) 90-degree polarization. The color scales are logarithmic, and in units of normalized charge per MeV per ps.

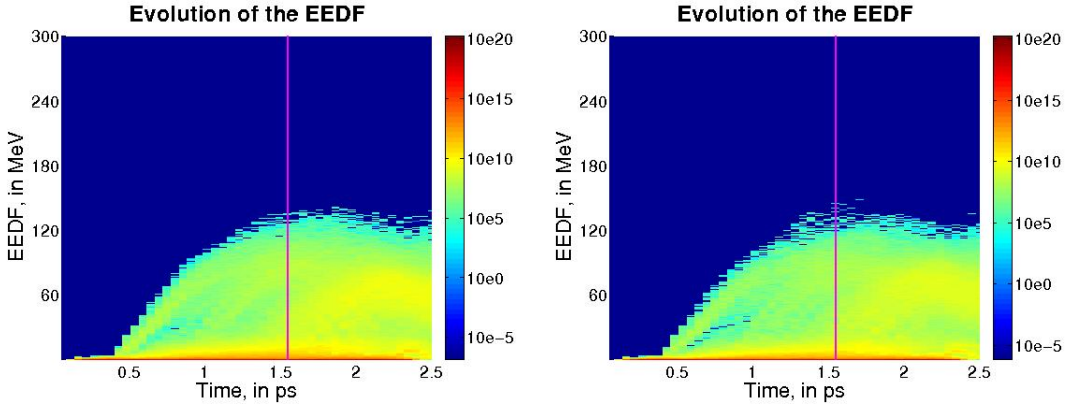


Figure 6.17: The time-evolution of the EEDF for the $\alpha = 0.2$ simulations for (left) 0-degree and (right) 90-degree polarization. The color scales are logarithmic, and in units of normalized charge per MeV per ps.

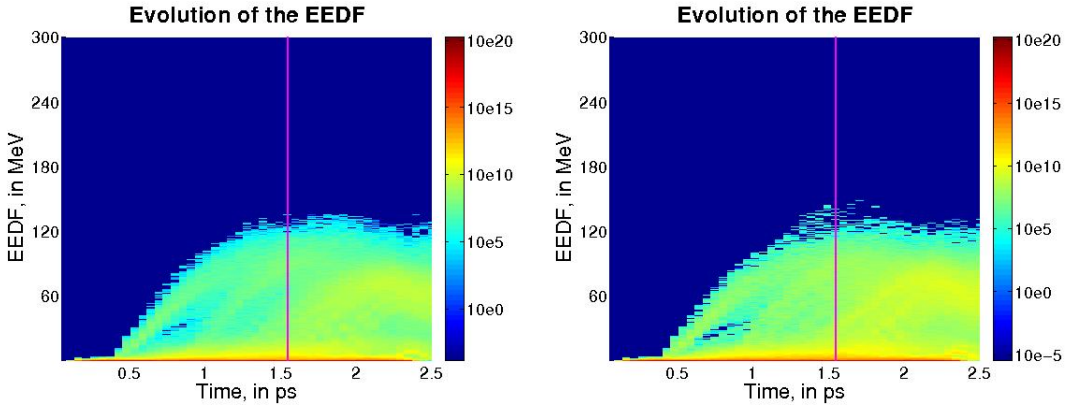


Figure 6.18: The time-evolution of the EEDF for the $\alpha = 0.3$ simulations for (left) 0-degree and (right) 90-degree polarization. The color scales are logarithmic, and in units of normalized charge per MeV per ps.

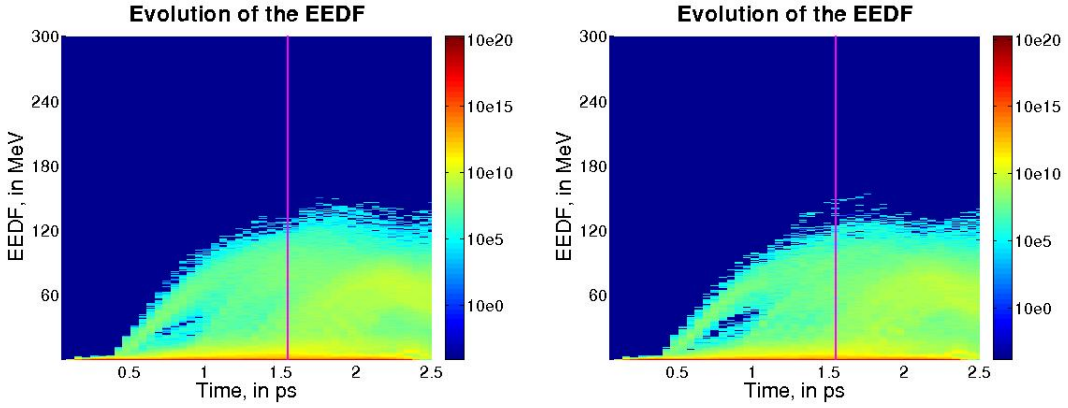


Figure 6.19: The time-evolution of the EEDF for the $\alpha = 0.4$ simulations for (left) 0-degree and (right) 90-degree polarization. The color scales are logarithmic, and in units of normalized charge per MeV per ps.

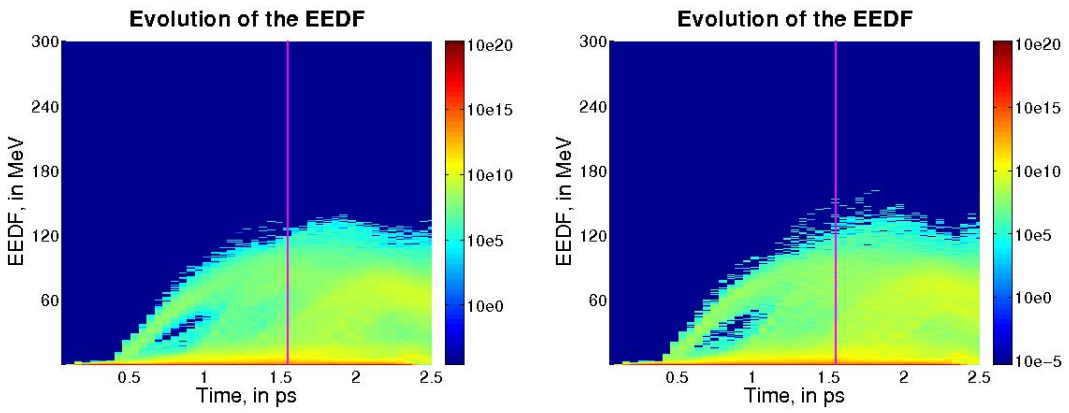


Figure 6.20: The time-evolution of the EEDF for the $\alpha = 0.5$ simulations for (left) 0-degree and (right) 90-degree polarization. The color scales are logarithmic, and in units of normalized charge per MeV per ps.

and very large-amplitude, low-frequency betatron motion in the direction of coma asymmetry. Conversely, for the simulations where the direction laser polarization and the direction of coma asymmetry are aligned (i.e., the 90-degree polarization cases), we see betatron motion only in the direction of coma asymmetry/laser polarization; moreover this motion appears to be predominantly of the high-amplitude, low-frequency type caused by the coma asymmetry, rather than the type caused by direct interaction with the laser. However, for these simulations, small-amplitude, high-frequency oscillations can be observed as perturbations in the dominant low-frequency motion. The disparity between these two effects becomes more pronounced as the severity of the coma increases.

It is abundantly clear from these data that, at these intensity/density conditions, the primary driver of the betatron motion of the electron beam is the field structure of the plasma wake, and not interaction with the laser. Consequently, alterations in the shape of the wake due to the presence of the coma strongly effect the betatron motion of the electron beam at this intensity and density. However, the results from the parameter sweep in the laser vector potential $a_0$ showed that, at higher laser intensities, the beam interaction with the laser field tends to become the dominant

driver for the beam's betatron motion. As a result, it is not clear whether or not the presence of a coma will have as dominant an effect on the beam betatron motion at these higher intensities.

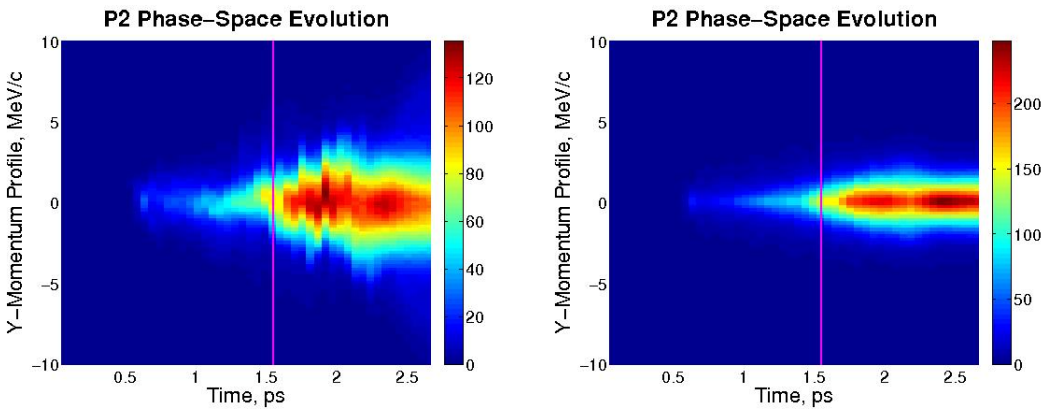
P2 Phase–Space Evolution
Y–Momentum Profile, MeV/c
Time, ps
P2 Phase–Space Evolution
Y–Momentum Profile, MeV/c
Time, ps

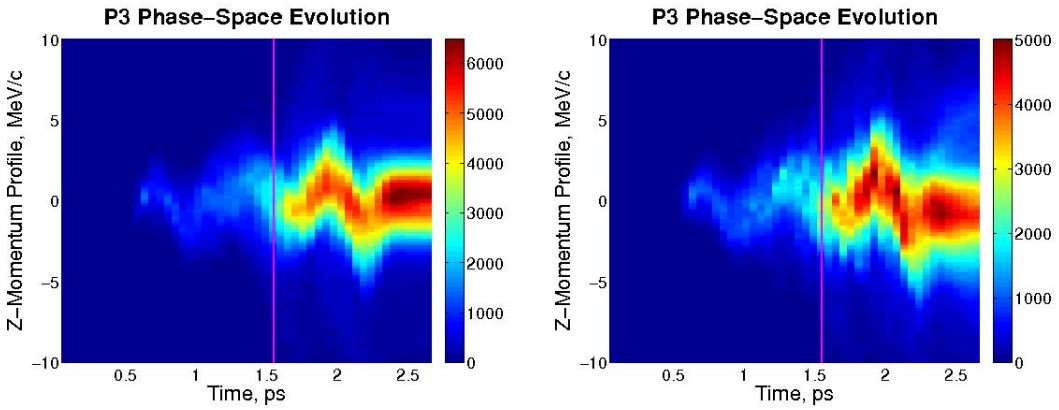


Figure 6.21: The time-evolution of the electron beam momentum phase-space profile in the laser polarization direction for the $\alpha = 0.1$ simulations. The left-hand images are the 0-degree polarization images (where the directions of coma asymmetry and laser polarization are perpendicular), while the right-hand images are the 90-degree polarization images (where the directions of coma asymmetry and laser polarization are aligned). The top images are in the p2 direction (perpendicular to the direction of coma asymmetry), while the bottom images are in the p3 direction (aligned with the direction of coma asymmetry). The color scales are linear, and are in units of normalized charge per $m_e c$ per ps.

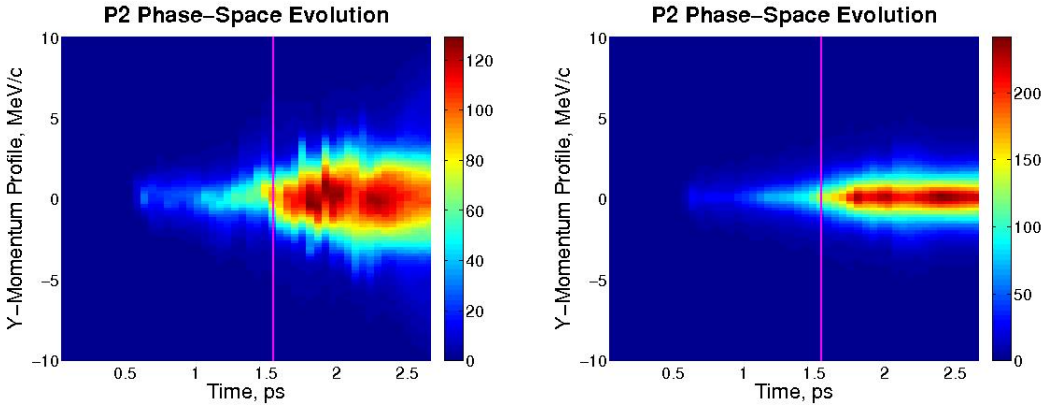

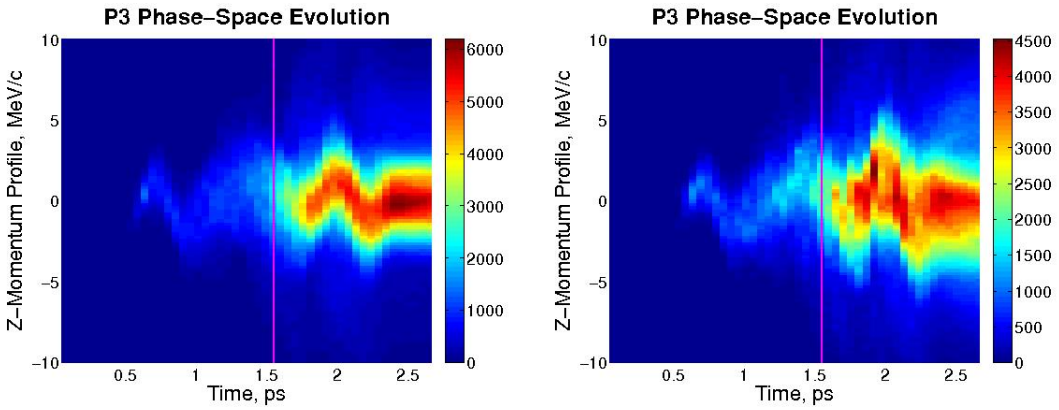


Figure 6.22: The time-evolution of the electron beam momentum phase-space profile in the laser polarization direction for the $\alpha = 0.2$ simulations. The left-hand images are the 0-degree polarization images (where the directions of coma asymmetry and laser polarization are perpendicular), while the right-hand images are the 90-degree polarization images (where the directions of coma asymmetry and laser polarization are aligned). The top images are in the p2 direction (perpendicular to the direction of coma asymmetry), while the bottom images are in the p3 direction (aligned with the direction of coma asymmetry). The color scales are linear, and are in units of normalized charge per $m_e c$ per ps.

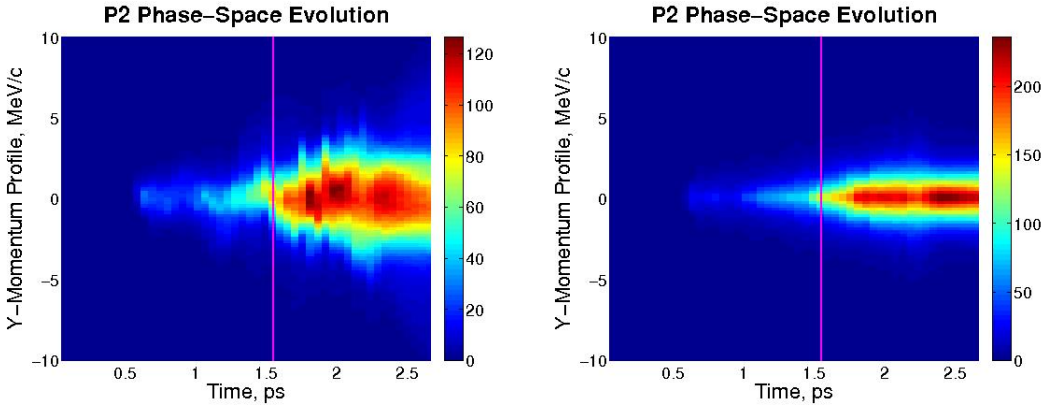

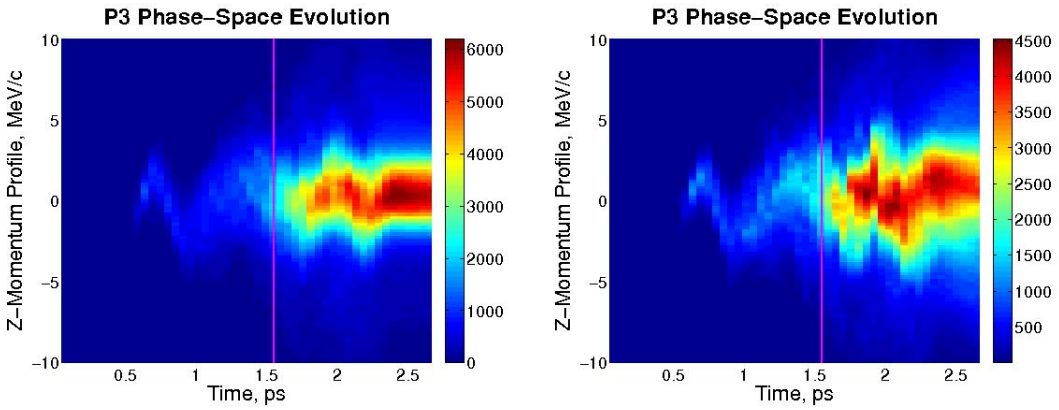


Figure 6.23: The time-evolution of the electron beam momentum phase-space profile in the laser polarization direction for the $\alpha = 0.3$ simulations. The left-hand images are the 0-degree polarization images (where the directions of coma asymmetry and laser polarization are perpendicular), while the right-hand images are the 90-degree polarization images (where the directions of coma asymmetry and laser polarization are aligned). The top images are in the p2 direction (perpendicular to the direction of coma asymmetry), while the bottom images are in the p3 direction (aligned with the direction of coma asymmetry). The color scales are linear, and are in units of normalized charge per $m_e c$ per ps.

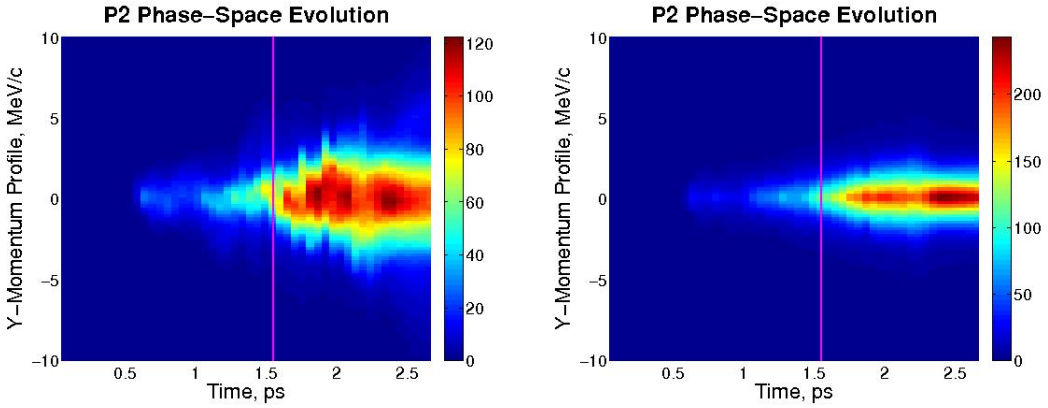

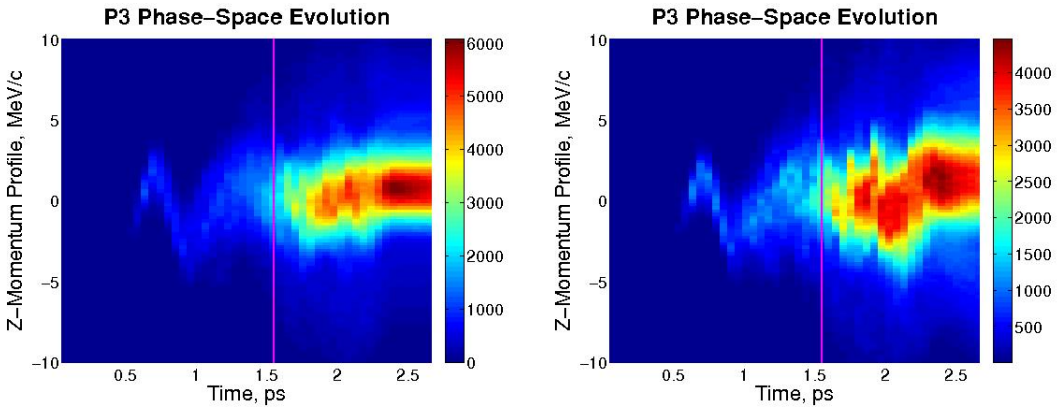


Figure 6.24: The time-evolution of the electron beam momentum phase-space profile in the laser polarization direction for the $\alpha = 0.4$ simulations. The left-hand images are the 0-degree polarization images (where the directions of coma asymmetry and laser polarization are perpendicular), while the right-hand images are the 90-degree polarization images (where the directions of coma asymmetry and laser polarization are aligned). The top images are in the p2 direction (perpendicular to the direction of coma asymmetry), while the bottom images are in the p3 direction (aligned with the direction of coma asymmetry). The color scales are linear, and are in units of normalized charge per $m_e c$ per ps.

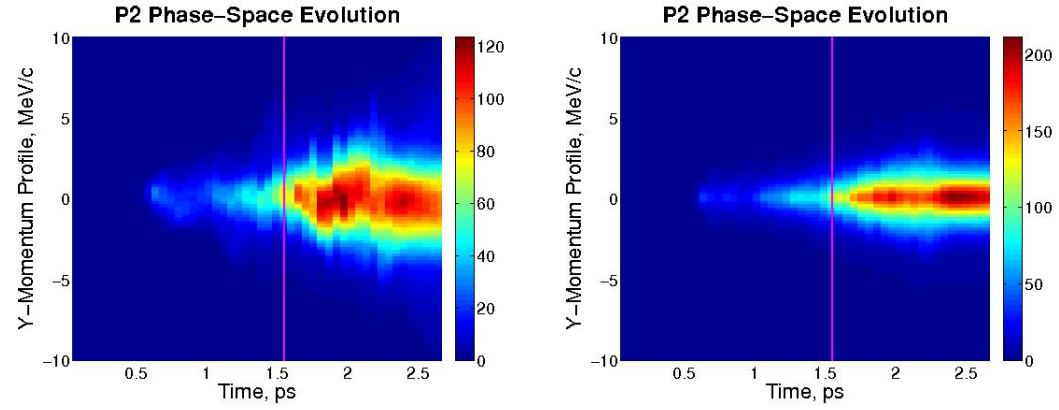

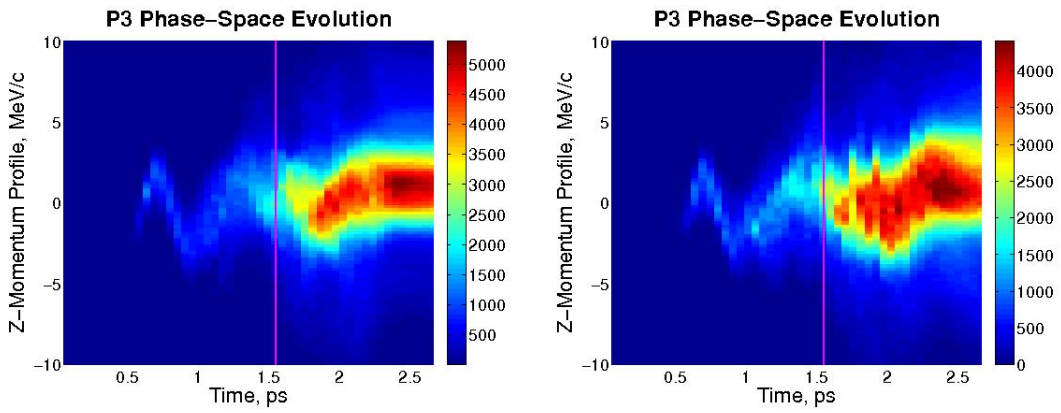


Figure 6.25: The time-evolution of the electron beam momentum phase-space profile in the laser polarization direction for the $\alpha = 0.5$ simulations. The left-hand images are the 0-degree polarization images (where the directions of coma asymmetry and laser polarization are perpendicular), while the right-hand images are the 90-degree polarization images (where the directions of coma asymmetry and laser polarization are aligned). The top images are in the p2 direction (perpendicular to the direction of coma asymmetry), while the bottom images are in the p3 direction (aligned with the direction of coma asymmetry). The color scales are linear, and are in units of normalized charge per $m_e c$ per ps.

### 6.7.4 Radiation Emission Results

As with the electron phase-space results, we plot the radiation results from the two different polarizations side-by-side. The time-evolution of the radiation spectra, shown in Figures 6.26 through 6.31, show consistent results; as with the $a_0$ parameter sweep, the peak radiation frequency (i.e. the tail of the spectrum) tends to slowly increase in time, before sharply dropping as the electron beam exits the plasma. This trend is more or less constant in both the polarization and coma severity. Similarly, the radiated power (shown in Figures 6.26 and 6.32 through 6.36) tends to increase as the laser pulse propagates, before sharply dropping as the system exits the plasma. This trend is also more or less constant in both the polarization and coma severity. As with other parameter sweeps, the radiated power also displays some noise-like fluctuations, however they do not appear to be as severe as those observed in the laser vector potential, electron density, and propagation distance sweeps.

The spectra for the $\alpha = 0.0, 0.1, \& \ 0.2$ and $\alpha = 0.3, 0.4, \& \ 0.5$ simulations are shown in Figures 6.37 and 6.38, respectively. While no trends are immediately apparent in these plots, plotting the total radiated energies and tail temperatures as functions of $\alpha$ (shown in Figures 6.39 and 6.40, respectively) immediately reveals some interesting trends. As with the $a_0$ and $n_e$ sweeps in Chapter 5, a high-frequency region is observed in the spectra and presumed to be a numerical artifact.

Figure 6.39 shows that, for both polarizations, initial increases in the coma severity from $\alpha = 0.0$ to $\alpha = 0.2$ increase the total radiated energy by $\sim 25\%$. Increasing the coma severity beyond this point, however, causes the radiated energy to drop again. The 90-degree polarization case, where the coma asymmetry and laser polarization are aligned, shows a much sharper drop in the radiated energy than the 00-degree polarization case.

Figure 6.40 demonstrates that the high-energy tail of the distribution is somewhat noisy, as the temperatures for the $\alpha = 0.0$ (i.e., Gaussian) Pulses vary between the two polarizations by $\sim 8\%$. Since none of the calculated temperatures vary by more than this, the only definitive conclusion we can draw about the effect of the coma on the temperature of the high-energy tail of the distribution is that it is small.

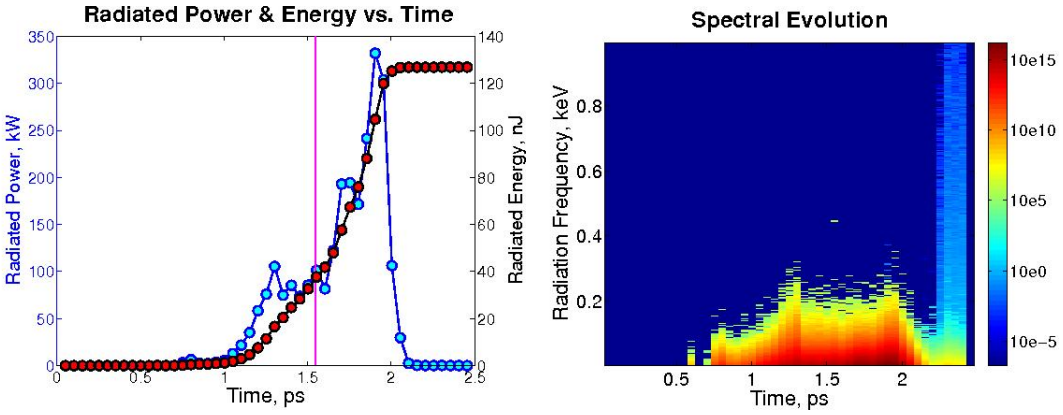


Figure 6.26: The radiated power and energy (left) and time-evolution of the radiation spectrum (right )for the $\alpha = 0.0$ simulations; note that the color scale on the left-hand plot is logarithmic and the units are Joules/(keV*second)

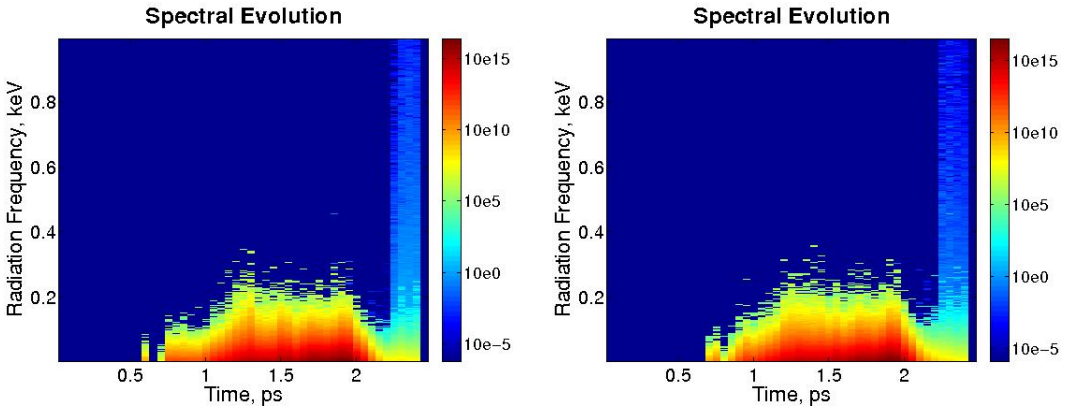


Figure 6.27: The time-evolution of the radiation spectrum for the $\alpha = 0.1$ simulations for (left) 0-degree and (right) 90-degree polarization; note that the color scale on these plots is logarithmic and the units are Joules/(keV*second)

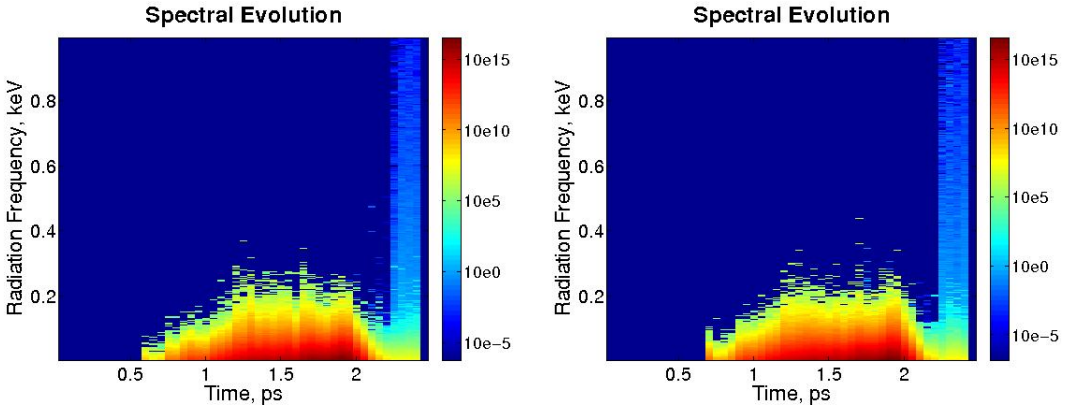


Figure 6.28: The time-evolution of the radiation spectrum for the $\alpha = 0.2$ simulations for (left) 0-degree and (right) 90-degree polarization; note that the color scale on these plots is logarithmic and the units are Joules/(keV*second)

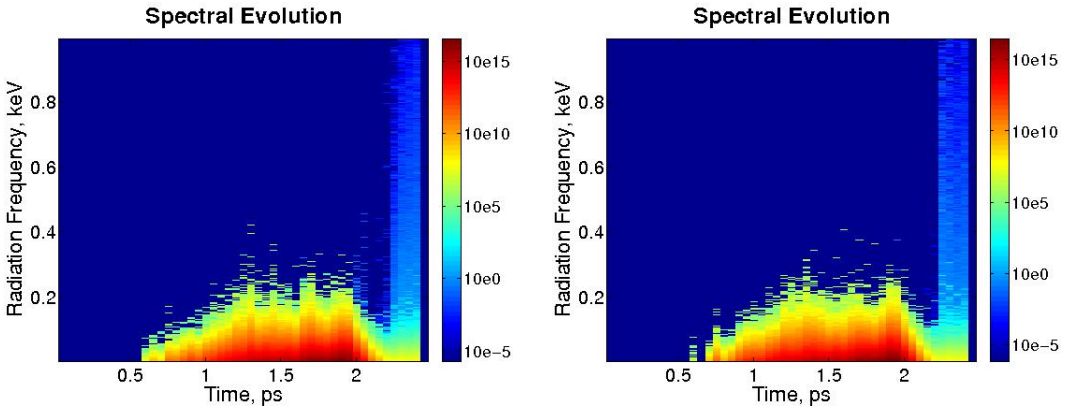


Figure 6.29: The time-evolution of the radiation spectrum for the $\alpha = 0.3$ simulations for (left) 0-degree and (right) 90-degree polarization; note that the color scale on these plots is logarithmic and the units are Joules/(keV*second)

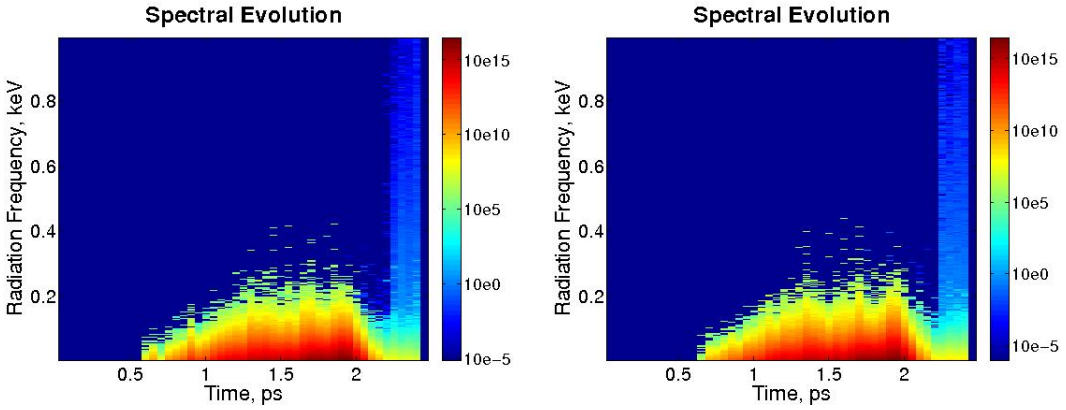


Figure 6.30: The time-evolution of the radiation spectrum for the $\alpha = 0.4$ simulations for (left) 0-degree and (right) 90-degree polarization; note that the color scale on these plots is logarithmic and the units are Joules/(keV*second)

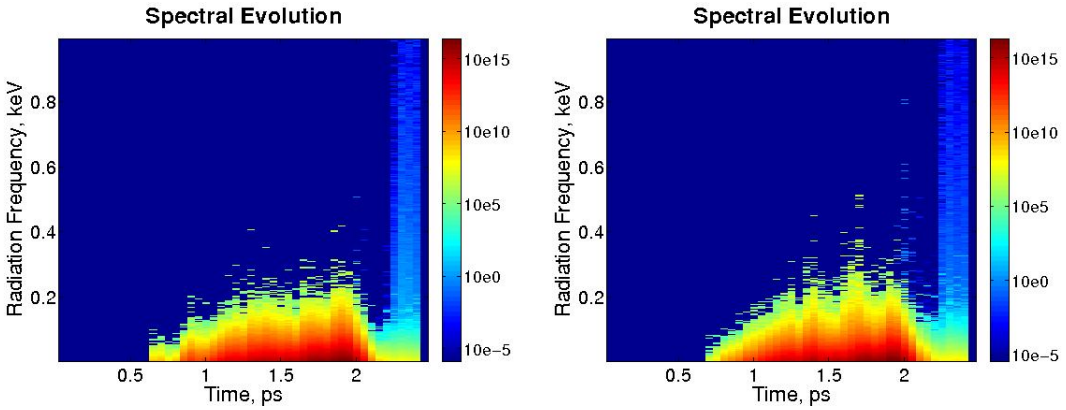


Figure 6.31: The time-evolution of the radiation spectrum for the $\alpha = 0.5$ simulations for (left) 0-degree and (right) 90-degree polarization; note that the color scale on these plots is logarithmic and the units are Joules/(keV*second)

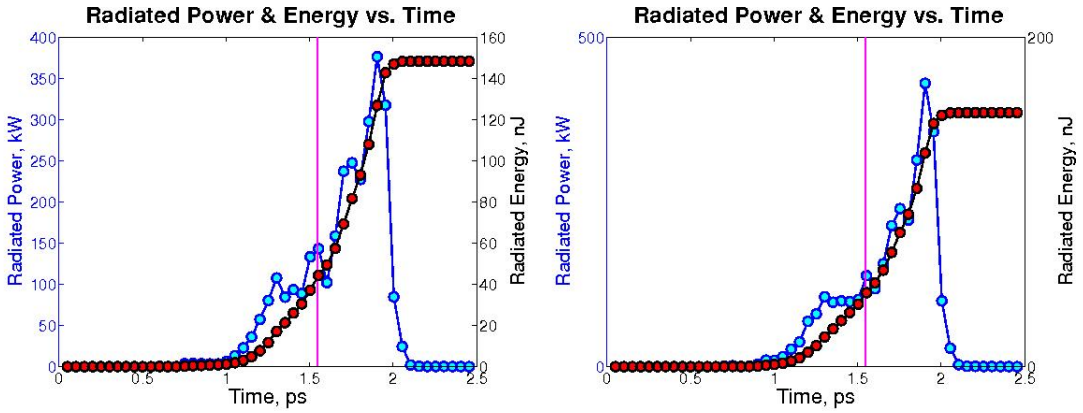


Figure 6.32: The time-evolution of the emitted power (blue) and total emitted radiation (red) vs. time for the $\alpha = 0.1$ simulations for (left) 0-degree and (right) 90-degree polarization.

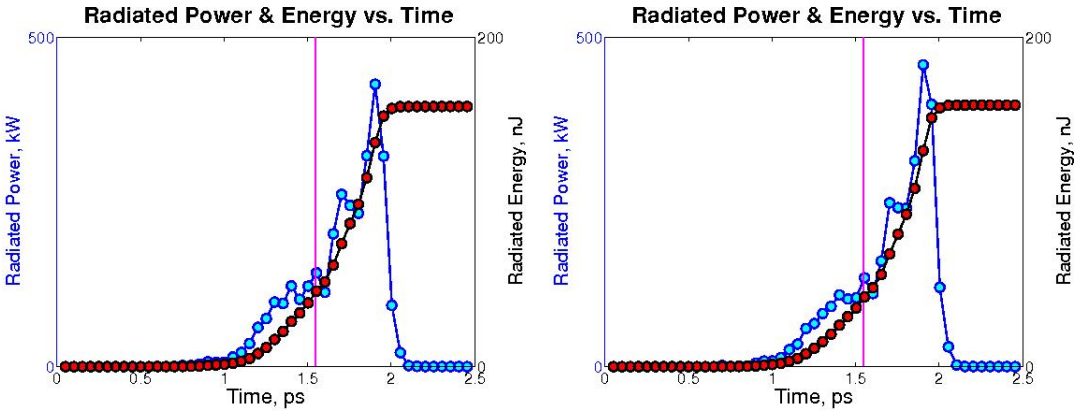


Figure 6.33: The time-evolution of the emitted power (blue) and total emitted radiation (red) vs. time for the $\alpha = 0.2$ simulations for (left) 0-degree and (right) 90-degree polarization.

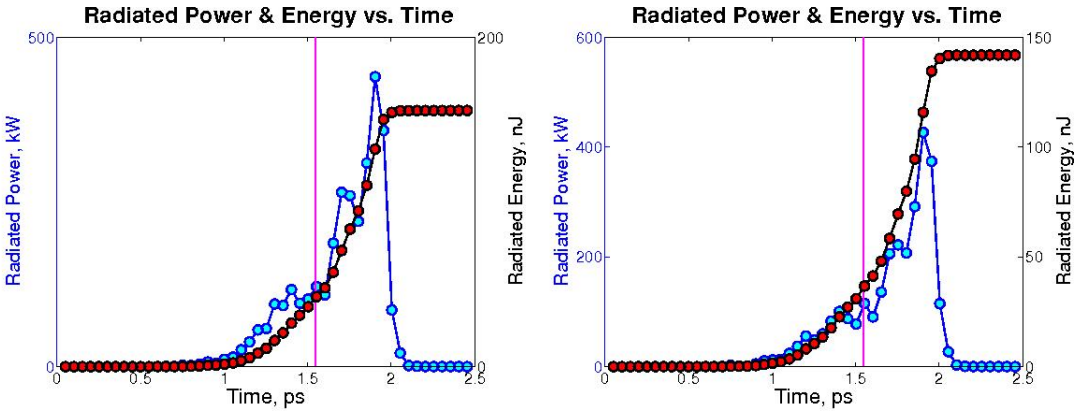


Figure 6.34: The time-evolution of the emitted power (blue) and total emitted radiation (red) vs. time for the $\alpha = 0.3$ simulations for (left) 0-degree and (right) 90-degree polarization.

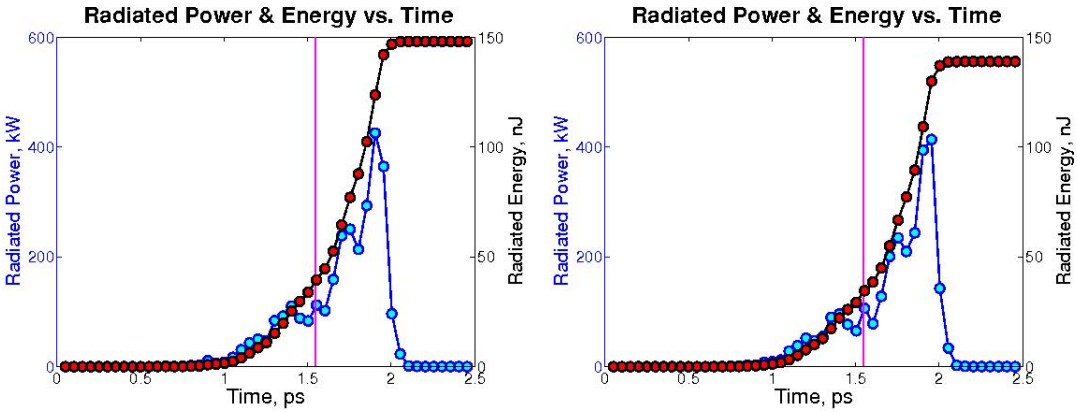


Figure 6.35: The time-evolution of the emitted power (blue) and total emitted radiation (red) vs. time for the $\alpha = 0.4$ simulations for (left) 0-degree and (right) 90-degree polarization.

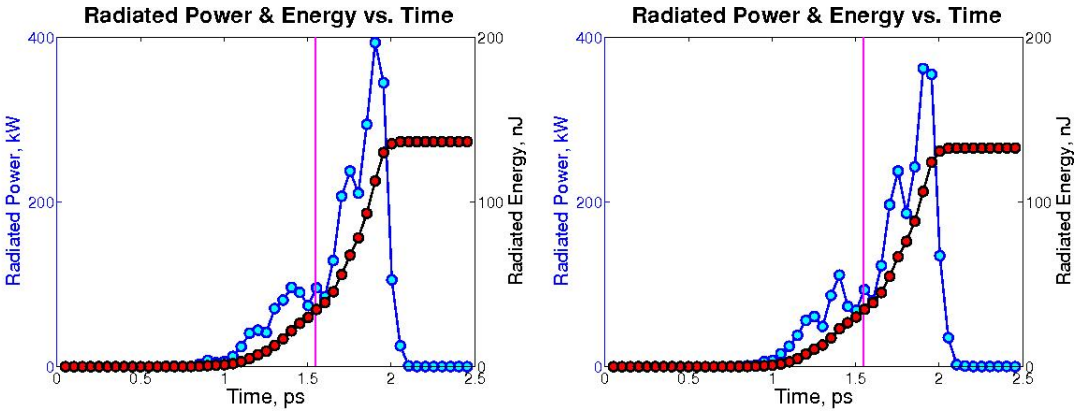


Figure 6.36: The time-evolution of the emitted power (blue) and total emitted radiation (red) vs. time for the $\alpha = 0.5$ simulations for (left) 0-degree and (right) 90-degree polarization.

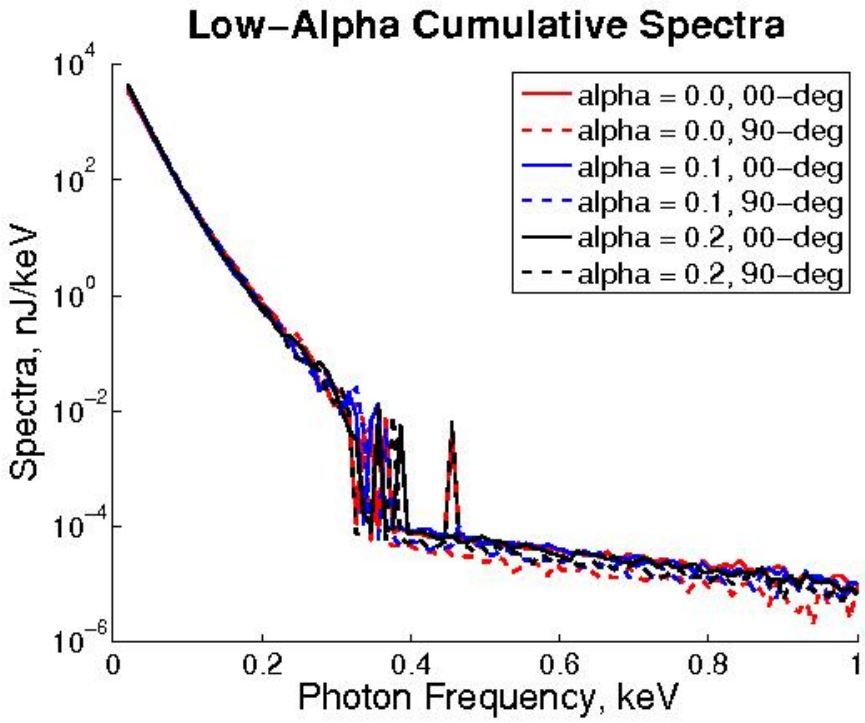


Figure 6.37: The logarithmic spectra for the coma simulations for $\alpha = 0.0, 0.1, \&0.2$

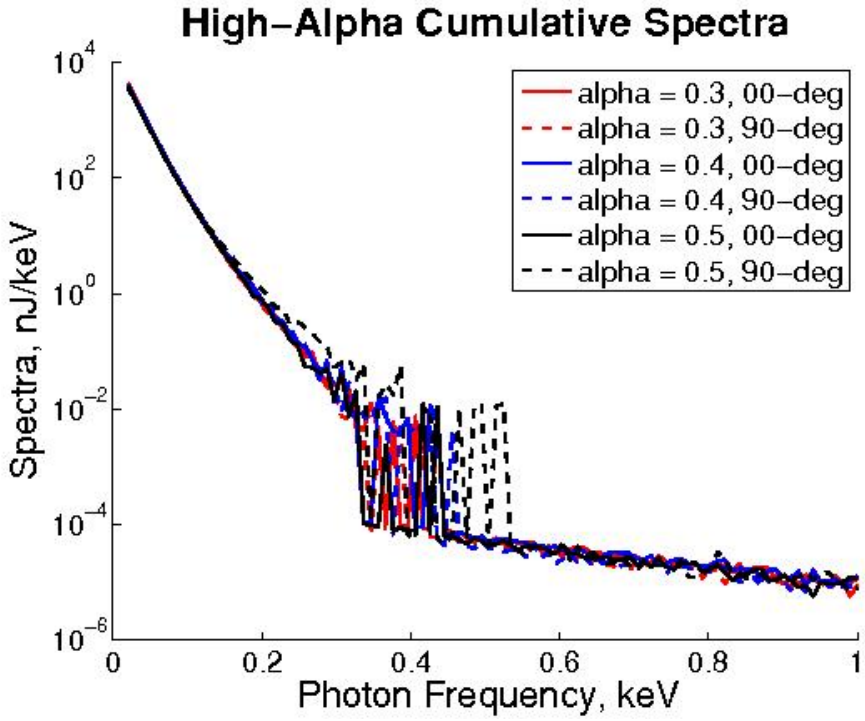


Figure 6.38: The logarithmic spectra for the coma simulations for $\alpha = 0.3, 0.4, \&0.5$

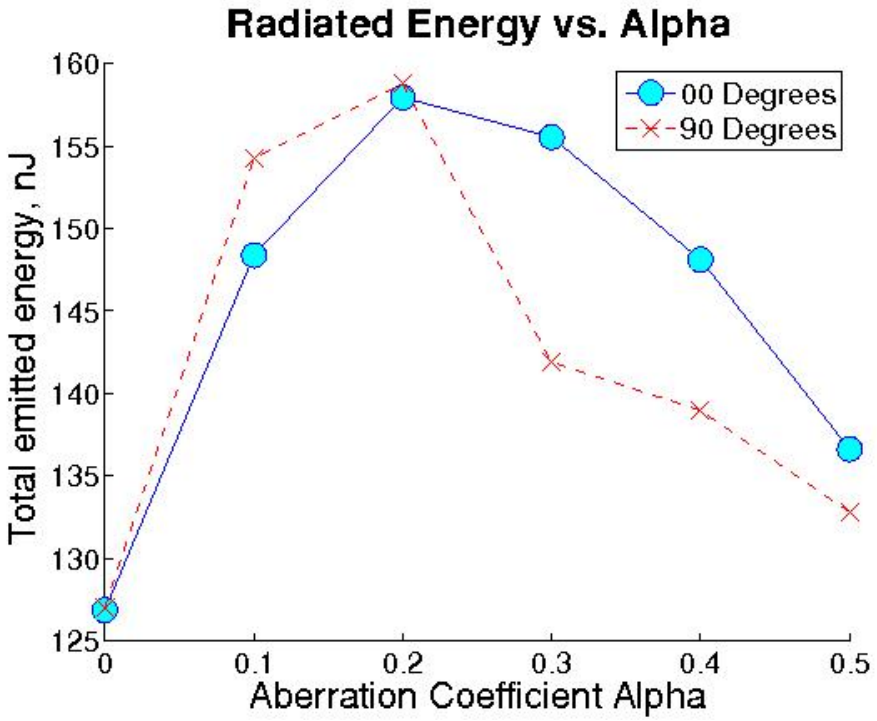


Figure 6.39: The total energy emitted produced by the simulation for the 0-degree (shown in blue) and 90-degree (shown in red) simulations..

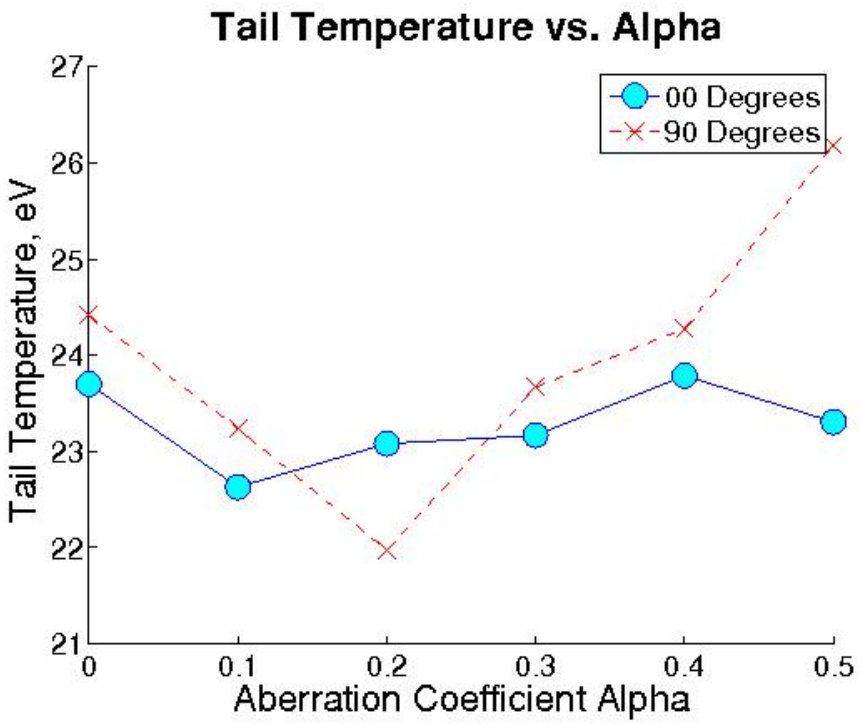


Figure 6.40: The temperature of the high-energy tail produced by the simulation for the 0-degree (shown in blue) and 90-degree (shown in red) simulations..

### 6.7.5 Radiation and Phase-Space Correlations

Both the electron energy/radiation frequency and electron trajectory radius-of-curvature/radiation frequency plots (shown in Figures 6.41 through 6.46) show consistent, relatively unchanged results as the severity of the coma is increased. The vast majority of the radiated energy is emitted by the high-energy electron beam, by electrons whose trajectories exhibit a spread of radii of curvatures. The highest frequency radiation is, unsurprisingly, emitted by the electrons whose trajectories have lower radii of curvatures.

For clarity, we show the radius of curvature/frequency correlation and electron energy/frequency correlation plots for both polarizations (i.e., four plots total) as a single figure for each value of $\alpha$ considered in the parameter sweep, as with the electron-phase space results.

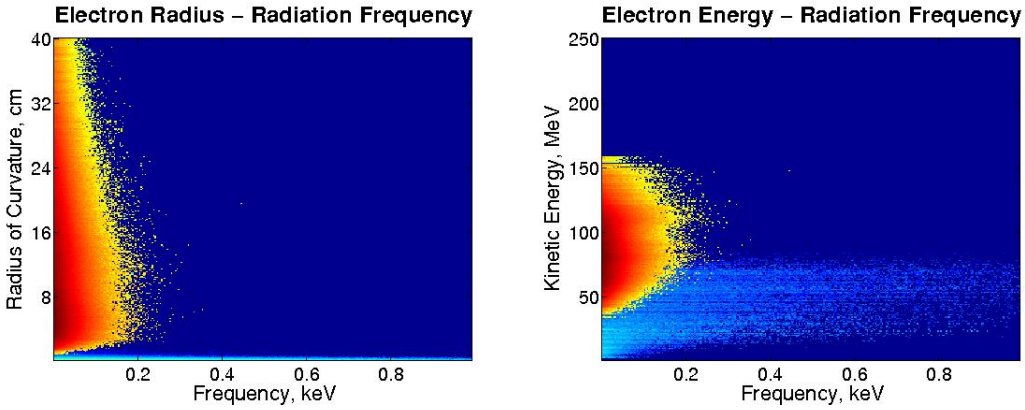


Figure 6.41: (Left) The correlation between the kinetic energy of the radiating electrons to the frequency of the emitted radiation and (right) the correlation between the radius of curvature of the radiating electron trajectories to the frequency of the emitted radiation for the $\alpha = 0.0$ case.

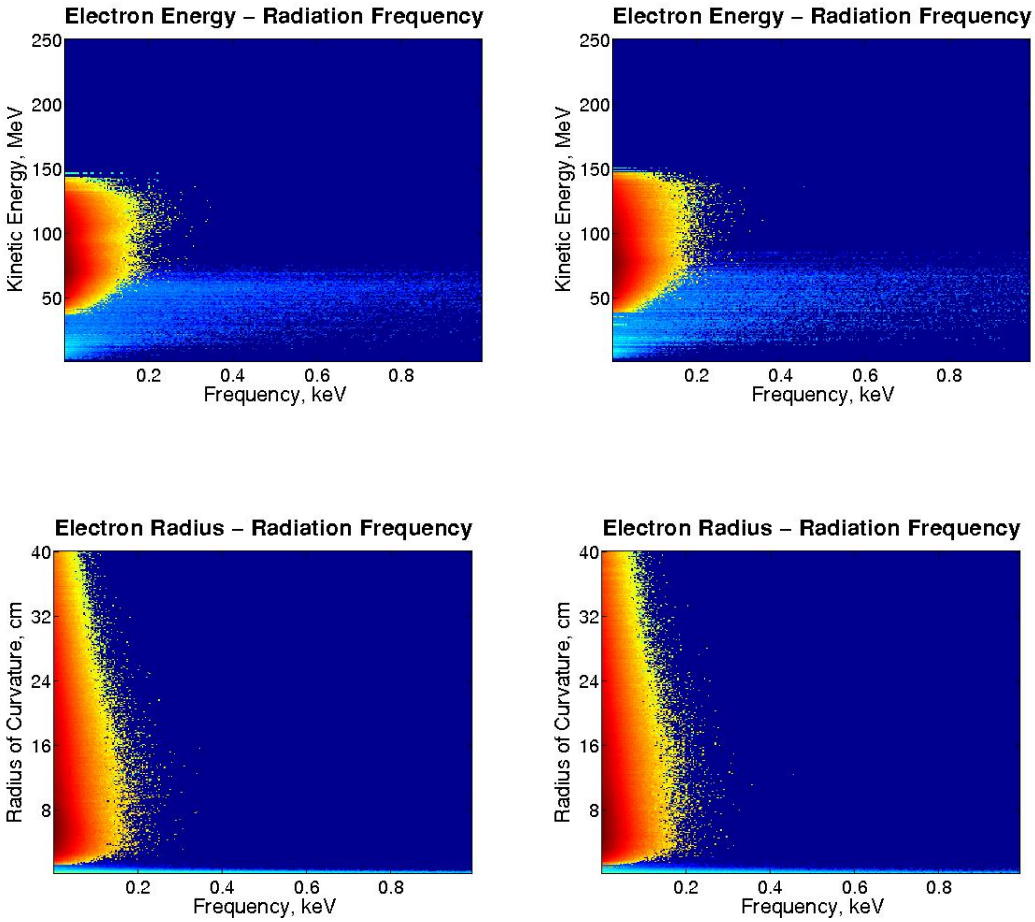


Figure 6.42: (Top) The correlation between the kinetic energy of the emitting electrons and the frequency of the emitted radiation and (bottom) the correlation between the radius of curvature of the emitting electrons' trajectories and the frequency of the emitted radiation for the $\alpha = 0.1$ simulation; the left-hand images are the 0-degree polarization images (where the directions of coma asymmetry and laser polarization are perpendicular), while the right-hand images are the 90-degree polarization images (where the directions of coma asymmetry and laser polarization are aligned)

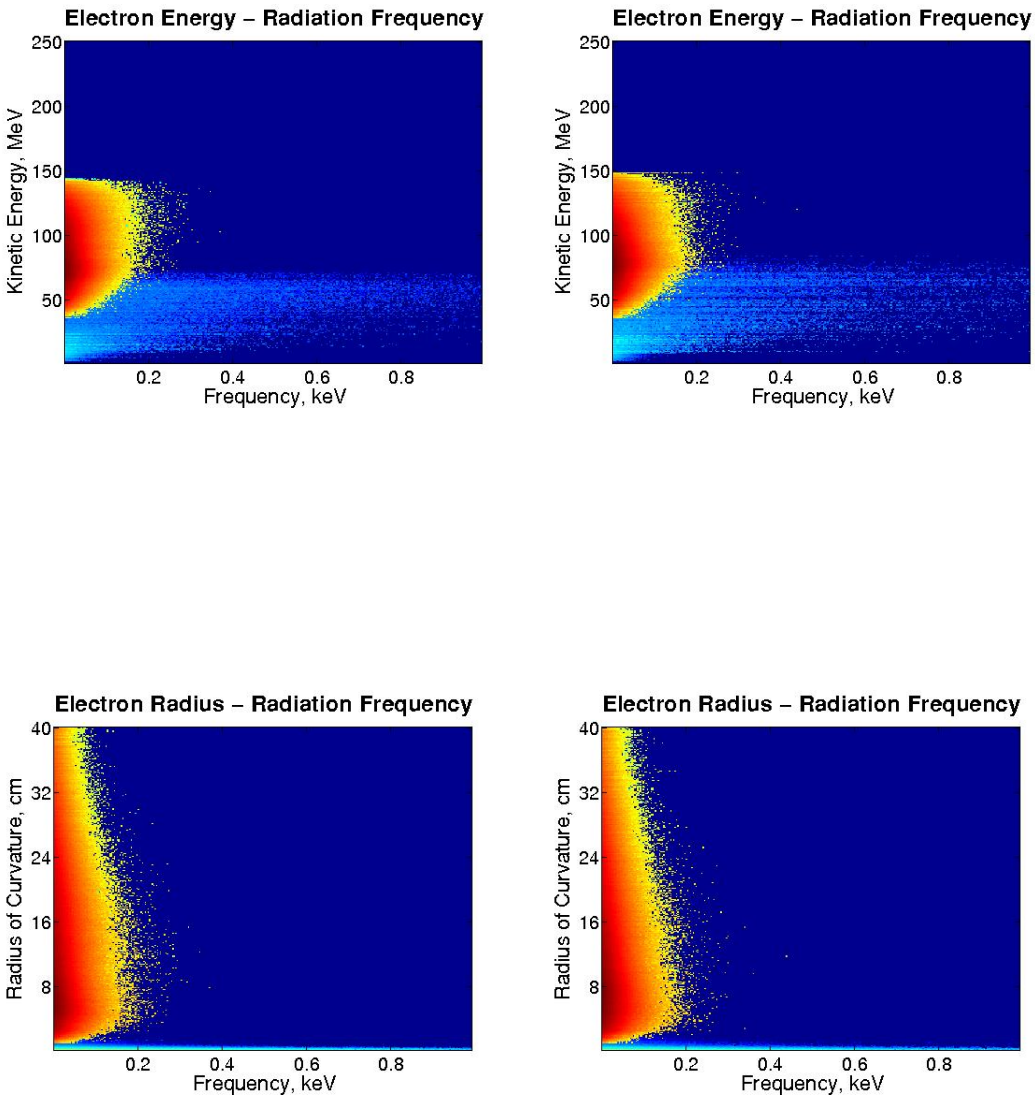


Figure 6.43: (Top) The correlation between the kinetic energy of the emitting electrons and the frequency of the emitted radiation and (bottom) the correlation between the radius of curvature of the emitting electrons' trajectories and the frequency of the emitted radiation for the $\alpha = 0.2$ simulation; the left-hand images are the 0-degree polarization images (where the directions of coma asymmetry and laser polarization are perpendicular), while the right-hand images are the 90-degree polarization images (where the directions of coma asymmetry and laser polarization are aligned)

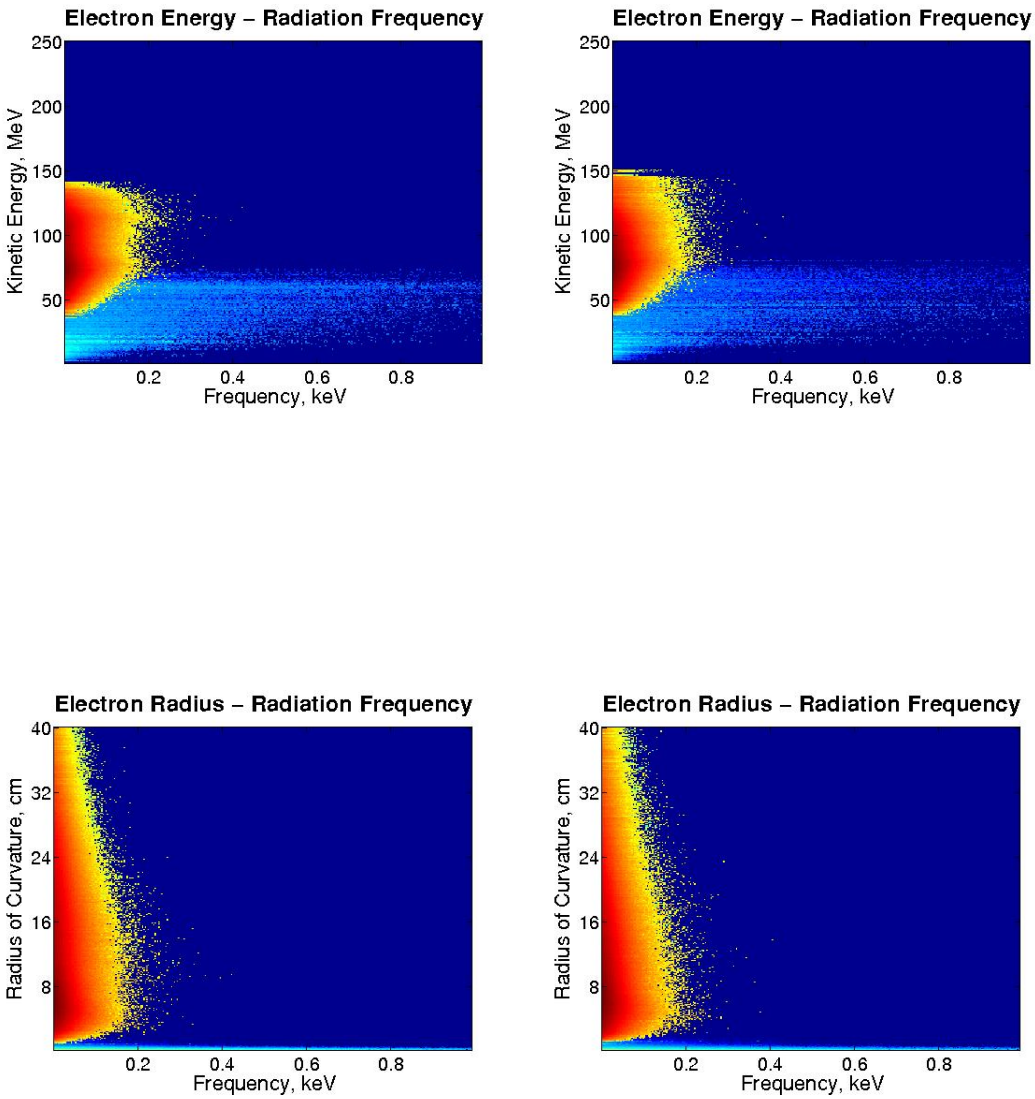


Figure 6.44: (Top) The correlation between the kinetic energy of the emitting electrons and the frequency of the emitted radiation and (bottom) the correlation between the radius of curvature of the emitting electrons' trajectories and the frequency of the emitted radiation for the $\alpha = 0.3$ simulation; the left-hand images are the 0-degree polarization images (where the directions of coma asymmetry and laser polarization are perpendicular), while the right-hand images are the 90-degree polarization images (where the directions of coma asymmetry and laser polarization are aligned)

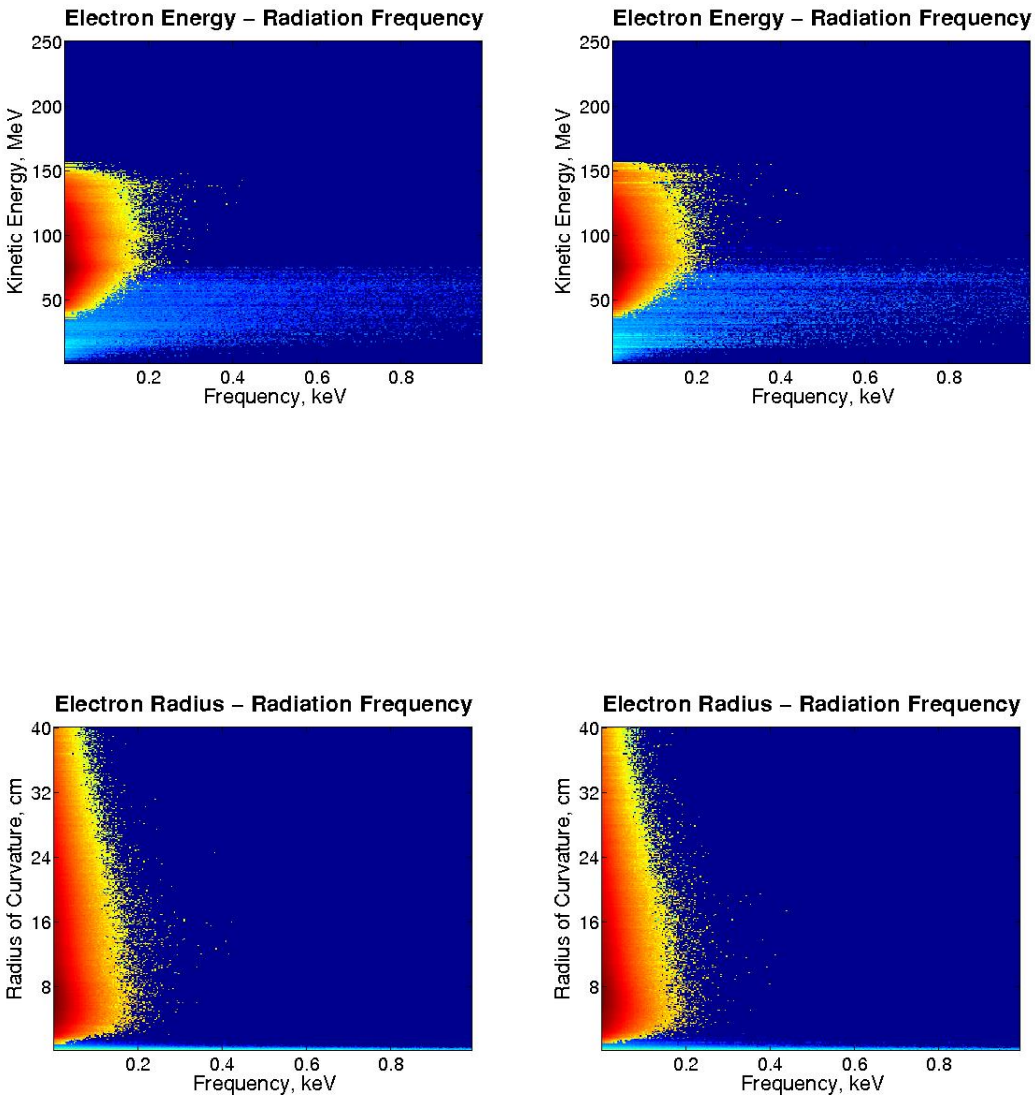


Figure 6.45: (Top) The correlation between the kinetic energy of the emitting electrons and the frequency of the emitted radiation and (bottom) the correlation between the radius of curvature of the emitting electrons' trajectories and the frequency of the emitted radiation for the $\alpha = 0.4$ simulation; the left-hand images are the 0-degree polarization images (where the directions of coma asymmetry and laser polarization are perpendicular), while the right-hand images are the 90-degree polarization images (where the directions of coma asymmetry and laser polarization are aligned)

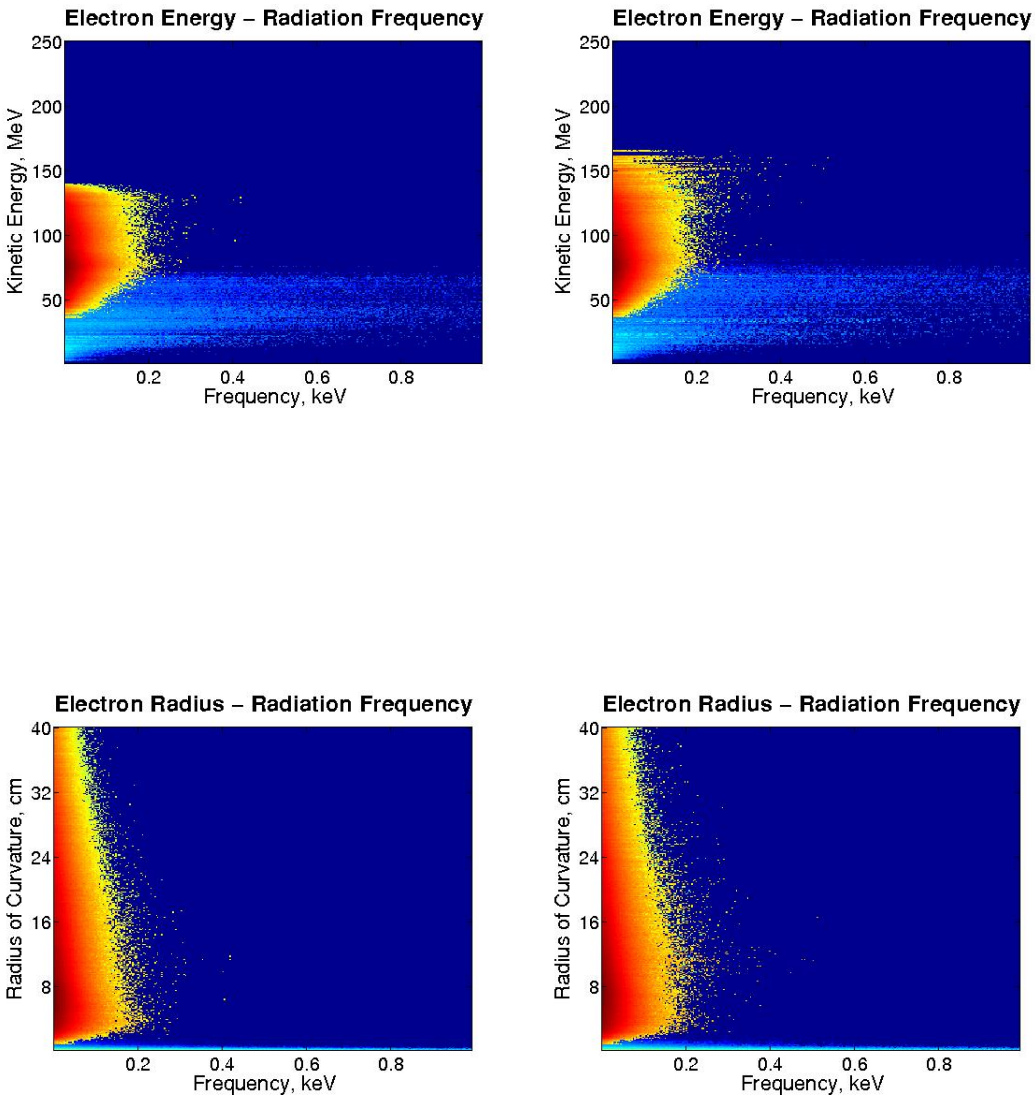


Figure 6.46: (Top) The correlation between the kinetic energy of the emitting electrons and the frequency of the emitted radiation and (bottom) the correlation between the radius of curvature of the emitting electrons' trajectories and the frequency of the emitted radiation for the $\alpha = 0.5$ simulation; the left-hand images are the 0-degree polarization images (where the directions of coma asymmetry and laser polarization are perpendicular), while the right-hand images are the 90-degree polarization images (where the directions of coma asymmetry and laser polarization are aligned)

# CHAPTER VII

# Summary, Conclusions, and Future Work

## 7.1 Summary

This dissertation presented the results from an array of computational studies of laser wake-field acceleration experiments. Specifically, the generation of synchrotron-like x-ray radiation via betatron motion, and the response of this radiation to various LWFA system parameters, was investigated.

An overview of the relevant theoretical concepts was presented. Basic plasma physics models were presented, along with more specific models regarding the physics laser wake-field acceleration. The physics of betatron motion in laser-wake-field accelerators was also discussed. An overview of several significant plasma optical phenomenon was presented. Finally, the generation of radiation by moving charge particles was also discussed.

An overview of the relevant computational methods was presented. Standard methods and concepts in computational electrodynamics are presented and discussed. An overview of the concepts and methodologies of particle-in-cell simulations was also presented. Finally, the particulars of OSIRIS 2.0's implementation of the PIC model was presented and discussed.

The particulars of the algorithm used to simulate the generation of radiation in this study was presented and discussed. Detailed discussions of the techniques used

were presented and discussed as well. Finally, the results of validation simulations of electrons undergoing simple cyclotron motion are presented and compared to the theory.

Results from using this algorithm to perform a number of computational parameters sweeps were presented and discussed. Parameter sweeps over the normalized laser vector potential $a_0$, electron plasma density $n_e$, and propagation distance $L$ were performed. Data regarding the electron phase-space properties, emitted radiation properties, and correlations between the emitting electron trajectories and radiation frequencies were presented and discussed.

Results from a computational parameter sweep of the impact of a comatic aberration in the driving laser on the performance of a LWFA system as a particle accelerator were presented and discussed. In addition to the electron beam properties, the properties of the emitted radiation were also presented and discussed. As before, data regarding the electron phase-space properties, emitted radiation properties, and correlations between the emitting electron trajectories and radiation frequencies were presented and discussed.

## 7.2 Conclusions

Validation simulations of the algorithm used showed excellent agreement with the theoretical models for cyclotron radiation across a wide range of electron energies $\gamma$ and radii of curvature $\rho$.

For the parameter sweep over the normalized laser vector potential $a_0$, both the total emitted energy and the tail temperature of the emitted spectrum showed excellent agreement with previously derived analytic scalings given by [[88]]. The total energy emitted scaled as $a_0^{9/2}$, in close agreement with the scalings. The tail temperature scaled roughly as $a_0^{5/2}$, however the calculated values of the tail temperature exhibited enough noise to prevent drawing absolute conclusions.

For the simulation used to effect a parameter sweep over the propagation length, it was observed that the majority of the energy radiation occurred after the system had passed the dephasing length, and coincided with a second period of acceleration that is most likely due to the electron beam re-entering the bulk plasma and driving the system into a beam-driven wake-field regime. It appears that the electron beam's betatron motion increases dramatically in this regime; this is hypothesized to be due to a hosing instability caused by the beam propagating through the bulk plasma.

For the parameter sweep over the plasma density $n_e$, both the total emitted energy and the tail temperature deviated sharply from the predicted analytic scalings given by [[88]]. Upon closer inspection, it appears that this deviation is caused by the fact that the majority of the radiation was emitted after the system passed twice the dephasing length; at this point, the beam re-enters the bulk plasma and is inferred to undergo a hosing instability. This effect appeared to dominate the emitted radiation in the simulations, yet was not considered in the derivation of the analytic scalings.

For the parameter sweep over the coma, the performance of the LWFA system as an electron accelerator showed a number of trends in response to the presence of a coma. One promising result was that neither the peak energy of the electron beam, nor the electron beams' energy, were significantly effected by the presence of even a severe coma, suggesting that in this regard, the LWFA is robust against the presence of a coma. However, noticeable differences between the beam emittance in the transverse and laser polarization directions were observed; these differences became magnified as the severity of the coma increased.

The most significant trend observed in the emitted radiation was in the total energy emitted, which increased significantly in the presence of a coma. However as the coma severity increased further, this effect reversed. The temperature of the high-energy tail was not found to vary significantly with the coma severity, when compared to the previously mentioned noise observed in the tail temperature calculation.

## 7.3 Future Work

The most significant finding of this dissertation is that the majority of betatron radiation occurs after the electron beam has passed the bubble regime. An analytic model of the electron beam propagation and betatron motion in this regime would provide key insight into this mechanism of radiation generation.

Significant fluctuations were consistently observed in the radiated power. Repeating the simulations multiple times to improve statistics would help determine whether or not these fluctuations are due to statistical noise or an underlying physical phenomenon.

For the sweep in $a_0$, a distinct transition from long-wavelength to short-wavelength betatron motion was observed as the normalized laser vector potential was increased. The high-frequency motion approached the sampling frequency, making it difficult to fully characterize this motion. Running these simulations with a higher temporal resolution would help determine the mechanism behind this shift in betatron wavelength.

Additionally, recall that the scalings for betatron motion in a laser wake-field accelerator given by [50], [2] are:

$$\omega_\beta = \frac{\omega_p}{\sqrt{2\gamma}}; \quad K = \gamma r_\beta \frac{\omega_\beta}{c}$$

A cursory analysis of the data according to this model suggests an $r_\beta$ of $\sim 1 - 10$ nanometers, which is substantially less than the motion observed in the simulation. However, consider the difference between the spatially averaged transverse electric field and magnetic fields alongside the electron density from the $\sim$ 20.3fs time frame in the $a_0 = 4.0$ simulation from the normalized laser vector potential sweep, as shown in Figure 7.1. The derivation of the previously-given equation was based on the trajectory of a single electron in an ion channel, such that the electron motion was

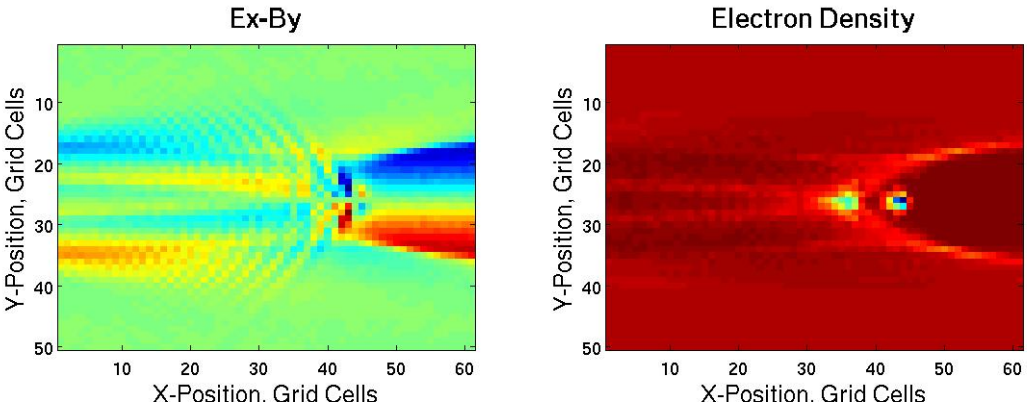


Figure 7.1: (Left) The transverse electric field and (right) the electron density for the $\sim 20.3$fs time frame in the $a_0 = 4.0$ simulation. The low resolution is due to a spatial-averaging algorithm used to reduce storage space.

governed by the external plasma fields. Figure 7.1 clearly shows that the fields generated by the electron beam are non-negligible, and in certain places even cause the Lorentz force to reverse direction. Clearly, the assumptions of the previously-given equation are violated, and new analytic scalings need to be derived.

In a broader sense, contemporary models of betatron motion (and the resulting radiation generation) in LWFA experiments assume a single driving mechanism: interaction between the electron beam and the fields of the laser wake, unperturbed by the presence of the electron beam. The results from the simulations presented in this dissertation strongly indicate that, instead, several distinct mechanisms can drive this motion: interaction between the electron beam and the unperturbed wake field, interaction between the electron beam and a wake field that is perturbed by the presence of the electron beam, direction interaction between the electron beam and the laser field, and hosing instabilities caused by the electron beam re-entering the bulk plasma.

Moreover, variations in basic LWFA parameters like normalized vector potential $a_0$, electron density $n_e$, and propagation length $L$ appear to cause the dominant mechanism of betatron motion to change. The observed changes in these parameters

involved increases or decreases within only a single order of magnitude. Analytical models of each of these regimes, and the transitions between them, would be of obvious utility when using LWFA to generate synchrotron-like radiation.

# APPENDICES

# APPENDIX A

# Theoretical Derivations

## A.1 One-Dimensional Derivation of the Laser Wake-Field

Initially, a comparatively simple calculation of the generation of a non-linear plasma wake in response to the propagation of a laser pulse can provide useful insight into the LWFA mechanism. We will derive a closed set of 5 equations that determine the evolution of the parameters $\gamma$ (the relativistic factor), $u_x$ (the electron velocity normalized to c), $\tilde{\phi}$ (the electrostatic potential normalized to $mc^2/e$), $a_y$ (the laser vector potential normalized to $mc^2/e$), and C$n_e$, the electron plasma density. These parameters define both the laser pulse and the plasma response in one dimension. The derivation begins with the relativistic Maxwell-Lorentz system of equations:

$$\frac{\partial \vec{p}}{\partial t} + \left(\vec{v} \cdot \vec{\nabla}\right) \vec{p} = -e \left[\vec{E} + \frac{1}{c}\left(\vec{v} \times \vec{B}\right)\right] \tag{A.1}$$

$$\vec{\nabla} \cdot \vec{E} = 4\pi \left(n_0 - n_e\right) \tag{A.2}$$

$$\vec{\nabla} \times \vec{E} = -\frac{1}{c}\frac{\partial \vec{B}}{\partial t} \tag{A.3}$$

$$\vec{\nabla} \times \vec{B} = -\frac{4\pi}{c} e n_e \vec{v} + \frac{1}{c}\frac{\partial \vec{E}}{\partial t} \tag{A.4}$$

$$\vec{\nabla} \cdot \vec{B} = 0 \tag{A.5}$$

We immediately assume a one-dimensional geometry, in the direction of laser propagation, with an arbitrary laser pulse defined by the vector potential:

$$\vec{A} = A_y \left(x - v_g t\right) \hat{y}$$

Under this assumption, we can calculate the electric and magnetic fields from the potentials:

$$\vec{E} = -\vec{\nabla}\phi - \frac{\partial \vec{A}}{\partial t} = -\frac{\partial \phi}{\partial x}\hat{x} - \left(\frac{\partial \phi}{\partial y} + \frac{\partial A_y}{\partial t}\right)\hat{y} - \frac{\partial \phi}{\partial z}\hat{z}$$

$$\vec{E} \approx -\frac{\partial \phi}{\partial x}\hat{x} - \frac{\partial A_y}{\partial t}\hat{y} - \frac{\partial \phi}{\partial z}\hat{z} \tag{A.6}$$

$$\vec{B} = \vec{\nabla} \times \vec{A} = -\frac{\partial A_y}{\partial z}\hat{x} + \frac{\partial A_y}{\partial x}\hat{z}$$

$$\vec{B} = \frac{\partial A_y}{\partial x}\hat{z} \tag{A.7}$$

Note that we have assumed that the electric field due to the scalar potential is negligible compared to the electric field due to the laser pulse in the expression for $\vec{E}$, and that the only contribution to $\vec{A}$ is from the laser in both expressions. We insert equations A.6 and A.7 into equation A.1 to find expressions for the components of

the electron momentum $\vec{p}$ in terms of $\vec{A}$, starting with the y-component:

$$\left[\frac{\partial}{\partial t} + \left(\vec{v}\cdot\vec{\nabla}\right)\right] p_y = \frac{dp_y}{dt} = -e\left[\vec{E} + \frac{1}{c}\left(\vec{v}\times\vec{B}\right)\right]_y = -e\left[E_y + \frac{1}{c}\left(v_z B_x - v_x B_z\right)\right]$$

$$\frac{dp_y}{dt} = -e\left[E_y - \frac{1}{c}\left(v_x B_z\right)\right] = -e\left[-\frac{1}{c}\frac{\partial A_y}{\partial t} - \frac{1}{c}\left(v_x\frac{\partial A_y}{\partial x}\right)\right] = \frac{e}{c}\left[\frac{\partial A_y}{\partial t} + \left(v_x\frac{\partial A_y}{\partial x}\right)\right]$$

$$\frac{dp_y}{dt} = \frac{e}{c}\left[\frac{\partial}{\partial t} + \left(v_x\frac{\partial}{\partial x}\right)\right] A_y = \frac{d}{dt}\left(\frac{e}{c}A_y\right)$$

Therefore, if there is no initial momentum in the y-direction, we may say:

$$p_y = \frac{e}{c}A_y \tag{A.8}$$

With equation A.8, we can derive the five equations of our closed set. For the first equation, we look at the x-component of equation A.1:

$$\left[\frac{\partial}{\partial t} + \left(\vec{v}\cdot\vec{\nabla}\right)\right] p_x = \frac{dp_x}{dt} = -e\left[\vec{E} + \frac{1}{c}\left(\vec{v}\times\vec{B}\right)\right]_x = -e\left[E_x + \frac{1}{c}\left(v_y B_z - v_z B_y\right)\right]$$

$$\frac{dp_x}{dt} = \frac{d}{dt}\left(\gamma m v_x\right) = -e\left[E_x + \frac{1}{c}\left(v_y B_z\right)\right] = -e\left[-\frac{\partial\phi}{\partial x} + \frac{1}{c}\left(v_y\frac{\partial A_y}{\partial x}\right)\right]$$

We use equation A.8 to find an expression for $v_y$ in terms of $A_y$, which we then insert into this expression:

$$p_y = \gamma m v_y = \frac{e}{c}A_y; v_y = \frac{eA_y}{\gamma m c}$$

$$\frac{d}{dt}\left(\gamma m v_x\right) = -e\left[-\frac{\partial\phi}{\partial x} + \frac{1}{c}\left(\frac{eA_y}{\gamma mc}\frac{\partial A_y}{\partial x}\right)\right] = \left[e\frac{\partial\phi}{\partial x} - \frac{e^2}{\gamma mc^2}\left(A_y\frac{\partial A_y}{\partial x}\right)\right]$$

$$m\frac{d}{dt}\left(\gamma v_x\right) = \left[e\frac{\partial\phi}{\partial x} - \frac{e^2}{2\gamma mc^2}\left(\frac{\partial A_y^2}{\partial x}\right)\right]$$

We define the following normalized quantities:

$$\tilde{\phi} \equiv \frac{e\phi}{mc^2}; \vec{a} \equiv \frac{e\vec{A}}{mc^2}; \vec{u} \equiv \frac{\vec{v}}{c} \tag{A.9}$$

Inserting equations A.9 into our expression for the x-component of the electron momentum yields:

$$mc\frac{d}{dt}\left(\gamma u_x\right) = \left[mc^2\frac{\partial\tilde{\phi}}{\partial x} - \frac{mc^2}{2\gamma}\left(\frac{\partial a_y^2}{\partial x}\right)\right]$$

$$\frac{d}{dt}\left(\gamma u_x\right) = c\left[\frac{\partial\tilde{\phi}}{\partial x} - \frac{1}{2\gamma}\left(\frac{\partial a_y^2}{\partial x}\right)\right] \tag{A.10}$$

Equation A.10 is the first expression in the closed, 1D LWFA set of equations. For the second equation, we consider the expression for the relativistic factor $\gamma$. If we assume that the velocity in the $\hat{z}$ direction (i.e., the direction orthogonal to both the direction of laser polarization and the direction of laser propagation) is negligible, $\gamma$ is given by:

$$\gamma \equiv \sqrt{\frac{1}{1-\frac{v^2}{c^2}}} = \sqrt{\frac{1}{1-\left(u_x^2+u_y^2\right)}}$$

We can rearrange this expression:

$$\frac{1}{\gamma^2} = 1 - u_x^2 - u_y^2; 1 + \gamma^2 u_y^2 = \gamma^2\left(1-u_x^2\right); \gamma^2 = \frac{1+\gamma^2 u_y^2}{1-u_x^2}$$

If we rewrite equation A.8 in terms of the normalized quantities defined in equations A.9, we find:

$$\gamma mcu_y = \frac{e}{c}\frac{mc^2}{e}a_y; \gamma u_y = a_y$$

and we may express $\gamma$ in terms of $a_y$ and $u_x$ to form the second expression of our closed set:

$$\gamma = \sqrt{\frac{1+a_y^2}{1-u_x^2}} \tag{A.11}$$

The third equation couples the electromagnetic field to the plasma density response, and begins with Ampere's law (equation A.4):

$$\vec{\nabla} \times \vec{B} = -\frac{4\pi}{c}en_e\vec{v} + \frac{1}{c}\frac{\partial \vec{E}}{\partial t}$$

where we substitute in the expressions for the fields $\vec{E}$ and $\vec{B}$ in terms of the potentials $\phi$ and $\vec{A}$, using the Coulomb gauge:

$$\vec{E} = -\vec{\nabla}\phi - \frac{\partial \vec{A}}{\partial t}; \vec{B} = \vec{\nabla} \times \vec{A}; \vec{\nabla} \cdot \vec{A} = 0$$

$$\vec{\nabla} \times \left(\vec{\nabla} \times \vec{A}\right) = -\frac{4\pi}{c}en_e\vec{v} + \frac{1}{c}\frac{\partial}{\partial t}\left(-\vec{\nabla}\phi - \frac{\partial \vec{A}}{\partial t}\right)$$

$$\vec{\nabla}\left(\vec{\nabla} \cdot \vec{A}\right) - \vec{\nabla}^2\vec{A} = -\frac{4\pi}{c}en_e\vec{v} - \frac{1}{c}\vec{\nabla}\frac{\partial \phi}{\partial t} - \frac{1}{c^2}\frac{\partial^2 \vec{A}}{\partial t^2}$$

$$\frac{1}{c^2}\frac{\partial^2 \vec{A}}{\partial t^2} - \vec{\nabla}^2\vec{A} = -\frac{4\pi}{c}en_e\vec{v} - \frac{1}{c}\vec{\nabla}\frac{\partial \phi}{\partial t}$$

We consider the $\hat{y}$-component of this equation (i.e., the direction of laser polarization); we may assume that the displacement current is negligible compared to the plasma current in this direction.

$$\frac{1}{c^2}\left(\frac{\partial^2 A_y}{\partial t^2} - \vec{\nabla}^2 A_y\right) = -\frac{4\pi}{c} e n_e v_y$$

We express this equation in terms of the normalized quantities defined in equations A.9:

$$\left(\frac{\partial^2 a_y}{\partial t^2} - c^2\vec{\nabla}^2 a_y\right) = \frac{ec}{m}\frac{4\pi}{c} e n_e u_y = -\frac{4\pi e^2 n_e}{m} u_y$$

We rewrite the electron plasma density $n_e$ as a fraction, n, of the bulk plasma density $n_0$, such that $n = n_e/n_0$, and immediately identify the electron plasma frequency:

$$\left(\frac{\partial^2 a_y}{\partial t^2} - c^2\vec{\nabla}^2 a_y\right) = -\frac{4\pi e^2 n_0}{m} n u_y = -\omega_{pe}^2 n u_y$$

Finally recalling that $\gamma u_y = a_y$, we have our third equation, coupling the electromagnetic wave to the plasma density response:

$$\left(\frac{\partial^2 a_y}{\partial t^2} - c^2\vec{\nabla}^2 a_y\right) = -\omega_{pe}^2 n \frac{a_y}{\gamma} \tag{A.12}$$

For the fourth equation, we take the well-known fluid continuity equation:

$$\frac{\partial n_e}{\partial t} + \nabla \cdot (n_e \vec{v}) = 0$$

and rewrite it in one dimension, and in terms of the normalized quantities from equations A.9 and in terms of $n = n_e/n_0$:

$$\frac{\partial n}{\partial t} + c\frac{\partial}{\partial x}(n u_x) = 0 \tag{A.13}$$

For the fifth and final equation, we begin with Poisson's equation, and also rewrite it in one dimension, and in terms of our normalized quantities:

$$-\vec{\nabla}^2\phi = 4\pi e\left(n_0 - n_e\right)$$

$$\frac{mc^2}{e}\frac{\partial^2\tilde{\phi}}{\partial x^2} = 4\pi e n_0\left(n-1\right)$$

$$\frac{\partial^2\tilde{\phi}}{\partial x^2} = \frac{4\pi n_0 e^2}{mc^2}\left(n-1\right) = \frac{4\pi n_0 e^2}{m}\frac{1}{c^2}\left(n-1\right)$$

$$\frac{\partial^2\tilde{\phi}}{\partial x^2} = \frac{\omega_{pe}^2}{c^2}\left(n-1\right) = k_{pe}^2\left(n-1\right) \tag{A.14}$$

In summary, we have a closed set of five equations for the five variables n, $u_x$, $\gamma$, $a_y$, and $\phi$:

$$\frac{d}{dt}\left(\gamma u_x\right) = c\left[\frac{\partial\tilde{\phi}}{\partial x} - \frac{1}{2\gamma}\left(\frac{\partial a_y^2}{\partial x}\right)\right]; \gamma = \sqrt{\frac{1+a_y^2}{1-u_x^2}}$$

$$\left(\frac{\partial^2 a_y}{\partial t^2} - c^2\vec{\nabla}^2 a_y\right) = -\omega_{pe}^2 n\frac{a_y}{\gamma}; \frac{\partial n}{\partial t} + c\frac{\partial}{\partial x}\left(n u_x\right) = 0; \frac{\partial^2\tilde{\phi}}{\partial x^2} = k_{pe}^2\left(1-n\right) \tag{A.15}$$

To extract a useful model from these equations, we employ a coordinate transformation, boosting to a comoving frame with an arbitrary group velocity $v_g$; the variables used in this frame, $\tau$ and $\xi$, are defined by:

$$\tau \equiv t; \xi \equiv x - v_g t \tag{A.16}$$

Partial derivatives in terms of these variables are therefore given by:

$$\frac{\partial}{\partial x} = \frac{\partial}{\partial \xi}; \frac{\partial}{\partial t} = \frac{\partial}{\partial \tau} - v_g \frac{\partial}{\partial \xi}$$

We take the first of equations A.15 and rewrite it according to equations A.16, starting with the left-hand side:

$$\frac{d}{dt}\left(\gamma u_x\right) = \left(\frac{\partial}{\partial t} + c u_x \frac{\partial}{\partial x}\right) \gamma u_x = \left(\frac{\partial}{\partial \tau} - v_g \frac{\partial}{\partial \xi} + c u_x \frac{\partial}{\partial \xi}\right) \gamma u_x$$

then the right-hand side:

$$c\left[\frac{\partial \tilde{\phi}}{\partial x} - \frac{1}{2\gamma}\left(\frac{\partial a_y^2}{\partial x}\right)\right] = c\frac{\partial \tilde{\phi}}{\partial \xi} - \frac{c}{2\gamma}\left(\frac{\partial a_y^2}{\partial \xi}\right)$$

giving:

$$\frac{\partial}{\partial \tau}\left(\gamma u_x\right) - v_g \frac{\partial}{\partial \xi}\left(\gamma u_x\right) + c u_x \frac{\partial}{\partial \xi}\left(\gamma u_x\right) = c\frac{\partial \tilde{\phi}}{\partial \xi} - \frac{c}{2\gamma}\left(\frac{\partial a_y^2}{\partial \xi}\right)$$

$$\frac{1}{c}\frac{\partial}{\partial \tau}\left(\gamma u_x\right) - \frac{v_g}{c}\frac{\partial}{\partial \xi}\left(\gamma u_x\right) + u_x \frac{\partial}{\partial \xi}\left(\gamma u_x\right) - \frac{\partial \tilde{\phi}}{\partial \xi} = -\frac{1}{2\gamma}\left(\frac{\partial a_y^2}{\partial \xi}\right)$$

We may rewrite the right-hand side of this expression by using the second of equations A.15:

$$\frac{1 + a_y^2}{1 - u_x^2} = \gamma^2; a_y^2 = \gamma^2\left(1 - u_x^2\right) - 1$$

$$\frac{\partial a_y^2}{\partial \xi} = \frac{\partial}{\partial \xi}\left[\gamma^2\left(1 - u_x^2\right) - 1\right] = \frac{\partial \gamma^2}{\partial \xi} - \frac{\partial}{\partial \xi}\left(\gamma^2 u_x^2\right) = 2\gamma\frac{\partial \gamma}{\partial \xi} - 2u_x^2\gamma\frac{\partial \gamma}{\partial \xi} - 2\gamma^2 u_x\frac{\partial u_x}{\partial \xi}$$

We therefore have:

$$\frac{1}{c}\frac{\partial}{\partial\tau}\left(\gamma u_x\right) - \frac{v_g}{c}\frac{\partial}{\partial\xi}\left(\gamma u_x\right) + u_x\frac{\partial}{\partial\xi}\left(\gamma u_x\right) - \frac{\partial\tilde{\phi}}{\partial\xi} = -\frac{\partial\gamma}{\partial\xi} + u_x^2\frac{\partial\gamma}{\partial\xi} + \gamma u_x\frac{\partial u_x}{\partial\xi}$$

$$\frac{1}{c}\frac{\partial}{\partial\tau}\left(\gamma u_x\right) = \frac{v_g}{c}\frac{\partial}{\partial\xi}\left(\gamma u_x\right) - u_x\frac{\partial}{\partial\xi}\left(\gamma u_x\right) + \frac{\partial\tilde{\phi}}{\partial\xi} - \frac{\partial\gamma}{\partial\xi} + u_x\frac{\partial}{\partial\xi}\left(\gamma u_x\right)$$

$$\frac{1}{c}\frac{\partial}{\partial\tau}\left(\gamma u_x\right) = \frac{\partial}{\partial\xi}\left[\phi - \gamma\left(1 - \frac{v_g u_x}{c}\right)\right] \tag{A.17}$$

Equation A.17 is, of course, equation A.10 boosted into the comoving frame defined by equations A.16. We repeat this process for the continuity equation, equation A.13:

$$\frac{\partial n}{\partial t} = -c\frac{\partial}{\partial x}\left(n u_x\right)$$

$$\left(\frac{\partial}{\partial\tau} - v_g\frac{\partial}{\partial\xi}\right)n = -c\frac{\partial}{\partial\xi}\left(n u_x\right)$$

$$\frac{\partial n}{\partial\tau} = v_g\frac{\partial n}{\partial\xi} - c\frac{\partial}{\partial\xi}\left(n u_x\right) = \frac{\partial}{\partial\xi}\left[n\left(v_g - c u_x\right)\right]$$

$$\frac{1}{c}\frac{\partial n}{\partial\tau} = \frac{\partial}{\partial\xi}\left[n\left(\frac{v_g}{c} - u_x\right)\right] \tag{A.18}$$

Equation A.18 is equation A.13 boosted into the comoving frame defined by equations A.16. At this point, we employ the quasi-static approximation (QSA), which says that, in this comoving frame, the characteristic time of the pulse evolution, in $\tau$, is

much longer than the period of the laser pulse. Effectively, the QSA lets us set:

$$\frac{\partial}{\partial \tau} = 0$$

when compared with derivatives with respect to $\xi$. We first apply this approximation to equation A.17 and integrate:

$$\frac{\partial}{\partial \xi}\left[\phi - \gamma\left(1 - \frac{v_g u_x}{c}\right)\right] = 0$$

$$\phi - \gamma\left(1 - \frac{v_g u_x}{c}\right) = const$$

By noting that, as $\xi$ goes to $\infty$, $u_x = 0$, $\phi = 0$, and $\gamma = 1$ (i.e. noting that, ahead of the pulse, there is no plasma wave), we find that the constant of integration must equal -1:

$$\phi - \gamma\left(1 - \frac{v_g u_x}{c}\right) = -1$$

Similarly, we apply the QSA to equation A.18 and integrate:

$$\frac{\partial}{\partial \xi}\left[n\left(\frac{v_g}{c} - u_x\right)\right] = 0$$

$$n\left(\frac{v_g}{c} - u_x\right) = const$$

Again, noting that, as $\xi$ goes to $\infty$ (i. e., ahead of the pulse), $u_x$ goes to 0 and the density fraction n must go to 1, we find that the constant of integration must equal

$v_g/c$:

$$n\left(\frac{v_g}{c} - u_x\right) = \frac{v_g}{c}$$

For clarity, we define $\beta_g \equiv v_g/c$, and we have:

$$\phi - \gamma\left(1 - \beta_g u_x\right) + 1 = 0 \tag{A.19}$$

$$n = \frac{\beta_g}{\beta_g - u_x} \tag{A.20}$$

Together with equation A.11:

$$\gamma = \sqrt{\frac{1 + a_y^2}{1 - u_x^2}}$$

and the Poisson equation (equation A.14) rewritten in the comoving coordinates:

$$\frac{\partial^2 \tilde{\phi}}{\partial \xi^2} = k_{pe}^2\left(n - 1\right) \tag{A.21}$$

equations A.19 and A.20 form a set of 3 algebraic relations and one differential equation which define the non-linear plasma response to a laser pulse, under the QSA in a frame moving with group velocity $v_g$. These equations can be further simplified through algebraic manipulations, until we have expressions for $\gamma$, $u_x$, and n exclusively as functions of $\phi$ and $a_y$. We begin with equation A.19:

$$\phi + 1 = \gamma\left(1 - \beta_g u_x\right)$$

$$\left(\phi + 1\right)^2 = \gamma^2\left(1 - \beta_g u_x\right)^2 = \gamma^2\left(1 - 2\beta_g u_x + \beta_g^2 u_x^2\right) = \gamma^2\left[2\left(1 - \beta_g u_x\right) + \beta_g^2 u_x^2 - 1\right]$$

We may eliminate $u_x$ in this expression by rearranging equations A.19 and A.11:

$$\gamma\left(1-\beta_g u_x\right)=\phi+1; 1-\beta_g u_x=\frac{\phi+1}{\gamma}$$

$$\gamma^2=\frac{1+a_y^2}{1-u_x^2}; 1-u_x^2=\frac{1+a_y^2}{\gamma^2}; u_x^2=1-\frac{1+a_y^2}{\gamma^2}$$

$$\left(\phi+1\right)^2=\gamma^2\left[2\left(1-\beta_g u_x\right)+\beta_g^2 u_x^2-1\right]=\gamma^2\left[2\left(\frac{\phi+1}{\gamma}\right)+\beta_g^2\left(1-\frac{1+a_y^2}{\gamma^2}\right)-1\right]$$

$$\left(\phi+1\right)^2=\gamma^2\left[2\left(\frac{\phi+1}{\gamma}\right)+\beta_g^2-\beta_g^2\frac{1+a_y^2}{\gamma^2}-1\right]$$

$$\left(\phi+1\right)^2=2\gamma\left(\phi+1\right)+\beta_g^2\gamma^2-\beta_g^2\left(1+a_y^2\right)-\gamma^2=2\gamma\left(\phi+1\right)-\beta_g^2\left(1+a_y^2\right)-\gamma^2\left(1-\beta_g^2\right)$$

We define the parameter $\gamma_g$:

$$\gamma_g=\sqrt{\frac{1}{1-\beta_g^2}}$$

such that:

$$1=\frac{2\gamma}{\phi+1}-\frac{\beta_g^2\left(1+a_y^2\right)}{\left(\phi+1\right)^2}-\frac{\gamma^2}{\gamma_g^2\left(\phi+1\right)^2}$$

$$\frac{\gamma_g^2+1-\gamma_g^2}{\gamma_g^2}=\frac{2\gamma}{\gamma_g^2\left(\phi+1\right)}-\frac{\beta_g^2\left(1+a_y^2\right)}{\gamma_g^2\left(\phi+1\right)^2}-\frac{\gamma^2}{\gamma_g^4\left(\phi+1\right)^2}$$

$$\frac{\gamma^2}{\gamma_g^4\left(\phi+1\right)^2}-\frac{2\gamma}{\gamma_g^2\left(\phi+1\right)}+1=\frac{\gamma_g^2-1}{\gamma_g^2}-\frac{\beta_g^2\left(1+a_y^2\right)}{\gamma_g^2\left(\phi+1\right)^2}$$

$$\left(1-\frac{\gamma}{\gamma_g^2\left(\phi+1\right)}\right)^2=\beta_g^2-\frac{\beta_g^2\left(1+a_y^2\right)}{\gamma_g^2\left(\phi+1\right)^2}$$

$$1-\frac{\gamma}{\gamma_g^2\left(\phi+1\right)}=\beta_g\sqrt{1-\frac{\left(1+a_y^2\right)}{\gamma_g^2\left(\phi+1\right)^2}}$$

$$\gamma=\gamma_g^2\left(\phi+1\right)\left[1-\beta_g\sqrt{1-\frac{\left(1+a_y^2\right)}{\gamma_g^2\left(\phi+1\right)^2}}\right]$$

For simplicity, we define:

$$\psi\equiv\sqrt{1-\frac{\left(1+a_y^2\right)}{\gamma_g^2\left(\phi+1\right)^2}} \tag{A.22}$$

such that $\gamma$, expressed as a function of $a_y$ and $\psi$, is given by:

$$\gamma=\gamma_g^2\left(\phi+1\right)\left(1-\beta_g\psi\right) \tag{A.23}$$

We may find a similar expression for $u_x$; we again begin with equation A.19; rearranging to solve for $u_x$, and using equation A.23 to cancel out $\gamma$ and $\phi$:

$$\phi+1=\gamma\left(1-\beta_g u_x\right)$$

$$u_x=\frac{1}{\beta_g}\left(1-\frac{\phi+1}{\gamma}\right)$$

$$u_x = \frac{1}{\beta_g}\left[1 - \frac{1}{\gamma_g^2\left(1-\beta_g\psi\right)}\right] = \frac{1}{\beta_g}\left[\frac{\left(1-\beta_g\psi\right) - \left(1-\beta_g^2\right)}{\left(1-\beta_g\psi\right)}\right]$$

$$u_x = \frac{\beta_g - \psi}{\left(1-\beta_g\psi\right)} \tag{A.24}$$

Equation A.24 is $u_x$ expressed as a function of $a_y$ and $\psi$; we may insert this expression into equation A.20 to find the density as a function of $a_y$ and $\psi$:

$$n = \frac{\beta_g}{\beta_g - u_x} = \frac{\beta_g}{\beta_g - \frac{\beta_g-\psi}{\left(1-\beta_g\psi\right)}} = \frac{\beta_g\left(1-\beta_g\psi\right)}{\beta_g\left(1-\beta_g\psi\right) - \beta_g + \psi} = \frac{\beta_g\left(1-\beta_g\psi\right)}{\psi\left(1-\beta_g^2\right)}$$

$$n = \beta_g\gamma_g^2\left(\frac{1}{\psi} - \beta_g\right) \tag{A.25}$$

We can take equation A.25 and use it to eliminate n in the Poisson equation (equation A.21:

$$\frac{\partial^2\tilde{\phi}}{\partial\xi^2} = k_{pe}^2\left(n-1\right) = k_{pe}^2\left[\beta_g\gamma_g^2\left(\frac{1}{\psi} - \beta_g\right) - 1\right] = k_{pe}^2\gamma_g^2\left(\frac{\beta_g}{\psi} - \beta_g^2 \ - \frac{1}{\gamma_g^2}\right)$$

$$\frac{\partial^2\tilde{\phi}}{\partial\xi^2} = k_{pe}^2\gamma_g^2\left[\frac{\beta_g}{\psi} - \beta_g^2 \ - \left(1-\beta_g^2\right)\right] = k_{pe}^2\gamma_g^2\left(\frac{\beta_g}{\psi} - 1\right)$$

Finally, we have a differential equation for $\tilde{\phi}$ in terms of $a_y$:

$$\frac{\partial^2\tilde{\phi}}{\partial\xi^2} = k_{pe}^2\gamma_g^2\left(\frac{\beta_g\left(1+\tilde{\phi}\right)}{\sqrt{\left(1+\tilde{\phi}\right)^2 - \gamma_g^{-2}\left(1+a_y^2\right)}} - 1\right) \tag{A.26}$$

which, together with equations A.22, A.23, A.24, and A.25:

$$\psi \equiv \sqrt{1 - \frac{\left(1 + a_y^2\right)}{\gamma_g^2 \left(\tilde{\phi} + 1\right)^2}};\ \gamma = \gamma_g^2 \left(\tilde{\phi} + 1\right)\left(1 - \beta_g \psi\right)$$

$$u_x = \frac{\beta_g - \psi}{\left(1 - \beta_g \psi\right)};\ n = \beta_g \gamma_g^2 \left(\frac{1}{\psi} - \beta_g\right)$$

provides a set of 4 algebraic equations and 1 differential equation that can be solved to find the non-linear one-dimensional response of a plasma to a propagating laser pulse. Equation A.26 can be solved numerically for an arbitrary $a_y\left(\xi, \tau\right)$. For a laser pulse with a Gaussian time envelope with the following parameters:

1. Peak laser field $a_{y0} = 5.0$
2. Bulk plasma density $n_0 = 0.01 n_{crit}$
3. Group velocity $\beta_g = 0.99$
4. Pulse spread $\sigma = 5\lambda_{Laser}$

the plasma response to the laser is shown in figures A.1 and A.2. It is immediately apparent that in this nonlinear wake, highly energetic electrons (shown by the peaks in $\gamma$ in figure A.1 and in $n_e/n_{crit}$ in figure A.2) co-propagate with the wake-field structure, gaining energy from the electrostatic potential shown in figure A.1.

Insight into the salient characteristics of the system can be gained by varying the fundamental system parameters and observing the response. If the peak laser potential $a_{y0}$ is reduced from 5.0 to 1.0, the wake structure is much more linear, as shown in figures A.3 and A.4. The wake response is also severely reduced if the pulse length is increased from $\sigma = 5\lambda_{Laser}$ to $\sigma = 10\lambda_{Laser}$ without varying $a_{y0}$, as shown in figures

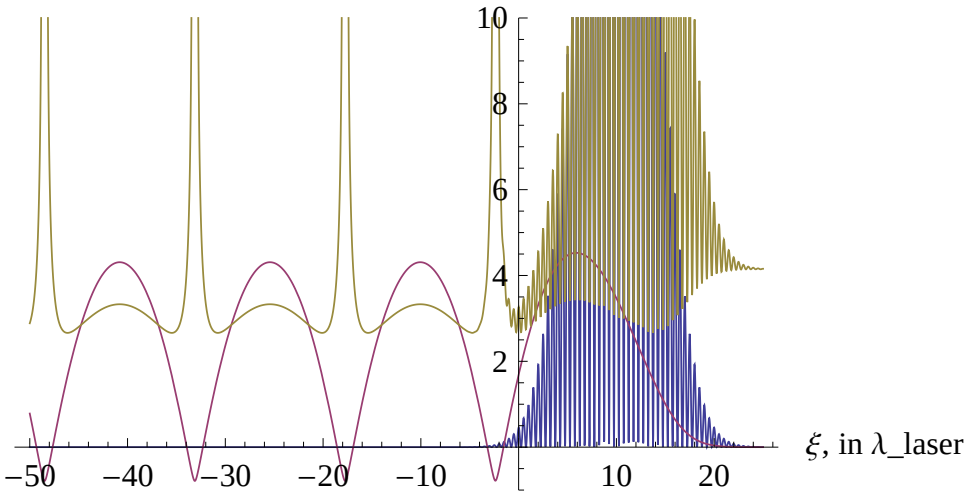


Figure A.1: The energetic parameters of the plasma in response to an intense, short laser pulse. The laser intensity is shown in blue. The electrostatic potential response $\tilde{\phi}$ is shown in maroon. The electron energy $\gamma$ is shown in gold.

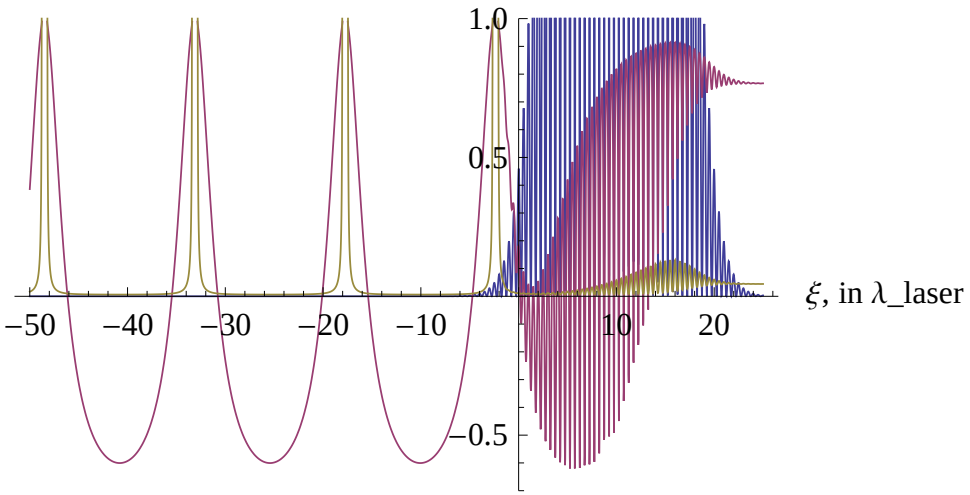


Figure A.2: The bulk parameters of the plasma in response to an intense, short laser pulse. The laser intensity is shown in blue. The electron velocity $u_x$ (normalized to the speed of light c) is shown in maroon. The electron density $n_e$ (shown as a fraction of the critical density $n_{crit}$) is shown in gold.

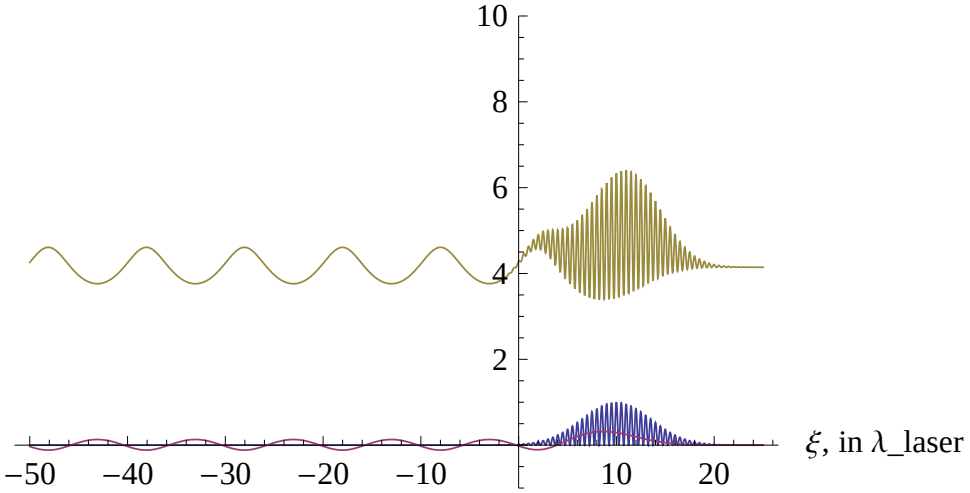


Figure A.3: The energetic parameters of the plasma in response to a low-intensity, short laser pulse. The laser intensity is shown in blue. The electrostatic potential response $\tilde{\phi}$ is shown in maroon. The electron energy $\gamma$ is shown in gold.

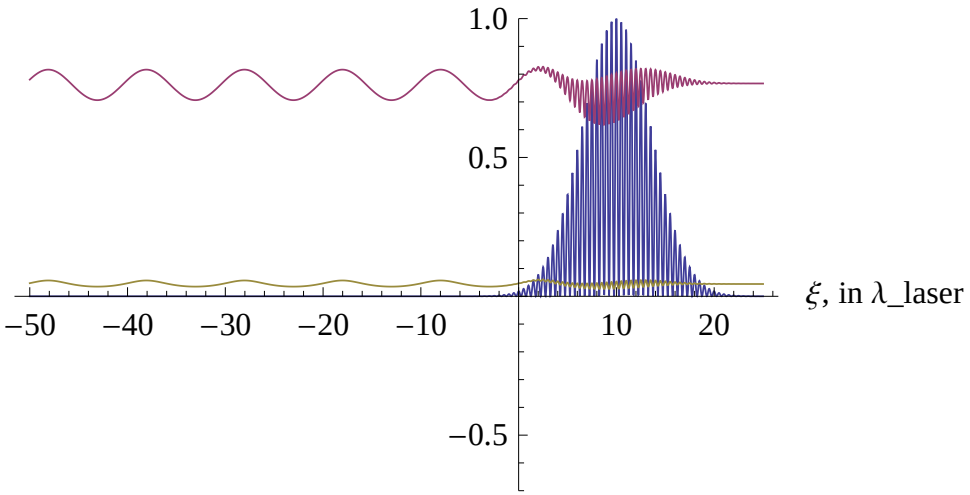


Figure A.4: The bulk parameters of the plasma in response to a low-intensity, short laser pulse. The laser intensity is shown in blue. The electron velocity $u_x$ (normalized to the speed of light c) is shown in maroon. The electron density $n_e$ (shown as a fraction of the critical density $n_{crit}$) is shown in gold.

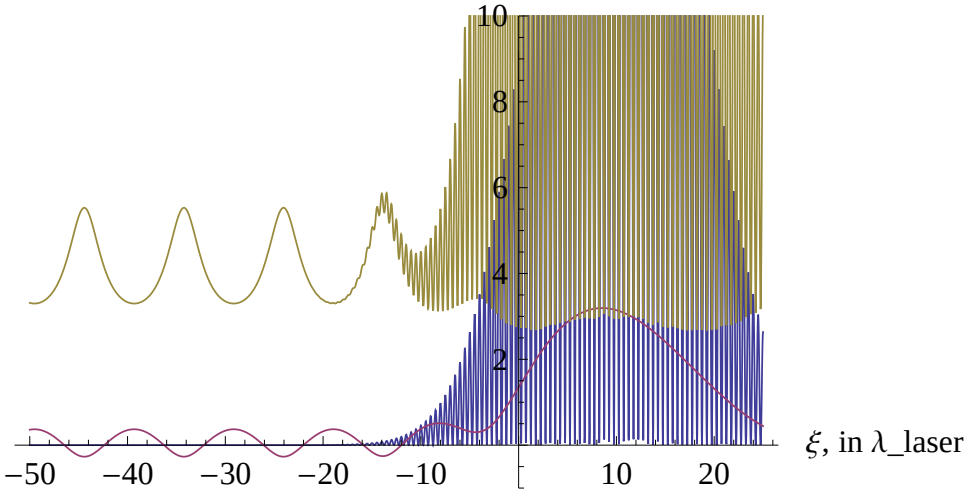


Figure A.5: The energetic parameters of the plasma in response to an intense, long laser pulse. The laser intensity is shown in blue. The electrostatic potential response $\tilde{\phi}$ is shown in maroon. The electron energy $\gamma$ is shown in gold.

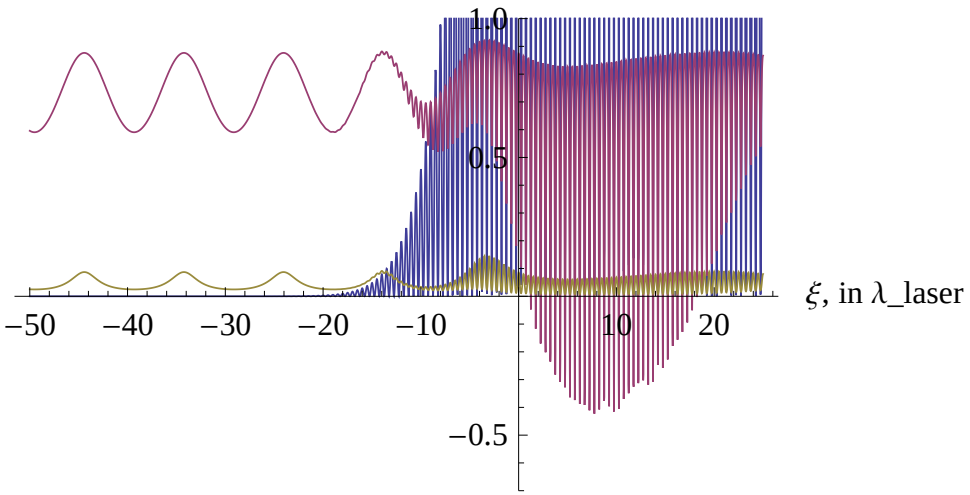


Figure A.6: The bulk parameters of the plasma in response to an intense, long laser pulse. The laser intensity is shown in blue. The electron velocity $u_x$ (normalized to the speed of light c) is shown in maroon. The electron density $n_e$ (shown as a fraction of the critical density $n_{crit}$) is shown in gold.

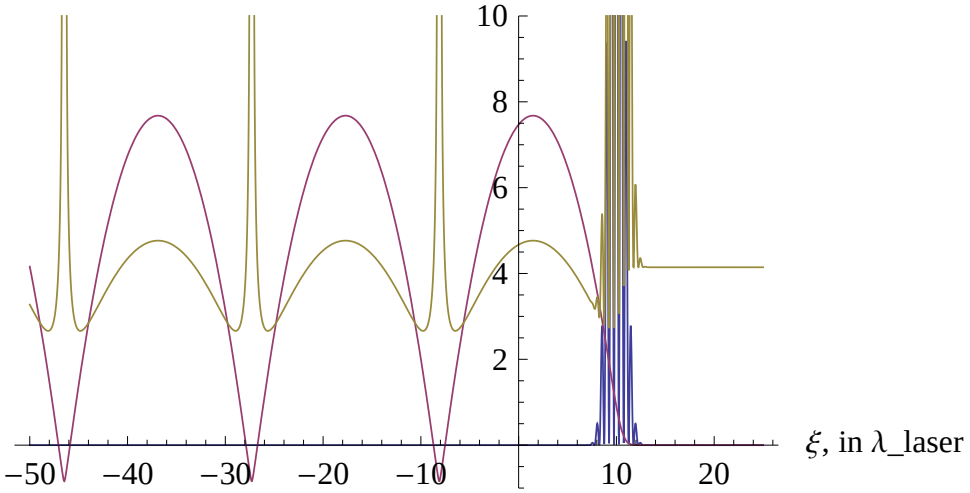


Figure A.7: The energetic parameters of the plasma in response to an intense, very short laser pulse. The laser intensity is shown in blue. The electrostatic potential response $\tilde{\phi}$ is shown in maroon. The electron energy $\gamma$ is shown in gold.

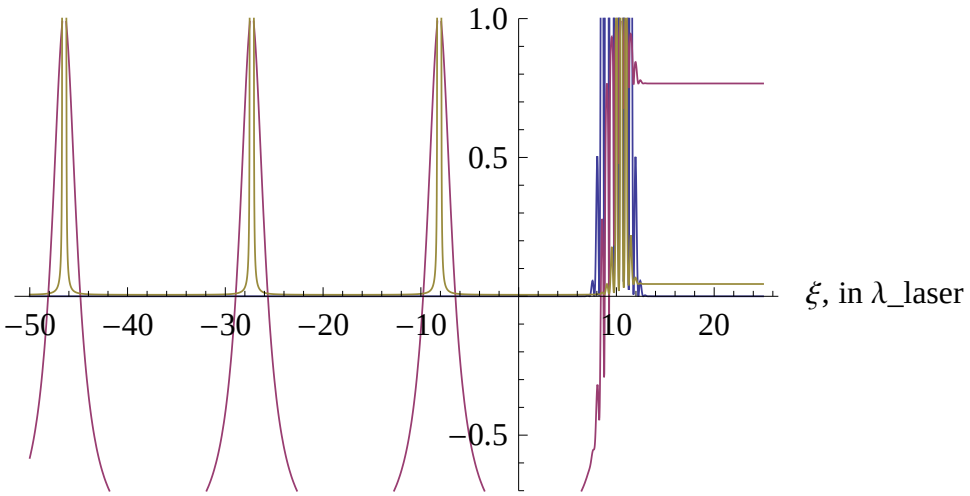


Figure A.8: The bulk parameters of the plasma in response to an intense, very short laser pulse. The laser intensity is shown in blue. The electron velocity $u_x$ (normalized to the speed of light c) is shown in maroon. The electron density $n_e$ (shown as a fraction of the critical density $n_{crit}$) is shown in gold.

A.5 and A.6. The wake response is actually strengthened by reducing the pulse length from $\sigma = 5\lambda_{Laser}$ to $\sigma = 2.5\lambda_{Laser}$ without varying $a_{y0}$, as shown in figures A.7 and A.8.

# APPENDIX B

# Published Manuscripts

## B.1 Introduction

For posterity, in this section we reproduce the manuscripts that were published in pursuit of this dissertation.

## B.2 Aberrant Pulse Simulations

The following manuscript was published as an article in the journal "Physics of Plasmas," Volume 18, page 053110, under the title "A Computational Investigation of the Impact of Aberrated Gaussian Laser Pulses on Electron Beam Properties in Laser-Wakefield Acceleration Experiments."

Realizing practical devices based on the LWFA scheme will require an understanding of the sensitivity of the system's performance as an accelerator to deviations from the ideal physics of the LWFA regime. Parameters of interest for characterizing the system's performance include the peak beam energy, beam emittance [**?** ], and peak beam current. One major possible deviation of the system from the idealized physics

consists of deviations from Gaussian in the pulse intensity profile. Additional deviations from an ideal pulse can take the form of aberrations in the phase front and variations in the temporal profile of the pulse.

Furthermore, recent experimental results [**?** ] indicate that the introduction of a comatic aberration in a LWFA system can enhance the production of synchrotron x-rays via an increase in the betatron oscillation amplitude. An analysis of the response of the LWFA system will enable supporting this research by providing robust computational tools for introducing a comatic aberration to a LWFA system, and analyzing the system's response to that aberration.

Computational methods provide an ideal avenue of investigation for these problems, as both the shape and magnitude of the pulse shape's deviation from the Gaussian can be precisely controlled. In particular, the particle-in-cell (PIC) method is an ideal computational method for studying the highly kinetic, collisionless, relativistic plasmas found in LWFA systems. This paper therefore presents the results of a computational investigation into the impact of non-Gaussian pulse intensity profiles, stemming from the comatic optical aberration, on the performance of a LWFA-based electron accelerator .

### B.2.1 Background

#### B.2.1.1 Overview of the Diffraction Theory of Optical Aberrations

Here we briefly review the diffraction theory of optics. In this theory, optical aberrations are characterized by an expansion of a diffraction integral [**?** ]:

$$U\left(u,v,\psi\right)=-\frac{i}{\lambda}\frac{Aa^{2}}{R^{2}}e^{i\left(\frac{R}{a}\right)^{2}u}\times$$

$$\int_0^1 \int_0^{2\pi} e^{i\left[k\phi\left(Y_1^*,\rho,\theta\right)-v\rho cos(\theta-\psi)-\frac{1}{2}u\rho^2\right]}\rho d\rho d\theta \tag{B.1}$$

in terms of basis functions, where u, v, and $\psi$ are the optical coordinates [**?** ]. This integral is defined such that the intensity is given by [**?** ]:

$$I\left(u,v,\psi\right)=\left|U\left(u,v,\psi\right)\right|^2 \tag{B.2}$$

For the diffraction pattern associated with a single aberration, equation B.1 can be expanded in terms of Bessel functions $J_n$ and Zernike Polynomials $R_n^m$ [**?** ]:

$$U\left(u,v,\psi\right)=4C{\sum_{s=0}^{\infty}}'\left(-i\right)^{(m-1)s}\cos\left(ms\psi\right)\times$$

$$\int_0^1 e^{-\frac{1}{2}iu\rho^2}J_s\left[\alpha_{lnm}R_n^m\left(\rho\right)\right]J_{ms}\left(v\rho\right)\rho d\rho \tag{B.3}$$

For small aberrations (i.e. where the constant $\alpha_{lnm}$ is small), the first Bessel function in the integral of equation B.3 can be expanded in a power series; this lets us rewrite equation B.3 as[**?** ]:

$$U\left(u,v,\psi\right)=C[U_0\left(u,v,\psi\right)+i\alpha_{lnm}U_1\left(u,v,\psi\right)$$

$$+\left(i\alpha_{lnm}\right)^2U_2\left(u,v,\psi\right)+\left(i\alpha_{lnm}\right)^3U_3\left(u,v,\psi\right)+$$

$$\left(i\alpha_{lnm}\right)^4U_4\left(u,v,\psi\right)+...] \tag{B.4}$$

where the expansion terms are given by the integrals[**?** ]:

$$U_0 = 2\int_0^1 e^{-\frac{1}{2}iu\rho^2} J_0(v\rho)\,\rho d\rho \tag{B.5}$$

$$U_1 = 2(-i)^m cos(m\psi) \times$$

$$\int_0^1 e^{-\frac{1}{2}iu\rho^2} R_n^m(\rho)\, J_m(v\rho)\,\rho d\rho \tag{B.6}$$

$$U_2 = \frac{1}{2!}\Big\{ \int_0^1 e^{-\frac{1}{2}iu\rho^2} \{R_n^m(\rho)\}^2 J_0(v\rho)\,\rho d\rho +$$

$$i^{2m}\cos(2m\psi)\int_0^1 e^{-\frac{1}{2}iu\rho^2} \{R_n^m(\rho)\}^2 J_2 m(v\rho)\,\rho d\rho\Big\} \tag{B.7}$$

$$U_3 = \frac{1}{2\times 3!}\Big\{3(-i)^m \cos(m\psi) \times$$

$$\int_0^1 e^{-\frac{1}{2}iu\rho^2} \{R_n^m(\rho)\}^3 J_m(v\rho)\,\rho d\rho$$

$$i^{2m}\cos(2m\psi)\int_0^1 e^{-\frac{1}{2}iu\rho^2} \{R_n^m(\rho)\}^2 J_2 m(v\rho)\,\rho d\rho\Big\} \tag{B.8}$$

The constants l, n, and m are integers specifying the type of aberration, as shown in table B.1:

Table B.1: Aberration Types and Integers[**?** ]

| *Aberration Type* | $l$ | $n$ | $m$ |
|---|---|---|---|
| Spherical | 0 | 4 | 0 |
| Comatic | 0 | 3 | 1 |
| Astigmatic | 0 | 2 | 2 |
| Curvature | 1 | 2 | 0 |
| Distortion | 1 | 1 | 1 |

#### B.2.1.2 Comatic Aberration Implementation

Recent experimental work [**?** ] indicates that the presence of comatic aberration may enhance x-ray production via synchrotron radiation in a LWFA device. Therefore, the comatic aberration is the first aberration we study in detail. The expansion given by equation B.4 was truncated after four terms; equations B.6 through B.8 (the expression for $U_4$, while included in the calculations, is omitted below for brevity), yield:

$$U_1 = i\cos(\psi)\frac{2J_4(v)}{v} \tag{B.9}$$

$$U_2 = \frac{1}{2v}\left\{\frac{1}{4}J_1(v) - \frac{1}{20}J_3(v) + \frac{1}{4}J_5(v)\right.$$

$$\left. -\frac{9}{20}J_7(v) - \cos(2\psi)\left[\frac{2}{5}J_3(v) + \frac{3}{5}J_7(v)\right]\right\} \tag{B.10}$$

$$U_3 = \frac{-i}{12v}\left\{3\cos(m\psi)\left\{\frac{3}{14}J_{10}(v) - \frac{6}{35}J_8(v)\right.\right.$$

$$+\frac{9}{70}J_6(v) - \frac{44}{105}J_4(v) + \frac{1}{15}J_2(v)\Bigg\}+$$

$$\cos(3m\psi)\left\{\frac{9}{28}J_{10}(v) + \frac{9}{20}J_6(v) - \frac{8}{35}J_4(v)\right\}\Bigg\} \tag{B.11}$$

Figure B.1 shows the results of equations B.9 through B.11, as well as the equation for $U_4$, for $\alpha \approx 1$, if the unperturbed pattern $U_0$ is take to be either an Airy pattern or a Gaussian pattern.

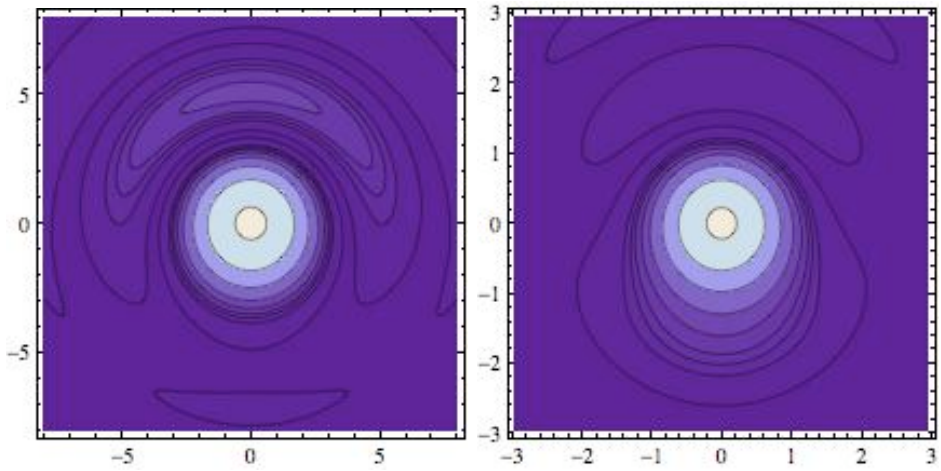


Figure B.1: The intensities of an Airy pattern (left) and a Gaussian pattern (right) perturbed with an $\alpha = 1.005$ coma.

### B.2.2 Simulation Methodology & Parameters

For this investigation, both two-dimensional and three-dimensional simulations were run using the particle-in-cell code OSIRIS 2.0. The three-dimensional version of the code was modified to explicitly include comatic aberrations. Both two- and three-dimensional simulations were performed; the two-dimensional simulations permitted a thorough parameter sweep, while the three-dimensional simulations permitted an accurate depiction of the comatic aberration.

#### B.2.2.1 Two-Dimensional Simulations

For small perturbations in 2D, the superposition of $TEM_{00}$ and $TEM_{10}$ modes is similar to the coma aberration. Additionally, OSIRIS 2.0 can simulate this pulse structure without any modifications to the source code. For these reasons, preliminary simulations consisted of a $TEM_{00}$ (i.e., a Gaussian) baseline pulse with a higher-order $TEM_{10}$ pulse superimposed.

For the 2D simulations, the relative intensities and positions of the pulses were varied to effect different degrees of mode mixing and asymmetry, while keeping the total pulse energy constant. Since pulse energy scales as the square of the normalized vector potential, pulse energy was kept constant by keeping the quadrature sum of the normalized vector potentials of the two pulses constant. The relative intensities between the two pulses were quantified via the mixing fraction, which is defined as follows; let $f_{00} \equiv \frac{a_{00}}{a_0}$ and $f_{10} \equiv \frac{a_{10}}{a_0}$:

$$a_0^2 = a_{00}^2 + a_{10}^2 = (f_{00}a_0)^2 + (f_{10}a_0)^2 = \left(f_{00}^2 + f_{10}^2\right) a_0^2$$

$$\left(f_{00}^2 + f_{10}^2\right) = 1$$

It is therefore most convenient to define the mixing fraction as the square of the ratio between the maximum normalized vector potential of the $TEM_{10}$-mode pulse, and the total maximum normalized vector potential of the pulse (i.e., the maximum normalized vector potential of the unperturbed pulse). A computational sweep of this mixing fraction was performed; for brevity, these initial simulations were performed using the two-dimensional version of OSIRIS.

For all two-dimensional simulations, the maximum plasma density was $n_{max} = 0.01 n_{crit}$, or $1.75 \times 10^{19} cm^{-3}$. The simulation box size was $38.2 \times 63.7 \mu m$; the box

moved at speed c in the laser propagation direction. The propagation time was $3475fs$, giving a propagation distance of $1.04mm$. The plasma density profile started with a linear ramp from $n = 0$ to $n = n_{max}$ over a distance of $63.5\mu m$, and ended with a linear ramp from $n = n_{max}$ to $n = 0$ over the same distance.

Computationally, the system was initialized with 2 particles per cell. The system had a grid size of $1200 \times 500$ (with the highest resolution in the propagation direction). This gave a grid spacing of $\Delta x \times \Delta y = 0.03185 \times 0.1274\mu m$.

For the two-dimensional simulations, the laser pulse's full-width, half-maximum spot size was $5.1\mu m$. The pulse's full-width, half-duration was $35fs$. The total normalized vector potential was $a_0 = 4.0$. The vector potentials of the $TEM_{00}$ and $TEM_{10}$ pulses were added together in quadrature to maintain a constant total pulse energy, i.e. $a_{00}^2 + a_{10}^2 = a_0^2$. This value of $a_0$ gives a peak pulse intensity of $3.5 \times 10^{19} W/cm^2$.

The emittance, current, and energy characteristics of the electron beams produced were then measured. These parameters were determined by analyzing the final frame of the simulation, at which point the plasma density was zero and the electron population could be assumed to consist entirely of the beam.

#### B.2.2.2 Three-Dimensional Simulations

The three-dimensional simulations consisted of a single Gaussian pulse, modified by a comatic aberration defined by the expansion parameter $\alpha$. The parameter $\alpha$ was varied from 0.2 to 1.0 for the computational sweep.

For all three-dimensional simulations, the maximum plasma density was $n_{max} = 0.01 n_{crit}$, or $1.75 \times 10^{19} cm^{-3}$. The simulation box size was $38.1\mu m \times 31.8\mu m \times 31.8\mu m$; the box moved at speed c in the laser propagation direction. The propagation time was $3392fs$, yielding a propagation distance of $1.02mm$. As with the two-dimensional simulations, the plasma density profile started and ended with a linear ramp from

$n = 0$ to $n = n_{max}$ over a distance of $63.5\mu m$.

Computationally, the system was initialized with 2 particles per cell. The system had a grid size of $1200 \times 250 \times 250$ (with the highest resolution in the propagation direction). This gave a grid spacing of $\Delta x \times \Delta y \times \Delta z = 0.03175 \times 0.1272 \times 0.1272 \mu m$.

As with the two-dimensional simulations, the laser pulse's full-width, half-maximum spot size was $5.1\mu m$, and the pulse's full-width, half-duration was $35fs$. The normalized vector potential was $a_0 = 4.0$, yielding a peak pulse intensity of $3.5 \times 10^{19} W/cm^2$. Again, as with the two-dimensional simulations, the emittance, current, and energy characteristics of the electron beams produced were then measured by analyzing the final frame of the simulation.

#### B.2.2.3 Parameter Characterization

For the three-dimensional simulations, the current data was extracted directly from the code. The peak forward current, i.e. the current parallel to the direction of laser propagation, was calculated from these distributions.

The beam emittance was calculated from:

$$\epsilon_i = 4\langle \Delta x_i \rangle \langle \Delta v_i \rangle$$

where the subscript i denotes whether or not the positions and velocities are taken in the polarization direction, or perpendicular to the polarization direction. The quantity $\langle \Delta x_i \rangle$ is the root-mean-square deviation of the particle position from the mean particle position in the $i^{th}$ direction, and the quantity $\langle \Delta v_i \rangle$ is the root-mean-square deviation of the particle velocity from the mean particle velocity in the $i^{th}$ direction, as a fraction of the velocity in the propagation direction.

Since OSIRIS prints the relativistic factor $\gamma$, calculating the beam energy distribution from the printed gamma distribution via $E = (\gamma - 1)\, m_0 c^2$ was straightforward.

For the three-dimensional simulations, the peak beam energies were calculated from the maximum of the energy spectra. However, for the two-dimensional simulations, the average beam energies were taken, as the two-dimensional energy spectra did not have clearly-defined single energy peaks.

### B.2.3 2D $TEM_{00}/TEM_{10}$ Mode-Mixing Preliminary Simulation Results

Figure B.8 shows, respectively, the initial laser pulse for the two-dimensional, mode-mixing simulations at mixing fractions of 0.05, 0.50, and 0.95. The results of these simulations are shown in Figures B.2 and B.3.

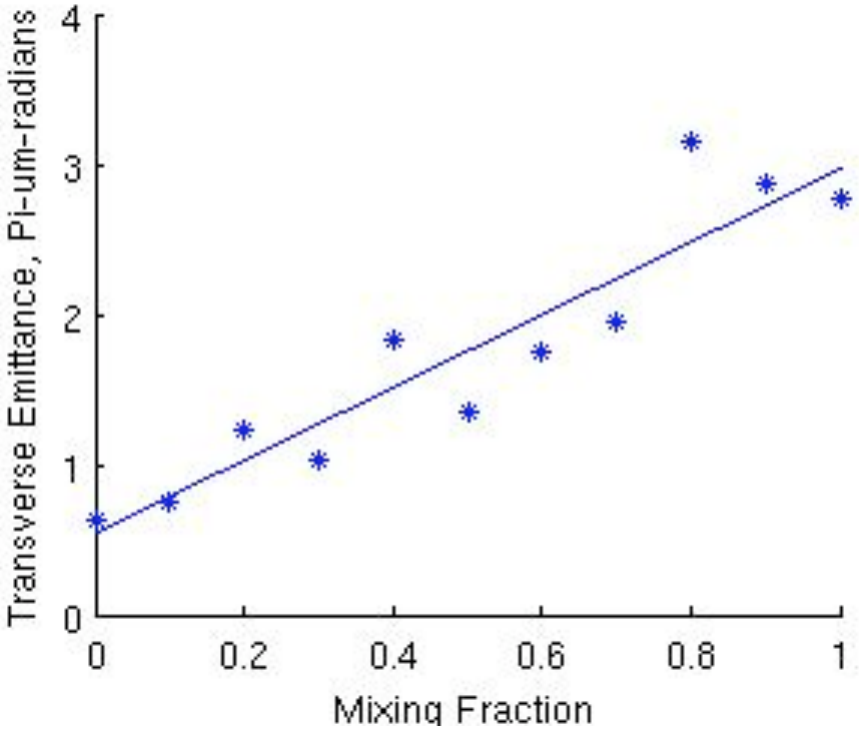


Figure B.2: The effect of mode mixing on the 2D perpendicular beam emittance

Figure B.2 shows the relationship between the beam's perpendicular emittance and the mode mixing fraction. The TEM 10 mode is functionally similar to a pair of copropagating pulses with 180 degree phase shift; it has been shown [**?** ] that

the nonlinear interaction of two such pulses will cause them to repel, resulting in the observed increase in the final beam emittance.

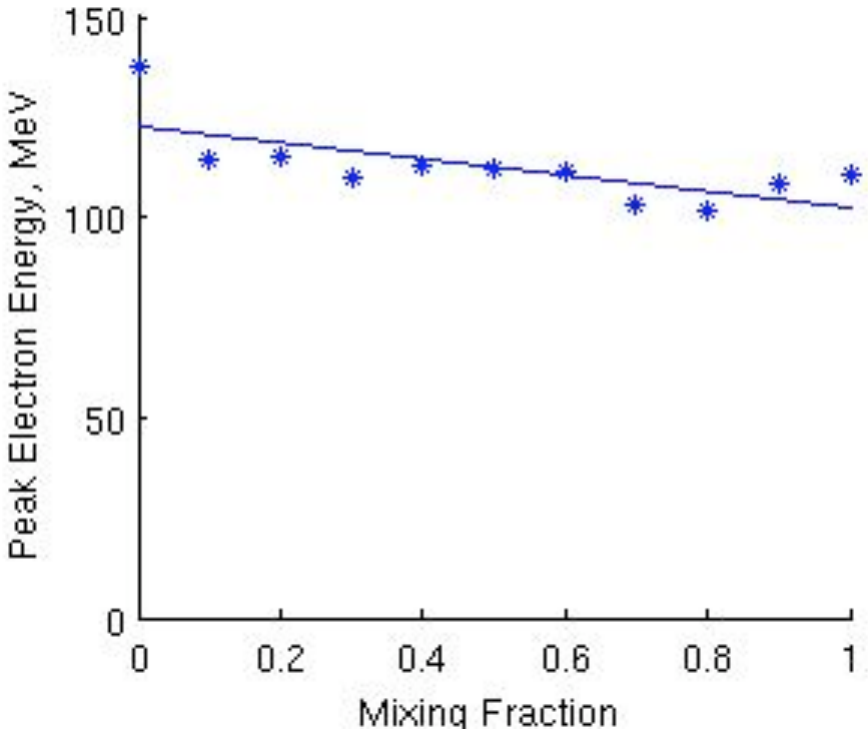


Figure B.3: The effect of mode mixing on the 2D beam averaged energy

Figure B.3 shows the relationship between the beam's peak energy and the mode mixing fraction. The beam energy showed weak correlation to the mixing fraction ($R^2 < 0.20$), oscillating between 200 and 400 MeV over the course of the parameter sweep.

### B.2.4 3D Explicit Coma Simulation Results

Figure B.9 shows the intensity profile for a three-dimensional simulation with an $\alpha = 1.005$ coma. The results of the three-dimensional simulations including a direct calculation of the comatic aberration are shown in Figures B.4 through B.7.

Figure B.4 shows the relationship between the aberration coefficient $\alpha$ and the peak beam current. The current varies by 20% over the parameter range, with a

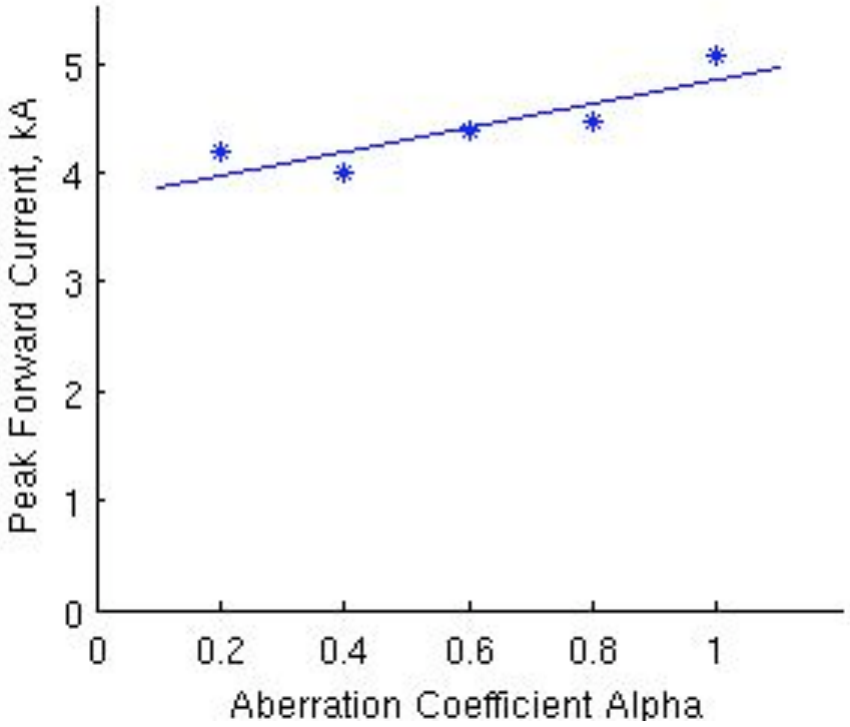


Figure B.4: The effect of a comatic aberration on the 3D peak beam current

correlation of $R^2 = 0.74$. This does not appear have a dramatic impact on the beam performance, as even after a severe aberration is applied, the peak current varies by less than 20%.

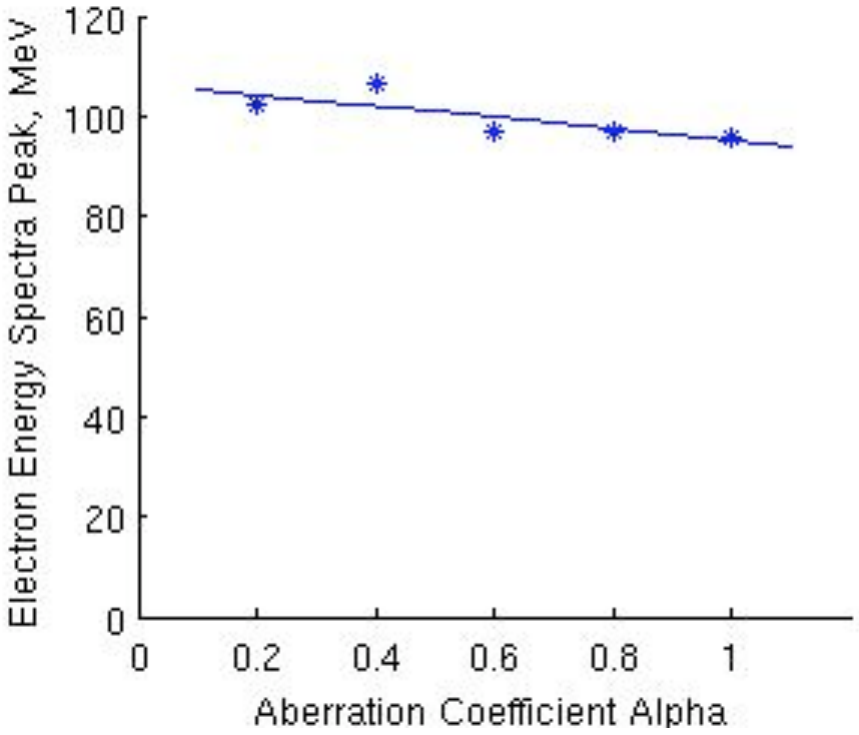


Figure B.5: The effect of a comatic aberration on the 3D peak beam energies

Figure B.5 shows the relationship between the aberration coefficient $\alpha$ and the peak beam energy. The peak energies vary by less than 10% over the entire parameter range, with a correlation of only $R^2 = 0.58$. These results indicate that even in the presence of a severe aberration, peak beam energy is relatively unaffected.

Figure B.6 shows how the shape of the beam electron energy spectra varies with $\alpha$. This figure shows that there is a weak relationship between the beam energy spread or general shape of the energy spectrum and the aberration strength.

Figure B.7 shows the relationship between the aberration coefficient $\alpha$ and both the polarization (top) and perpendicular (bottom) emittances. Note that the primary aberration axis was in the polarization direction; Figure B.7 shows that a strong co-

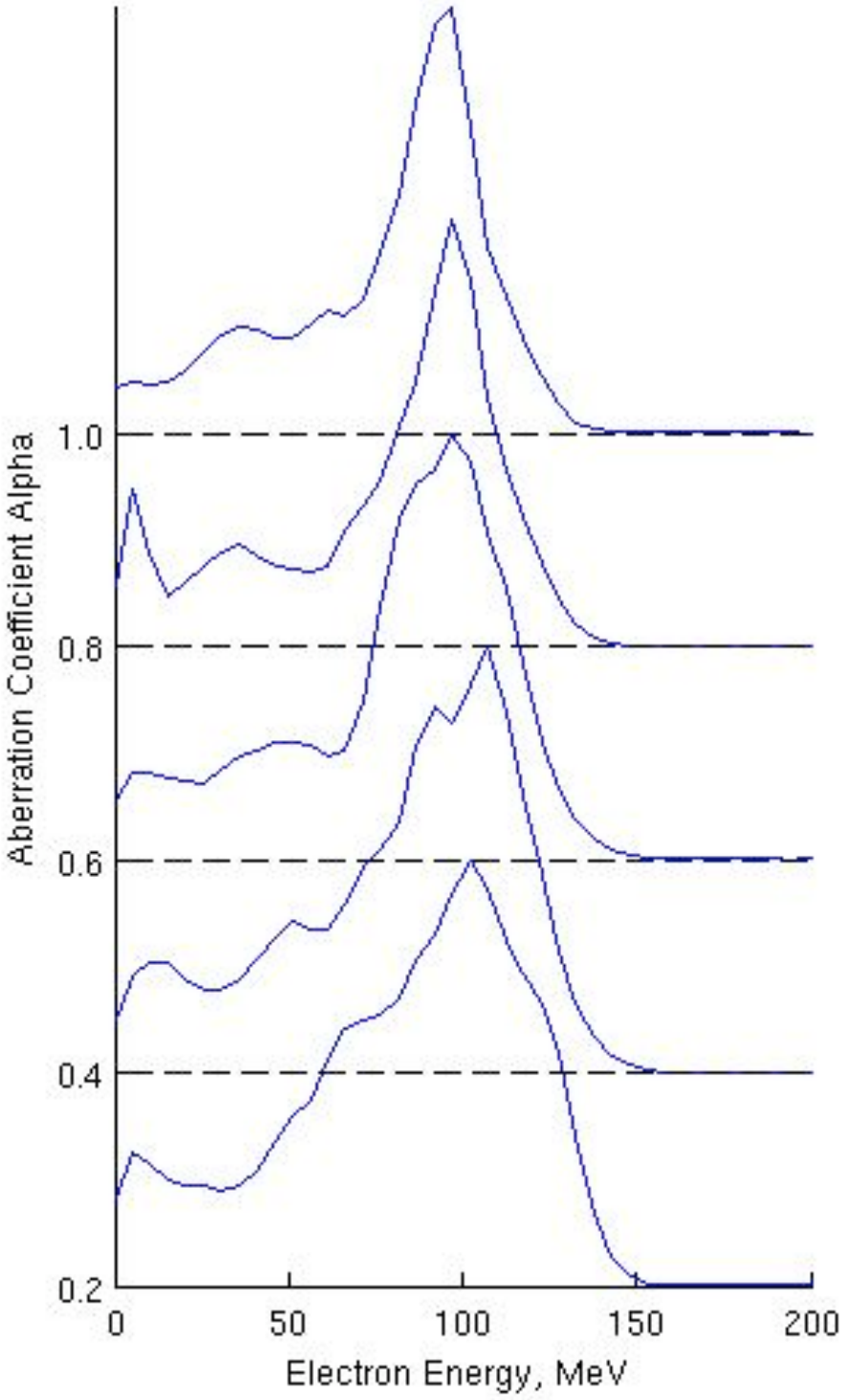


Figure B.6: The effect of a comatic aberration on the 3D beam electron energy spectra; note that the spectral heights have been arbitrarily scaled for clarity; the corresponding values of $\alpha$ are, from bottom to top: $\alpha = 0.2, 0.4, 0.6, 0.8, \&1.0$ 231

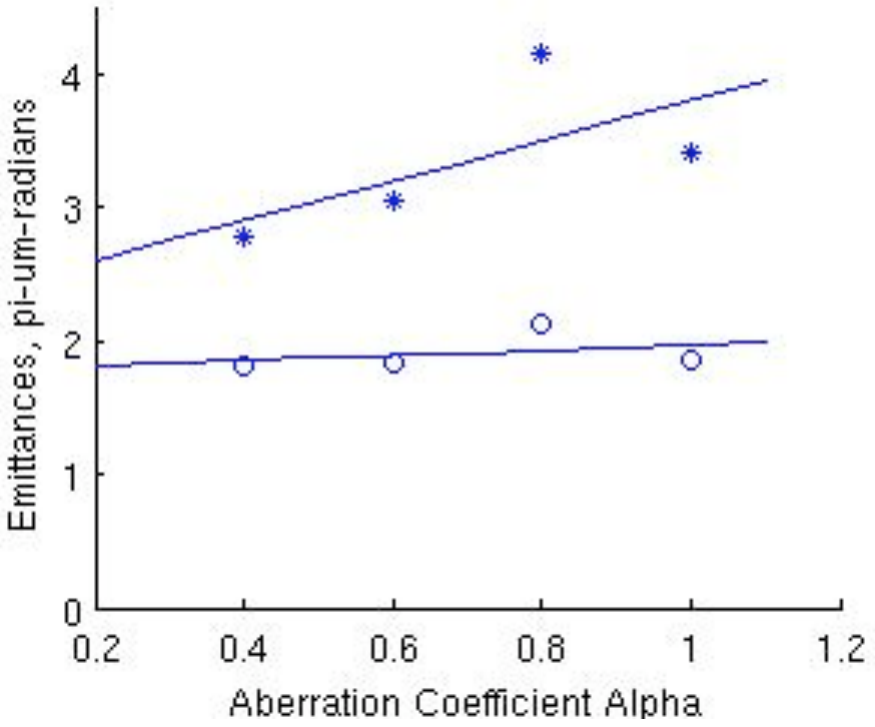


Figure B.7: The effect of a comatic aberration on both the polarization (top) and perpendicular (bottom) 3D beam emittances

matic aberration increases polarization emittance noticeably, while leaving the perpendicular emittance relatively unaltered.

These results support the conclusions of recent experimental work indicating that a comatic aberration can increase the amplitude of the betatron oscillation produced by the undulating beam in a laser-wakefield accelerator. [**?** ]. The difference between the polarization and perpendicular emittances indicates that there is a high beam ellipticity, a condition which enhances x-ray generation by synchrotron radiation [**?** ].

### B.2.5 Conclusion

The results of this computational sweep are promising on two fronts. First, the results indicate that the performance of a LWFA device will be relatively unaffected by the presence of even a strong comatic aberration. Neither the peak beam energy, nor the electron energy spread, were significantly affected by the presence of a strong comatic aberration for the three-dimensional simulations. Second, the trends in perpendicular and polarization emittances indicate that the beam ellipticity increases with the strength of the comatic aberration. This supports recent experimental work indicating that the presence of a coma can enhance the production of x-rays via synchrotron radiation.

### B.2.6 Acknowledgements

This work was supported by the NSF/DOE under grant (PHY-09-03557). The authors would like to acknowledge the OSIRIS Consortium (UCLA, IST Portugal) for the use of the OSIRIS 2.0 framework. The authors would also like to acknowledge the support of the Michigan Institute for Plasma Science and Engineering.

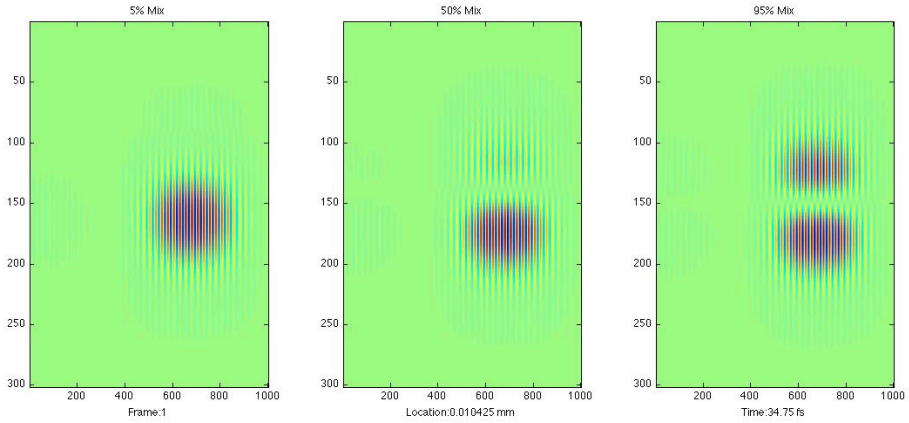


Figure B.8: The initial laser pulses for mixing fractions of, from left to right, 5%, 50%, and 95%

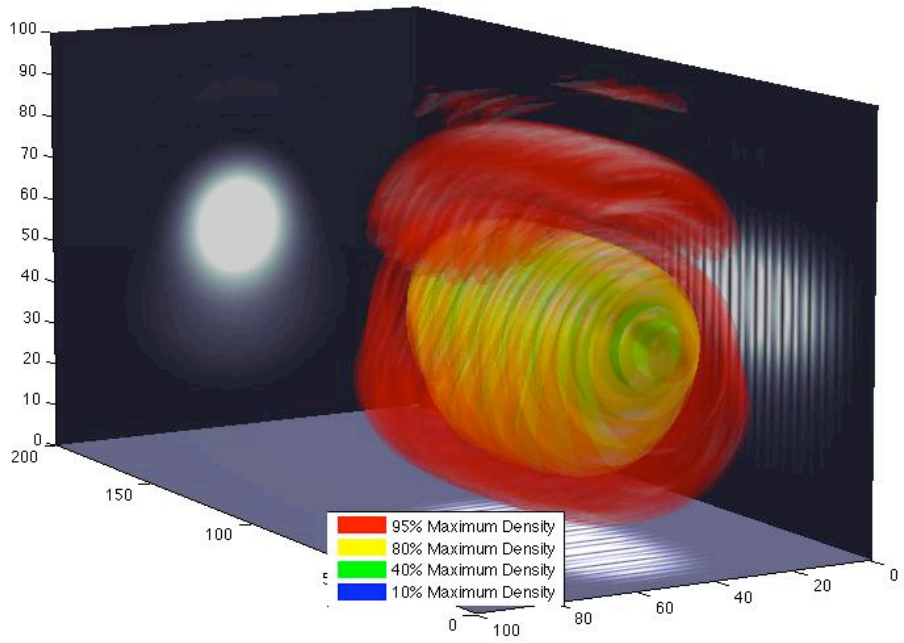


Figure B.9: The 3D intensity profile of the pulse for an aberration coefficient $\alpha = 1.005$

# BIBLIOGRAPHY

# BIBLIOGRAPHY


[1] Lcls public space: $https://portal.slac.stanford.edu/sites/lcls_public/comm/pages/$[...], 2014.

[2] S. Kneip, C. McGuffey, J. L. Martins, S. F. Martins, C. Bellei, V. Chykov, F. Dollar, R. Fonseca, C. Huntington, G. Kalintchenko, A. Maksimchuk, S. P. D. Mangles, T. Matsuoka, S. R. Nagel, C. A. J. Palmer, J. Schreiber, K. Ta Phouc, A. G. R. Thomas, V. Yonvsky, L. O. Silva, K. Krushelnick, and Z. Najmudin. Bright spatially coherent synchrotron x-rays from a table-top source. *NatPhys*, 6.

[3] J. D. Jackson. *Classical Electrodynamics*. John Wiley & Sons, United States of America, 3rd edition, 1999.

[4] International linear collider website: $http://www.linearcollider.org/$, 2014.

[5] S. Corde, K. T. Phuoc, G. Lambert, R. Fitour, V. Malka, and A. Rousse. Femtoseconds x rays from laser-plasma accelerators. *RMP*, 85(1):1–48, Jan 2013.

[6] Soleil website: $http://www.synchrotron-soleil.fr/$, 2014.

[7] Swiss light source website: $http://www.psi.ch/sls/$, 2014.

[8] Lcls website: $https://portal.slac.stanford.edu/sites/lcls_public/pages/default.aspx$, 2014.

[9] Flash website: $http://flash.desy.de/$, 2014.

[10] Xfel website: $http://www.xfel.eu/$, 2014.

[11] D. A. G. Deacon, L. R. Elias, J. M. J. Madey, G. J. Ramian, H. A. Schwettman, and T. I. Smith. First operation of a free-electron laser. *Phys. Rev. Lett.*, 38:892–894, Apr 1977.

[12] C. Vieu, F. Carcenac, A. Pepin, Y. Chen, M. Mejias, A. Lebib, L. Manin-Ferlazzo, L. Couraud, and H. Launois. Electron beam lithography: resolution limits and applications. *Applied Surface Science*, 164.

[13] C. Chiu, M. Fomytskyi, F. Grigsby, F. Raischel, M. C. Downer, and T. Tajima. Laser electron accelerators for radiation medicine: a feasibility study. *Medical Physics*, 31.

[14] W. Bertozzi and R. J. Ledoux. Nuclear resonance fluorescence imaging in non-intrusive cargo inspection. *Nuclear Instruments and Methods in Physics Research Section B: Beam Interactions with Materials and Atoms*, 241.

[15] T. E. Cowan, A. W. Hunt, T. W. Phillips, S. C. Wilks, M. D. Perry, C. Brown, W. Fountain, S. Hatchett, J. Johnson, M. H. Key, T. Parnell, D. M. Pennington, R. A. Snavely, and Y. Takahashi. Photonuclear fission from high energy electrons from ultraintense laser-solid interactions. *Phys. Rev. Lett.*, 84:903–906, Jan 2000.

[16] J. Magill, H. Schwoerer, F. Ewald, J. Galy, R. Schenkel, and R. Sauerbrey. Laser transmutation of iodine-129. *Applied Physics B*, 77(4):387–390, 2003.

[17] S. A. Reed, V. Chvykov, G. Kalintchenko, T. Matsuoka, P. Rousseau, V. Yanovsky, C. R. Vane, J. R. Beene, D. Stracener, D. R. Schultz, and A. Maksimchuk. Photonuclear fission with quasimonoenergetic electron beams from laser wakefields. *Applied Physics Letters*, 89(23):–, 2006.

[18] K. W. D. Ledingham, I. Spencer, T. McCanny, R. P. Singhal, M. I. K. Santala, E. Clark, I. Watts, F. N. Beg, M. Zepf, K. Krushelnick, M. Tatarakis, A. E. Dangor, P. A. Norreys, R. Allott, D. Neely, R. J. Clark, A. C. Machacek, J. S. Wark, A. J. Cresswell, D. C. W. Sanderson, and J. Magill. Photonuclear physics when a multiterawatt laser pulse interacts with solid targets. *Phys. Rev. Lett.*, 84:899–902, Jan 2000.

[19] M. Seto, Y. Yoda, S. Kikuta, X. W. Zhang, and M. Ando. Observation of nuclear resonant scattering accompanied by phonon excitation using synchrotron radiation. *Phys. Rev. Lett.*, 74:3828–3831, May 1995.

[20] V. G. Kohn, A. I. Chumakov, and R. Rüffer. Nuclear resonant inelastic absorption of synchrotron radiation in an anisotropic single crystal. *Phys. Rev. B*, 58:8437–8444, Oct 1998.

[21] R. Abela and B.D. Patterson. Time-resolved scattering from chemical systems at the proposed swissfel x-ray laser project. *TrAC Trends in Analytical Chemistry*, 29(6):538 – 543, 2010. ¡ce:title¿Analytical applications of synchrotron radiation¡/ce:title¿.

[22] R. Fourme, E. Girard, R. Kahn, A.-C. Dhaussy, and I. Ascone. Advances in high-pressure biophysics: Status and prospects of macromolecular crystallography. *Annual Review of Biophysics*, 38.

[23] S.K. Burley and J.B. Bonanno. Structuring the universe of proteins. *Annual Review of Genmoics and Human Genetics*, 3.

[24] A.K.-L. Ng., H. Zhang, K. Tan, Z. Li, J.-H. Liu, P. K.-S. Chan, S.-M. Li, W.-Y. Chan, S. W.-N. Au, A. Joachimiak, T. Walz, J.-H. Wang, and P.-C. Shaw. Structure of the influenza virus a h5n1 nucleoprotein: implications for rna binding, oligomerization, and vaccine design. *Journa of the Federation of American Societies for Experimental Biology*, 22.

[25] R. Xu, R. McBride, J. C. Paulson, C. F. Basler, and I. A. Wilson. Structure, receptor binding, and antigenicity of influenza virus hemagglutinins from the 1957 h2n2 pandemic. *Journal of Virology*, 84.

[26] I. Wilson. The compact linear collider {CLIC}. *Physics Reports*, 403404(0):365 – 378, 2004. ¡xocs:full-name¿CERN - the second 25 years¡/xocs:full-name¿.

[27] C. Gahn, G. D. Tsakiris, A. Pukhov, J. Meyer-ter Vehn, G. Pretzler, P. Thirolf, D. Habs, and K. J. Witte. Multi-mev electron beam generation by direct laser acceleration in high-density plasma channels. *Phys. Rev. Lett.*, 83:4772–4775, Dec 1999.

[28] T. Tajima and J. M. Dawson. Laser electron accelerator. *Phys. Rev. Lett.*, 43(4):267–270, Jul 1979.

[29] C. E. Clayton, C. Joshi, C. Darrow, and D. Umstadter. Relativistic plasma-wave excitation by collinear optical mixing. *Phys. Rev. Lett.*, 54:2343–2346, May 1985.

[30] A E Dangor, A K L Dymoke-Bradshaw, and A E Dyson. Observation of relativistic plasma waves generated by the beat-wave with 1 m lasers. *Physica Scripta*, 1990(T30):107, 1990.

[31] C. E. Clayton, M. J. Everett, A. Lal, D. Gordon, K. A. Marsh, and C. Joshi. Acceleration and scattering of injected electrons in plasma beat wave accelerator experiments*. *Physics of Plasmas (1994-present)*, 1(5), 1994.

[32] K. Nakajima, D. Fisher, T. Kawakubo, H. Nakanishi, A. Ogata, Y. Kato, Y. Kitagawa, R. Kodama, K. Mima, H. Shiraga, K. Suzuki, K. Yamakawa, T. Zhang, Y. Sakawa, T. Shoji, Y. Nishida, N. Yugami, M. Downer, and T. Tajima. Observation of ultrahigh gradient electron acceleration by a self-modulated intense short laser pulse. *Phys. Rev. Lett.*, 74:4428–4431, May 1995.

[33] A. Ting, C. I. Moore, K. Krushelnick, C. Manka, E. Esarey, P. Sprangle, R. Hubbard, H. R. Burris, R. Fischer, and M. Baine. Plasma wakefield generation and electron acceleration in a self-modulated laser wakefield accelerator experiment. *Physics of Plasmas (1994-present)*, 4(5), 1997.

[34] Eisuke Miura, Kazuyoshi Koyama, Susumu Kato, Naoaki Saito, Masahiro Adachi, Yoichi Kawada, Tatsufumi Nakamura, and Mitsumori Tanimoto. Demonstration of quasi-monoenergetic electron-beam generation in laser-driven plasma acceleration. *Applied Physics Letters*, 86(25):–, 2005.

[35] B. Hidding, K.-U. Amthor, B. Liesfeld, H. Schwoerer, S. Karsch, M. Geissler, L. Veisz, K. Schmid, J. G. Gallacher, S. P. Jamison, D. Jaroszynski, G. Pretzler, and R. Sauerbrey. Generation of quasimonoenergetic electron bunches with 80-fs laser pulses. *Phys. Rev. Lett.*, 96:105004, Mar 2006.

[36] B. Hidding, M. Geissler, G. Pretzler, K.-U. Amthor, H. Schwoerer, S. Karsch, L. Veisz, K. Schmid, and R. Sauerbrey. Quasimonoenergetic electron acceleration in the self-modulated laser wakefield regime. *Physics of Plasmas (1994-present)*, 16(4):–, 2009.

[37] S. V. Bulanov, F. Pegoraro, A. M. Pukhov, and A. S. Sakharov. Transverse-wake wave breaking. *Phys. Rev. Lett.*, 78:4205–4208, Jun 1997.

[38] A. Modena, Z. Najmudin, A.E. Dangor, C.E. Clayton, K.A. Marsh, C. Joshi, V. Malka, C.B. Darrow, C. Danson, D. Neely, and F. N. Walsh. Electron acceleration from the breaking of relativistic plasma waves. *Letters to Nature*, 377.

[39] Z. Najmudin, K. Krushelnick, E. L. Clark, S. P. D. Mangles, B. Walton, A. E. Dangor, S. Fritzler, V. Malka, E. Lefebvre, D. Gordon, F. S. Tsung, and C. Joshi. Self-modulated wakefield and forced laser wakefield acceleration of electrons. *Physics of Plasmas (1994-present)*, 10(5), 2003.

[40] V. Malka, S. Fritzler, E. Lefebvre, M.-M. Aleonard, F. Burgy, J.-P. Chambaret, J.-F. Chemin, K. Krushelnick, G. Malka, S.P.D. Mangles, Z. Najmudin, M. Pittman, J.-P. Rousseau, J.-N. Scheurer, B. Walton, and A. E. Dangor. Electron acceleration by a wake field forced by an intense ultrashort laser pulse. *Science*, 298.

[41] S.P.D. Mangles, C.D. Murphy, Z. Najmudin, A.G.R. Thomas, J.L. Collier, A.E. Dangor, E.J. Divall, P.S. Foster, J.G. Gallacher, C.J. Hooker, D.A. Jaroszynski, A.J. Langley, W.B. Mori, P.A. Norreys, F.S. Tsung, R. Viskup, B.R. Walton, and K. Krushelnick. Monoenergetic beams of relativistic electrons from intense laserplasma interactions. *Letters to Nature*, 431.

[42] J. Faure, Y. Glinec, A. Pukhov, S. Kiselev, S. Gordienko, E. Lefebvre, J.-P. Rousseau, F. Burgy, and V. Malka. A laserplasma accelerator producing monoenergetic electron beams. *Letters to Nature*, 431.

[43] C.G.R. Geddes, Cs. Toth, J. van Tilborg, E. Esarey, C.B. Schroeder, D. Bruhwiler, C. Nieter, J. Cary, and W.P. Leemans. High-quality electron beams from a laser wakefield accelerator using plasma-channel guiding. *Letters to Nature*, 431.

[44] W.P. Leemans, B. Nagler, A.J. Gonsalves, Cs. Toth, K. Nakamura, C.G.R. Geddes, E. Esarey, C.B. Schroeder, and S.M. Hooker. Gev electron beams from a centimetre-scale accelerator. *Nature Physics*, 2.

[45] K. Krushelnick, Z. Najmudin, and A. E. Dangor. Particle acceleration using intense laser produced plasmas. *Laser Physics Letters*, 4(12):847–862, 2007.

[46] V. Malka, J. Faure, G.A. Yann, E. Lefebvre, A. Rousse, and K. Ta Phuoc. Principles and applications of compact laserplasma accelerators. *Nature Physics*, 4.

[47] E. Esarey, C. B. Schroeder, and W. P. Leemans. Physics of laser-driven plasma-based electron accelerators. *Rev. Mod. Phys.*, 81:1229–1285, Aug 2009.

[48] S. Kiselev, A. Pukhov, and I. Kostyukov. X-ray generation in strongly nonlinear plasma waves. *Phys. Rev. Lett.*, 93:135004, Sep 2004.

[49] Antoine Rousse, Kim Ta Phuoc, Rahul Shah, Alexander Pukhov, Eric Lefebvre, Victor Malka, Sergey Kiselev, Fréderic Burgy, Jean-Philippe Rousseau, Donald Umstadter, and Daniéle Hulin. Production of a kev x-ray beam from synchrotron radiation in relativistic laser-plasma interaction. *Phys. Rev. Lett.*, 93:135005, Sep 2004.

[50] E. Esarey, B. Shadwick, P. Catravas, and W. P. Leemans. Synchrotron radiation from electron beams in plasma-focusing channels. *PRE*, 65.

[51] A. G. R. Thomas and K. Krushelnick. Betatron x-ray generation from electrons accelerated in a plasma cavity in the presence of laser fields. *Physics of Plasmas (1994-present)*, 16(10):–, 2009.

[52] I. Kostyukov, S. Kiselev, and A. Pukhov. X-ray generation in an ion channel. *Physics of Plasmas (1994-present)*, 10(12), 2003.

[53] A.G. Khachatryan, F.A. van Goor, and K.-J. Boller. Coherent and incoherent radiation from a channel-guided laser wakefield accelerator. *New Journal of Physics*, 10.

[54] A. G. R. Thomas, C. P. Ridgers, S. S. Bulanov, B. J. Griffin, and S. P. D. Mangles. Strong radiation-damping effects in a gamma-ray source generated by the interaction of a high-intensity laser with a wakefield-accelerated electron beam. *Phys. Rev. X*, 2:041004, Oct 2012.

[55] Igor V. Sokolov, Natalia M. Naumova, John A. Nees, and Gérard A. Mourou. Pair creation in qed-strong pulsed laser fields interacting with electron beams. *Phys. Rev. Lett.*, 105:195005, Nov 2010.

[56] Lorenzo Sironi and Anatoly Spitkovsky. Synthetic spectra from particle-in-cell simulations of relativistic collisionless shocks. *The Astrophysical Journal Letters*, 707(1):L92, 2009.

[57] Brian Reville and John G. Kirk. Computation of synthetic spectra from simulations of relativistic shocks. *The Astrophysical Journal*, 724(2):1283, 2010.

[58] J.L. Martins, S.F. Martins, R.A. Fonseca, and L.O. Silva. Radiation in 1.5 gev and 12 gev laserwakefield acceleration stages from pic simulations. *Advanced Accelerator Concepts: 14th Workshop*, pages 191–196, 2010.

[59] A. G. R. Thomas. Algorithm for calculating spectral intensity due to charged particles in arbitrary motion. *Phys. Rev. ST Accel. Beams*, 13:020702, Feb 2010.

[60] Peter H. Yoon. Effects of spontaneous fluctuations on the generalized weak turbulence theory. *Physics of Plasmas (1994-present)*, 12(4):–, 2005.

[61] V I Gerasimenko, T V Ryabukha, and M O Stashenko. On the structure of expansions for the bbgky hierarchy solutions. *Journal of Physics A: Mathematical and General*, 37(42):9861, 2004.

[62] T. P. Coffey. Breaking of large amplitude plasma oscillations. *Physics of Fluids (1958-1988)*, 14(7), 1971.

[63] E. Esarey and M. Pilloff. Trapping and acceleration in nonlinear plasma waves. *PoP*, 2:1432–1436, Jan 1995.

[64] C. B. Schroeder, E. Esarey, B. A. Shadwick, and W. P. Leemans. Trapping, dark current, and wave breaking in nonlinear plasma waves. *PoP*, 13:033103–1–033103–9, Jan 2006.

[65] P. Gibbon. *Short Pulse Laser Interactions With Matter*. Imperial College Press, 57 Shelton Street, Covent Garden, London, WC2H, 9HE, 1st edition, 2005.

[66] K. P. Singh. Self-injection and acceleration of electrons during ionization of gas atoms by a short laser pulse. *Physics of Plasmas (1994-present)*, 13(4):–, 2006.

[67] Changquan Xia, Jiansheng Liu, Wentao Wang, Haiyang Lu, Wang Cheng, Aihua Deng, Wentao Li, Hui Zhang, Xiaoyan Liang, Yuxin Leng, Xiaoming Lu, Cheng Wang, Jianzhou Wang, Kazuhisa Nakajima, Ruxin Li, and Zhizhan Xu. Effects of self-focusing on tunnel-ionization-induced injection in a laser wakefield accelerator. *Physics of Plasmas (1994-present)*, 18(11):–, 2011.

[68] F. F. Chen. *Introduction to Plasma Physics and Controlled Fusion*. Springer Science + Business Media, LLC, 233 Spring Street, New York, NY, 10013, 2nd edition, 2006.

[69] Brice Quesnel and Patrick Mora. Theory and simulation of the interaction of ultraintense laser pulses with electrons in vacuum. *Phys. Rev. E*, 58:3719–3732, Sep 1998.

[70] W. Lu, C. Huang, M. Zhou, M. Tzoufras, F. S. Tsung, W. B. Mori, and T. Katsouleas. A nonlinear theory for multidimensional relativistic plasma wave wakefields. *PoP*, 13:056709–1–056709–13, Oct 2006.

[71] E. Esarey, C. B. Schroeder, and W. P. Leemans. Physics of laser-driven plasma-based electron accelerators. *RMP*, 81(3):1229–1285, Aug 2009.

[72] W. B. Mori. The physics of nonlinear optics of plasmas at relativistic intensities for short-pulse lasers. *IEEE JQE*, 33.

[73] A. Taflove and S. C. Hagness. *Computational Electrodynamics*. Artech House, Inc., 685 Canton Street, Norwood, MA, 02062, 2nd edition, 2000.

[74] R. Courant, K. Friedrichs, and H. Lewy. On the partial difference equations of mathematical physics. *MA*, 100.

[75] S. Jardin. *Computational Methods in Plasma Physics*. CRC Press, Taylor & Francis Group, LLC, 6000 Broken Sound Parkway NW, Suite 300, Boca Raton, FL, 33487, 1st edition, 2010.

[76] T. Tajima. *Computational Plasma Physics*. Westview Press, 5500 Central Avenue, Boulder, CO, 80301, 1st edition, 2004.

[77] F. F. Chen. *Plasma Physics and Controlled Fusion: Volume 1*. Springer, 2nd edition, 2006.

[78] F. S. Tsung, W. Lu, M. Tzoufras, W. B. Mori, C. Joshi, J. M. Vieira, L. O. Silva, and R. A. Fonseca. Simulation of monoenergetic electron generation via laser wakefield accelerators for 5-25 tw lasers. *PoP*, 13.

[79] E. L. Lindman. "free-space" boundary conditions for the time dependent wave equation. *JCP*, 18.

[80] C. K. Birdsall and A. B. Langdon. *Classical Electrodynamics*. Taylor & Francis Group, 270 Madison Avenue, New York, NY, 10016, 1st edition, 2005.

[81] J. P. Boris and R. Lee. Nonphysical self forces in some electromagnetic plasma-simulation algorithms. *JCP*, 12.

[82] R. A. Fonseca, L. O. Silva, F. S. Tsung, V. K. Decyk, W. Lu, C. Ren, S. Mori, W. B. Deng, S. Lee, T. Katsouleas, and J. C. Adam. Osiris: A three-dimensional, fully relativistic particle in cell code for modeling plasma based accelerators. *ICCS Proceedings*, 2331.

[83] R. L. Morse and C. W. Nielson. Numerical simulation of the weibel instability in one and two dimensions. *PoF*, 14.

[84] Problems and developments of classical electrodynamics, itp website: *http* : *//www.itp.uni − hannover.de/ giulini/heraeus/seminar*475/*talks/vranic.pdf*, 2014.

[85] Igor V. Sokolov, Natalia M. Naumova, and John A. Nees. Numerical modeling of radiation-dominated and quantum-electrodynamically strong regimes of laser-plasma interaction. *Physics of Plasmas (1994-present)*, 18(9):–, 2011.

[86] Julian Schwinger. On gauge invariance and vacuum polarization. *Phys. Rev.*, 82:664–679, Jun 1951.

[87] S.T. Thornton and J. B. Marion. *Classical Dynamics of Particles and Systems*. Brooks/Cole, 10 Davis Drive, Belmont, CA, 94002, USA, 5th edition, 2004.

[88] A. G. R. Thomas. Scalings for radiation from plasma bubbles. *PoP*, 17.

[89] C. M. Huntington, A. G. R. Thomas, C. McGuffey, T. Matsuoka, V. Chvykov, G. Kalintchenko, S. Kneip, Z. Najmudin, C. Palmer, V. Yanovsky, A. Maksimchuk, R. P. Drake, T. Katsouleas, and K. Krushelnick. Current filamentation instability in laser wakefield accelerators. *Phys. Rev. Lett.*, 106:105001, Mar 2011.

[90] M. C. Kaluza, S. P. D. Mangles, A. G. R. Thomas, Z. Najmudin, A. E. Dangor, C. D. Murphy, J. L. Collier, E. J. Divall, P. S. Foster, C. J. Hooker, A. J. Langley, J. Smith, and K. Krushelnick. Observation of a long-wavelength hosing modulation of a high-intensity laser pulse in underdense plasma. *PRL*, 105.

[91] A. Popp, J. Vieira, J. Osterhoff, Zs. Major, R. Horlein, M. Fuchs, R. Weingartner, T. P. Rowlands-Rees, M. Marti, R. A. Fonseca, S. F. Martins, L. O. Silva, S. M. Hooker, F. Krausz, F. Gruner, and S. Karsch. All-optical steering of laser-wakefield-accelerated electron beams. *PRL*, 105.

[92] Y. Glinec, J. Faure, A. Lifschitz, J. M. Vieira, R. A. Fonseca, L. O. Silva, and V. Malka. Direct observation of betatron oscillations in a laser-plasma electron accelerator. *EPL*, 81.

[93] M. Born and E. Wolf. *Principles of Optics*. Pergamon, 1975.

[94] S. P. D. Mangles, G. Genoud, S. Kneip, M. Burza, K. Cassou, Cros. B., Dover. N. P., C. Kamperidis, Z. Najmudin, A. Persson, J. Schreiber, F. Wojda, and C.-G. Wahlstrom. Controlling the spectrum of x-rays generated in a laser-plasma accelerator by tailoring the laser wavefront. *APL*, 95.

[95] C. Ren, B. J. Duda, R. G. Evans, R. A. Fonseca, R. G. Hemker, and W. B. Mori. Controlling the spectrum of x-rays generated in a laser-plasma accelerator by tailoring the laser wavefront. *PoP*, 9.